UNIVERSITY OF SOUTHAMPTON

FACULTY OF ENGINEERING AND THE ENVIRONMENT

Civil and Environmental Engineering

An evaluation of the Rouse theory for the suspension of sand in a tidal inlet

by

Alanoud N. Al-Ragum

Thesis for the degree of Doctor of Philosophy

August 2015

UNIVERSITY OF SOUTHAMPTON

ABSTRACT

FACULTY OF ENGINEERING AND THE ENVIRONMENT

Thesis for the degree of Doctor of Philosophy

AN EVALUATION OF THE ROUSE THEORY FOR THE SUSPENSION OF SAND IN A TIDAL INLET

Alanoud Nasser Al-Ragum

The Rouse theory for the suspension of sand in the Oka estuary has been evaluated. The Rouse profile, which is often used to represent the vertical distribution of sand in suspension, is a function of the ratio of the sediment fall velocity to bed friction velocity. This ratio, w_s/u_*, varied with height above the bed, as it is dependent on grain diameter. The grain size of sampled suspended sand was finer near the surface and coarser near the bed. This was evident at the three anchor stations occupied at the Oka estuary, where the field work was carried out. The values of the Rouse parameter showed that the sand transport in suspension took place throughout the benthic boundary layer. The suspension threshold of Bagnold (1966) was found to discriminate accurately between bedload and suspended load. The critical Shields parameter for suspension of sand, derived from the field measurements, defines the suspension threshold better when the friction velocity is assumed constant. Laboratory work carried out to evaluate the vertical distribution of the friction velocity throughout the benthic boundary layer result in a constant distribution with height above the bed in the lower 10%. This supports the assumption made in the Rouse theory. The sand concentration profile is more complex than just Roussian, as three layers have been recognized: a Roussian layer; a buffer layer; and an inner layer. The majority (90%) of the mass flux of sand took place within the inner layer. The concentration in this layer is characterized by an exponential increase towards the bed. This profile was not asymptotic to the normally accepted bed concentration (0.65). A new simplified equation to predict sand concentration in the inner layer was generated whereby: $C_{(\frac{z}{h})} = ae^{-b(\frac{z}{h})}$, where z is height above bed and h is water depth. The reference concentration, C_a, of the Rouse profile is predicted using the inner layer equation and solving at the upper limit of the

inner layer ($z/h = 0.1$). The concentration gradient and magnitude (at a given height) were not related to shear stress or near bed flow velocity. Therefore, it is recommended that a near-bed measurement be used to define concentration at the bed, a, from which the concentration profile may be constructed.

Table of Contents

List of tables

List of figures

DECLARATION OF AUTHORSHIP

I, Alanoud Al-Ragum declare that this thesis “An evaluation of the Rouse theory for the suspension of sand in a tidal inlet” and the work presented in it are my own and has been generated by me as the result of my own original research.

I confirm that:

1. This work was done wholly or mainly while in candidature for a research degree at this University;
2. Where any part of this thesis has previously been submitted for a degree or any other qualification at this University or any other institution, this has been clearly stated;
3. Where I have consulted the published work of others, this is always clearly attributed;
4. Where I have quoted from the work of others, the source is always given. With the exception of such quotations, this thesis is entirely my own work;
5. I have acknowledged all main sources of help;
6. Where the thesis is based on work done by myself jointly with others, I have made clear exactly what was done by others and what I have contributed myself;
7. Parts of this work have been published as:

> Al-Ragum, A., Monge-Ganuzas, M., Amos, A., Cearretta, A., Townend, I., and Manca, E. 2014. An evaluation of th Rouse theory for sand transport in the Oka estuary, Spain. Continental Shelf Research, 78: 39-50.

Signed:...

Date: ....

Acknowledgements

First I would like to offer my sincere gratitude to my supervisor Prof. Carl Amos who has supported me throughout my PhD with his knowledge, guidance and patience. Thank you for introducing me to the world of sediment transport. Your valuable time, advice, and encouragement are highly appreciated.

I would like to thank Prof. Ian Townend for his wisdom and advice. Thank you for your involvement in the field work and for helping me analyze a problem from a different perspective. I would also like to express appreciation to Dr. Charlie Thompson for all her help in the lab. Thank you for taking our calls all the way from Spain to help us on some technical issues with the equipment.

I would like to thank the whole team who took part in the field work at Oka estuary and the funding projects K-Egokitzen II (Basque Government, Etortek 2010) and Harea-Coastal Geology Group (Basque Government, 80IT365-10) for allowing this campaign to happen. I thank Manu Monge and Alex Carreata for providing me with all the background information on Oka estuary and their valuable comments. I would also like to thank Eleonora Manca for documenting the whole trip with her excellent photography skills.

I would like to thank my friends and colleagues at the Coastal Engineering Program at KISR for all their support and encouragement.

Special thanks go to my friend Hachem Kassem, my Matlab genius. Thank you for taking the time of your own PhD to offer your technical and nontechnical support. I cannot thank you enough for your thoughtfulness and encouragement.

To my lovely officemates, my little brothers and sisters, thank you for your kindness and your much needed hugs. You made the office a cheerful place to work in, in spite of all the stress we go through.

To my dear friends who were there from the beginning. Thank you for being so supportive and for keeping me sane through it all. I am grateful for your encouragement.

You made me laugh when I was down and you pushed me when I felt like I could not do it anymore. I am grateful to have you in my life.

Finally, to my loving family, Sharifa, Shaima, Mohammed, Salem, Yousef, Fatma, Sara and my parents, who put their lives on hold to be my side, thank you for being there for me when I needed you the most, your love and support kept me going. I wouldn’t have been able to be where I am now without you by my side.

Definitions and Abbreviations

Symbol	Dimensions	Name
A	L	Sediment particle exposed area
a	L	Reference concentration height
a	ML^{-3}	Concentration at the bed
α	-	Impact angle sediment particle comes with the bed
$\alpha_{s,scat}$	-	Attenuation due to sediment scattering
$\alpha_{s,visc}$	-	Viscous sediment attenuation
α_w	-	Attenuation due to water absorption
b	-	Slope of concentration profile in the inner layer
β	-	Ratio of eddy diffusivity to eddy viscosity
C_a	ML^{-3}	Sand concentration at reference height a
C_D	-	Drag coefficient
C_0	ML^{-3}	Sand concentration at the bed
C_z	ML^{-3}	Sand concentration at height z above bed
D	L	Grain diameter
D_{50}	L	Median grain diameter
D_*	-	Dimensionless grain diameter
ξ_v	-	Viscous absorption term
ε_v	L^2/T	Eddy viscosity
ε_s	L^2/T	Eddy diffusivity
E	M/L^2T^2	Turbulent kinetic energy per unit volume
F_D	F	Drag force
F_G	F	Gravitational force
F_L	F	Lift force
f	-	Angular velocity of rotation
h	L	Water depth

k	-	Von Karman's constant
k_s	L	Roughness height
L	L	Length dimensional unit
L_E	L	Ekman's depth
M_g	M	Total mass
m	-	Slope of the profile of concentration using Rouse equation
P	-	Pivotal point
q_s	L^2/T	Volumetric suspended load transport rate per unit width
R	-	Rouse parameter
R_e	-	Reynolds number
ρ	ML^{-3}	Seawater density
ρ_s	ML^{-3}	Sediment density
s	-	Specific gravity
S	MLT^{-2}	Excess shear stress
δ	L	Boundary layer thickness
δ_v	L	Viscous sub-layer thickness
δ_l	L	Boundary layer thickness for turbulent smooth flow
δ_t	L	Boundary layer thickness for turbulent rough flow
θ	-	Shields parameter
θ_c	-	Critical Shields parameter
ϕ	-	Angle of repose
T	-	Transport stage
τ_0 or τ_b	MLT^{-2}	Bed shear stress
τ_c	MLT^{-2}	Critical bed shear stress
τ_t	MLT^{-2}	Turbulent shear stress
τ_v	MLT^{-2}	Viscous shear stress
τ_z	MLT^{-2}	Shear stress at height z

U	LT^{-1}	Horizontal instantaneous velocity
$\bar{U}$	LT^{-1}	Mean averaged flow velocity
U_g	LT^{-1}	Trajectory velocity
U_e	LT^{-1}	Ejection velocity
u_*	LT^{-1}	Bed friction velocity (shear velocity)
$u_{*\mathrm{crit}}$	LT^{-1}	Critical bed friction velocity
U	LT^{-1}	Horizontal velocity
u'	LT^{-1}	Instantaneous horizontal velocity fluctuation in a turbulent flow
V	LT^{-1}	Transverse instantaneous velocity
υ	L^2T^{-1}	Kinematic viscosity
V	LT^{-1}	Transverse velocity
v'	LT^{-1}	Instantaneous crosswise velocity fluctuation in a turbulent flow
W	LT^{-1}	Vertical instantaneous velocity
w_{s}	LT^{-1}	Still water grain settling velocity
W	LT^{-1}	Vertical velocity
w'	LT^{-1}	Instantaneous vertical velocity fluctuation in a turbulent flow
w'_{up}	LT^{-1}	Mean amplitude of upward-directed component of turbulent flow
w_{rms}	LT^{-1}	Root mean square amplitude of vertical component of turbulent flow
W'	F	Submerged weight
χ	-	Coefficient of proportionality of the movability number for $D_*<10$
x	L	Horizontal distance over which a boundary layer is developed
z	L	Height above bed
z_0	L	Bed roughness

Chapter 1: Introduction

Nearshore and estuarine environments serve as a domain for coastal and marine life as well as the industrial and leisure aspects of human activities (Bolaños et al., 2012). In order to manage and maintain such environments, knowledge of the physical processes at play is required. One of the most important phenomena affecting coastal habitats, water quality, and morphology, is sediment transport, which depends on the interaction between the local hydrodynamics and sediment properties (Soulsby, 1997; Nielson, 2009).

Coastlines react to various forcing mechanisms that provide the energy and momentum to drive sediment transport (Kraus, 2009). These forces can be short term, such as waves, currents, winds, and storms, or long term, such as sea level rise (Cowell et al., 2006). To date, a complete understanding of sediment transport is not possible, due to the complexity of the subject. Despite the effort of many researchers for many years, results and interpretations of various theories can differ by several orders of magnitude (Heathershaw et al., 1981).

Sediment transport is one of the biggest unknowns in estuarine morphodynamics and the evolution of a lagoon or an estuary is often governed by the net flux of the material passing through its inlet (Brunn, 1978; Jarrett, 1976). In order to predict the morphological changes of an inlet, the hydrodynamics must be known, and more specifically, the sediment transport must be determined. This budget is governed by the movement of material as bed load, in saltation, and in suspension. While the transport of sediment (sand) as bedload has been subject to considerable study (Khorram and Ergil, 2010) the movement of sand in suspension is less well understood. This is particularly true of sediment with relatively high settling rates in still water, w_s. Initiation of motion (threshold) and vertical sediment concentration distribution are important factors pertaining to sand transport in suspension. Inlets are formed largely in sandy settings. They are regions of active sand transport and are largely sheltered from waves. Therefore, they are an ideal natural laboratory to examine the factors governing sand in suspension in a tidal setting.

This thesis aims to evaluate the Rouse theory for sand in suspension and its applicability to a tidal inlet. The Rouse theory relies on empirical constants and several assumptions that may not be valid under natural conditions. A few of these assumptions were examined in the following chapters, through both field and laboratory works, where the hydrodynamics, grain size, and sand concentration in the vertical were measured under varying flows.

1.1 Scientific background

1.1.1 Tidal inlets

Tidal inlets play a major role in the sand budget of many shorelines as they influence the longshore transport of sand (Dean and Darymple, 2004). An inlet is a small waterway that connects a bay, lagoon, or an estuary to a larger body of water such as the sea (Escoffier, 1977).

The tidal flows that pass through an inlet are caused by water level differences, (the hydraulic gradient) between the sea and the lagoon (Dean and Dalrymple, 2004). The dynamics of inlet flow rely on several factors such as the geometry of the inlet and its bay, the characteristics of the bed roughness, the grain size of bottom sediments, ocean waves and tides, and sediment movement (Bruun, 1978). Diversity in tidal inlets morphology, hydraulic signature, and sediment transport patterns all adjure to the complexity of their processes (FitzGerald, 2005). Tidal inlets are typically dynamic or unstable in a natural state. As they are often used as trade or commercial shipping routes, their stability and management is of great importance. For this reason, an in-depth description of inlets follows.

1.1.1.1 Inlet Morphology

Tidal inlets can be divided into three main sections (Hume and Herdendorf, 1988): The gorge channel or the throat, where the cross-sectional area is at its minimum and wave action is relatively low; the bay with its shoals and channels, where tides are the main driving force; and finally, the ocean, where wave action is often the dominant factor. Inlets often trap the longshore transport of sand on beaches and barrier islands and can influence the onshore movement of sand.

Sand shoals that are associated with tidal inlets are located on both landward and seaward sides of the inlets. Flood currents deposit sand landward forming flood-tidal deltas, while ebb currents carry sand back out of the inlet and deposit a portion seaward, forming ebb-tidal deltas. Both the flood and ebb tidal delta's existence and size depend on the tidal range and sediment supply (Mehta and Joshl, 1988). The deepest part of an inlet, the inlet throat, is where the currents reach their maximum velocity. Figure 1.1 is a diagram of a typical inlet and its features on a barrier island coast. The strength of the currents at the throat causes sand to be removed from the channel floor and moved in suspension (Atkins, 2005). As a result, tidal inlets may be considered as a natural laboratory for the study of sand transport in suspension.

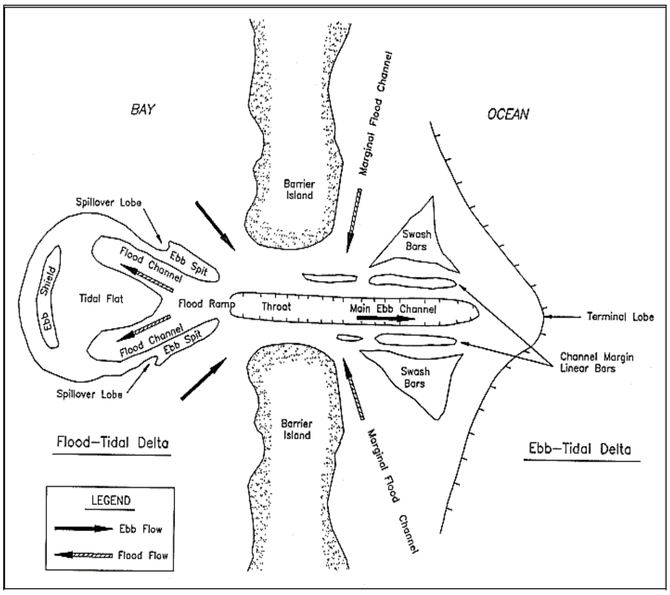

Figure 1.1: A tidal inlet with well developed flood and ebb deltas on a barrier island coast (from Morang and Parson, 2002).

The flood tidal delta's size and development are related to the region's tidal range, wave energy, sediment supply, and back barrier setting (Fitzgerald, 1982). For instance, tidal inlets that are backed by tidal channels and salt marshes usually contain a single horseshoe shaped flood tidal delta. On the other hand, inlets that are backed by large shallow bays can contain multiple flood tidal deltas. The size of the flood tidal delta increases as the amount of open water area increases (the tidal prism) (O'Brien, 1931; Bruun and Gerritson, 1959). Flood tidal deltas are found in areas with a tidal range between 1.5 to 3.0 m. They are dominated by landward oriented bedforms, which change their orientation with the change of tide (Hayes, 1980). Sand transport on flood tidal deltas is controlled by tidal elevation and tidal current strength and direction.

The ebb tidal delta results from the accumulation of sand deposited by ebb-tidal currents and is often modified by waves and tidal currents (Hayes, 1980). The general shape of an ebb-tidal delta can be used to infer the sand transport process operating at the tidal inlet. Tidal inlets are classified based on the wave energy and the tidal range of the coastal system. Davies (1964) characterized three types of coastlines: microtidal (< 2 m), mesotidal (2 to 4 m), and macrotidal (> 4 m).

Tidal inlets may be classified based on the hydrodynamic conditions of the coast (Van Rijn, 1998; Komar, 1996). These are:

- tide dominated, where tidal currents dominate the coastal morphology and the tidal range is usually mesotidal or macrotidal. The inlets are large and funnel shaped and barrier beaches are scarce or nonexistent;
- wave dominated, where the tidal range is usually microtidal and the inlets have well-developed flood deltas with small or nonexistent ebb deltas; and
- mixed energy, where the sediment transport and morphological changes are significant and inlets have well-developed ebb deltas.

The inlet of this study falls into the third category of mixed energy tidal inlets. The tidal range has an influence on the current speed which therefore affects the benthic boundary layer structure and bed shear stress distribution in inlets; aspects which will be discussed further in this thesis.

1.1.1.2 Sediment dynamics

Sediment transport to an inlet channel has a major role in determining channel stability (Goodwin, 1996). Kraus (2009) states, "*It is conceptually reasonable that the equilibrium area of a tidal inlet is determined by a balance between the transporting capacity of the inlet current and the littoral or longshore transport*". In other words, in order to obtain a stable tidal inlet there must be a sufficient supply of sand initially and this sand, which is deposited in the inlet bottom, is moved by tidal currents as both bed and suspended load into and out of the inlet. The inlet currents must not be too high or sand can either be lost from the system or accumulate at either or both ends (Hume and Herdendorf, 1988; Bruun and Gerritson, 1959).

Tidal inlets can move along the coast or remain fixed in one location (Morang and Parson, 2002). Not all of the sediment in littoral transport is trapped at inlet mouths; some of this sand may be transported through dispersion or advection. The mechanism where sand is transferred from the updrift side to the downdrift is called sediment bypassing. The main characteristics of sand bypassing of natural inlets include: 1) stable inlet processes, where sand bypassing occurs at inlets fixed in one location and the majority of the sand is dumped in the main channel and transported seawards by ebb tidal currents; 2) ebb-tidal delta breaching, where bypassing occurs at inlets with migrating main ebb channels whose throat is fixed at one position; and 3) inlet migration and spit breaching, where sediment bypassing occurs across migrating inlets in which spits are formed at the end of the barriers due to an abundant sand supply. The frequency of spit breaching is influenced by the size of the inlet, rate of migration, and backbarrier dynamics (Fitzgerald, 2005).

1.1.1.3 Human influences

Nearshore and estuarine environments support many human activities, both industrial and recreational, and provide important habitats for coastal life. Therefore it is important to monitor and manage the coastal region to provide a more sustainable development (Bolaños et al., 2012). Sediment transport is one of the most important processes in the coastal environment as it has an impact on habitats, water quality, and morphology. Natural changes in factors affecting the sediment transport processes in an inlet system result in recurring dynamic equilibrium. Any human influence on these processes will cause temporary or permanent changes to the equilibrium state. Therefore, it is difficult to establish a balance between the impact of human activities and natural conservation of the coastal environment (Liria et al., 2009).

The most common activity that significantly affects the coastal environment is the construction of seawalls (structures parallel to the shore) and jetties or groynes (structures perpendicular to the shore) (Morang and Parson, 2002; Kamphius, 2000). Jetties are usually built to protect a navigational channel from waves, stabilize a migrating inlet, or maintain a specific channel depth by reducing the required amount of dredging. On the other hand, jetties affect sand bypassing and other inlet processes. Similarly, groynes interrupt the sediment transport process causing erosion on one side and accretion on the other, therefore changing the alongshore sediment transport rates. Seawalls do not have a major impact on the alongshore sediment transport, however, under high waters, they are exposed to direct wave action. As a result, the waves will move sand away from the structures; disturbing the water flow and causing deep scour holes. Other human activities can have effects on inlet shores, especially those associated with changes of the inlet's tidal prism, sediment supply, and longshore sediment transport (Davis and Zarillo, 2003). These include construction of causeways, backbarrier filling and dredging projects, as well as engineering constructions at the shoreline. For example, dredging can increase the cross section of a gorge, while landfilling reduces the estuary's tidal prism. Most of these structures are used for shoreline protection purposes and some of their effect on sediment transport may be predicted during the design phase, but unforeseen conditions may arise, which lead to further problems (Morang and Parson, 2002).

1.1.2 Types of flow in tidal inlets

When studying sediment transport, it is essential to first determine the type of flow of the system as the motion of sediment in an inlet depends on flow structure and magnitude (Yalin, 1972). There are different types of flow that reflect the characteristics of the fluid structure and dynamics and, as a result, sediment dynamics (Liu, 2001; Leeder, 1982). These are:

- Steady versus unsteady: When flow properties such as density, velocity and pressure are constant at any point with respect to time in the inlet, the flow is considered steady. Otherwise, the flow is described as unsteady. Most flows in tidal inlets are unsteady over time scales longer than about 10 minutes.
- Uniform versus non-uniform: The flow is considered uniform when the flow has a constant velocity magnitude in the flow direction. The flow is non-uniform over ripples, dune bedforms or irregular bed topography. Most flows in tidal inlets are non-uniform.
- Laminar versus turbulent: Laminar flow usually occurs at low fluid velocity and may be visualized as fluid layers that move smoothly without mixing. Laminar flow rarely exists in coastal settings. Turbulent flow is generated by flow instability, which leads to vortices and eddies. The most common flow type is turbulent in coastal marine settings.

The distinction between flow types was first investigated by Osborne Reynolds (1883). He injected dye into a flow of water passing through a tube (Chadwick et al., 2004). The resulting flow was characterized as either laminar or turbulent using the dimensionless Reynolds number (R_e). The Reynolds number is the ratio of inertial forces to viscous forces at play and can be expressed using various length and velocity scales. In general the Reynolds number is defined as:

$$R_e = \frac{UL}{v} \tag{1.1}$$

where, U is the mean flow velocity (m/s), L is the length scale of interest (m), and v is the kinematic viscosity (m^2/s). Sediment transport and the nature of the boundary layer is strongly affected by R_e. When viscous forces dominate, R_e is small and the flow is laminar, but when inertial forces govern, R_e is large and flow is turbulent (Leeder, 1982). In open channels, the hydraulic radius were to be taken as the length scale, the corresponding threshold between laminar and turbulence (transitional) flow is at a Reynolds number of 500 (Chow, 2009). Therefore, as a general rule, open channel flow is laminar when R_e is less than 500 and turbulent when it is greater.

1.1.2.1 Turbulence

According to Reynolds, flow can be decomposed into steady and turbulent parts (the Reynolds decomposition). In context of a tidal inlet, the turbulent nature of the flow is a manifestation of the momentum flux to the bed or the bed shear stress that drives sediment transport.

Eddies in a turbulent flow generate fluctuations in the velocity (Liu, 2001). Turbulent flow is usually decomposed in Cartesian coordinates as follows:

$$U = u + u' \tag{1.2}$$

$$V = v + v' \tag{1.3}$$

$$W = w + w' \tag{1.4}$$

where U, V, and W are the instantaneous velocities in longitudinal (along flow), transverse (across flow), and vertical directions respectively; u, v, and w are the time-averaged velocities in the longitudinal, transverse, and vertical directions respectively; and *u'*, *v'*, and *w'* are the respective instantaneous velocity fluctuations (Bowden, 1978).

1.1.3 Benthic boundary layers in the coastal zone

The process of sediment transport by currents or waves is dominant in the near-bed region known as the benthic boundary layer (Van Rijn, 1993). The benthic boundary layer is that region of the flow influenced by the drag force induced by bed friction and form drag (Figure 1.2). It is a manifestation of the momentum flux (or force per unit area) imparted by the flow. It is thus important to know the magnitude and direction of the near-bed velocities and stresses in this layer in order to predict sediment transport. In rivers, it is normal to assume that the shear stress, τ, in the benthic boundary layer decreases linearly with height above the bed; it is at its maximum near the bed and zero on the surface (Yalin, 1972).

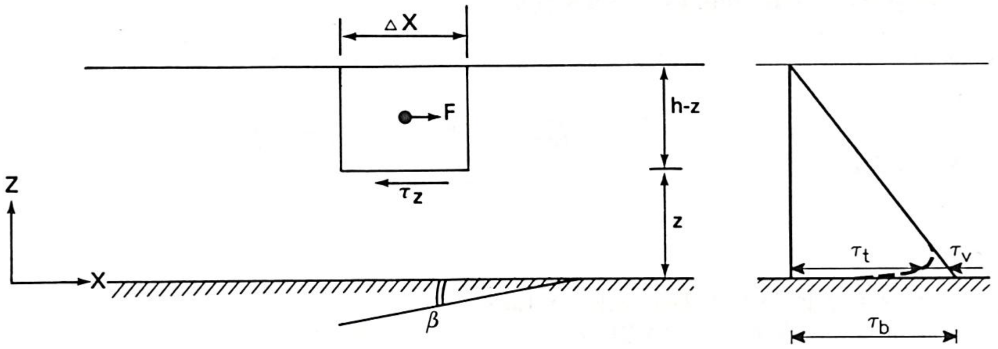

Figure 1.2: Flow force (F) and fluid shear stress (τ_z) (left) and the distribution of shear stress with height above the bed (right) where, τ_t is the turbulent-transmitted part of the stress, τ_b is the total bed shear stress, and τ_v is the viscous-transmitted part of the stress (from Van Rijn, 1993).

Derived from the equation of motion for a steady uniform turbulent flow, the shear stress at a height *z* above the bed is given by:

$$\tau_z = \rho g(h-z)sin\beta \tag{1.5}$$

where ρ is the fluid density, g is gravitational acceleration, h is water depth, and β is the bed slope. In this case, the shear stress is defined in terms of the bed slope.

At the bed (where z = 0) the bed-shear stress, τ_b, under steady uniform flow is defined as:

$$\tau_b = \rho g h \, sin\beta \tag{1.6}$$

In estuaries, where the flow is driven by the pressure gradient, bed slope is less important in defining the shear stress. In this case, shear stress at height z in a steady, uniform turbulent flow can be defined as:

$$\tau_z = \rho \upsilon \frac{du}{dz} - \rho \overline{u'w'} \tag{1.7}$$

The first term of Equation 1.7 is the viscous-transmitted part of the stress and the second term is the turbulent (Reynolds) stress. The turbulent shear-transmitted stress, τ_t, is usually dominant in the majority of the water column. The layer very close to the bed may be influenced by molecular viscosity if the bed is smooth. In the presence of roughness elements (ripples), horizontal variations in the velocity profiles and turbulence around or just above them may dominate (Soulsby, 1983). The layer dominated by viscosity is called the viscous sub-layer. Here, the shear stress is constant and the shear is transmitted by viscosity (Figure 1.3).

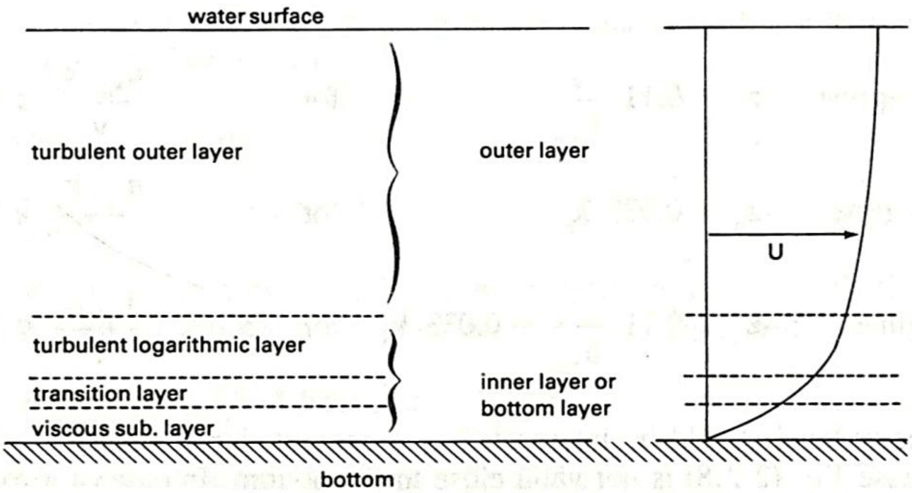

Figure 1.3: The distribution of velocity with height above bed and the current boundary layer (from Van Rijn, 1993)

The viscous sub-layer thickness, δ_v, is calculated by (Fredsϕe and Deigaard, 1992) as:

$$\delta_v = 11.6 \frac{\upsilon}{u_*} \tag{1.8}$$

where u_* is the bed friction velocity and defined as:

$$u_* = \sqrt{\frac{\tau_b}{\rho}} \tag{1.9}$$

The friction velocity, u_*, is a measure of the momentum flux to the bed and has units of m/s. It is related to the near bed turbulence and therefore is vital in understanding boundary layer dynamics (Bagherimiyab and Lemmin, 2013). When the grain size or roughness of the bed is less than $\delta_{v,}$ the bed roughness does not impact the bed shear stress or the sediment transport phenomenon.

Measurements have shown that in the viscous sub-layer, there is a linear increase of velocity with height above the bed and a slower rate of increase in the transition zone (Leeder, 1982). Above the viscous sub-layer the flow is turbulent and the velocity is proportional to the logarithm of the height above the bed. The transitional layer between the viscous sublayer and the logarithmic layer is called the buffer layer where viscosity and turbulence are equally important in the transmission of momentum to the bed. Finally, an outer layer may be found above the logarithmic layer, where the velocity is almost constant due to the presence of large eddies producing strong mixing of the flow (Liu, 2001).

The shear stress in the logarithmic layer, the most important turbulent sub-layer, is considered to be constant. This is based upon a number of assumptions and simplifications which results in an equation called the von Karman-Prandtl equation, commonly referred to as “Law of the Wall”. Because of its importance in sediment transport, its derivation is discussed below.

The Law of the Wall may be derived from a mixing length concept introduced by Prandtl (1925). Figure 1.4 shows a schematic (simplified) view of a single turbulent eddy. The speed of the upper part of the turbulent eddy in a boundary layer is $u + ½\, l\, du/dy$ and the speed of the lower part is $u – ½\, l\, du/dy$, where du/dy is the velocity gradient, where l is the mixing length across the eddy.

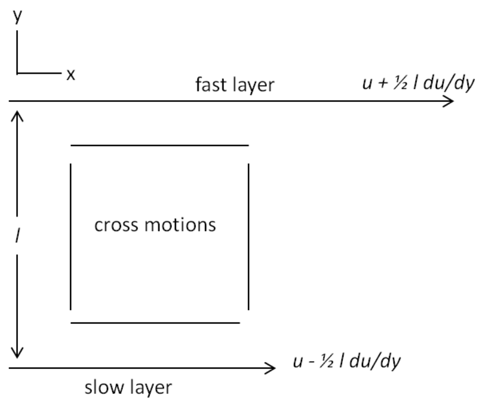

Figure 1.4: A schematic definition of flow across a turbulent eddy used in the derivation of the Karman-Prandtl equation (modified from Leeder, 1982)

In a steady state, the shear stress opposes the tendency of the active momentum transport flux to eliminate the velocity gradient. Therefore,

$$\tau' = \frac{1}{2}\rho\left(l\frac{du}{dy}\right)^2 \tag{1.10}$$

where density, ρ, is introduced to express the exchange of mass (Leeder 1982). A constant, *k*, von Karman's, is introduced to the above equation, to preserve the equality between τ', *l*, and *du*/*dy*, so that,

$$\tau = \frac{1}{2}k\rho\left(l\frac{du}{dy}\right)^2 \tag{1.11}$$

The following assumptions are usually made when deriving the Law of the Wall:

1) the boundary shear stress is equal to bed shear stress, $\tau = \tau_0$;
2) the quantity (*kl*) is proportional to the distance (*z*) from the boundary.

Rearranging Equation 1.11 we arrive at:

$$\left(\frac{\tau}{\rho}\right)^{\frac{1}{2}} = \left(\frac{k}{2}\right)^{\frac{1}{2}} l\frac{du}{dz} \tag{1.12}$$

Substituting $(k/2)^{1/2}\,l$ with 0.4*z*, the above equation can be written as,

$$du = \left(\frac{\tau}{\rho}\right)^{\frac{1}{2}} \frac{1}{0.4z} dz \tag{1.13}$$

Integrating the above equation from the bed, where $u = 0$, to height z, yields,

$$u = \left(\frac{\tau}{\rho}\right)^{\frac{1}{2}} \frac{1}{0.4} \left[\log_e z\right] + C \tag{1.14}$$

where C is the constant of integration and is defined as,

$$C = \left(\frac{\tau}{\rho}\right)^{\frac{1}{2}} \frac{1}{0.4} \log_e \frac{1}{z_0} \tag{1.15}$$

where z_0 is a constant and defined as the height where $u = 0$,

$$u = \left(\frac{\tau}{\rho}\right)^{\frac{1}{2}} \frac{1}{0.4} \left[\log_e z + \log_e \frac{1}{z_0}\right] \tag{1.16}$$

which can be simplified to,

$$u = \left(\frac{\tau}{\rho}\right)^{\frac{1}{2}} \frac{1}{0.4} \left[\log_e \frac{z}{z_0}\right] \tag{1.17}$$

The Law of the Wall is usually applied to the lowest 10 to 20% of the benthic boundary layer and is usually written as:

$$u_z = \frac{u_*}{k} \ln \frac{z}{z_0} \tag{1.18}$$

where u_z is the velocity at height z above the bed, k is the von Karman’s constant and has the value of 0.41, z_0 is the roughness length, the height above the bed at which the velocity, u, goes to zero. This equation is only applicable to turbulent rough flows (*i.e.* where no viscous sub-layer is present).

1.1.4 Hydraulic regimes

The effect of the bed roughness on the velocity distribution close to the bed may be important due to the eddies generated by these roughness elements (Van Rijn, 1993). The relative importance of the roughness is dependent on R_e. The type of flow regime (smooth, transitional, or rough) is related to the ratio of the bed roughness, k_s, to the length scale of the viscous sublayer, ν/u_*, as follows (Liu, 2001):

- for hydraulically smooth flow ($k_s/(\nu/u_*) \leq 5$), the roughness elements are smaller than the viscous sublayer thickness and therefore do not affect the velocity distribution;
- for hydraulically rough flow ($k_s/(\nu/u_*) \geq 70$), a viscous sublayer does not exist and therefore the velocity distribution is independent of the fluid viscosity and roughness influences the boundary layer;
- for hydraulically transitional flow ($5 < k_s/(\nu/u_*) > 70$), the velocity distribution is affected by both fluid viscosity and bed roughness.

The bed roughness, k_s, also known as the Nikuradse roughness, has the following suggested values (Liu, 2001):

• concrete bottom	$k_s = 0.001 – 0.01$ m
• for flat sand bed	$k_s = (1 – 10) \times D_{50}$ (where D_{50} is the median grain diameter of bed sediment)
• bed with sand ripples	$k_s = (0.5 – 1) \times$ ripple height

1.1.5 Sand transport in the benthic boundary layer

The main properties that are important in the study of sand transport include particle size, shape, density, specific weight, and fall velocity (Yang, 1996). The sediment fall velocity, w_s, is related to the flow conditions between the particle and water and can be calculated from the balance of forces between the fluid drag force and the gravitational force (Van Rijn, 1993, Figure 1.5). The fluid forces acting on a sediment particle resting on a horizontal bed consist of skin friction and pressure differences. The drag force, F_D, and lift force, F_L, are generated by the pressure differences along the surface of the particle. The gravitational force acting on the sediment particle is the particle's submerged weight, W'. A particle settling in still water will accelerate until $F_D = W'$. When the two forces are equal the settling rate, w_s, is constant. This concept is fundamental to the derivation of the laws governing non-cohesive sediment transport.

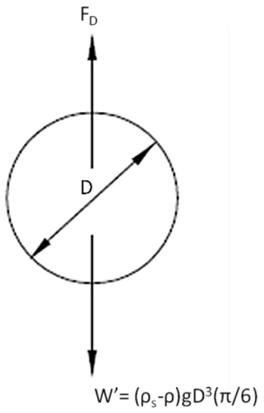

Figure 1.5: The balance of forces acting on a sediment particle (modified from Liu, 2001)

The drag force is defined as:

$$F_D = \frac{1}{2}\rho C_D A w_s^2 \tag{1.19}$$

where C_D is the drag coefficient, A is the sediment particle exposed area, and w_s is the particle fall velocity in still water. For spherical sediment particles, the balance of forces will be expressed by the following:

$$\frac{1}{2}\rho C_D \frac{\pi D^2}{4} w_s^2 = (\rho_s - \rho) g \frac{\pi D^3}{6} \tag{1.20}$$

The right hand side of Equation 1.20 is the submerged weight of a settling particle. Solving Equation 1.20 for the fall velocity, w_s, yields the following equation:

$$w_s = \left[\frac{4(s-1)gD}{3C_D}\right]^{\frac{1}{2}} \tag{1.21}$$

where $s = \rho_s/\rho$ is 2.65 for sand and D is the sediment grain diameter. The drag coefficient is a function of the Reynolds number (Van Rijn, 1993). The grain Reynolds number in this case differs in form from Equation 1.1 and is expressed as:

$$R_e = \frac{w_s D}{v} \tag{1.22}$$

For low values of Reynolds number ($R_e < 1$), the drag coefficient is defined as the following:

$$C_D = \frac{24}{R_e} \tag{1.23}$$

Equation 1.21 then can be rewritten as Stoke's Law:

$$w_s = \frac{(s-1)gD^2}{18v} \tag{1.24}$$

The drag coefficient is (nearly) constant outside the Stoke's region where $10^3 < Re < 10^5$ (Van Rijn, 1993). This results in the Impact Law, whereby:

$$w_s = \sqrt{\frac{4(s-1)gD}{3}} \tag{1.25}$$

Soulsby (1997) defined the fall velocity (w_s) based upon an empirical formula that covers the range of sizes of sand in suspension such that:

$$w_s = \frac{v}{D}\left(\sqrt{10.36^2 + 1.049D_*^3} - 10.36\right) \tag{1.26}$$

The dimensionless particle diameter, D_*, introduced in Equation 1.26 is defined as,

$$D_* = \left[\frac{(s-1)g}{v^2}\right]^{1/3} D_{50} \tag{1.27}$$

where D_{50} is the median grain diameter.

Relative density, fluid viscosity, sediment surface roughness, size, shape, suspended sediment concentration, and turbulence intensity are all factors that have an influence on the fall velocity (Yang, 1996).

1.1.5.1 Initiation of motion

Sediment particles will start to move when the flow conditions satisfy or exceed the criteria for incipient motion. There are three modes of particle motion: 1) rolling and sliding, 2) saltation, and 3) suspension (Van Rijn, 1984b). There is a certain velocity at which the fluid forces acting on the sediment particles will be adequate to move them from their stationary position. This velocity is known as the critical or threshold velocity and there is an equivalent critical or threshold bed shear stress (Dyer, 1986).

Consider a group of sediment grains with their centres lying in the plane parallel to the direction of the flow, as shown in Figure 1.6.

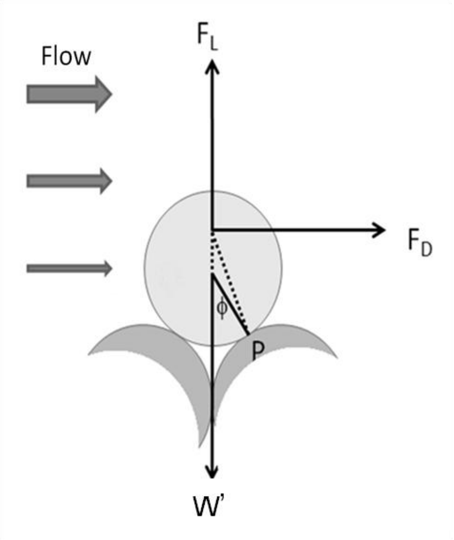

Figure 1.6: A sediment grain resting on a bed of similar grains parallel to direction of flow and their point of contact (P), angle of repose (ϕ), and F_L, F_G (W'), and F_D are the lift, gravitational, and drag forces respectively (modified from Helsby, 2008)

The angle between the line through the centre of the sediment particle at the point of contact and the line through the particle centre normal to the bed surface is called the angle of repose, ϕ, about a pivotal point, P. Balancing the forces at threshold conditions under steady near-bed flow yields:

$$W' \cos \phi = F_D \sin \phi \tag{1.28}$$

where the drag force at threshold can be written as:

$$F_D = W' \tan \phi \tag{1.29}$$

The incipient motion criterion can be derived using two parameters of the flow: (1) the bed shear stress or (2) velocity at height z (Yang, 1996). For this study, the shear stress approach is used, which is directly related to the forces at play in the transport of (non-cohesive) bed sediment.

Shields (1936) applied dimensional analysis to establish his well-known diagram of incipient motion for traction where he assumed that the drag force is equal to the submerged weight. The parameters involved in the Shields approach are shear stress, particle diameter, kinematic viscosity, and gravitational acceleration (Yang, 1996). The general equation of the entrainment function, θ, as defined by Shields is:

$$\theta = \frac{\tau}{W'} \tag{1.30}$$

Replacing the submerged weight, W', the critical threshold of the Shields function can be expressed in dimensionless form as:

$$\theta_c = \frac{\tau_c}{(\rho_s - \rho) g D_{50}} \tag{1.31}$$

where, the critical shear stress, $\tau_c = \rho u_{*crit}^2$ and u_{*crit} is the critical friction velocity. Typical values of the critical Shields parameter are in the order of 0.05 for fully turbulent flow. The critical Shields parameter becomes much larger for grain sizes in the silt range (0.004 < D < 0.063 mm) (Nielsen, 1992).

The critical bed shear stress depends on the hydraulic conditions near the bed. These conditions can be expressed by the Reynolds number, Re (Van Rijn, 1993).
Shields sub-divided the response to Re into four regions as shown in Figure 1.7:

- Region I, where $R_e < 2$ and the flow is considered laminar;
- Region II, where $2 < R_e < 10$ and the flow is considered transitional;
- Region III, where $10 < R_e < 1000$ (turbulent smooth) and the thickness of the viscous sub-layer is comparable to the particle diameter; and
- Region IV, where $R_e > 1000$, where the flow is considered hydrodynamically rough and the viscous sub-layer is thin.

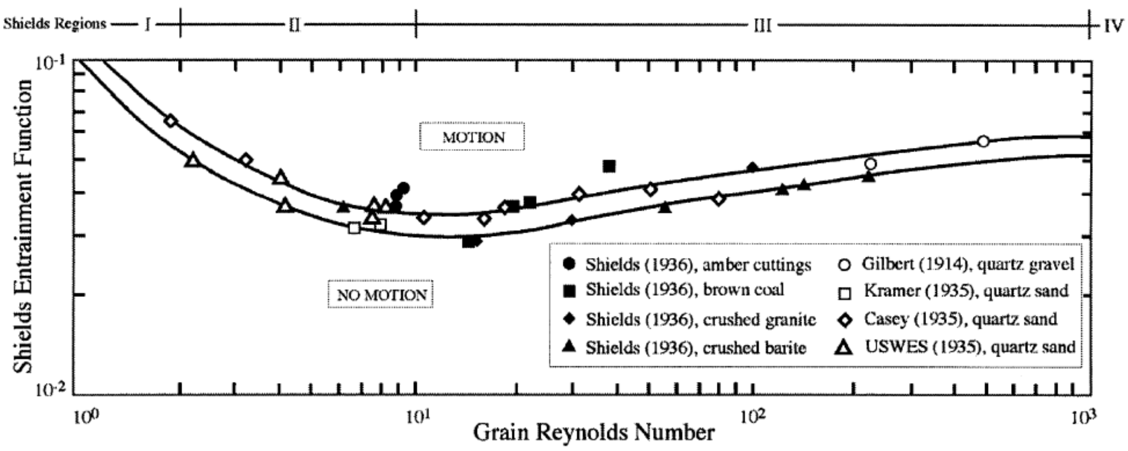

Figure 1.7: The Shields curve for the initiation of motion (from Paphitis, 2001).

Bonnefille (1963) and Yalin (1972) showed that the Shield's curve can be expressed in terms of the dimensionless Shield's parameter, θ_{cr}, and the dimensionless particle diameter, D_* (Van Rijn, 1993). Bonnefille and Yalin came up with the following algorithms:

- For $1 < D_* \leq 4$, $\theta_{cr} = 0.24D_*^{-1}$ (1.32a)
- For $4 < D_* \leq 10$, $\theta_{cr} = 0.14D_*^{-0.64}$ (1.32b)
- For $10 < D_* \leq 20$, $\theta_{cr} = 0.04D_*^{0.1}$ (1.32c)
- For $20 < D_* \leq 150$, $\theta_{cr} = 0.013D_*^{0.29}$ (1.32d)
- For $150 > D_*$, $\theta_{cr} = 0.055$ (1.32e)

1.1.5.2 Bed load transport

Bed particles will roll or slide in contact with the seabed when the shear stress just exceeds the critical value for initiation of motion (Van Rijn, 1984a). As the shear increases, the particles will move along the bed with intermittent jumps known as saltations. Rolling, sliding, and saltating are all types of bed-load transport (Van Rijn, 1993). Bagnold (1956) described bedload transport, where the particles are in continuous contact with the bed, as strictly limited by the effect of gravity. Einstein (1950) defined bedload transport as the transport of particles in a layer equal to the diameter of two particles just above the bed by sliding and rolling, therefore the effect and influence of turbulence is too small to cause suspension of particles. He believed that saltation belongs to suspended load transport and not bed load.

1.1.5.3 Initiation of suspension

It has traditionally been considered that when the value of the bed shear velocity approaches the fall velocity of the sediment particle, the particle will go into suspension. The ratio (u_*/w_S), termed the movability number by Collins and Rigler (1982) and the inverse Rouse parameter by Lee et al. (2004), is the ratio of the downward gravitational force to upward fluid force acting on a sediment particle (Van Rijn, 1993).

Bagnold (1966) developed a sand transport theory based on general physics, whereby the motion of suspended particles are governed by the following assumptions: 1) suspension of a grain occurs when its settling velocity, w_s, is equal to or less than the upward instantaneous velocity of the turbulent flow in the water column, w'_{up}; 2) the upward velocity in the water column, w'_{up}, is equal to 1.56 times the root-mean-square vertical turbulent fluctuations, w'_{rms}; and 3) the root-mean-square vertical turbulent fluctuations, w'_{rms}, is 0.8 times the friction velocity, u_*. These assumptions result in the following:

$$w_s = 1.56(0.8u_*) = 1.25u_* \tag{1.33}$$

The critical ratio (u_*/w_S) is equivalent to a constant, 0.8. Substituting w_s into the critical Shields parameter for suspension we arrive at:

$$\theta_{c,susp} = \frac{\rho u_{*,crit}^2}{(\rho_s - \rho) g D_{50}} = \frac{0.64 w_s^2}{(s-1) g D_{50}} \tag{1.34}$$

Bagnold's (1966) assumption yields:

$$\theta_{c,susp} = 0.4 \frac{w_s^2}{g D_{50}} \tag{1.35}$$

McCave (1971) suggests a similar approach to that of Bagnold, but (w'_{rms}) is 1.2 times the friction velocity, yielding:

$$\theta_{c,susp} = 0.19 \frac{w_s^2}{g D_{50}} \tag{1.36}$$

The Shields diagram showing the threshold of suspension according to Bagnold (1956) and McCave (1971) is shown in Figure 1.8.

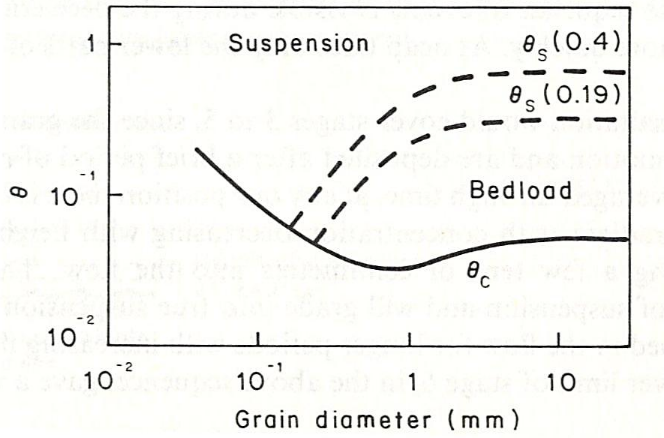

Figure 1.8: Shields diagram showing Bagnold (1956) and McCave (1971) threshold for suspension (from Dyer, 1986).

Engelund (1965) assumed that the critical ratio (u_*/w_s) for suspension is equivalent to 0.25. Delft (1982) carried out experiments to define this ratio and concluded the following:

- For $1 < D_* \leq 10$, $u_*/w_s = 4/D_*$ and

$$\theta_{c,susp} = \frac{16w_s^2}{D_*^2(s-1)gD_{50}} \tag{1.36a}$$

- For $10 < D_*$, $u_*/w_s = 0.4$ and

$$\theta_{c,susp} = \frac{0.16w_s^2}{(s-1)gD_{50}} \tag{1.36b}$$

Van Rijn (1993) modified the Shields diagram for suspension and developed the famous Shield’s curve showing the different initiation of suspension curves according to various authors as shown in Figure 1.9.

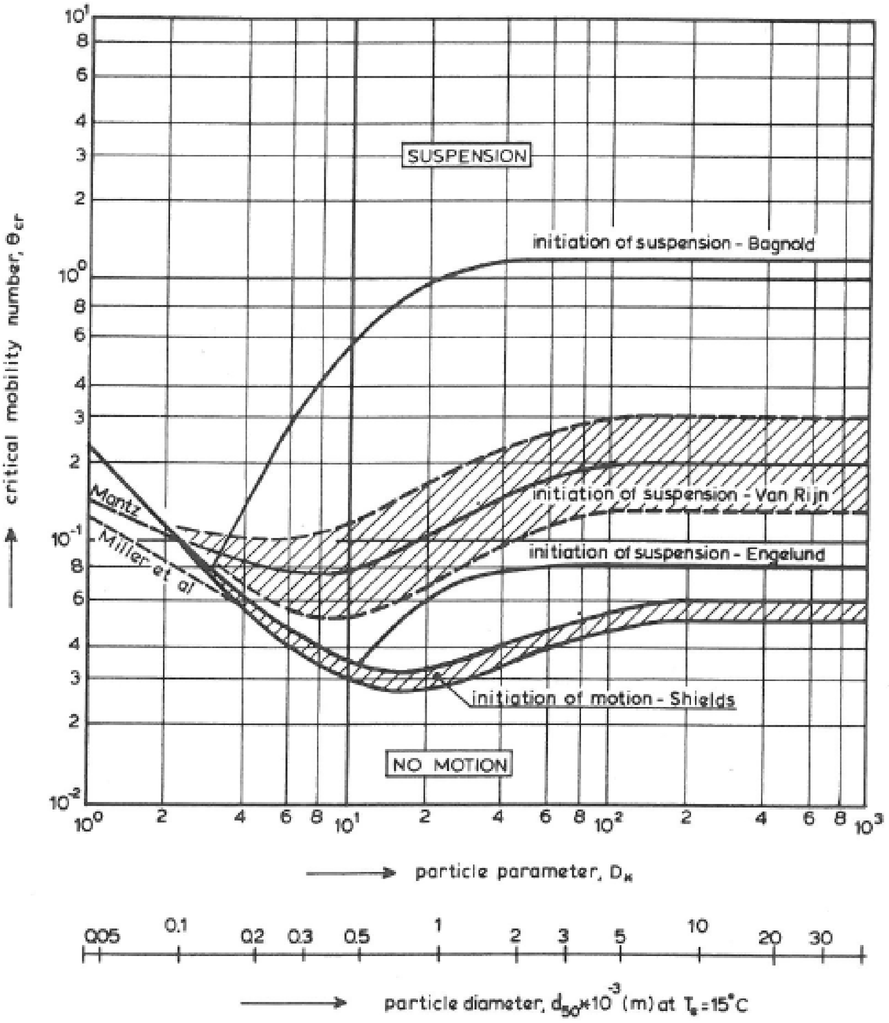

Figure 1.9: The current Shields parameter (critical mobility number) versus the dimensionless grain diameter, showing different threshold curves including the initiation of suspension curves derived in the text (modified from Van Rijn, 1993).

w_s/u_* is a key parameter in the Rouse equation, which will be discussed further, and is used in computing the distribution of sand in suspension through the Rouse equation.

1.1.5.4 Suspended load and the Rouse profile

Suspension of sand occurs when the grains are disrupted by the upward turbulent motion of the flow. The sand particles are lifted to a level in which upward turbulent drag on the sand is balanced by the submerged weight (Van Rijn, 1984b).

Several mechanisms have been proposed to account for the observed characteristics of suspension (Atkins, 2005). The behaviour of the suspended sediment particles is described in terms of sediment concentration, which is the solid mass per unit fluid volume (Van Rijn, 1993).

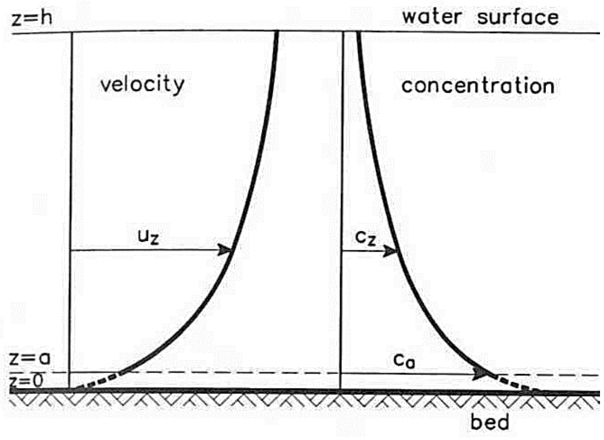

Figure 1.10: Distribution of sand concentration, c_a, with height, z, above the bed (from Van Rijn, 1993).

Observations show that suspended sediment concentration decreases hyperbolically with increasing height above the bed as shown in Figure 1.10. The rate of the decrease depends on the ratio of fall velocity to bed-shear velocity as (w_s/u_*) discussed previously.

Suspended load transport, q_s, is defined as the integration of the product of velocity, u_z, and concentration, c_z, from the bed-load layer ($z = a$), where a is defined as a reference height (top of the bedload layer), to water surface ($z = h$). The general equation of suspended load transport is:

$$q_s = \int_a^h \overline{u_z c_z}\, dz \tag{1.37}$$

where $\overline{u_z}$and $\overline{c_z}$ are time-averaged velocity and sediment concentration by volume at distance *z* above the bed (Van Rijn, 1993). Most of the flux takes place close to the bed where u and C are changing the most. Under equilibrium conditions, the downward movement of sediment due to its fall velocity (w_sC) is balanced with the upward movement due to turbulent fluctuations.

$$w_s C + \varepsilon_s \frac{dc_z}{dz} = 0 \tag{1.38}$$

where ε_s is the turbulent diffusion coefficient for sediment. The turbulent diffusion or mixing coefficient for suspended sand is defined as $\varepsilon_s = \beta v$, where v is the kinematic eddy viscosity and β is a factor used to describe the difference in the diffusion of a fluid particle and a sediment particle and it is assumed to be constant over depth (Van Rijn, 1993). Many models exist for ε_s with height and β is questionable. Theoretical and laboratory investigations indicate that β is not simply a function of particle parameters alone; as turbulent characteristics of the flow may influence how mass diffuses in momentum (Hill et al., 1988). In a constant stress region, analysis of the vorticity dynamics results in a value of β of unity (Tennekes and Lumely, 1972). Therefore, diffusivity of mass in relation to that of momentum depends on vorticity dynamics of the flow. This will not be evaluated as part of this thesis and β is assumed to be unity.

Using the Law of the Wall yields a turbulent diffusion coefficient as:

$$\varepsilon_s = \beta u_* k \frac{z}{h}(h - z) \tag{1.39}$$

Re-arranging Equation 1.37 and replacing $\frac{w_s}{ku_*}$ with R, we get

$$\frac{dc}{C} = -\frac{Rdz}{\beta \frac{z}{h}(h - z)} \tag{1.40}$$

Integrating Equation 1.39 with respect to z, yields to

$$\int_a^z \frac{dc}{C} = -\int_a^z \frac{Rh}{z(h - z)} dz \tag{1.41}$$

which results in the Rouse (1937) Equation:

$$\frac{C}{C_a} = \left(\frac{h-z}{z} \frac{a}{h-a}\right)^R \tag{1.42}$$

Rouse (1937) initially proposed upward diffusion as the main mechanism where the particles move across concentration gradients from areas of high concentration to areas of low concentration in a turbulent boundary layer (Atkins, 2005). The Rouse profile is often used to represent the vertical distribution of suspended sediment but the approximation of the Rouse profile is valid only when the sediment is largely transported in the benthic boundary layer (Amos et. al, 2010a). The reference height, a, and the concentration at this height, C_a, has various expressions in the literature based on different assumptions and the question of its existence is still unanswered.

The Rouse parameter is defined as:

$$R = \left(\frac{w_s}{\beta \kappa u_*}\right) \tag{1.43}$$

The von Karman's constant, *k*, is usually set to an accepted value of 0.41. Reviews to experimental data led to values of *k* from 0.33 to 0.43 (Bailey et al., 2014). The validity of this constant has been evaluated by Villatoro et al., (2010) and Amos et al., (2010b), where the average values of 0.42 ± 0.08 and 0.37± 1 were obtained by the inversion of the Law of the Wall. These values correspond well with the accepted value of 0.41 used in the literature. Since there are many reviews in the literature on the value of *k*, which all result in the range of the accepted value, therefore 0.41 will be used and the von Karman's constant will not be evaluated as part of this thesis.

The Rouse equation was derived from a two dimensional logarithmic velocity distribution of a turbulent flow. This assumes a constant shear stress, and since friction velocity is related to shear stress through $u_* = \sqrt{\frac{\tau}{\rho}}$, it is also assumed constant. Since the Rouse theory is based on a single grain size, w_s is assumed to be constant, therefore the ratio w_s/u_* is constant. The validity of these assumptions will be evaluated further in the thesis.

Van Rijn (1993) defined the type of distribution of suspended sand over depth in the following Table:

Table 1.1: The type of suspended distribution over depth for different Rouse parameters.

$\left(\frac{w_s}{\beta \kappa u_*}\right)$	$\left(\frac{u_*}{w_s}\right)$ (k = 0.41, β = 1)	Suspended distribution over depth
5	0.5	Suspension in near-bed layer ($z < 0.1h$)
2	1.25	Suspension up to mid-depth ($z < 0.5h$)
1	2.5	Suspension up to water depth
0.1	25	Suspension almost uniformly distributed over depth

1.2 Aim and objectives

The aforementioned theories contain considerable uncertainties that influence the mass transport of sand in a tidal inlet. This thesis endeavours to examine some of these uncertainties.

The aim of this study is to evaluate the validity of the Rouse theory for describing the distribution of sand in suspension throughout a turbulent benthic boundary layer of a tidal inlet. In order to achieve this aim, the following objectives must be accomplished:

- to define the vertical distribution of sand in suspension over a range of tidal conditions;
- to evaluate the relevance of the concept of a reference level, a, and reference concentration, C_a, in the Rouse equation;
- to evaluate the magnitude of friction velocity, u_*, through the boundary layer under varying flow types; and

- to determine the threshold conditions for traction and suspension in a tidal inlet; and
- to quantify total mass transport of sand in the near-bed layer over a tidal cycle in a tidal inlet.

One of the assumptions in the Rouse (1937) theory is that the ratio of the settling velocity of sand in suspension to the bed friction velocity (w_s/u_*) is a constant, when in fact it is not (Van Rijn, 1993). There is growing evidence to suggest that it is dependent on height above the bed, Reynold's number, and grain size. Accurate predictions of sand transport are not possible unless this ratio is accurately defined (Amos et. al, 2010b; Villatoro et. al, 2010). The analysis of this ratio is one of the objectives of this study.

Another issue that is not well-defined in sediment transport is the distinction of the transition zone in the vertical between bed-load and suspended load (Van Rijn, 1993). The level at which bed-load is considered to be suspended load is called the reference level, a, which is one of the parameters in the Rouse equation. It is commonly assumed that the reference level is slightly above the seabed, a couple of multiples of the grain size, or at the height of the bed roughness (Dyer 1986). Due to the essential role in scaling of the concentration profiles, a reference concentration level and its magnitude must be clearly defined. A second objective of this study will be to define the existence, and where relevant, the magnitude of the reference concentration.

Bottom shear stress is usually represented by the friction velocity (Liu, 2001). Since shear stress decreases linearly with height in the benthic boundary layer, friction velocity, u_*, is also assumed to decrease with height. The Rouse formulation takes u_* to be constant in the vertical. Determining whether the friction velocity (u_{*z},) varies with height or remains constant is the third objective of this study.

In the present study, the Rouse profile will be evaluated by collecting field data as well as by undertaking laboratory work. The main factors that influence sand transport, such as grain size and water flow, will be used to define a more precise relationship between sand in suspension and sand and flow properties for prediction purposes. The perceived outcome is a better understanding of sand transport in tidal inlets and better model predictions.

Chapter 2: Study region

2.1 Introduction

This study was undertaken in a sandy tidal inlet where exchanges of sand are known to take place. The Basque coast was chosen as the study region as it has been the focus of many studies on tidal inlets for the past three decades (for a full list, please refer to Rallo and Borja, 2004). Although the coastal zone represents only 12% of the Basque country's total surface area, it is occupied by 60% of the population (Cearreta et al., 2004). The human impact during the last two centuries on the coastal area is manifest in the local physical, chemical, and biological oceanography. The region has more than 25 coastal municipalities, two large ports, Bilbao and Pasaia, 14 fishing ports, and five marinas (Borja and Collins, 2004). The Basque coast is influenced in many marine activities, both industrial and touristic. Recently, the Basque local authorities have expressed a growing concern on the environmental importance of the region and great efforts have been dedicated to its conservation and restoration (Cearreta et al., 2004).

Given the great importance of the Basque coastline in general and the Oka estuary in particular, investigating the sedimentary processes is a necessity to increase the knowledge of the area for purposes of coastal zone management (Monge-Ganuzas 2008). The focus of the present study is the Oka estuary due to its UNESCO Biosphere Reserve status. Different names are used for this estuary. For example Mundaka, Oka, and Urdaibai all refer to the same estuary (Borja and Collins, 2004). In order to avoid confusion, a criterion was adopted to name the estuary according to the river that flows through it. Therefore, throughout the rest of the thesis, the estuary will be referred to as the Oka estuary.

2.2 General background on the Basque coast

2.2.1 Morphology

The Basque country is located in the innermost part of the Bay of Biscay (Figure 2.1). It serves as a hinge between the rocky coasts of Spain and France's sandy beaches (Borja and Collins, 2004). The nature of inner part of the Bay of Biscay along the Basque coast is either flat with marshes and dunes or rocky with high and sharp cliffs (Rallo and

Borja, 2004). The northern Basque coastline (150 km long) and the adjacent continental shelf system comprise an interesting area consisting of 1) high and steep mountainous areas adjacent to the coastline, 2) a coastline of semi-enclosed embayments surrounded by cliffs from 20 to 150 m high, and 3) a very narrow continental shelf (less than 20 km wide) cut by tectonically-controlled obliquely-oriented submarine canyons (Cearreta et al., 2004; Pascual et al., 2004). Most of the coastal depositional areas are confined within small estuaries up to 15 km maximum length and less than 1 km wide. The dominant wind direction is from the northwest, which causes sand transport to form spits on the eastern margin of the estuary mouths (Cearreta et. al., 2004).

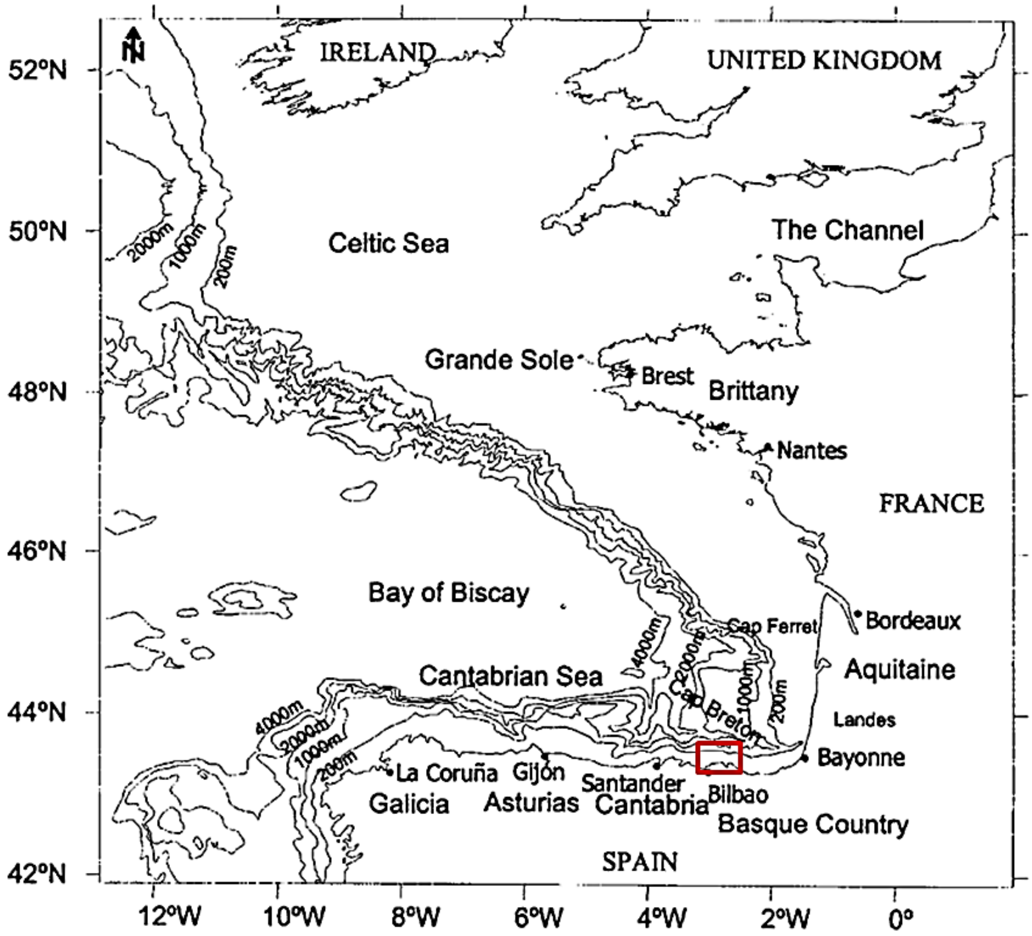

Figure 2.1: The location of the Basque coast in relation to the Bay of Biscay. The red box indicates the study area (modified from Borja and Collins, 2004).

Most of the largest beaches of the region are associated with the sand bodies on the adjacent continental shelf (Pascual et al., 2004). The sand deposits are moulded into ripples and megaripples caused mainly by wave action, since steady currents velocities in the region are usually low. An unusual characteristic of most of the sandy spits on the estuarine mouths is that they lie to the east of the main rivers discharging to the sea (Monge-Ganuzas et al., 2014). This could be due to the orientation of the coast to the predominant wave climate. As waves originate from the northwest the rivers find protection in the cliffs to the west of the embayment. This allows the growth of the beaches to the east of the river mouths (Pascual et. al., 2004). This growth is opposite to the direction of wave propagation to the shoreline and has led to considerable speculation on sand transport mechanisms in the coastal zone of the region.

2.2.2 Sediment transport

Uriarte et al. (2004) were the first to establish a general model explaining the pattern of sediment transport on the Basque coast and adjacent continental shelf (Figure 2.2). In the nearshore zone, sediment transport is governed by various combinations of wind-, wave-, and tidally-induced current patterns, while offshore, wind-induced currents are the most common driving forces (Monge-Ganuzas et al., 2014). However, wind-induced currents are insignificant to the transport of coarse material. In the offshore area, tidal currents do not influence sediment transport. Overall, the currents tend to cause sediment dispersion onto the shelf, with a tendency for net easterly transport (Uriarte et al., 2004).

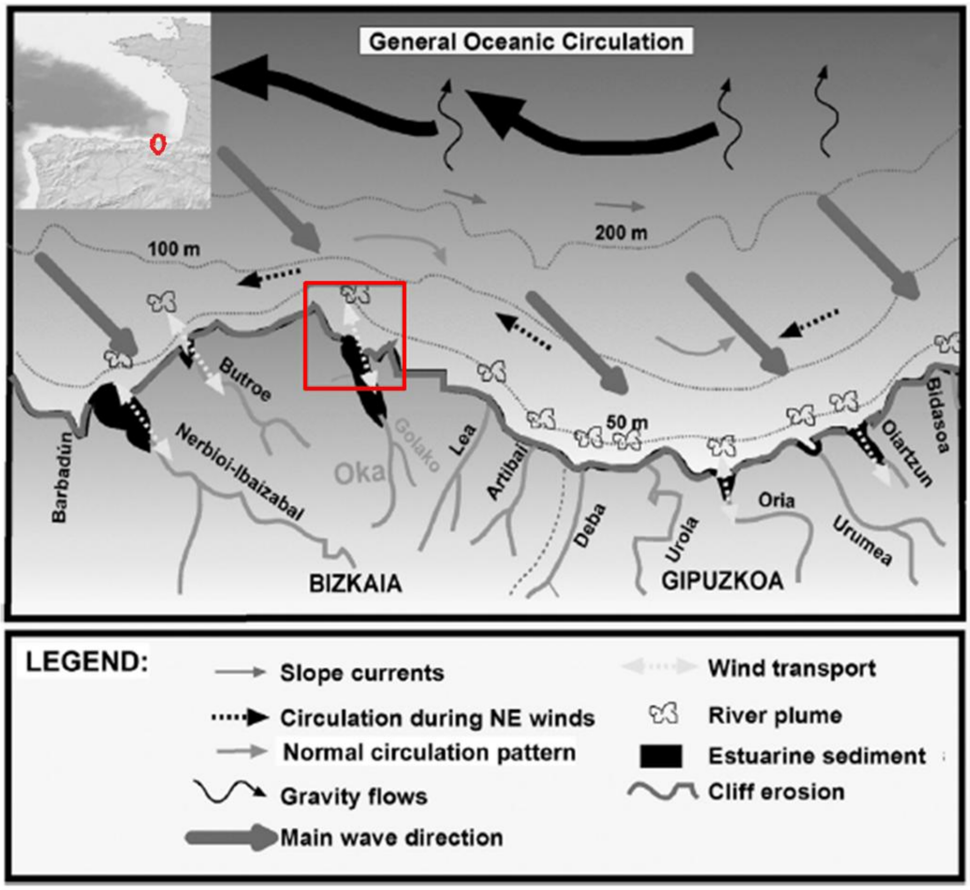

Figure 2.2: A schematic representation of the sediment supply and dispersion on the Basque coast and adjacent continental shelf. The study area is highlighted with a red border (modified from Monge-Ganuzas et al., 2014).

In general, the major part of the sediment supplied by rivers (1.57 x 10^6 t/yr) is trapped within estuaries and is reworked by estuarine water circulation (Evans and Prego, 2003), while the rest of the sediment is transported to the continental shelf as suspended load. Also, sand is introduced from the open sea into the estuaries due to wave and tidal action (Monge-Ganuzas et al., 2014). Hence, an estuary can be considered as a sedimentary trap filled with sand, from the adjacent continental shelf, and mud, from nearby rivers in a manner described by Dalrymple et al. (1992).

A unique feature of the Basque coastline is that the majority of the sand spits or the barriers of the beach sands extend westwards while eastwards is the expected direction since the dominant wave approach is from the northwest (Uriarte et al., 2004). In terms of sediment distribution and transport processes, limited information is available for the continental shelf of the Basque country. The Oka estuary has been chosen as the study area specifically due to its well-preserved natural conditions (Monge-Ganuzas et al., 2014). The study outcomes may then be implemented on other estuaries of similar nature.

2.3 Oka Estuary

The Oka estuary is located in the southeast of the Bay of Biscay (Figure 2.3). The estuary has an elongated morphology in the north-south direction with a maximum width of 1 km and is 12 km long with an intertidal area of about 2 km^2 (Monge-Ganuzas, 2008).

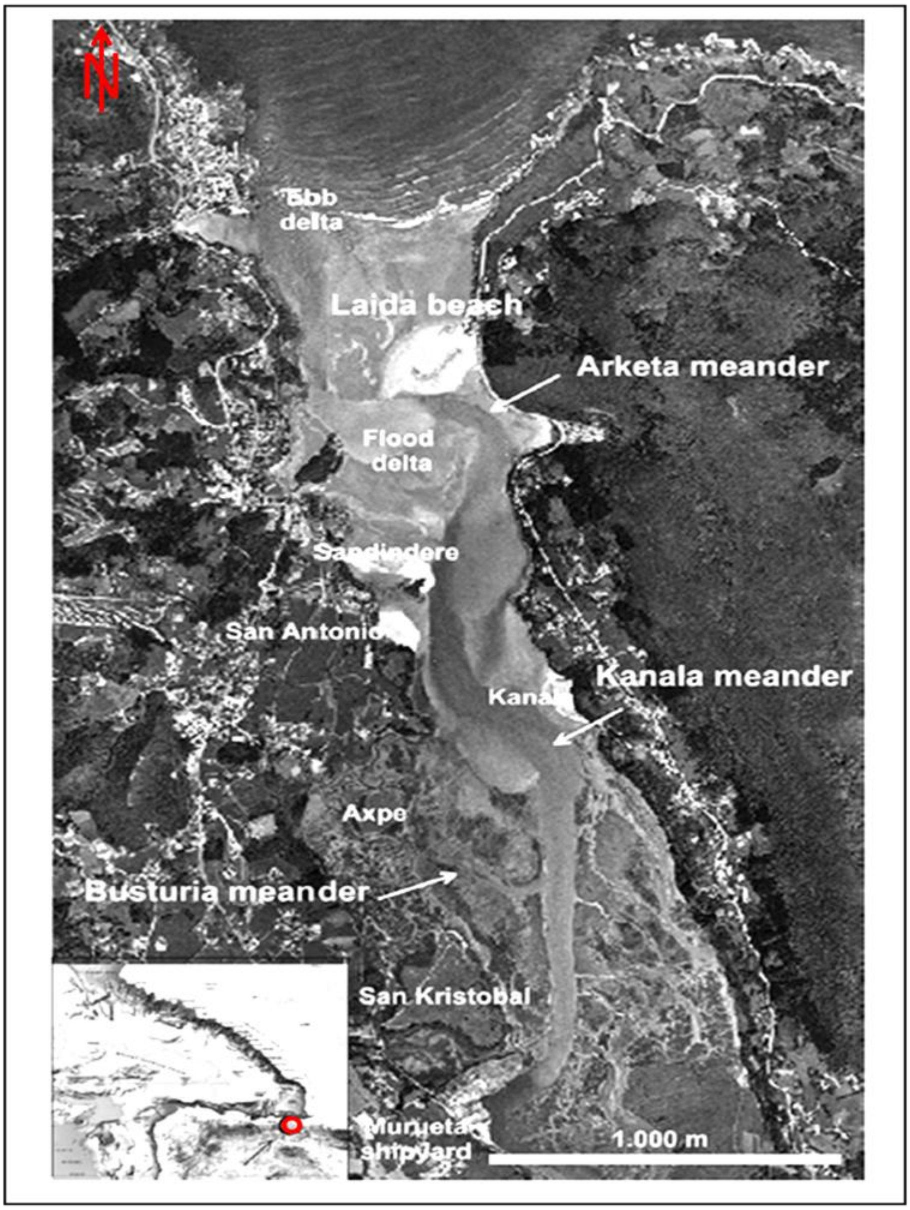

Figure 2.3: Location of the Oka estuary highlighting the major morphological features. The red circle indicates the location within the Bay of Biscay (modified from Monge-Ganuzas et al., 2013).

It is one of the main estuaries of the Bay of Biscay as it covers 22 municipalities situated between Cape Matxitxako and Cape Ogoño (Figure 2.4). The Oka estuary is bounded by the Cantabrian Sea and Izaro Island from the north, Sollube Mountain from the west, and holm oak forests and Mountain Oiz from the south. The sides of the estuary reach a maximum altitude of 400 m. The slopes of the estuary are steep, especially in the east (where elevation varies between 200 to 250 m), while the west side is more levelled (Monge-Ganuzas, 2008).

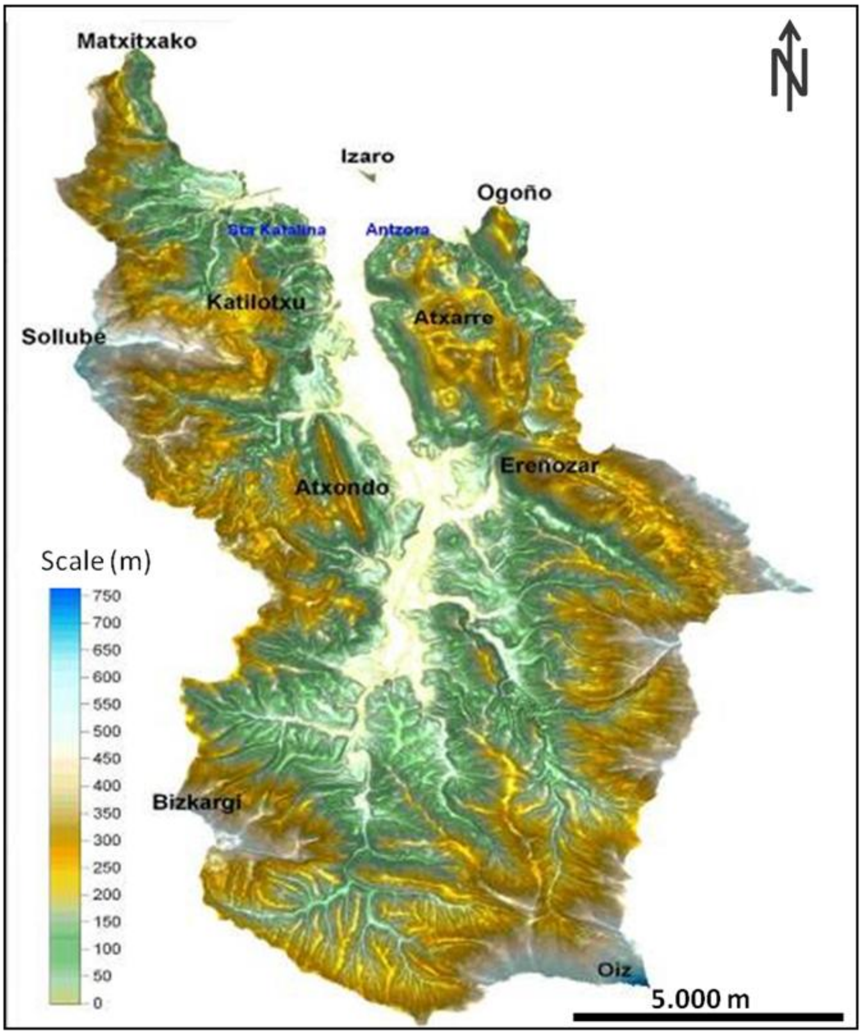

Figure 2.4: A digital terrain model of the Oka estuary and its surrounding mountains. The highest point is at Mountain Oiz (800 m) (from Monge-Ganuzas, 2008).

By the second half of the 19th century, human activity had transformed 60% of the original Oka estuary through marsh reclamation for agricultural purposes (Cearreta et al., 2004). In 1984 the Oka estuary was granted a UNESCO Biosphere Reserve status and it is considered as the best preserved estuary of the Basque coast.

2.3.1 The evolution of Oka estuary

The main physical impact on the Oka estuary has resulted from dredging of the sand by the shipyard company “Astilleros de Murueta” (Cearreta et al., 2004). The first dredging operation was carried out in 1977 (Pascual et al., 2004) and the last dredging activity (287,000 m^3) was carried out in 2003; however, the natural infilling with sand continues to the present day (Monge-Ganuzas et al., 2008).

The morphological evolution and development of the Oka estuary during the past 50 years has been monitored and assessed using Geographical Information System (GIS) along with photos and historical information (Monge-Ganuzas et al., 2013). Figure 2.5 demonstrates the morphological changes from 1957 to 2005, thus before and after dredging operations.

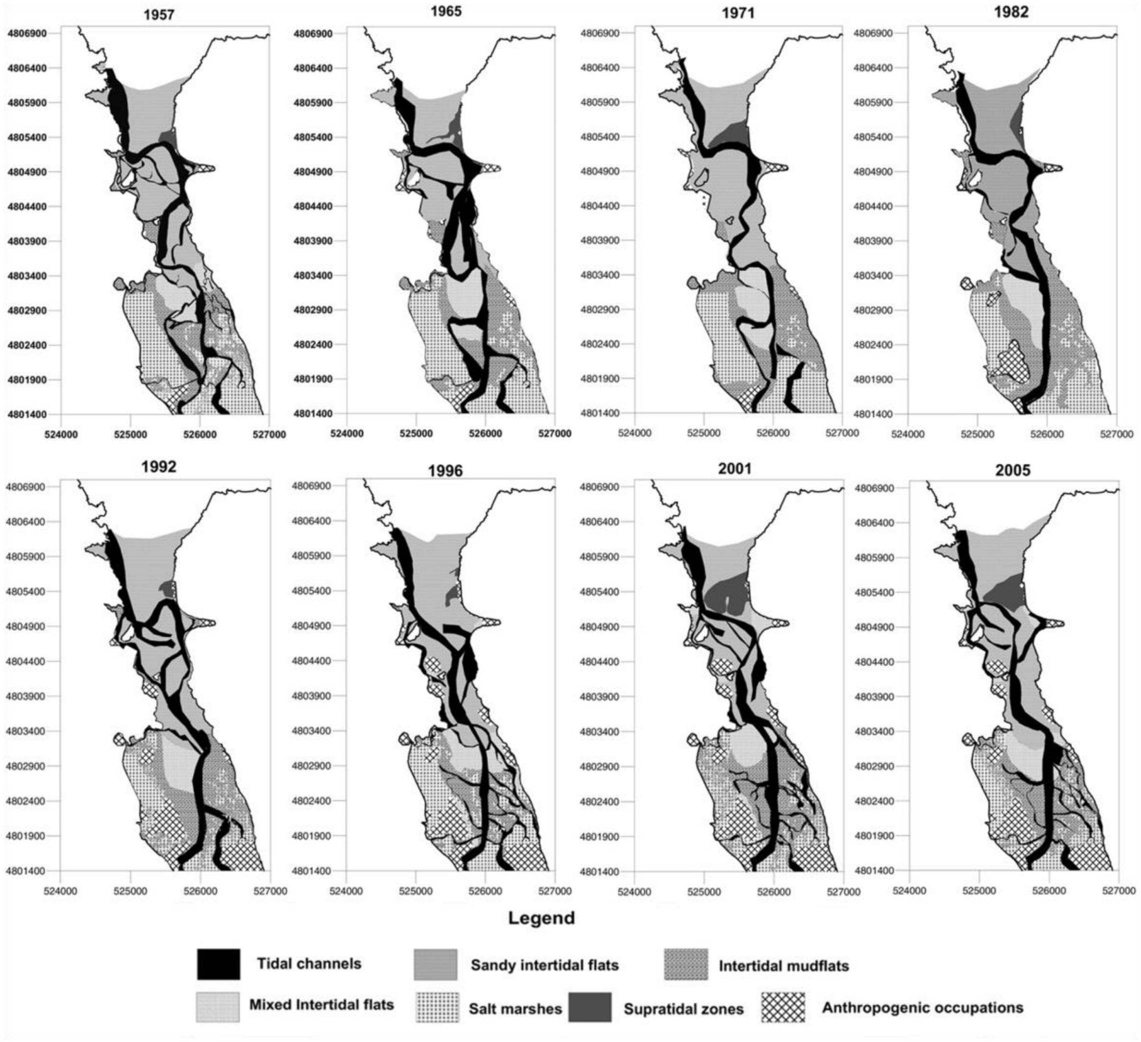

Figure 2.5: The morphological evolution of the Oka estuary for the period 1957 to 2005 (from Monge-Ganuzas et al., 2013).

During the period 1957 – 1977 no dredging was carried and therefore no significant changes occurred and any sedimentary movement was due to natural dynamics of the system (Monge-Ganuzas, 2008). For the first dredging activity, a total of 223,000 m^3 of sand was dredged from the main ebb channel of the estuary and dumped at San Kristobal and Axpe salt marshes (Figure 2.6) (Monge-Ganuzas et al., 2013). This dredging activity affected the meandering channels of Busturia and Kanala (Figure 2.3) and transformed them into a single straight channel. During this time Laida beach was eroded and its morphology continued to vary throughout the years. Dredging and dumping activities carried out the following years altered the natural distribution of the flow channels, such as the deterioration of the Arketa meander, and the sediment dynamics of the lower Oka estuary (Monge-Ganuzas, 2008).

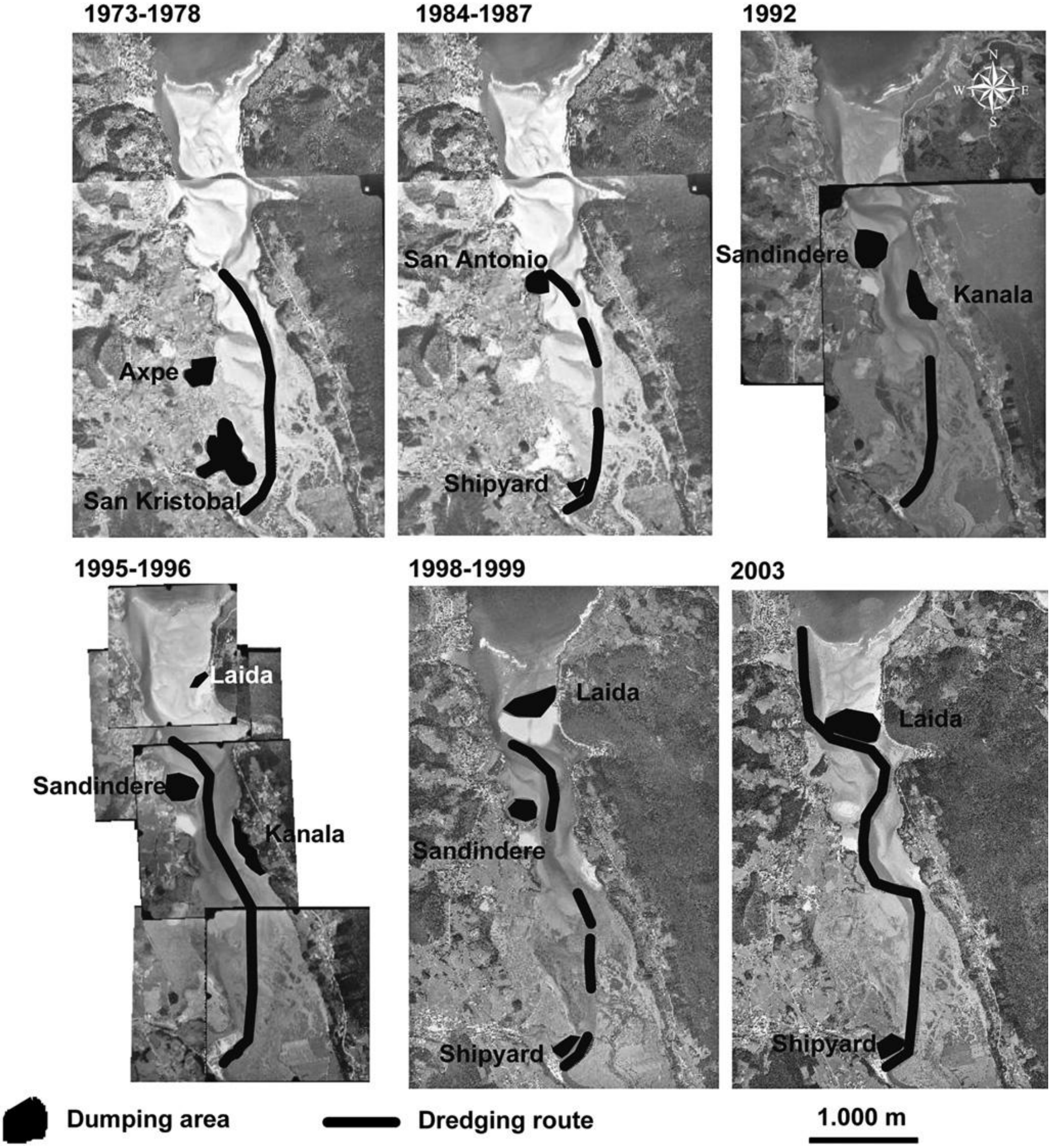

Figure 2.6: The dredging routes and dumping areas carried out in the Oka estuary for the period between 1957 and 2005 (from Monge-Ganuzas et al., 2013).

In order to maintain the main ebb channel's width of 40 m, a total of 50,600 m^3 of sand was dredged in 1998 (Monge-Ganuzas et al., 2013). The same area was dredged again in 1999 extracting an additional 42,000m^3 of sand. Most of the sand was dumped at Laida beach causing its supratidal zone to expand (Monge-Ganuzas 2008). The width of the tidal inlet decreased and the flood delta was developed. The ebb-tidal delta channel migrated in a northwest direction in an attempt to restore the original configuration.

In 2003, during the last dredging activity, 243,000 m^3 of the extracted sand was deposited on Laida beach (Monge-Ganuzas et al., 2013). The main ebb channel once again started to migrate to the north. The sand deposits at Laida beach increased the amount of sediment available for transport into the mouth of the estuary. The length of the flood tidal delta increased and prograded to the east. Since then, Laida beach developed a more stable supratidal zone, and hence, decreased the variability in its morphology (Monge-Ganuzas, 2008).

The continuous dredging and dumping activities altered the natural channel distribution of the lower Oka estuary and its sediment dynamics. These operations caused a morphological and sedimentary imbalance of the ebb and flood channels and the adjacent intertidal zones (Monge-Ganuzas et al., 2013).

2.3.2 General climate

The Basque country is located in the middle latitudes of the eastern North Atlantic Ocean, where the climate is temperate (Usabiaga et al., 2004). The winters are moderate and summers are warm. Rain is more frequent during autumn and less frequent in July with average values close to 6 mm (Monge-Ganuzas et al., 2014). The temperature during autumn-winter season varies from 5 to 20 °C, with January being the coldest month with a mean temperature of 7.6°C. During spring-summer it ranges from 15 °C and can reach above 30 °C. August is the warmest month with a mean temperature of 18.6°C. Relative humidity was highest during autumn-winter with an average of 80% and during spring-summer the average reached 70%.

Part of the Basque coast is exposed to large storms from the North West due to its location within the Bay of Biscay and the North Atlantic (Gonzalez et al., 2004). During the summer, local North East winds predominate, generating North East waves within the bay. The dominant wind direction at the Oka estuary from October to March is from the north-west, with an average speed of 4 m/s and a maximum of 11 m/s. During the period from April to September, dominant winds come from the east-southeast with an average speed ranging from 1 to 2 m/s and a highest value recorded was 6 m/s.

Waves propagate mainly from the North West direction and are categorized as either swell (long period waves resulting from non local winds) or sea (short period waves forced by local winds) (Monge-Ganozas et al., 2008; Liria et al., 2009; Thomson and Rogers, 2014). Data collected by the Bilbao Buoy (N 43.64º, W 3.05º) for the period between 1999 and 2003 were used to characterize the offshore wave climate affecting the Oka estuary (Monge-Ganozas et al., 2008). The wave climate seasonal changes summarized in Figure 2.7 as follows: in the summer (June – August), sea waves dominate with a maximum period of 9 s. Waves with periods longer than 10 s occur less than 25% of the time. Waves are usually low with a significant wave height of 1.5 m. Waves higher than 2 m occur only 10% of the time. During winter (December – February) swell waves are dominant with a maximum period of 13 s and waves occur shorter than 10 s less than 20% of the time. Waves are usually high where heights exceed 2 m more than 50% of the time. The significant wave height is 2.5 m (Monge-Ganozas et al., 2008; Liria et al., 2009). Spring and autumn are considered transition periods where intermediate values are observed. Under extreme conditions and large storms, wave heights can exceed 10 m with a 20 year return period (Liria et al., 2009).

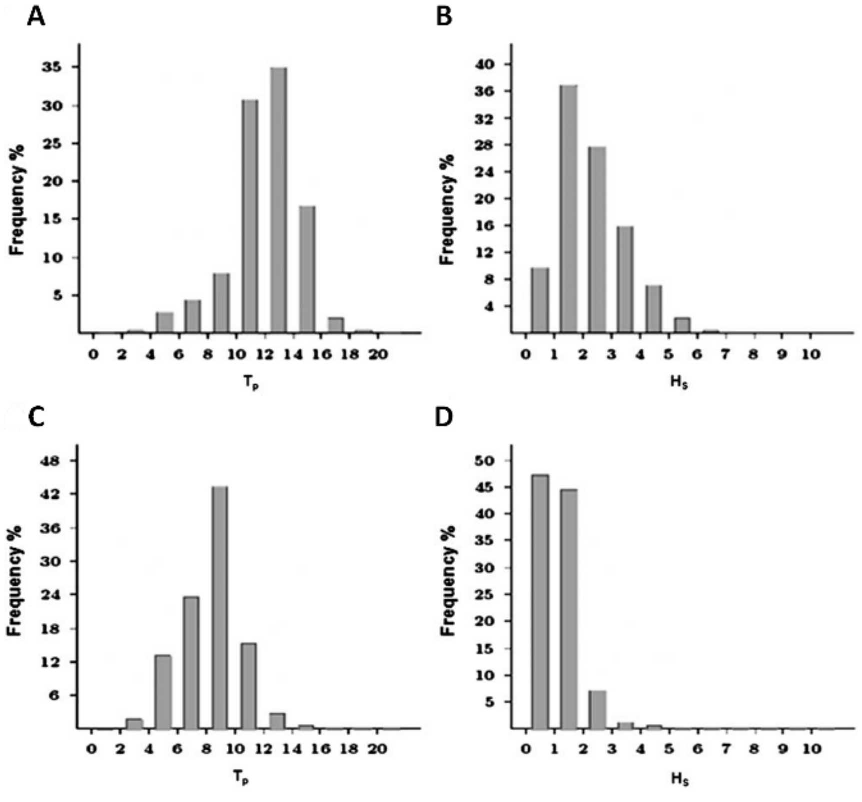

Figure 2.7: The average wave data (from Bilbao Buoy) showing the frequency of the wave period, T_p, and significant wave height, H_s, during winter (A, B) and summer (C, D) (modified from Liria et al., 2009)

Waves break on the ebb tidal at the Oka estuary mouth, near the Mundaka port, under normal conditions. During large swell and low tide, the wave fronts with the ebb tidal delta and the bottom slope generates a wave that covers over 400 m. This wave is known as the “Mundaka left wave” as it breaks from right to left when viewed from the sea. The most suitable conditions to form the famous Mundaka surfing wave are moderate to intense waves, low tide (more likely during spring tide), and southerly or westerly winds (Monge-Ganozas et al., 2008). Therefore, winter is the most likely period for surfing at Mundaka. However, the quality of surfing depends on the morphological changes of the ebb tidal delta throughout the year.

The effect of tidal currents is minimal along the Basque coast and increases towards the north west of the Bay of Biscay (Gonzalez et al., 2004). The effect of the astronomical tides on sea surface oscillations is greater than the effect of wind. Along the Basque coast, the combined effect of waves and currents is the main cause of sediment transport. Wave-induced currents cause the resuspension of the sediments which are then transported by wind- and tidally-induced currents.

2.3.3 Hydrodynamics

The Oka river's average flow input is 3.74 m^3/s (Monge-Ganuzas, 2008). The tidal wave in the Bay of Biscay is semi-diurnal and standing (*i.e.* peak flows at mid tide) (Monge-Ganuzas 2008). It enters from the west and progresses northwards along the eastern coastline. The mean tidal prism is $4.5x10^6$ m^3. The mean tidal range during neap tides is 1.5 m and during spring tides the tidal range is 4 m. Therefore, the region is characterized as 'low meso-tidal' and 'high meso-tidal' during neap and spring tides respectively (Hayes, 1975). The flood phase is shorter than the ebb during spring tides and as a result, stronger currents are produced on the flood and periods of slack water are longer during low tide (Monge-Ganuzas et al., 2013).

The energy around the lower estuary (entrance) has speeds of around 1m/s (Monge-Ganuzas, 2008). As the tidal wave enters the estuary it decreases its capacity, due to the dissipation of energy along the margins of the estuary and the seabed. Therefore, lower speeds were recorded at Kanala (0.25 m/s). On the eastern part of the outer estuary along the rocky cliffs is the most energetic area due to wave action that transports sediment by surf and swash processes.

2.3.4 Sediment dynamics

Sand in the Oka estuary is mixed and mainly composed of quartz (84%). The grain size pattern of the surface sediments throughout the estuary is shown in Figure 2.8 (Monge-Ganuzas et al., 2014). The subtidal zone is mainly composed of fine sand while medium sand covers the intertidal zones. Coarse sand is found on both margins of the mouth of the estuary. The line separating the fine and medium sand indicates the limit between the subtidal and intertidal zones. Coarse sand on the eastern margin can be a result of wave-induced currents, as fine sand is transported towards the inlet while coarser sand remains in the eastern margin of the bay. Coarse sand is also found in the western margin, where the main ebb channel is located, due to high energy processes that are generated by ebb tidal currents. These currents transport sediment from the inlet towards the ebb delta during ebb-tide periods (Monge-Ganuzas et al., 2008).

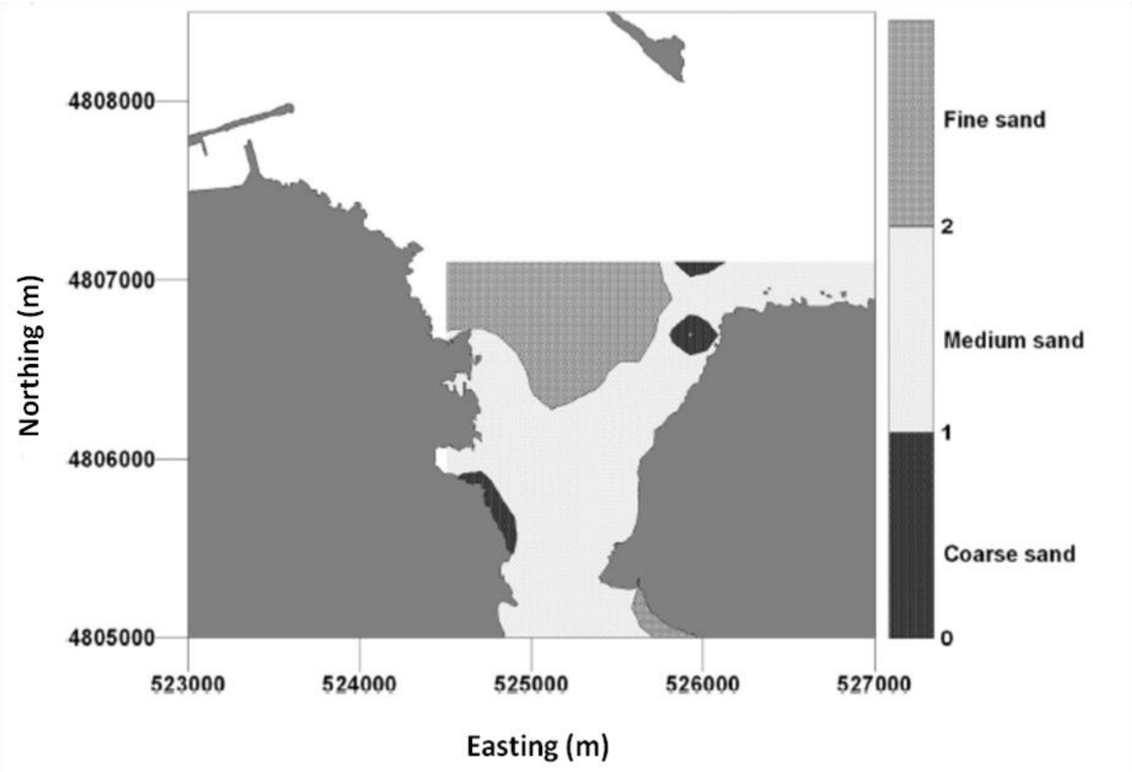

Figure 2.8: The mean grain size of the surface sediments of the Oka Estuary (from Monge-Ganuzas et al., 2014)

Waves approaching from the northwest direction transport sand from the main tidal delta to the east towards the intertidal zone of a developed beach dune barrier (Monge-Ganuzas et al., 2014). The established dune system accumulated 44,000 m^3 of sand in an area of 82,000 m^2 to an average thickness of 1.50 since the last dredge (Monge-Ganuzas, 2008). Like many beaches worldwide, Laida beach changes its morphology according to the season, depending on the intensity of the incident waves. Thus it erodes in winter (September to April) and is restored in the summer (May to August). During the summer 2005, as short period waves (6-8 s) with moderate heights (0.5-1.5 m) approached the shore, sand was transported from the northeast side of the bay to Laida beach and the mouth of the estuary (Figure 2.9). Erosion was observed of the north and west borders of the beach while sediment accumulation in the proximal and distal ends of the delta occurred between the months July and September. A bar was formed north of the beach which increased in thickness between September and October. In winter, however, as intense high waves (1.5-4 m) with longer periods (12-16 s) approached the shore, the sediment formed north of the beach was transported in the west direction and deposited on the corner of the beach during December to February (shown in yellow). Some of this sand was then reintroduced into the estuary as it passed through the mouth. There was extensive erosion around the north border of Laida beach between February and April 2006 (Monge-Ganuzas, 2008).

During storm events these sandy deposits are sometimes breached and when they are accompanied by high river flows, additional channels are formed that cause the original deposits to split from the main tidal channel (Monge-Ganuzas et al., 2014). Once the conditions return to normal, a continuous beach dune barrier is restored which extends from the edge of the tidal deltas to the rocky headlands on the east of the estuary. Seasonal beach morphological changes are mainly due to the variability of the incident wave energy level (such as the Oka estuary). A cross-shore sediment exchange between the supratidal beach and the surf zones resulted, leading to a wide, non-barred beach in winter and a barred beach in summer (Lorenzo et al., 2003).

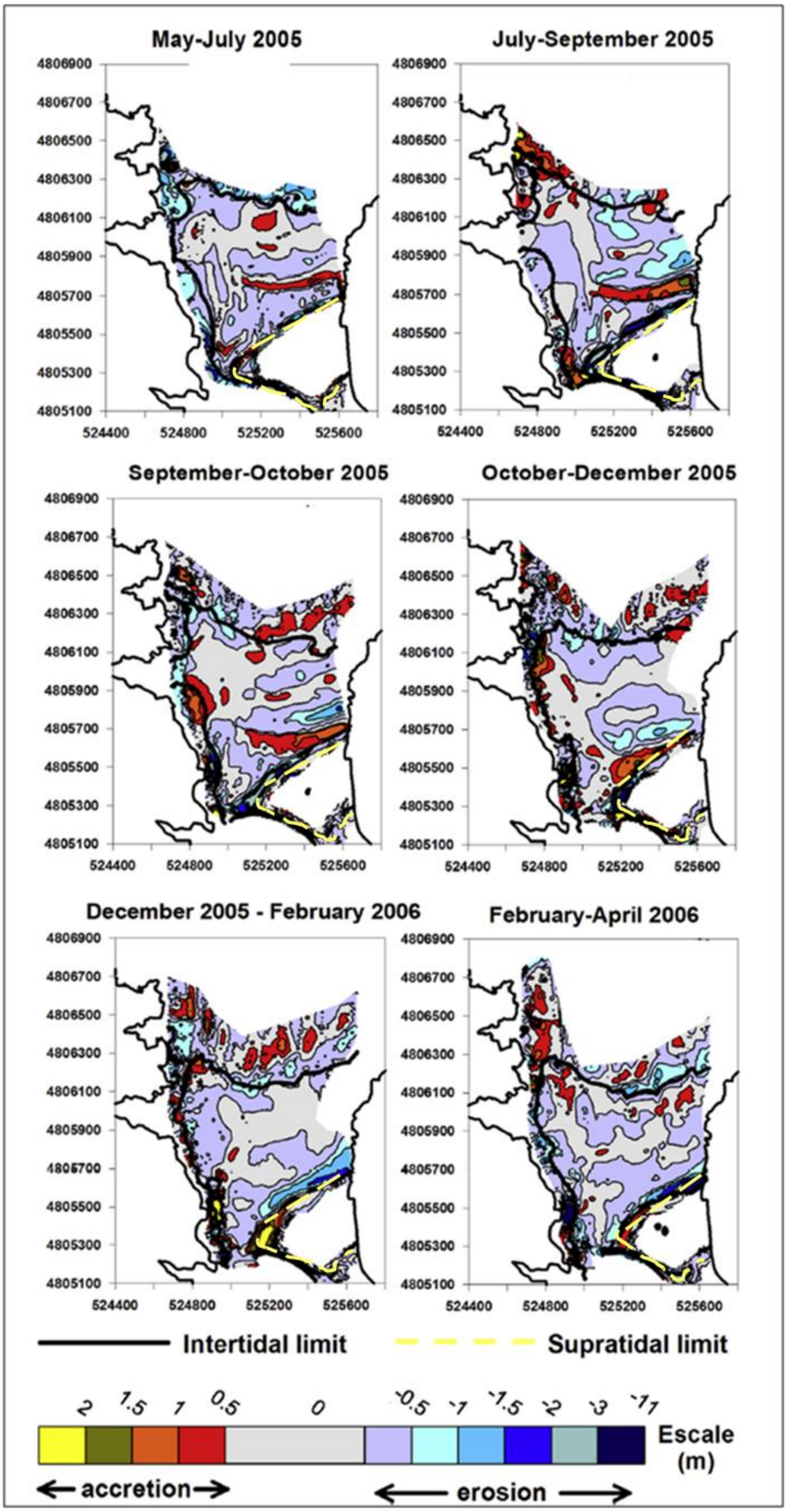

Figure 2.9: Sedimentary balance (erosion and accretion) of the lower Oka estuary for the period May 2005 – April 2006 (from Monge-Ganuzas et al., 2014).

2.4 Summary

Tidal inlets play a major role in coastal processes serving as a link where exchange of salt and fresh water, sediments, and nutrients between the open seas and sheltered tidal lagoons or estuaries (Kraus, 2009). As a natural coastal setting, the Oka estuary serves as the perfect “natural laboratory” to study sand transport in general and the major factors influencing sand to move in suspension. The Oka estuary is a sandy environment, which is an essential characteristic as the main objective of this thesis is to evaluate the Rouse theory for suspension of sand in a tidal inlet. Each location studied in this thesis differed in bedform morphology, water level, flow velocity, and grain size thus offering a wide range of settings for understanding the complexity of sediment transport. There is a keen interest from the Basque community to do more research on the Oka estuary since it is a natural Biosphere Reserve; therefore access to the site was easily provided. The use of high resolution equipment in the field together with reliable numerical modelling will benefit the requirements needed to address the objectives of this study.

Chapter 3: An evaluation of the Rouse theory for sand transport in the Oka Estuary

3.1 Introduction

Sediment suspension plays a major role in the bed evolution of rivers, lakes, estuaries, and coastal areas (Cheng et al., 2013). Suspension is a common behaviour for sediments moving under water flows, therefore, the interaction between turbulent flow and sand particle motion is of great interest in hydraulic, coastal and geological engineering. Due to turbulent diffusion, suspended sediment is distributed over the water column from the near-bed region up to the free surface. This suspended sediment concentration profile became an intriguing topic in scientific and engineering application research during the past decades. However, there are still some disparities due to the complexity of the subject.

Sand in suspension is usually defined by the Rouse (1937) theory. Rouse proposed a formulation, taking into account turbulent diffusion effects and sediment concentration gradients, to define the general distribution of suspended-sediment concentration in a fully turbulent flow. This formulation, named by Vanoni (1975) as the "Rouse's equation", has an important parameter known as the Rouse parameter which expresses the relative magnitudes of downward particle transfer by settling and upward particle transfer by turbulent mixing (Rouse, 1937).

There are several assumptions in the Rouse theory that do not necessarily apply in the present case. One of these is that the (inverse) movability number (the dimensionless ratio of the settling velocity of sand in suspension to the bed friction velocity, w_s/u_*) is a constant, whereas it is not (Van Rijn, 1993). Accurate predictions of sand transport in suspension are not possible unless this ratio is accurately defined (Amos et al., 2010b; Villatoro et al., 2010). In situ sand trapping is an increasingly attractive method of assessing this theory.

The aim of this chapter is to evaluate the validity of the Rouse theory in describing the distribution of sand in suspension throughout the turbulent benthic boundary layer of the Oka estuary, Spain (Figure 3.1).

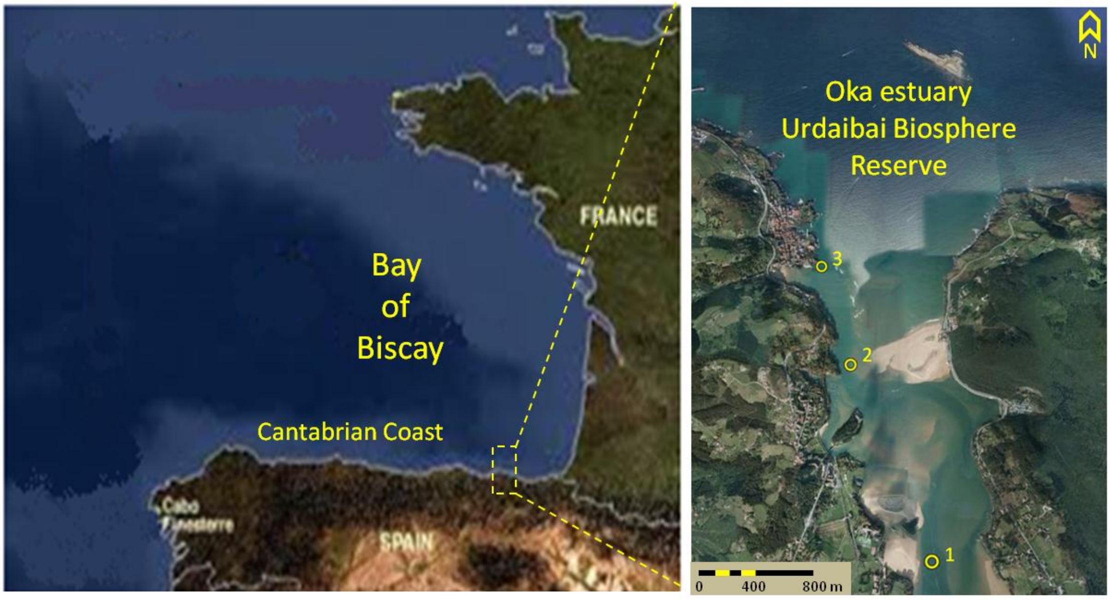

Figure 3.1: The location of the Bay of Biscay and Oka estuary showing the position of three sampling stations in this study.

This is achieved by the measurements of sand concentration with elevation above the bed, and through sampling the suspended material by trapping in order to determine the in-situ grain size and settling rate of suspended material. The vertical distribution of sand in suspension was examined over a range of tidal conditions to provide a wide range of flow conditions and concentration profiles on which to undertake a robust assessment. The perceived outcome is more accurate sand transport evaluations and better model predictions. This study provides an opportunity to extend the Venetian work of Amos et al. (2010a) and Villatoro et al. (2010) over a wider range of sand sizes. The difference between the two sites is that in the Venice inlets the sediment in suspension was restricted to fine sand, whereas in the Oka estuary the sand is coarser and has a wider size range. As a result, field information on the suspension threshold will be obtained from situations where none exist at present.

3.2 Methodology and data collection

An indirect method was used to measure sediment transport in suspension in the Oka estuary, which is based on simultaneous measurements of independent time-averaged velocity and sediment concentrations. Soulsby's (1997) definition of the fall velocity, w_s, one of the key properties to assess in the study of sediment transport, is used in this study. Sediment particles are thus assumed to be spherical which is not true in reality. As a result, prediction of w_s from grain size may be inaccurate. Furthermore, assumptions on sediment density are made which may lead to further errors. Therefore, field trapping and direct measurements of sand settling velocity in a laboratory settling column is also used in this study, thus avoiding several sources of errors including shape effects.

A modified version of the Helley-Smith sampler (Helley and Smith, 1971) was used to measure the vertical distribution of sand in the water column. This sampler has been successfully used in previous similar field studies in two tidal inlets of Venice lagoon (Amos et al., 2010a; Villatoro et al., 2010). In addition to being easy to handle, the Helley-Smith samplers can collect sufficient sand for analysis (>100 g). The sand traps consist of a nozzle, a sample bag, and a frame (Figure 3.2A). The sample bag is made of 60-micron polyester mesh, commonly used for plankton nets. Four sand traps were used in this study (Figure 3.2B). Two sand traps had a square entrance nozzle of 120 x 120 mm and two sand traps had a smaller square entrance nozzle of 60 x 60 mm. The smaller traps were used in the water column, whereas the larger (more stable) traps were used in the benthic and epi-benthic modes as defined by Villatoro et al. (2010). The sand traps were deployed hourly from an anchored boat for a duration of 10 to 15 minutes (in order to collect vertical profiles) throughout a complete tidal cycle. As the traps were lowered in the water, they aligned with the flow. The benthic and epi-benthic traps were lowered to the seabed once aligned. The epi-benthic trap was attached to a base that lifted the sample mouth 0.12 m above the seabed. The middle sand trap was lowered to about mid-depth. When the water depth $h < 2$ m, the middle sand trap was omitted. The surface trap was lowered into the water only until the nozzle was completely submerged. The mean time delay between sampling of the lower two and upper two traps was 10 minutes, but for present purposes sampling was considered to be synchronous, as the record length can go up to 12 minutes for data to be considered synchronous (Soulsby, 1980).

The sand samples obtained were used to determine the sand concentration as a function of elevation in the benthic boundary layer. A pump sampler was used to collect approximately 400 L of seawater which was then passed through a 63-micron sieve. This was used to derive a calibrated concentration from the dry mass of sand retained on the sieve. The surface sand concentration was determined as the mass (M) trapped by the sieve divided by the pumped volume of water (V). Simultaneously, a surface trap was deployed and the material collected and analysed for sand concentration. Calibration of a 60-micron mesh size yielded a sampling efficiency of between 4 and 7% (Amos et al., 2010a) in the plankton rich waters of Venice lagoon. Sand traps generally are less than 100% efficient due to the influence of the trap on the flow, (bio-) fouling, blockage and drag caused by the fine mesh of the trap nets (Smith et al., 1968). The trap efficiency was evaluated at the surface and it was assumed to be constant throughout the water column. Our initial assumption is that all four sand traps (including the benthic trap) can be used to define the suspended profile.

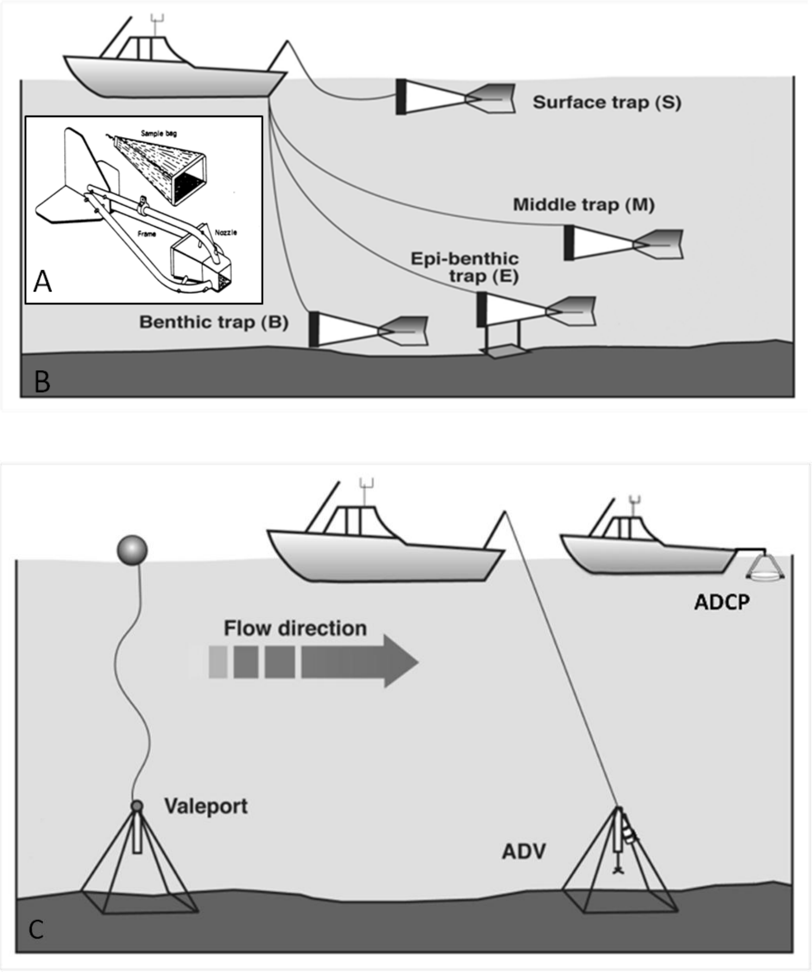

Figure 3.2: A) Sketch of Helley-Smith sand sampler showing the nozzle and sample bag (from Helley and Smith, 1971), B) A diagram showing the general sand trap deployment, and C) the deployments of the Valeport, ADV, and ADCP (Al-Ragum et al., 2014)

The sand samples were analyzed in the sediment analysis lab of the National Oceanography Centre, Southampton (NOCS). A sub sample of 4 to 5 g was used from each sample and settled in the water of a settling column where the cumulative weight settling from time 0 to 500 s was measured and recorded. The data was processed using a specifically written script for the NOCS settling column where the settling velocity is used to determine the grain size following Soulsby (1997). The particle size distributions (PSDs) from benthic traps are more negatively (coarsely) skewed than the surface traps. All analysed samples exhibited well to very well sorted leptokurtic distributions. A statistical summary of the sample PSDs including median and mean grain sizes, sorting, skewness, and kurtosis, were calculated following Folk and Ward (1957) (Figure 3.3).

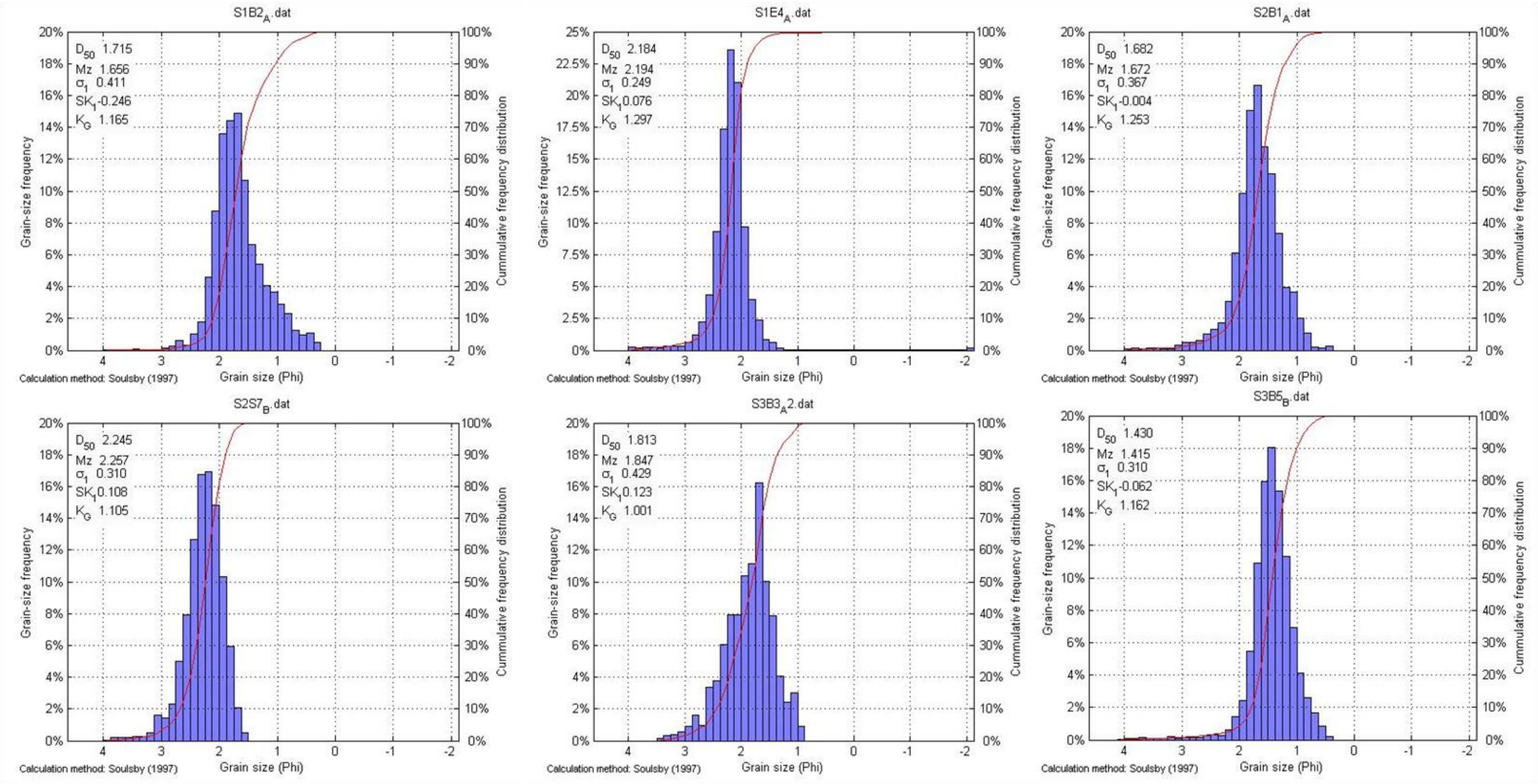

Figure 3.3: The grain size distribution of samples S1B2A, S1E4A, S2B1A, S2S7B, S3B3A2, and S3B5B, showing the median grain size (D_{50}), mean grain size (M_z) in Phi units, standard deviation (σ), skewness (SK), and kurtosis (K).

Optical and acoustic sensors were also used in order to supplement the sand concentrations collected from the traps. An RDI Workhorse Acoustic Doppler Current Profiler (ADCP) was used to record hourly measurements of acoustic backscatter, flow direction and velocity throughout the water column (up to 5-min long bursts). The ADCP was mounted downward from a stationary boat (Figure 3.2C) and measured at a frequency of 1200 kHz with a 0.5 m vertical cell size. The bottom and surface 0.3 m of the water column were not recorded by this instrument and were extrapolated for velocity assuming Law of the Wall as described by Helsby (2008). The ADCP recorded data for the period during which the middle and surface sand traps were deployed in the water so the values of mean flow from the ADCP can be used for sand concentration collected from the sand traps.

Two self-recording Valeport® 802 current meters were fixed on a triangular frame (Figure 3.2C) and deployed at two locations (Station 1 and Station 2) in the estuary to measure turbidity, suspended particulate matter, and mean flow for a duration of six days. The Valeport units comprise an electromagnetic current meter situated at $z = 0.18$ m above bed, an optical backscatter sensor (OBS) at $z = 0.35$ m, and a pressure sensor at $z = 0.4$ m. The Valeports recorded continuously at 4 Hz for 6 minutes every 30 minutes. The Valeports were deployed a day before the survey period and retrieved a day after. The water depth and current speed recorded are shown in Figure 3.4.

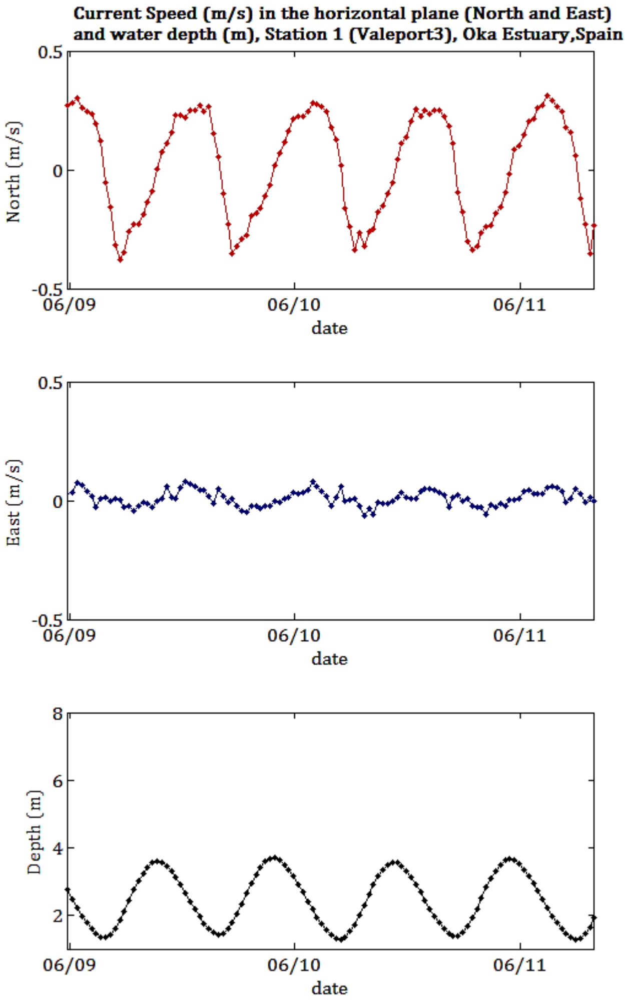

Current Speed (m/s) in the horizontal plane (North and East) and water depth (m), Station 1 (Valeport3), Oka Estuary,Spain

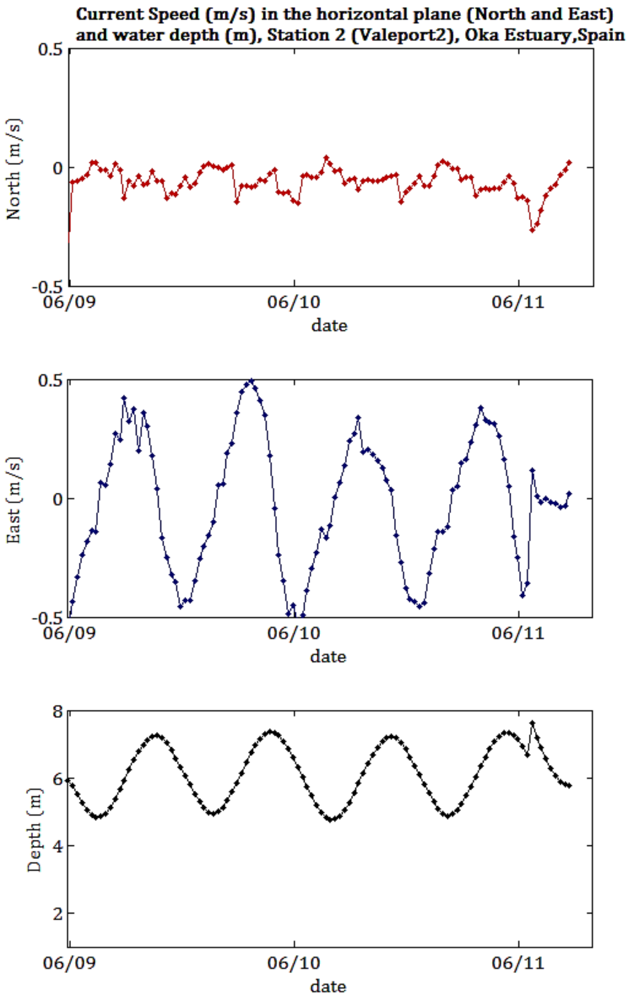

Current Speed (m/s) in the horizontal plane (North and East) and water depth (m), Station 2 (Valeport2), Oka Estuary,Spain

Figure 3.4: The horizontal current speed (m/s) and water depth (m) recorded using Valeports 3 and 2 at Stations 1 and 2 respectively.

A Nortek® Acoustic Doppler Velocimeter (ADV) was used to provide burst-sampled three-dimensional flow, which was used to derive the friction velocity using the turbulent kinetic energy (TKE) method. This method is independent of estimates of bed friction. The ADV measured the flow at 25 Hz at z = 0.22 m. The Law of the Wall was then used to calculate the water flow at the sampling height of the lower traps. The ADV was fixed on a triangular frame (Figure 3.2C) and deployed from a stationary boat hourly for a duration of about 5 minutes yielding approximately 7000 data points per burst. The “Vectrino plus” firmware was used to measure, record, and convert data was supplied by Nortek AS. The output files from the ADV includes the velocity in three orthogonal directions. The velocity records were processed using a Matlab code where axis rotation and smoothing of the data were applied. Figure 3.5 shows the velocity in the x, y, and z directions after processing for a run carried out at 10:46 on 09/06/2011, including the mean velocity and a statistical summary given by the skewness and kurtosis of the distributions. A detailed version of the Matlab code is given in Appendix B.

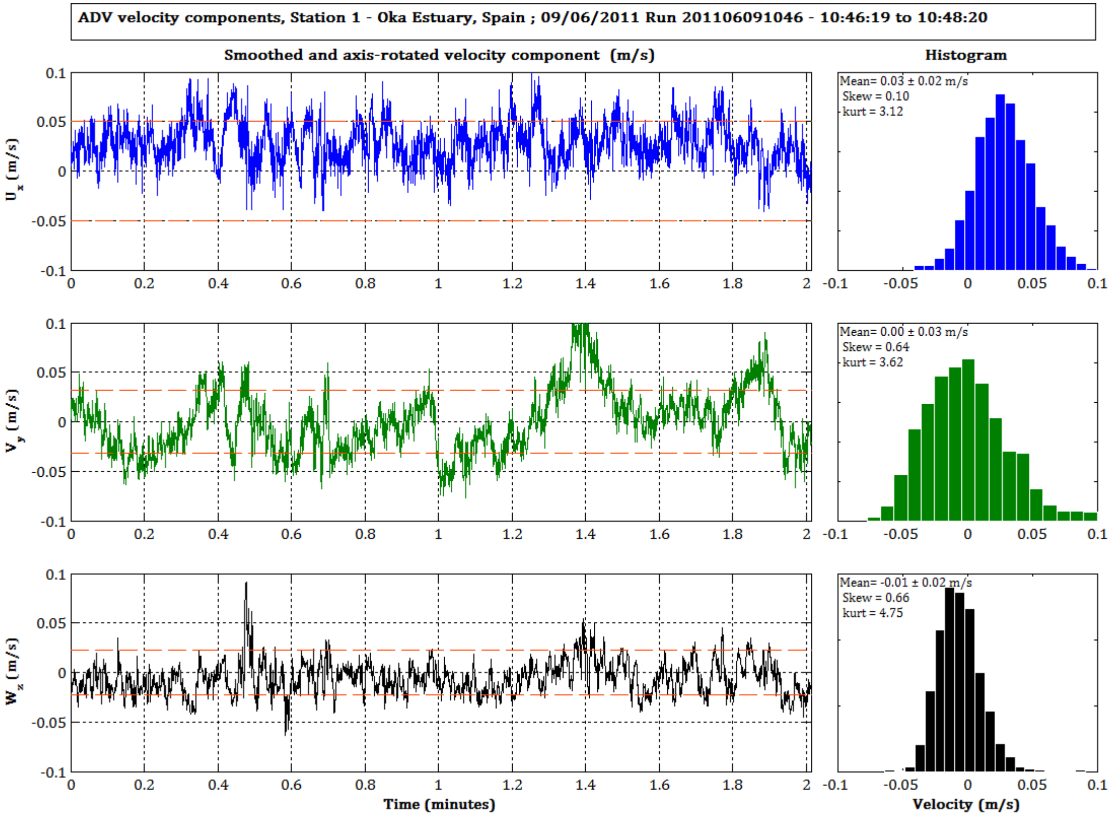

Figure 3.5: The processed ADV velocity 3D components (u, v, and w) for a run carried out at 10:46 on 09/06/2011of Station 1 in the Oka estuary. The red dotted lines indicate $\pm 1.\sigma$ from mean velocity. A statistical summary is given on the right including the mean, skewness, and kurtosis of the distributions.

The latter ADV data were extracted for comparison with the concentration data derived from the epi-benthic trap, which sampled at the same height and at the same time period.

Finally, water samples were collected hourly using a one litre Niskin bottle to measure the content of fines ($D_{50} < 63$ microns) in the water column, at three different levels (bottom, middle, and surface). Water samples were filtered through 47 mm (diameter) glass microfibre filters (GF/F) to yield mass concentration of fines, after first passing through a 63-micron sieve to remove the sand. In all cases, the organic material in the sediment was removed by ashing in a muffle furnace at 450 ºC for 4.5 hours. The organic content was evaluated by the loss on ignition (LOI), which is the difference between the initial weight and the weight after incineration.

The field survey was based on a two boat operation. An anchored boat (Starfisher) was used to deploy the sand traps and the ADV. The ADCP measurements and Niskin water samples were collected from a small 4 m zodiac.

3.3 Results

Data were collected in the Oka estuary in June, 2011 at three different locations in the vicinity of the main tidal inlet shown in Figure 3.1. The first survey location, Station 1 (N 43.39°, W 2.69°), was inside the estuary where it is sheltered from waves; and flood-tide dominated and has a relatively broad estuary section. Station 2 (N 43.40°, W 2.69°) was in the inlet mouth which is ebb-tide dominated and has a narrow estuary section. Station 3 (N 43.41°, W 2.70°) was on the ebb tide delta where it is exposed to waves. Because the field work was carried out during the summer, under low and steady river flows, and due to the estuary's small size and shallow depth, salinity distribution was the same throughout the entire estuary, at 35.5 ppt. The effect of river flow (mean value of 0.59 m^3/s) during the survey period was insignificant compared with the mean tidal prism of 5×10^6 m^3 (Liria et al., 2009). In addition, the weather conditions were calm as was the sea state, therefore there were no waves and the water column was clear and well-mixed.

3.3.1 Hydrodynamics

The Oka estuary is well-mixed (Monge-Ganuzas, 2008) with an average temperature of 18.3 ºC and kinematic viscosity of 1.08 x 10^{-6} m^2/s. The tides are semidiurnal. The flow Reynolds numbers for all three stations show that the flow was rough turbulent (Re > 5 x 10^5). That is, the drag coefficient used in the derivation of bed stress may be considered as constant. Hydrodynamic data of the three stations are summarized in Table 3.1. Estimates of u_* are based on the assumption that the ADV was in the constant stress layer. In order to validate this assumption, the boundary layer thickness, δ, has been calculated using two methods. The first method is using Ekman's theory which is based on the Earth's rotation (Bowden, 1978). Ekman's depth, L_E, is given by:

$$L_E = 0.4u_*f \tag{3.1}$$

where f is the angular velocity of rotation (f = 2$w$sin ϕ, w is the rate of angular rotation of Earth, 6.94 x 10^{-4}, and ϕ is the latitude of Oka estuary, 43º). In the lower part of this layer, $0.1L_E$, stress is generally assumed constant. In the second method (using Liu, 2001), for turbulent flow, the boundary layer thickness is expressed as:

$$\delta = 0.4x\left(\frac{Ux}{v}\right)^{-0.2} \tag{3.2}$$

where x is the horizontal distance over which the boundary layer has developed which has been scaled from Google Earth. The estimates of boundary layer thickness using equations (3.1) and (3.2) are given in Table 3.1. The Ekman boundary layer occupies the entire water column in most cases, and the constant stress layer is never less than 0.5 m, therefore, the ADV (z = 0.22 m) is within this constant stress layer.

Table 3.1: Hydrodynamic data of stations 1, 2, and 3 including tide stage, average velocity (U_z) at z = 0.22m and average velocity (U_h) at the surface, friction velocity (u_*), water depth (h), kinematic viscosity (ν), Reynolds number (Re), and boundary layer thickness (δ) calculated using: (a) Ekman's theory (Bowden, 1978) and (b) Liu (2001).

Station	Profile	Stage of tide	Average velocity at z = 0.22m $\bar{U}_z$ (m/s)	Average velocity at surface $\bar{U}_h$ (m/s)	Friction velocity u_* (m/s)	Roughness height z_0 (m)	Water depth h (m)	Water temp. (°C)	Kinematic viscosity ν (m^2/s)	Reynolds number R_e [ ]	Ekman boundary layer thickness (m)	Boundary layer thickness for turbulent flow, δ (m)
1	1	ebb	0.205	0.397	0.0123	0.0003	3.18	18.27	1.092E-06	1.156E+06	5.20	4.46
	2	ebb	0.325	0.548	0.0176	0.0001	2.74	18.78	1.079E-06	1.392E+06	7.44	4.17
	3	ebb	0.415	0.500	0.0271	0.0005	2.22	19.30	1.065E-06	1.042E+06	11.45	4.24
	4	ebb	0.168	0.441	0.0550	0.0543	1.75	19.81	1.053E-06	7.332E+05	23.24	4.33
	5	flood	0.293	-	0.0205	0.0005	1.31	19.64	1.057E-06	-	8.66	-
	6	flood	0.293	-	0.0205	0.0005	1.26	19.64	1.057E-06	-	8.66	-
	7	flood	0.493	0.660	0.0345	0.0005	1.96	19.81	1.053E-06	1.229E+06	14.58	4.00
	8	flood	0.344	0.469	0.0217	0.0003	2.61	18.61	1.083E-06	1.130E+06	9.17	4.30
2	1	flood	0.134	0.539	0.0168	0.0071	4.10	17.93	1.101E-06	2.008E+06	7.10	2.02
	2	flood	0.475	0.432	0.0130	5.77E-08	5.61	17.76	1.105E-06	2.193E+06	5.49	2.11
	3	flood	0.400	0.429	0.0232	0.0002	5.49	18.10	1.096E-06	2.148E+06	9.80	2.11
	5	ebb	0.450	0.604	0.0203	0.0002	3.66	18.27	1.092E-06	2.025E+06	8.58	1.97
	6	ebb	0.110	0.757	0.0350	0.0524	3.18	18.61	1.083E-06	2.223E+06	14.79	1.88
	7	ebb	0.450	0.737	0.0268	0.0003	3.11	19.81	1.053E-06	2.178E+06	11.32	1.88
	8	ebb	0.450	-	0.0268	0.0003	2.00	19.81	1.053E-06	-	11.32	-
3	1	ebb	0.428	0.602	0.0411	0.0027	2.46	18.78	1.079E-06	1.373E+06	17.37	5.36
	2	ebb	0.256	0.409	0.0263	0.0042	2.50	18.61	1.083E-06	9.442E+05	11.11	5.79
	3	ebb	0.051	-	0.0129	0.0451	2.53	18.61	1.083E-06	-	5.45	-
	4	flood	0.338	0.510	0.0253	0.0009	5.07	18.44	1.087E-06	2.378E+06	10.69	5.54
	5	flood	0.222	0.380	0.0216	0.0037	5.46	17.93	1.101E-06	1.885E+06	9.13	5.90
	6	ebb	0.204	-	0.0194	0.0036	7.00	18.10	1.096E-06	-	8.20	-
	8	ebb	0.204	-	0.0194	0.0036	5.00	18.10	1.096E-06	-	8.20	-

3.3.2 Sand trap efficiency

The sand trap efficiency depends on the geometry of the sampler nozzle, the volume of material collected, the percentage of blocking material (i.e. organic material), and the disturbances generated at the start and end of the sampling period (Van Rijn and Gaweesh, 1992). Some of the shortcomings of the modified Helley-Smith sand traps are over-sampling, due to resuspension of material when the trap is placed on the bed, and under-sampling, due to clogging of the mesh by organic matter and very fine sand (Villatoro, 2010).

In this study the trap efficiency is assumed constant in the vertical. This is justified as the water column is well mixed (the benthic boundary layer extends to the surface) during periods of sand in suspension and is low in phytoplankton, which affects bio-fouling of the nets (Smith et al., 1968). During the survey some phytoplankton was caught mainly in the surface trap. Another factor that can influence the sand trap efficiency is the grain size variation in the vertical, as finer sand was collected near the surface and coarser sand near the bed. The trap efficiency decreases with height above the bed, since fine sand may clog up the mesh and reduces its efficiency. Hence, a constant trap efficiency in the vertical using the surface trap will yield conservative results. To eliminate error relating to the geometry of the nozzle mouth, as two different sizes were used, the calculated concentration was per meter width. Also, the same mesh size was used for both the large and small sand traps; therefore the same calibration is suitable.

Figure 3.6 shows the regression line from which the sand trap efficiency was determined using the surface measurements from all three stations. The observed concentration varied over a range of 0.06 mg/l to 8 mg/l. The linear best fit regression yielded SC = 0.44CC mg/l, where SC is the surface trap concentration and CC is the calibration concentration. The relationship is significant at $p = 0.01$. The trap efficiency for the Oka estuary was therefore 44%. This value was used to adjust the sand concentration calculated for all sand trap deployments.

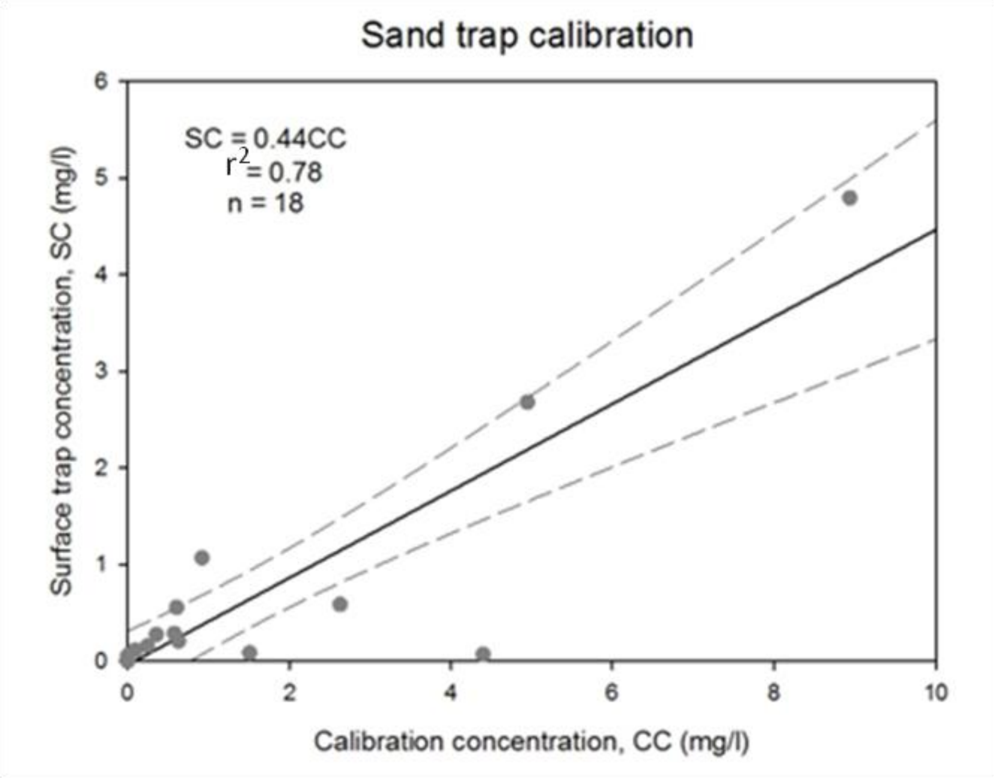

Figure 3.6: Sand trap calibration showing the regression between the surface trap concentration and the calibration concentration, with 95% confidence intervals.

3.3.3 Grain size and sand concentration

A total of eight profiles were collected with the sand traps at each station. The material collected was used to determine the sand median particle size, the settling velocity (derived from settling column experiment (in fresh water) on retrieved samples, and adjusted for salinity), and the vertical sand concentration (Table 3.2).

Table 3.2: Average values of sand concentration (SC), organic content, median grain diameter (D_{50}), dimensionless grain diameter (D_*) (see section §3.4.1), and settling velocity (w_s) for the surface, middle, benthic and epi-benthic samples, at all stations.

Station	Sample	Ebb Tide					Flood Tide				
		Organic %	D_{50} mm	D_*	w_s m/s	SC mg/l	Organic %	D_{50} mm	D_*	w_s m/s	SC mg/l
1	surface	17.08	0.11	2.602	0.010	0.089	9.71	0.09	2.158	0.006	0.253
	middle	27.56	0.08	1.935	0.005	0.070	-	-	-	-	-
	epi-benthic	11.03	0.18	4.283	0.021	5.008	2.78	0.20	4.592	0.023	3.544
	benthic	1.80	0.30	6.885	0.041	15.705	1.10	0.31	7.116	0.042	65.431
2	surface	2.17	0.21	4.805	0.025	16.369	16.65	0.13	3.109	0.012	0.637
	middle	1.43	0.23	5.369	0.029	25.063	9.70	0.16	3.834	0.017	1.756
	epi-benthic	2.12	0.22	5.138	0.027	440.603	15.57	0.18	4.177	0.020	5.256
	benthic	1.13	0.26	6.150	0.035	2981.468	1.60	0.29	6.732	0.040	135.750
3	surface	11.97	0.11	2.460	0.009	1.875	16.07	0.10	2.365	0.007	0.631
	middle	6.59	0.16	3.731	0.016	-	2.74	0.35	8.041	0.049	2.150
	epi-benthic	2.33	0.33	7.667	0.046	127.411	7.10	0.23	5.297	0.029	0.901
	benthic	1.37	0.38	8.854	0.054	3693.444	1.18	0.37	8.513	0.052	214.247

3.3.3.1 Station 1

The vertical concentration of organic content of sand decreased from 17% to 2% during ebb-tide and from 10% to 1% during flood-tide towards the bed at this station, while the sand concentration increased from 0.09 mg/l to 15.70 mg/l during the ebb and from 0.25 mg/l to 65.43 mg/l during the flood. The grain size also increased towards the bed, reflecting greater settling rates. Medium sand (0.20 mm < D_{50} <0.30 mm) was found in the benthic and epi-benthic traps while only very fine sand (0.08 mm < D_{50} <0.11 mm) was found in the upper levels of the water column. Figure 3.7A shows sand concentration distribution through the water column for 8 profiles over a tidal cycle for Station 1.

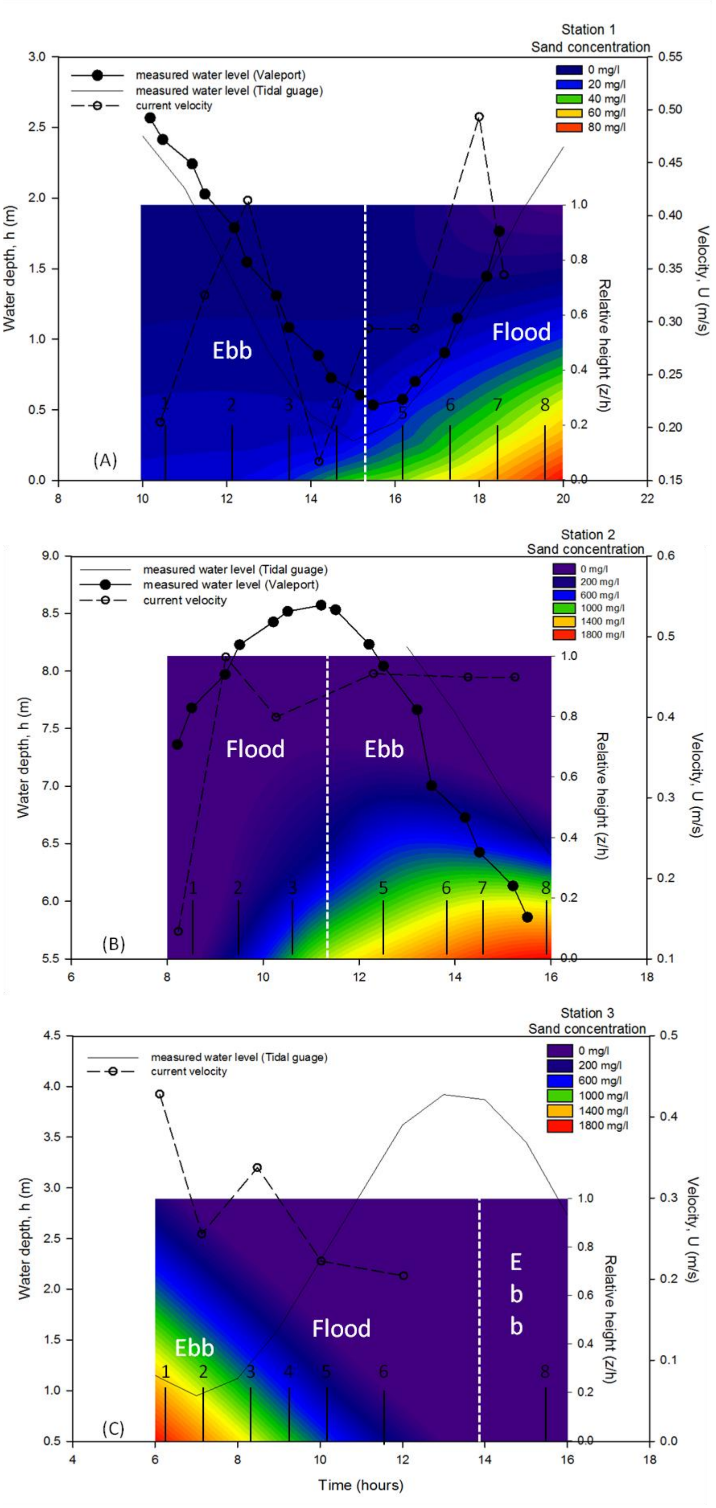

Figure 3.7: Vertical profiles of sand concentration at Station 1 (A), Station 2 (B), and Station 3 (C) throughout the tidal cycle and the corresponding water level measurements. Flood and ebb are defined based on observed flow direction and therefore do not correspond to the tidal elevation.

The concentration of sand appears higher on the flood-tide than the ebb-tide suggesting a net landward movement over the survey period. This result was also evident in the ADCP backscatter data previously collected by Monge-Ganuzas (2008) and analysed for sand transport by Vianna (2012).

3.3.3.2 Station 2

Figure 3.7B shows the sand concentration through the water column over a tidal cycle for Station 2. The organic content (maximum value up to 17%) was higher during flood tide but shows no trends with depth. The material is classified as fine-medium sand (0.24 mm) in the lower water column and fine sand (0.18 mm) in the upper. The sand concentration increased towards the bed and was sensitive to the change of tide. In addition, the sand concentration during the ebb-tide was ten times higher than during the flood-tide. This suggests that the sand transport on the tidal inlet is, as expected, dominantly seawards.

3.3.3.3 Station 3

The results of the sand trap sampling at Station 3 are shown in Figure 3.7C. The organic content decreased towards the bed (from 12% to 1% during ebb and from 16% to 1% during flood) and was greatest at the surface at the proximal ebb delta (Table 3.2). The grain size increased with depth; in the lower part of the water column it was three times that of the surface. The sand in the upper water column was very fine (0.10 mm); in the middle part was medium sand (0.30 mm), and near the bed was medium to coarse sand (0.23 mm to 0.38 mm). There was a large difference in sand concentration throughout the water column as well as throughout the tidal cycle. The sand concentration during the ebb-tide was greater than during the flood-tide by an order of magnitude. The sand concentration increased significantly in the lower part of the water column. As in station 2, the sand transport in the proximal ebb delta (station 3) was seawards and also presents higher sand concentrations than Station 2.

Due to tidal asymmetry in the estuary, where the ebb phase is longer than the flood phase, sand transport was dominantly seawards at stations 2 and 3, even when there was a net inflow of water (as occurs on a neap to spring phase of the tide).

3.4 Discussion

3.4.1 Rouse parameter and moveability number

Various versions of the Rouse (1937) equation have been proposed by varying the expression of relative depth (z/h). In its simplest form, the Rouse equation is expressed as:

$$C_z = C_a \left(\frac{z}{h-a}\right)^{-R} \tag{3.3}$$

Where C_z is the sand concentration of height z above the bed, C_a is the reference concentration at reference height a, h is the water depth, and R is the Rouse parameter (Amos et al., 2010b). In this study, a simple form of relative depth was used. This overcomes the uncertainty in defining the reference concentration height (a). In order to calculate the Rouse parameter, the sand concentrations were plotted against the relative height to obtain a best fit line. Each profile had a maximum of four data points. To increase the number of data points for each profile, backscatter measurements from the ADCP were converted to concentration units (mg/l) and added to the sand trap concentrations. Since the ADCP backscatter is sensitive to the type of suspended particulate matter, it was calibrated in-situ. Figure 3.8 shows the calibration of the ADCP backscatter from all surface and middle samples for the three stations; backscatter (db) is plotted against sand concentration. A simple correlation is presented as beam spreading data was not available to improve the correlation.

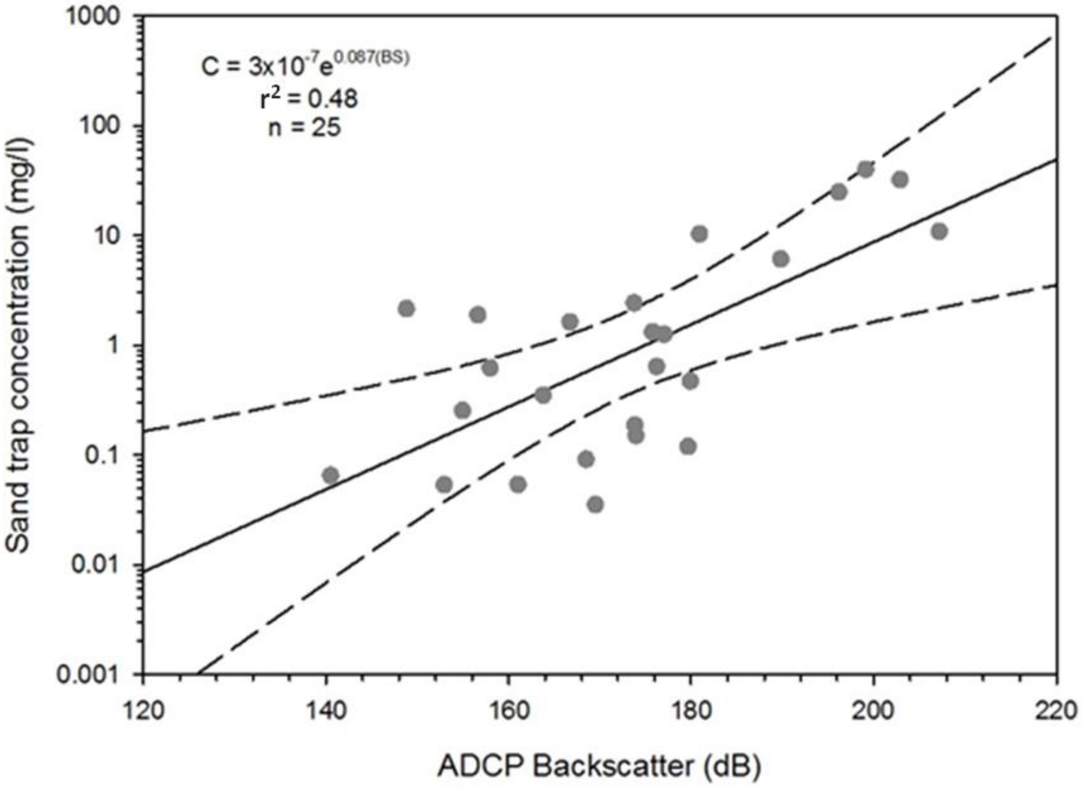

Figure 3.8: The ADCP backscatter calibration showing the equation of the best fit line between the sand trap concentration (C) and ADCP backscatter (BS) with 95% confidence intervals.

The slope, intercept, and correlation coefficient of each profile is shown in Table 3.3. The movability number (w_s/u_*) was calculated from the Rouse parameter, R = ($w_s/\beta k u_*$), where $\beta = 1$ and $k = 0.41$. From the power function ($y = bx^m$) of the regression lines (Figure 3.9), for each profile we calculated the Rouse parameter as follows:

$$log_{10}\frac{z}{h} = m\,log_{10}\,C + b \tag{3.4}$$

then,

$$C = \left(\frac{z}{h}\right)^{\frac{1}{m}} 10^{-\frac{b}{m}} \tag{3.5}$$

where C is the sand concentration and R = -1/m. The movability number (w_s/u_*) can then be calculated from the slope as follows:

$$\frac{1}{m} = \frac{w_s}{\beta k u_*} \tag{3.6}$$

The sand concentration fits a power law in all profiles and slopes of the profiles are similar in value (Table 3.3).

Table 3.3: Number of samples (n), inverse slope (1/m), intercept (b), correlation coefficient (r^2), movability number (w_S/u_*), and tide stage for the profiles of all stations.

Station	**profile**	**n**	**1/m**	**B**	**r^2**	**w_s/u_***	**Tide**
1	1	6	-0.53	0.09	0.55	0.22	ebb
	2	6	-0.44	0.17	0.38	0.18	ebb
	3	6	-0.45	0.18	0.58	0.18	ebb
	4	4	-0.48	0.26	0.69	0.20	ebb
	5	2	-0.26	0.08	1.00	0.11	flood
	6	2	-0.33	0.07	1.00	0.14	flood
	7	4	-0.46	0.35	1.00	0.19	flood
	8	4	-0.51	0.14	0.57	0.20	flood
2	1	4	-0.66	0.25	0.73	0.27	flood
	2	6	-0.92	0.60	0.85	0.38	flood
	3	6	-0.69	0.42	0.79	0.28	flood
	5	6	-1.18	3.1	0.77	0.48	ebb
	6	6	-0.54	2.95	0.95	0.22	ebb
	7	6	-0.70	3.79	0.93	0.29	ebb
	8	2	-0.65	0.68	1.00	0.27	ebb
3	1	4	-0.47	0.78	0.99	0.19	ebb
	2	4	-0.38	0.70	1.00	0.16	ebb
	3	2	-0.25	0.12	1.00	0.10	ebb
	4	4	-0.47	0.23	0.43	0.19	flood
	5	6	-0.53	2.39	0.57	0.22	flood
	7	2	-0.25	0.03	1.00	0.10	flood

The average Rouse parameter for Station 1 was 0.48 ± 0.035 (profiles with two data points were omitted). The average movability number (w_S/u_*) was 0.20 ± 0.015. This value will be compared to other movability numbers derived using different methods, as defined by Amos et al. (2010b). The same analysis was repeated for stations 2 and 3. The average Rouse parameter for Station 2 was 0.78 ± 0.23. The Rouse parameter varied slightly with the tide, and the values were higher on the flood-tide than on the ebb-tide. The average movability number, w_S/u_*, was 0.32 ± 0.095. The Rouse parameter did not vary during the tidal cycle at station 3. The average Rouse parameter for this station was 0.46 ± 0.06. The average movability number for the survey was 0.19 ± 0.025.

The Rouse parameter at all three stations was less than unity suggesting full suspension uniformly distributed throughout the boundary layer (Van Rijn, 1993). As can be seen from Figure 3.7 this was not the case. Unlike that described by Villatoro et al. (2010), there was no apparent trend with stage of the tide (flood versus ebb) as mean velocities were similar. The sensitivity of the Rouse parameter to grain size is ambiguous: Coarser sand was found at station 3, whereas the highest values of the Rouse parameter were found at station 2. Given the vertical variation in grain size of suspended material evident in Table 3.2, it appears that the Rouse profile is as strongly influenced by sediment sorting (sediment availability to feed the vertical variation) as by the median grain size. That is, the Rouse profile cannot develop if the appropriate sediment sizes are not available at the bed to feed it.

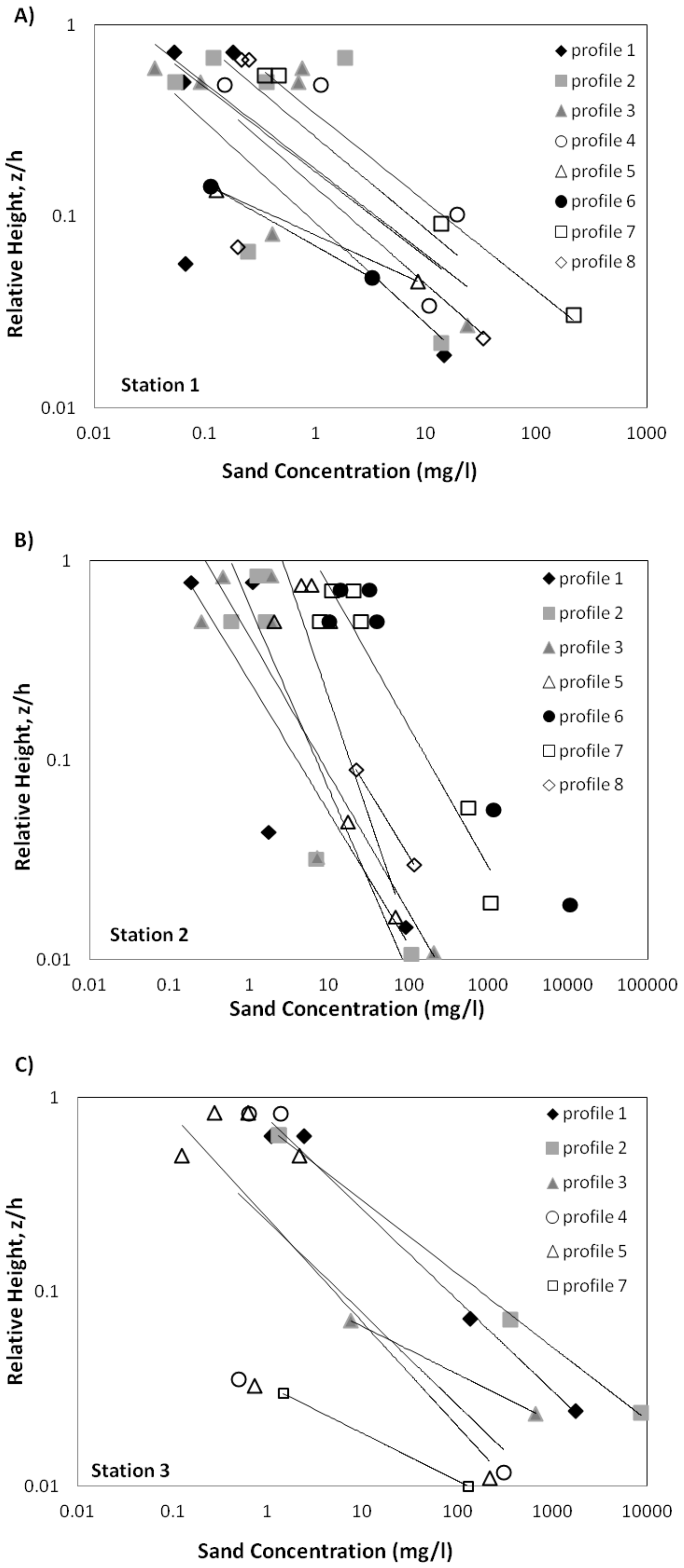

Figure 3.9: Sand concentration profiles of A) Station 1, B) Station 2, and C) Station 3 with relative height (z/h).

The ratio w_s/u_* is considered fundamental in determining the distribution of sand in suspension as well as estimating the critical Shields parameter for suspension. Different methods have been used to test the accuracy of the estimations of this ratio as follows:

- The first method is based on measured profiles of sand concentration. The movability number is calculated by associating the inverse slope to the Rouse parameter ($1/m = w_s/\beta k u_*$), and assuming the ratio of eddy diffusivity to eddy viscosity, $\beta = 1$ and von Karman's constant, $k = 0.41$.
- The second method uses the National Oceanography Centre settling column to obtain direct measurements of the settling velocity (w_s). Friction velocity (u_*) is derived from independent ADV measurements and using the TKE method (Thompson et al., 2003).
- The third method is based on Bagnold's (1966) sand transport theory where the motion of suspended particles are governed by the following assumptions: 1) suspension of a grain occurs when its settling velocity (w_s) is equal to, or greater than, the upward instantaneous velocity of the turbulent flow in the water column (w'_{up}); 2) the upward velocity in the water column (w'_{up}) is equal to 1.56 times the root-mean-square vertical turbulent fluctuations (w'_{rms}); and 3) the root-mean-square vertical turbulent fluctuations (w'_{rms}) is 0.8 times the friction velocity, u_*. These assumptions result in a value of $w_s/u_* = 1.25$. Values of w'_{up} were extracted from the ADV and plotted against friction velocity in Figure 3.10.

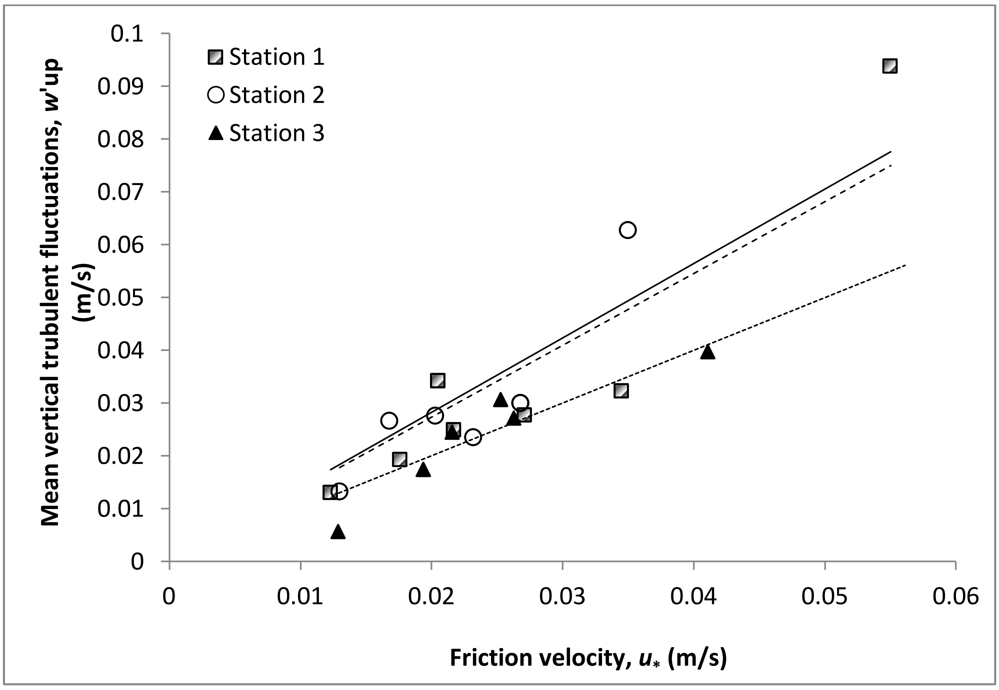

Figure 3.10: The upward vertical turbulent eddies (w'_{up}) plotted against friction velocity (u_*) for all stations. Best fit line for Station 1 with equation $w'_{up}/u_* = 1.41$ ($r^2 = 0.82$) is shown in a solid line, for Station 2 ($w'_{up}/u_* = 1.36$; $r^2 = 0.71$) is shown in a dashed line and for Station 3 ($w'_{up}/u_* = 1.00$; $r^2 = 0.86$) is shown in a dotted line.

The results from stations 1 and 2 gave values higher than those of Bagnold (1966), as w_s/u_* is 1.41 and 1.36 respectively; those of station 3, on the other hand, were lower with a value close to unity.

- The fourth method is based on the relationship between the movability number and the dimensionless grain diameter, D_*. According to Van Rijn (1993), the movability number, $w_s/u_* = \frac{D_*}{\chi}$ for $D_* < 10$ and it is constant when $D_* > 10$. The value of χ is set as 4 by Van Rijn (1993). The dimensionless grain diameter is calculated using:

$$D_* = \left[\frac{(s-1)g}{v^2}\right]^{1/3} D_{50} \tag{3.7}$$

where D_{50} is the median grain size, s is the specific density, v is the kinematic viscosity and g is gravitational acceleration (Van Rijn 1984). The movability number is plotted against the dimensionless grain diameter showing a positive correlation in Figure 3.11.

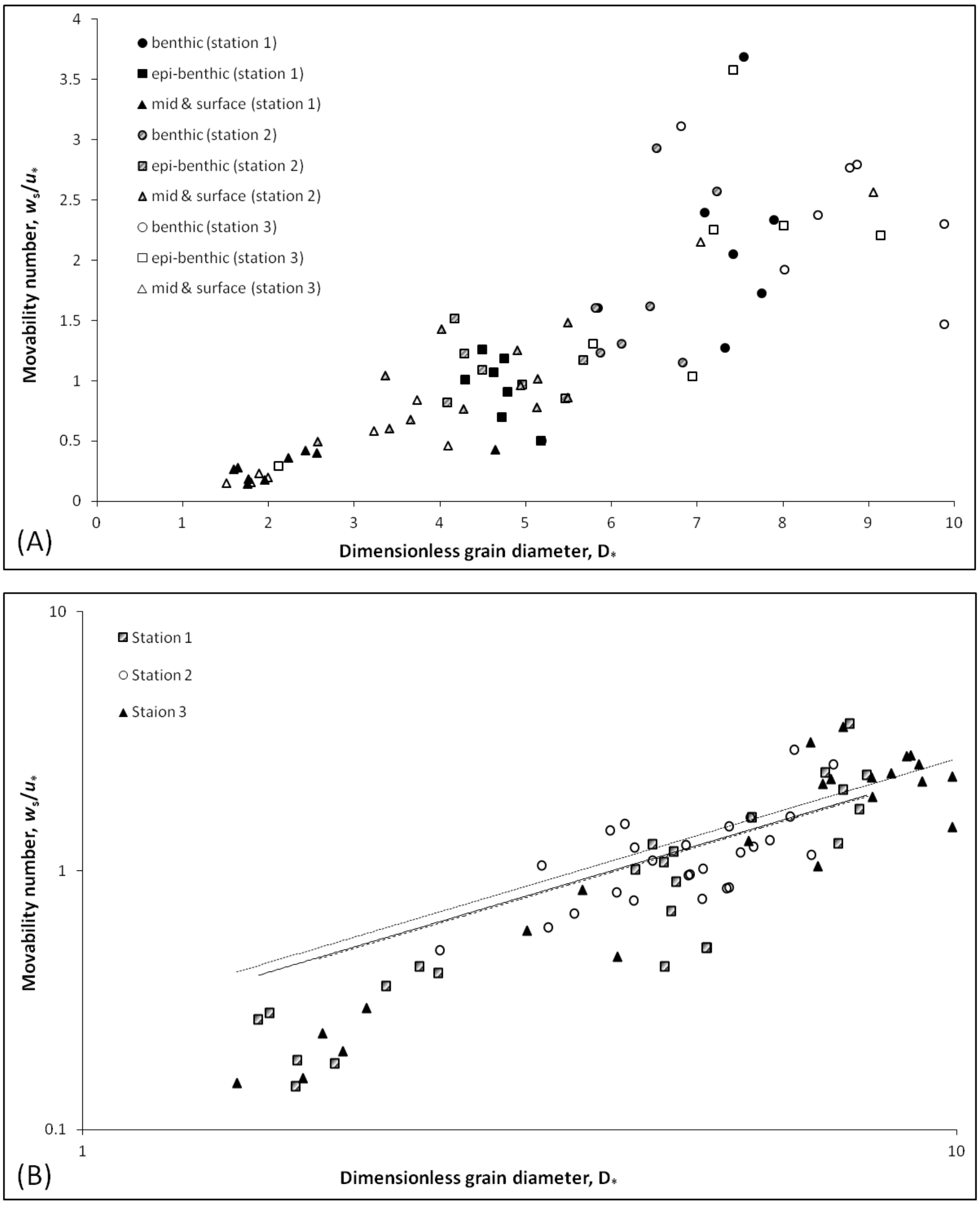

Figure 3.11: The movability number (w_s/u_*) plotted against the dimensionless grain diameter (D_*) for all stations. A) Benthic, epi-benthic, middle, and surface samples plotted individually to show the increase of the movability number with height above the bed and increasing grain size. B) Best fit line of samples from all traps for Station 1 with equation $w_s/u_* = 0.25\ D_*$ ($r^2 = 0.63$) is shown in a straight line, for Station 2 ($w_s/u_* = 0.24\ D_*$; $r^2 = 0.40$) is shown in a dashed line and for Station 3 ($w_s/u_* = 0.27\ D_*$; $r^2 = 0.69$) is shown in a dotted line.

The values of χ for stations 1, 2, and 3 are 4, 4.2, and 3.7 respectively. These values are similar to Van Rijn (1993), which supports the conclusion that the ratio varies in the vertical in proportion to the varying value of D_*. An average value of D_* was calculated for each station and divided by its corresponding χ in order to calculate w_s/u_* (Table 3.4).

Table 3.4: Comparison of the movability number (w_s/u_*) obtained using four different methods: (1) based on measured profiles of sand concentration, (2) the laboratory direct measurements of the settling velocity (w_s) and friction velocity (u_*), (3) Bagnold's (1966) sand transport theory, and (4) the relationship between the movability number (w_s/u_*) and the dimensionless grain diameter D_*.

Method	**w_s/u_***					
	Station 1		**Station 2**		**Station 3**	
1	0.20 ± 0.02		0.32 ± 0.10		0.19 ± 0.03	
2	surface	0.31	surface	0.84	surface	0.30
	middle	0.27	middle	1.09	middle	1.86
	epi-benthic	0.92	epi-benthic	1.09	epi-benthic	1.85
	benthic	1.95	benthic	1.78	benthic	2.39
	average 0.86 ± 0.78		average 1.20 ± 0.40		average 1.60 ± 0.90	
3	1.41		1.36		1.00	
4	surface	0.61	surface	0.98	surface	0.65
	middle	0.48	middle	1. 14	middle	1.78
	epi-benthic	1.17	epi-benthic	1.13	epi-benthic	1.80
	benthic	1.75	benthic	1.54	benthic	2.34
	average 1.00 ± 0.58		average 1.20 ± 0.24		average 1.64 ± 0.71	

The results varied between all four methods. Methods 2 and 4 yielded similar values for station 1; methods 2, 3, and 4 gave similar results for station 2; and for station 3, methods 2 and 4 yielded similar values. Method 1 yielded the lowest values of less than unity for all stations. Methods 2 and 4 yielded the movability number in the vertical. Note that benthic and epi-benthic traps are within the estimated constant stress layer, where a constant u_* value is justified in the derivation. The middle and surface traps however, show reductions in this number perhaps reflecting that the bed u_* is higher than expected for the measured settling rate of suspended sand or that w_s/u_* is decreasing in the vertical as a function of decreasing dimensionless grain size, D_*, as described by Van Rijn (1993). In general, method 2 where the settling velocity is measured in the lab, and friction velocity is derived from turbulent kinetic energy in the field is preferred to calculate the movability number. It offers the advantages of being based on direct measurements with fewer assumptions whilst providing information on vertical changes in this ratio.

3.4.2 Shields parameter for suspension

When the velocity of the fluid flowing over a bed of sediments increases, the fluid exerts a force that is sufficient enough to move the sediment particles from the bed and transport them into the flow (Komar and Miller, 1973). This phase is known as the threshold of sediment movement. The forces that act on a sediment particle are mainly drag, lift, and pressure forces (Nielsen, 2009) and initiation of motion will occur when these forces are larger than the resisting forces relating to the particle submerged weight (Van Rijn, 1993). The Shields parameter is a measure of sediment movability that accounts for pressure gradients and drag.

Suspension thresholds of Bagnold (1966), McCave (1984), Engelund (1965), and Van Rijn (1993) have been added to the classical Shields diagram. There is considerable variability in the suspension threshold as a function of D_*. It is generally considered that when $D_* < 3$, sand goes directly into suspension at the onset of motion (Amos *et al.*, 2010b). For $D_* > 3$, traction (bedload) takes place initially, which may be followed by suspension at higher bed shear stresses. It is this upper threshold that dictates the onset of sand in suspension. Its accurate assessment is considered a necessary pre-cursor to the evaluation of Rouse theory and so is part of this study.

Bagnold (1956) assumed sand goes to suspension when bed friction velocity, u_*, is 0.8 times the particle settling velocity, w_s. Using Bagnold's assumption, Lane and Kalinske (1941) defined the suspension criteria using the dimensionless ratio (w_s/ u_*) = 1.25. This ratio is redefined by Van Rijn (1984) and Niño et al. (2003) as 2.5 for high Reynolds numbers. Samaga et al. (1986) proposed a value of 2 while Komar and Clemens (1985) suggested that this ratio should be close to unity. Van Rijn (1993) proposed that the ratio w_s/ u_* is not always constant and depends on the dimensionless grain diameter, D_*.

The Shields parameter of each sample was plotted against its dimensionless grain diameter, D_*, on the Shield's diagram (after Van Rijn, 1993) in order to evaluate the published thresholds evident in Figures 3.12 to 3.14. Two approaches were used to solve for the Shields parameter. The first is based on the assumption of a constant friction velocity in the vertical (u_*), taken from the level of the ADV measurements at z = 0.22 m and the second assumed a varying friction velocity in the vertical (u_{*_z}) following a linear decrease in shear stress with height above the bed:

$$u_{*z}^2 = constant; \qquad z < 0.1\delta \tag{3.5a}$$

$$u_{*z}^2 = u_*^2\left(1 - \frac{z}{h - 0.1\delta}\right); \qquad z > 0.1\delta \tag{3.5b}$$

Equation (3.5b) is considered appropriate for a benthic boundary layer in a channel (modified from Liu, 2001).

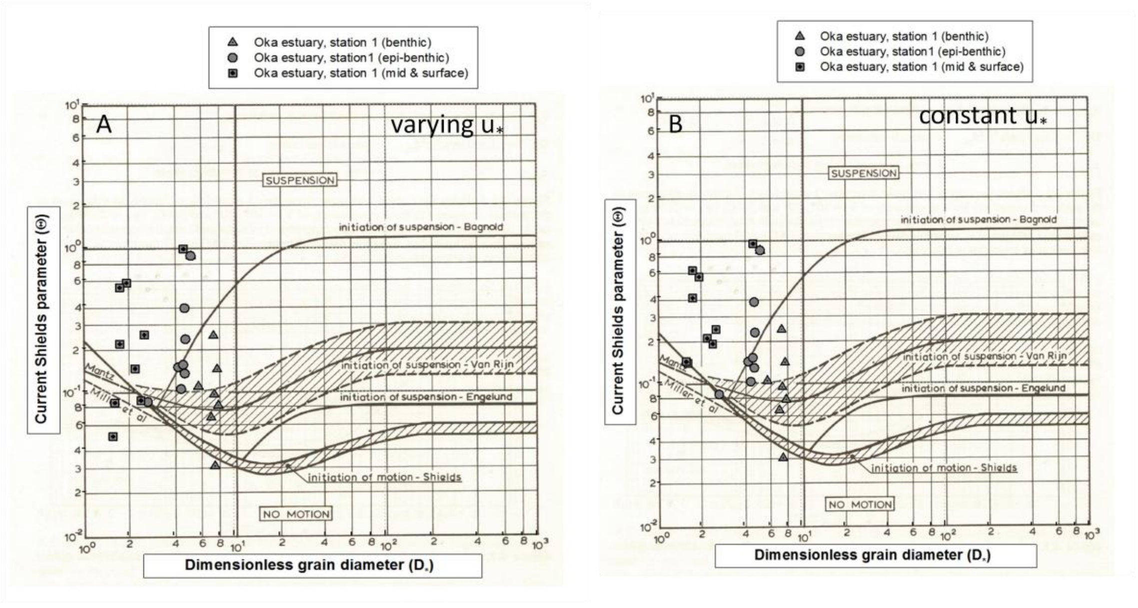

Figure 3.12: The Shields parameter plotted against dimensionless diameter with varying (A) and constant (B) friction velocity for Station 1(modified from Van Rijn, 1993).

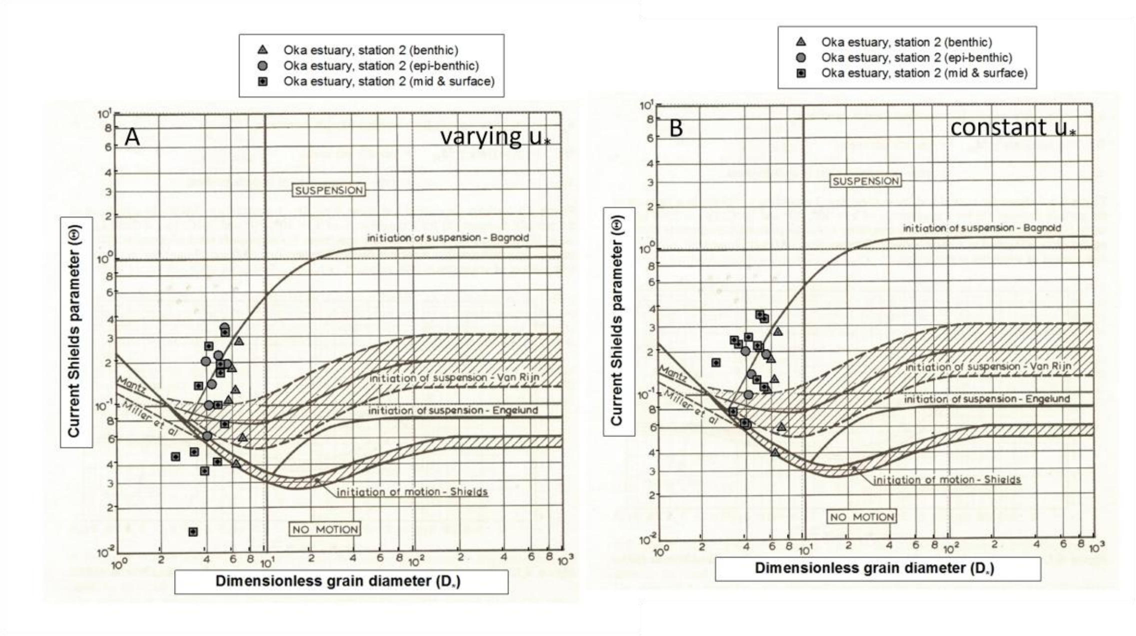

Figure 3.13: The Shields parameter plotted against dimensionless diameter with varying (A) and constant (B) friction velocity for Station 2 (modified from Van Rijn, 1993).

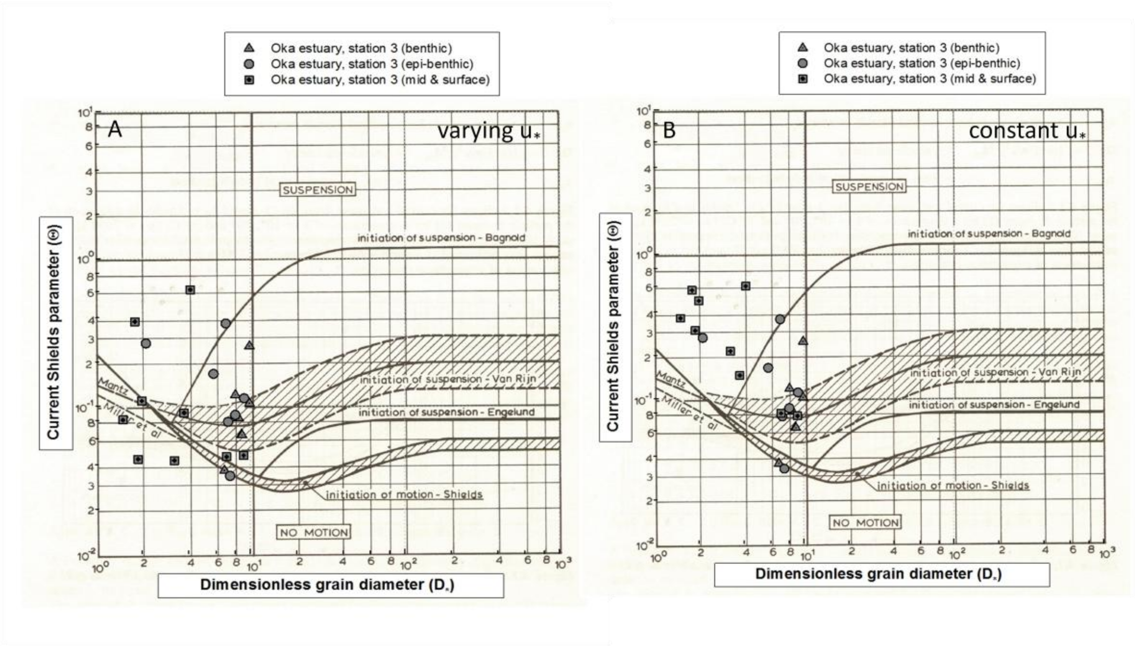

Figure 3.14: The Shields parameter plotted against dimensionless diameter with varying (A) and constant (B) friction velocity for Station 3 (modified from Van Rijn, 1993).

All the benthic and epi-benthic data fall in the $4 < D_* < 10$ region, while most of the surface and middle data fall in the $2 < D_* < 4$. The suspension threshold of Bagnold (1966) appears to separate well bed load and suspended load in this study. For all stations, the Shields parameters derived from surface and mid-water traps fall above this threshold when a constant u_* is assumed, but this is not the case when a depth varying u_* (using equations 3.5a and 3.5b) is used. This could be a result of either underestimating the values of u_* in the vertical or is a verification of our initial assumption that u_* is in fact constant in the vertical. The values of the epi-benthic Shields parameters for stations 1 and 2 straddle the suspension threshold of Bagnold (1966) suggesting a mixed population of bed load and suspended load (possibly saltation or intermittent suspension). The results from station 3 appear to show that the epi-benthic load was below the suspension threshold and hence dominated by bed load (saltation). This is probably due to the coarse nature of the sand in transport (Table 3.2). The benthic Shields parameters fall between the thresholds for traction and suspension suggesting that the sediment transport at the height of this trap is dominated by bedload.

3.5 Conclusions

This chapter reports on a field campaign to measure sand transport in a sandy tidal ria in northern Spain. It expands on previous work undertaken in Venice lagoon (on fine and very fine sand) by extending the range of grain sizes monitored for the suspension threshold and the applicability of the Rouse theory to coarse sand. The following are the major points of conclusion of this study.

Sand transport took place during the survey as both bedload and in suspension at all stations. Sand was mixed to the surface of the water column during peak flows. During periods of sand suspension, the grain size was considerably finer near the surface and coarser near the bed reflecting the fact that the settling velocity, w_s, was not constant in the vertical. This was evident at all stations and shows that predictions of a full concentration profile needs to consider a range of grain sizes, not just from the mean/median.

The values of the Rouse parameter confirmed that the sand transport in suspension was taking place throughout the benthic boundary layer. The D_* values for sand in suspension for the three stations were less than 10. This suggests that w_s/u_* is dependent on D_* and in time. This dependency had a value of $D_*/4$ which is close to the value suggested by Van Rijn (1993).

The Shields parameter derived from the field measurements defines the suspension thresholds better when friction velocity is assumed constant throughout the water column. This implies that the constant stress layer of the boundary layer is present to the surface. Finally, the suspension threshold of Bagnold (1996) was found to discriminate best between bed load and suspended load measured in this study.

Chapter 4: Nearbed suspension of sand

4.1 Introduction

Sediment transport in the marine environment is very difficult to predict as the interaction between waves, currents, sediments, and the seabed is complex, and therefore cannot be described in a simple manner (Absi, 2010). The concentration of suspended sediments in the water column of a benthic boundary layer depends on the interaction between the sediment properties and the flow turbulence. This interaction is at the foundation of predicting sand suspension and has dominating effects on sediment transport (Conley et al., 2008). An important area of research that is related to accurate predictions of suspended sand in transport is the formulation of the magnitude and shape of the time-averaged suspended sand concentration profile in a tidal channel (Rose and Thorne, 2001). The process of constructing time-averaged suspended-sediment concentration profiles for combined waves and currents is broken down into two steps: The first is to specify the amount of sediment in suspension; the second is to define the vertical distribution of this sediment throughout the water column (Nielsen, 1986; Lee et al., 2004).

Previous studies on sand transport have provided significant observations on how flow velocity and sediment concentration profiles vary with height above the bed (Whitehouse, 1995). Thorn (1975) and Lees (1981) showed that the Karman-Prandtl and Rouse equations could provide acceptable descriptions of the flow and sediment profiles. However, these observations were based on limited amount of data where velocity and sediment concentration measurements were taken at different heights. Dyer (1980) used a different approach where he measured the velocity and sediment concentration at one height near the bed but had to assume a reference height, a, and reference concentration, C_a, in order to determine the vertical sediment concentration profile. One of the limitations regarding sediment concentration profile measurements is not having enough data points in the vertical where both the velocity and sediment concentration are measured at the same height and time.

Another restriction in measuring suspended sand concentration is the difficulty of using point measurement devices or pump sampling equipment very close to the bed without causing disturbance (Rose and Thorne, 2001). Accurate measurement of suspended sediment concentration profiles is essential for understanding sediment dynamics in coastal environments, therefore substantial efforts have been dedicated to develop measuring techniques and to improve data accuracy (Ha et al., 2011).

The main objectives of this chapter are: to define the vertical distribution of sand in suspension and establish the existence of the reference concentration height and where relevant, its magnitude; to determine the main driver of the sand concentration profile; and finally, to develop a new simplified equation for concentration with height above the bed, C_z, without relying on a reference height, a, and reference concentration, C_a. This will be achieved by using high resolution and non-intrusive acoustic backscatter data using a sonar imaging technique, which will provide enough data to define a concentration profile in the vertical.

4.2 Suspended sediment transport

Total sand transport in a marine setting consists of two major modes: suspension and bed load transport (Nielson, 1984). Grain particles are considered to be in suspension when supported by fluid turbulence and move as bed load when the immersed weight is supported by other grains at the bed. There are three modes of sediment particle motion: 1) rolling or sliding, 2) saltation, and 3) suspension (Van Rijn, 1993). When the bed shear stresses exceed the critical value of initiation of motion, sediment particles will start to roll or slide along the bed. As the bed shear stresses increase, sediment particles move by jumping or saltation. Once the bed shear stresses exceed the sediment fall velocity of grains in motion, the particles are lifted by upward turbulence which causes them to move in suspension. The movement of sand as bed-load or suspended load can occur simultaneously and the concentration is called the total load.

Einstein (1950) defines bedload transport as the rolling and sliding of sediment particles in a thin layer equal to two particle diameters within the bed. He believes that saltation is part of suspended load transport as the jump lengths of sediment particles are larger by far than a few grain diameters. Moving by saltation is the most typical movement of bed load sediment particles in the coastal marine environment (Van Rijn, 1993). Saltation is bound in a layer with a maximum thickness of about ten particle diameters. During the rising of the trajectory, the vertical component of both the fluid drag force and the gravitational force are downwards (Figure 4.1).

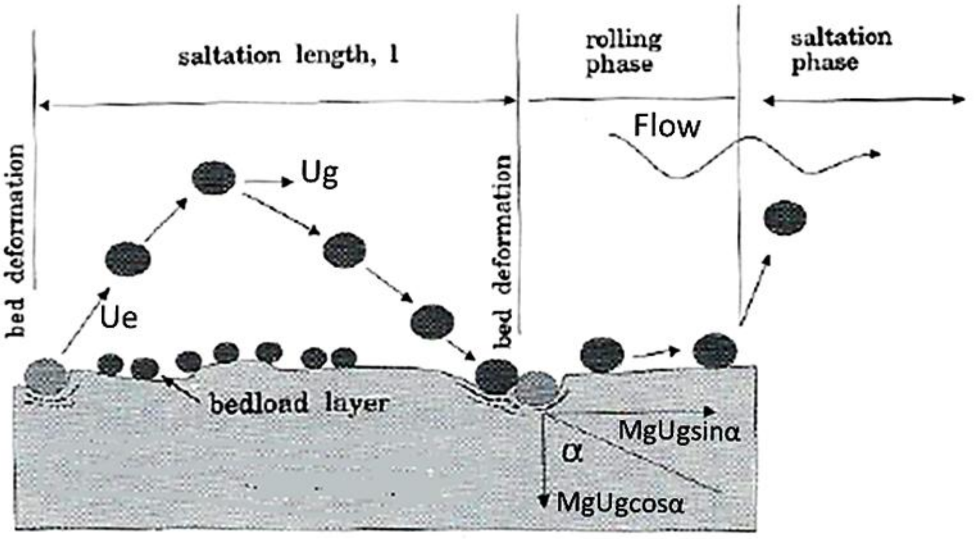

Figure 4.1: A schematic diagram of grain saltation process showing how the particle motion can be broken down into a saltation phase and a rolling phase. The saltating grain terminal velocity is represented by Ug and Ue is the trajectory or ejection velocity, which is assumed negligible. Mg is the total mass of the saltating grain and α is the impact angle at which the grain touches the bed (modified from Amos et al., 1998).

Throughout the falling trajectory, the vertical component of each force opposes each other. The lift force for both cases is always directed upwards. Since the momentum flux is derived from the flow and the vertical component is due to the gravitational force, the saltating grains absorb momentum from the flow. This causes a reduction in flow velocity (Wiberg and Rubin, 1989). When the sediment particle comes in contact with the bed at an impact angle, α, most of its momentum is dissipated by the bed material. The vertical component of the momentum flux ($M_gU_g\cos\alpha$) is delivered to the bed while the horizontal component ($M_gU_g\sin\alpha$) initiates the rolling mode of transport, also known as surface creep. Sediment particles alternate between periods of successive saltations and periods of resting on the bed (Amos et al., 1998; Van Rijn, 1993).

Van Rijn (1993) stated that "*the separation between the bedload and the suspended load is an idealisation of actual conditions*", as there is not a clear indicator of where the transition line should be. An arbitrary distinction is made at what is called the reference level, a: The concentration at this level is the reference concentration, C_a. Determining the values of the reference concentration and reference level is required to verify the distribution of sand in suspension using the Rouse method.

4.2.1 The reference concentration

The general understanding of the dynamics of sediment particles in the benthic boundary layer subject to combined wave and current velocities, is that the sum of the combined wave and current bottom stresses generate an equilibrium between sediment resuspension and settling near the bed, which determines the "reference concentration" (Agrawal and Traykovski, 2001). The reference concentration is a controversial parameter of suspended sand transport and the accurate quantification of its magnitude remains one of the most obscure problems in sand transport (Rose & Thorne, 2001). Indeed, it is unclear if it exists. The reference level has been mostly rationally assumed in the literature as the upper surface of the bedload layer thickness ($a = \delta_b$) and the reference concentration is equal to the bedload concentration for flat beds (Van Rijn, 1993).

There are various definitions of the bed-load layer thickness, δ_b. Van Rijn (1984a) expressed δ_b to be in the range of two to ten times the median grain diameter. Einstein (1950) assumed that the thickness is twice the d_{35} of the bed sand. Engelund and Fredsϕe (1976) assumed δ_b to be twice the median grain diameter, whereas Smith and Mclean (1977) defined it as equal to the zero velocity level, z_0. These definitions prescribe a reference concentration at a reference level very close to the bed which is unrealistic in the case of bedforms, and which can lead to large errors (Van Rijn, 1984b). Therefore, the reference level related to the bed-form height is introduced, where it is assumed to be equal to half of the bed-form height. When the dimensions of the bed-form are not known, the roughness height, k_s, is used instead. A minimum value of $0.01h$ is used where h is the water depth (Dyer and Soulsby, 1988).

4.2.2 Suspended sand concentration profiles and the benthic boundary layer

Suspended concentration profiles are usually expressed as the product of a reference concentration close to the bed and a shape function (Bolaños et al., 2012). The reference concentration defines the level of the suspended load and the shape function describes the variation in the concentration profile with height above the bed. The shape function is represented by one of the semi-empirical formulas that are based on uniform (Equation 4.1), linear (Equation 4.2) or parabolic (Equation 4.3) variations of sediment diffusivity in the vertical, which result in exponential, power law, or Rouse shape functions respectively (Soulsby, 1997).

uniform eddy diffusivity: $$\frac{C_z}{C_a} = e^{-\alpha\left(\frac{w_s}{\beta k u_*}\right)\left(\frac{z-a}{h}\right)} \tag{4.1}$$

linear eddy diffusivity: $$\frac{C_z}{C_a} = \left(\frac{a}{z}\right)^{\alpha\left(\frac{w_s}{\beta k u_*}\right)} \tag{4.2}$$

parabolic eddy diffusivity: $$\frac{C_z}{C_a} = \left(\frac{h-z}{z}\frac{a}{h-a}\right)^{-\left(\frac{w_s}{\beta k u_*}\right)} \tag{4.3}$$

where, C_z is the sand concentration at height z above the bed, C_a is the reference concentration at reference height a, h is the water depth, and $(\frac{w_s}{\beta k u_*})$ is the Rouse parameter where w_s is the grain settling velocity, u_* is the flow friction velocity, k is von Karman constant (= 0.41), and β is the ratio of eddy diffusivity to eddy viscosity (= 1).

The Rouse shape function is approximated by the power law in the bottom 25% of the water column. Generally, the exponential profile is specified by a vertical mixing length that is dependent on grain size and bedforms while the Rouse and power law profiles are dependent on the Rouse parameter, which is dependent on grain size and the friction bed velocity. The Rouse shape function based on parabolic eddy diffusivity is used in this study.

In deep water (≈ 400 m), the benthic boundary layer is thin (≈ 10 m) (Lueck and Victoria, 2009). On the other hand, in coastal regions where depths are shallow, the benthic boundary layer can take up most of the water column for unidirectional flows. Generally the log-layer occupies most of the boundary layer, wherein the velocity increases logarithmically with height above the bed (Bowden, 1978; Soulsby, 1983). In the benthic boundary layer, the upward turbulent diffusion of sediment is balanced by the sediment's tendency to fall out of suspension, which results in a concentration profile that decreases with height above the bed (Glenn and Grant, 1987).

4.3 Methodology

A field survey was carried out in June 2011 at three different locations in the vicinity of the main tidal inlet of the Oka estuary (see §3.3). The first location, Station 1, was inside the estuary where it is sheltered from waves and is flood-tide dominated, Station 2 was in the inlet mouth which is ebb-tide dominated, and Station 3 was on the ebb tide delta. Each location differs in grain size such that the median size D_{50} of the grains near the bed at Station 1 was 0.31 mm, 0.28 mm at Station 2, and 0.38 mm at Station 3. Figure 4.2 shows the general deployment and setup of the equipment used in the survey. A detailed description of the sand traps, ADV, and ADCP is found in Chapter 3. This chapter focuses on the Sediment Imaging Sonar (SIS) and its use to measure sand concentration in the vertical.

The SIS is a single-beam sediment imaging sonar produced by Marine Electronics Ltd. (Guernsey). It is an Image Profiling Sonar 1640/2640 that emits a pencil-beam sound wave (beam width angle 1.8°) at a frequency of 1.1 MHz (Lefebvre, 2009). The SIS was fixed on a vertical rod from the side of the boat facing downwards (Figure 4.2B). It was lowered to the water until it was completely submerged, for a maximum of 5 minutes every hour to measure backscatter intensities in the water column. The SIS is connected to a computer to allow real-time display and recording of the data. The sonar beam is swept at right angles to the sonar body and sweeps can be of any angle to a full 360° with beams emitted every 0.9°. Data are displayed and recorded by the Sediment Imager Control Software® and backscatter intensity along the beams are recorded for each sweep (.img file) and converted to ASCII image intensity (.xyz file) with specially written software (Sediment Imager Converter 1.0 provided by Marine Electronics Ltd).

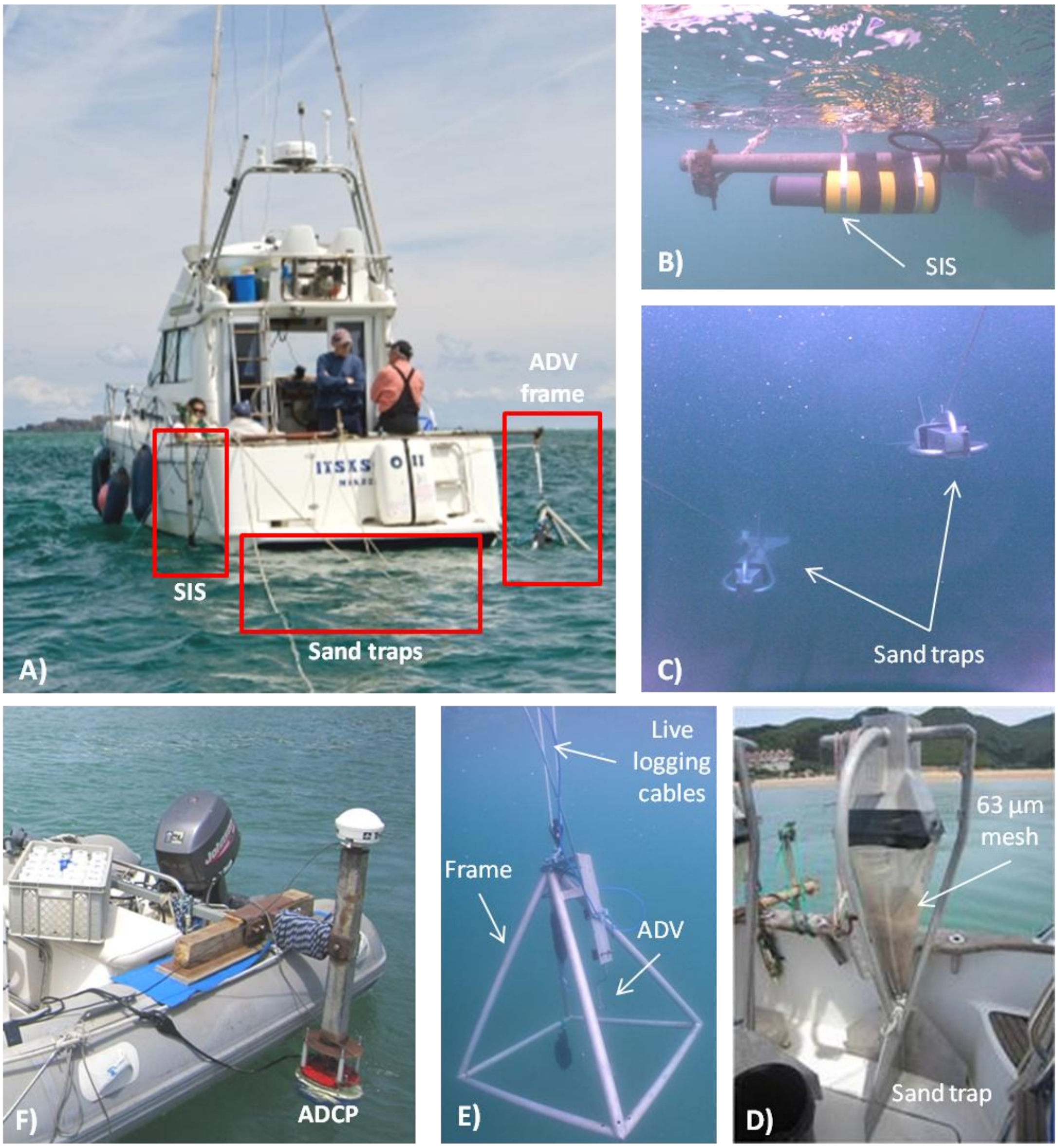

Figure 4.2: A) Photo showing the general deployments of the sand traps, SIS, and ADV on the stationary boat (Starfisher). B) The SIS attached horizontally to an L-shaped rod lowered to just below the surface. C) Surface and middle traps deployed and oriented with water flow. D) Recovered sampler showing the sand trapped in the plankton net after 15 minutes of deployment. E) Deployed ADV attached to a triangular frame. F) Downward looking ADCP fixed on a vertical rod mounted from zodiac. (All photos courtesy of Eleonora Manca)

The data available after conversion are beam angle (θ, in degrees), distance from the transducer (R, in m) and backscatter (B, dimensionless). The backscatter intensity values are given in relative integer values (0 to 255, linear). Backscatter data for one sweep is shown in Figure 4.3 where the sub-horizontal line of maximum backscatter is taken as the seabed. The vertical backscatter at point 0 m (beam angle 180°) was then extracted for future analysis.

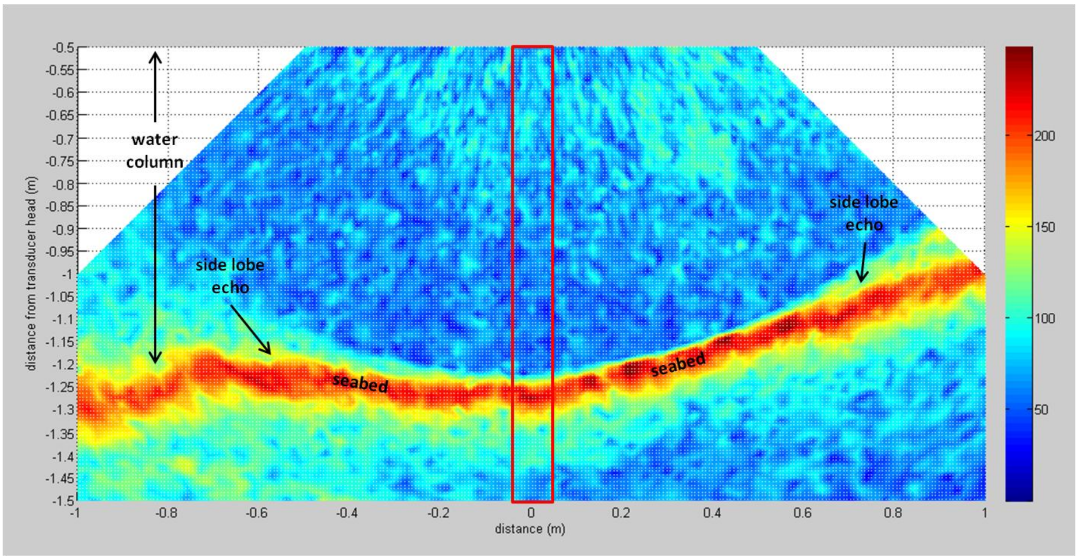

Figure 4.3: The image file of the backscatter intensity recorded from the transducer for run a090611c_20 of Station 1 on 09/06/2011. The colour scale indicates the backscatter amplitude (dimensionless). The red border indicates the extracted vertical data at point 0 m and converted as explained in the text.

Any data below the detected seabed is removed. Data along the surface is also eliminated as it is in the near field region of acoustical signal and thus influenced by the sonar head. The remaining data were then corrected for attenuation, α, due to absorption by the water, α_w, and scatter from suspension of fine particles, α_s, after Moore (2012). Attenuation due to absorption by water, α_w, is expressed as:

$$\alpha_w = (55.9 - 2.37T + 4.77 \times 10^{-2}T^2 - 3.48 \times 10^{-4}T^3)10^{-15}F^2 \tag{4.4}$$

where T is water temperature in degrees Celsius and F is the beam frequency in Hz. The attenuation due to sediments, α_s, includes both the particle scattering, $\alpha_{s,scat}$, and absorption by viscosity of the surrounding boundary layer, $\alpha_{s,vsc}$. Both are linearly proportional to the mass concentration, M, of the scatterers and are written as:

$$\alpha_{s,scat} = \frac{3M\langle a_s^2 X\rangle}{4\rho_s\langle a_s^3\rangle} \tag{4.5}$$

where, ρ_s is the particle density, a_s is particle radius, and

$$X = \frac{0.29x^4}{0.95 + 1.28x^2 + 0.25x^4} \tag{4.6}$$

where, the non-dimensional wave number $x = ka_s$ and k is the acoustic wave number. Viscous sediment attenuation is expressed as:

$$\alpha_{s,visc} = M\langle \xi_v \rangle \tag{4.7}$$

where, the viscous absorption term, ξ_v, is written as:

$$\xi_v = \frac{k(\sigma - 1)^2}{2\rho_s}\left[\frac{s}{s^2 + (\sigma + \delta)^2}\right] \tag{4.8}$$

where, $s = \frac{9}{4\beta a_s}\left[1 + \frac{1}{\beta a_s}\right]$, $\sigma = \frac{\rho_s}{\rho_w}$, $\delta = \frac{1}{2}\left[\frac{9}{2\beta a_s}\right]$, $\beta = \sqrt{\frac{\omega}{2v}}$, ω is 2π times the frequency, and v is the kinematic viscosity (1.1 x10^{-6} m^2/s). The angular brackets indicate an average over the number size distribution of the suspended sediment. The corrected backscatter intensity profiles are smoother than the original as shown in Figure 4.4 of the same run. Applying these corrections to the data results in an improved outcome, where they are better correlated. This corrected backscatter was used for the rest of the analysis.

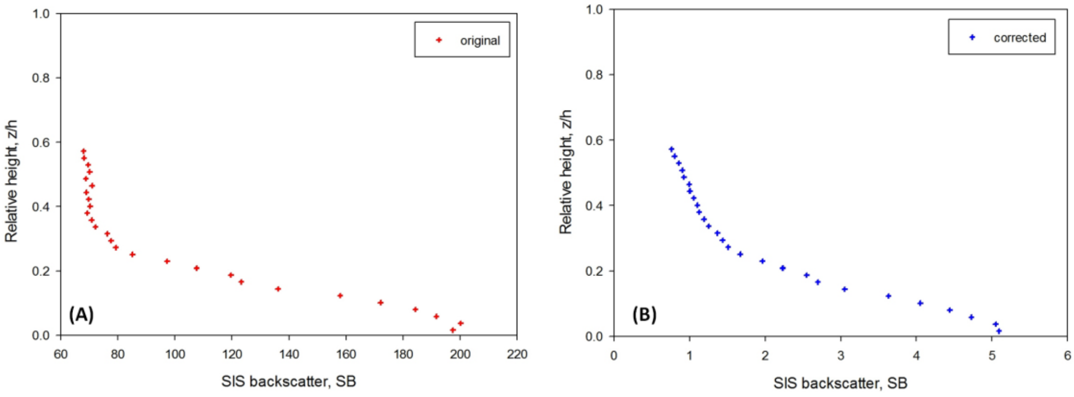

Figure 4.4: A comparison between the extracted original backscatter intensity profile (red) and the corrected backscatter intensity profile (blue) with relative height for run a090611_3 for Station 1, 09/06/2011.

4.4 Results

4.4.1 Calibration of SIS

The corrected SIS backscatter is calibrated against the sand trap measurements and converted to mass concentration units (mg/l). Sand concentrations from the surface, middle, epi-benthic, and benthic traps from each profile were compared to their corresponding value from the SIS (Table 4.1). Each station was calibrated separately due to the differences in grain size of the suspended sand. Figure 4.5 shows the calibration plots of the SIS backscatter for all stations.

The statistical significance is not high due to the limited number of samples. The exponential best fit regression yielded $SC = 0.0036e^{2.54SB}$ mg/l for station 1, $SC = 1.05e^{0.19SB}$ mg/l for station 2, and $SC = 0.59e^{0.46SB}$ mg/l for station 3. Once the backscatter is converted and plotted, the depth with the highest concentration is assumed to be the seabed. A total of three to seven sweeps were averaged to obtain one sand profile. This was based on the time the SIS was deployed in the water.

Table 4.1: Sand trap concentration (mg/l) and the corresponding SIS backscatter for profiles 1, 2, 3, and 5 of Station 1; profiles 1 and 5 of Station 2; and profiles 1, 2, 4, 5, 6, and 8 of Station 3.

Sample	Sand trap concentration (mg/l)	SIS backscatter
S1B1	14.583	3.159
S1E1	0.067	1.799
S1M1	0.065	0.925
S1S1	0.053	1.042
S1B2	13.902	3.310
S1E2	0.245	1.675
S1M2	0.054	0.913
S1S2	0.119	0.988
S1B3	23.560	3.067
S1E3	0.409	2.339
S1M3	0.091	1.240
S1S3	0.035	0.964
S1B5	8.464	2.551
S1E5	0.127	1.937
S2B1	92.165	21.116
S2E1	1.731	15.580
S2S1	0.186	1.265
S2B5	67.846	18.261
S2E5	17.425	12.765
S2M5	10.323	6.481
S2S5	6.084	1.139
S3B1	1768.160	11.786
S3E1	137.578	9.549
S3S1	2.424	1.105
S3B2	8642.846	9.478
S3E2	363.924	6.733
S3S2	1.326	1.113
S3B4	305.861	11.394
S3E4	0.495	9.095
S3S4	0.642	1.120
S3B5	217.665	9.800
S3E5	0.734	8.416
S3M5	2.150	5.157
S3S5	0.620	1.144
S3B6	202.916	16.134
S3E8	0.545	8.590

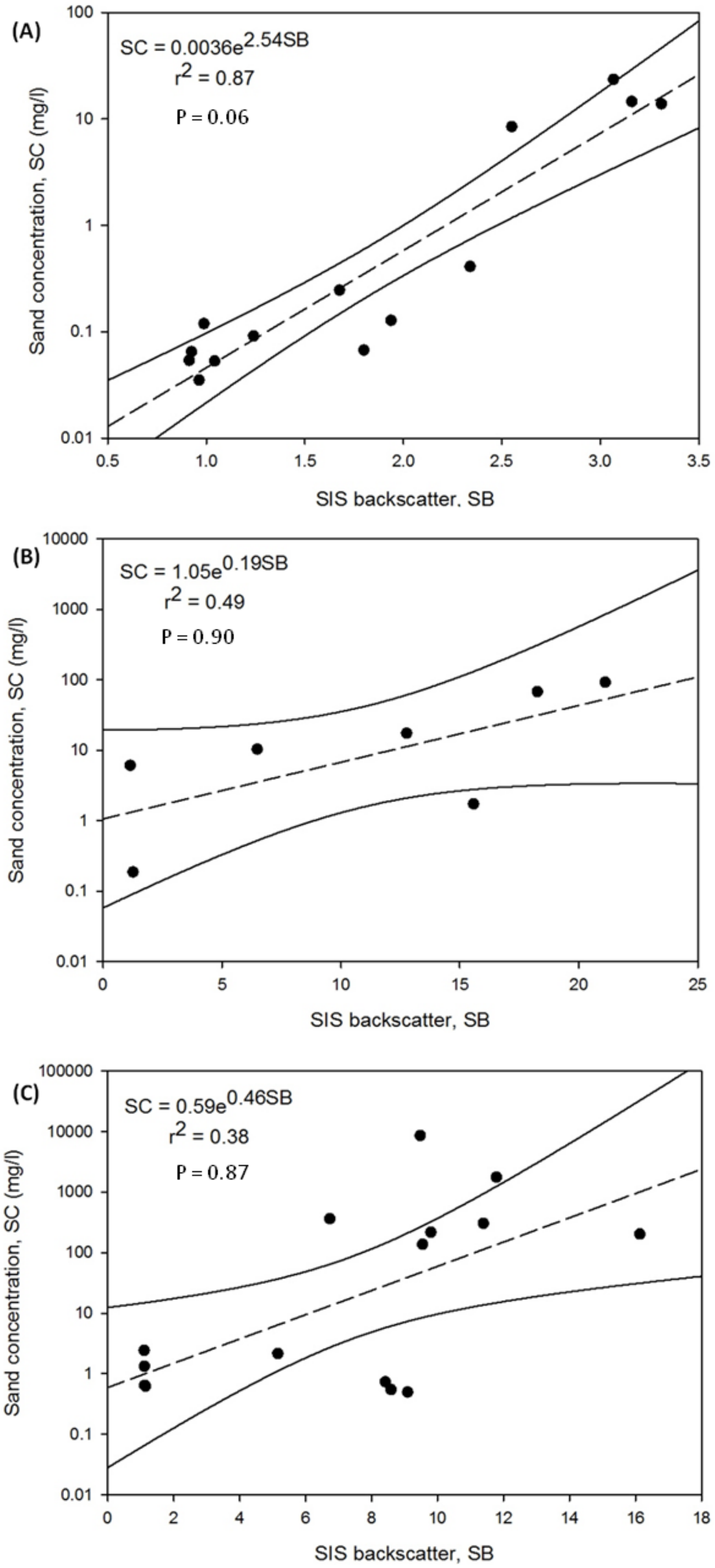

Figure 4.5: The SIS backscatter calibration for (A) station 1 (n = 14, P = 0.06), (B) station 2 (n = 7, P = 0.90), and (C) station 3 (n = 15, P = 0.87), showing the equation of the best fit line between the sand trap concentration (SC) and SIS backscatter (SB) with 95% confidence intervals.

4.4.2 Sand concentration in suspension

The vertical distribution of suspended sand concentration for all three stations showed a consistent decrease with height above the bed, regardless of grain size, flow velocity, stage of tide, or water depth. These profiles were sub-divided into layers. The layers are based upon trends in concentration with elevation (z) dc/dz and were defined statistically.

The sand concentration profile is divided into a 4-layer model: starting from the top a surface layer, a Roussian layer, a buffer layer, and an inner layer. Figure 4.6 shows the sand concentration profiles for all stations in relation to relative height with each layer labelled. Each layer is governed by a specific function that determines its shape and thickness. The boundary of each layer is the point where a change of slope occurs. The absolute height is variable, such that each profile had a different water depth; therefore relative height was used instead to better represent the data.

The inner layer, the layer closest to the sea bed, is where the sand concentration is at its maximum. This layer has an average relative height of 0.10. Above the inner layer, is a layer that takes up most of the water column (average relative thickness of 0.56) and it fits the Roussian theory. Between the Roussian and inner layer is a transitional or buffer layer where the profile changes slope. The buffer layer varies between the profiles, as it was visible in some profiles, while in other profiles it did not exist. The Roussian layer does not go all the way to the surface; thus a surface layer is present. But the surface layer is considered to be in the near field region and therefore is neglected. Therefore, only three layers (Roussian, buffer, and inner) are recognized and discussed in further detail.

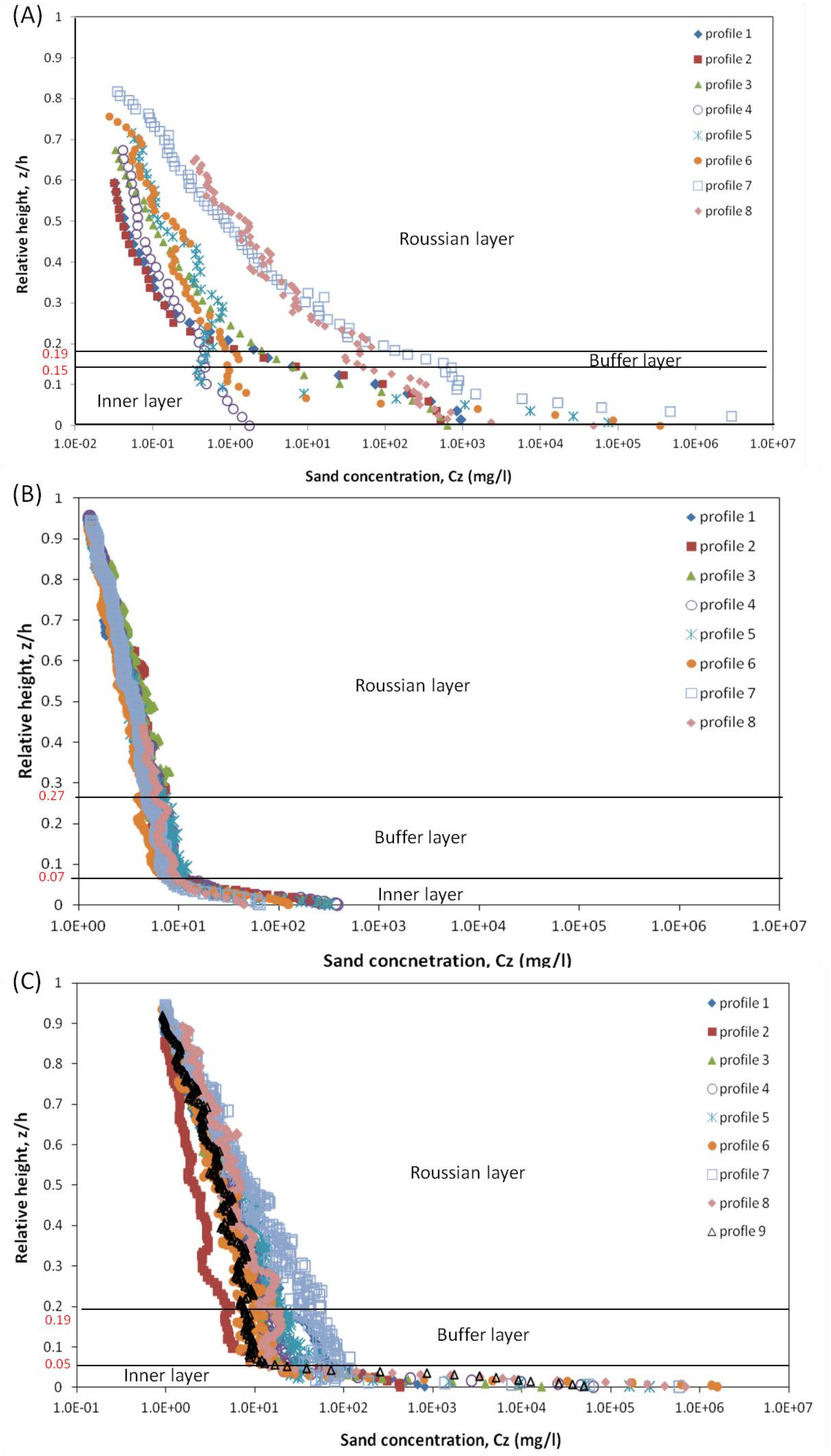

Figure 4.6: Sand concentration (mg/l) with relative height for A) Station 1, B) Station 2, and C) Station 3. The surface, Roussian, buffer, and inner layers are labelled and their corresponding relative heights are highlighted in red.

For all three stations the Roussian layer is the thickest layer with an average thickness of 0.47 for Station 1, 0.60 for Station 2, and 0.62 for Station 3 (Table 4.2). The Roussian layer starts at an average relative height of 0.68 at Station 1, but was much higher at Stations 2 and 3, both with a relative height of 0.81. The buffer layer varied significantly as in some profiles it did not exist (*e.g.* profiles 1 to 3 of Station 1 and profiles 1 and 8 of Station 2), while in profile 3 of Station 2 it was as thick as the Roussian layer. Station 3 was the only station where the buffer layer was present in all profiles. The maximum inner layer thickness was 0.34 in profile 1 of Station 1 and the minimum was 0.02 at Station 3. The average inner layer thickness for all three stations was 0.10.

Table 4.2: The thicknesses and the relative heights of the Roussian, buffer, and inner layers of all profiles of Stations 1, 2, and 3. The average thickness for each layer of each station is highlighted in Bold.

	Profile	Layer thickness			Relative height		
		Roussian	Buffer	Inner	Roussian	Buffer	Inner
Station 1	1	0.25	0	0.34	0.59	-	0.34
	2	0.34	0	0.25	0.59	-	0.25
	3	0.55	0	0.12	0.67	-	0.12
	4	0.4	0.13	0.14	0.67	0.27	0.14
	5	0.43	0.18	0.11	0.72	0.29	0.11
	6	0.6	0.05	0.11	0.76	0.16	0.11
	7	0.69	0.07	0.05	0.81	0.12	0.05
	8	0.56	0.05	0.04	0.65	0.09	0.04
Average		**0.48**	**0.06**	**0.15**	**0.68**	**0.19**	**0.15**
Station 2	1	0.62	0.03	0.05	0.70	0.08	0.05
	2	0.57	0	0.06	0.63	-	0.06
	3	0.42	0.46	0.07	0.95	0.53	0.07
	4	0.59	0.29	0.08	0.96	0.37	0.08
	5	0.76	0.12	0.05	0.93	0.17	0.05
	6	0.6	0.21	0.13	0.94	0.34	0.13
	7	0.8	0.06	0.08	0.94	0.14	0.08
	8	0.4	0	0.04	0.44	-	0.04
Average		**0.60**	**0.15**	**0.07**	**0.81**	**0.27**	**0.07**
Station 3	1	0.73	0.09	0.07	0.89	0.16	0.07
	2	0.66	0.09	0.10	0.85	0.19	0.10
	3	0.73	0.13	0.06	0.92	0.19	0.06
	4	0.44	0.02	0.05	0.51	0.07	0.05
	5	0.41	0.04	0.02	0.47	0.06	0.02
	6	0.75	0.14	0.04	0.93	0.18	0.04
	7	0.68	0.24	0.02	0.94	0.26	0.02
	8	0.61	0.23	0.05	0.89	0.28	0.05
	9	0.57	0.27	0.08	0.92	0.35	0.08
Average		**0.62**	**0.14**	**0.05**	**0.81**	**0.19**	**0.05**

Four sand concentration profiles at different tidal stages (start of ebb, end of ebb, start of flood, and end of flood) are given in Figures 4.7 to 4.9 for Stations 1 to 3 respectively. The Reynolds number, $R_e = \bar{U}d/\nu$, is calculated twice, once for the Roussian layer and once for the inner layer (Table 4.3). The values show that the flow is turbulent rough throughout the water column. The average velocity at the surface, using the ADCP measurement, was used to calculate the Roussian layer R_e. The average velocity recorded from the ADV was used for the inner layer R_e as the ADV was positioned at an absolute height of 0.22 m above the bed (within the inner layer). The upper layer R_e for Station 1 had an average of 5.77 x 10^5, 2.2 x 10^6 for Station 2, and 1.63 x 10^6 for Station 3. The inner layer had smaller values of R_e, with 6.54 x 10^4, 6.52 x 10^4, and 5.75 x 10^4 for Stations 1, 2, and 3 respectively.

Table 4.3: The mean velocity at z = 0.22 m, mean velocity at the surface, and the upper and lower Reynolds numbers for all profiles at Stations 1, 2, and 3.

Station	SIS Profile	Average velocity at z = 0.22 m $\bar{U}$ (m/s)	Average velocity at surface $\bar{U}$ (m/s)	Reynolds number (upper layer) Re	Reynolds number (inner layer) Re
1	1	0.205	0.397	2.982E+05	4.131E+04
	2	0.325	0.548	4.166E+05	6.629E+04
	3	0.415	0.500	4.037E+05	8.571E+04
	4	0.168	0.441	3.603E+05	3.512E+04
	5	0.293	-	-	6.100E+04
	6	0.293	-	-	6.100E+04
	7	0.493	0.660	1.035E+06	1.030E+05
	8	0.344	0.469	9.485E+05	6.989E+04
	Average	**0.317**	**0.503**	**5.770E+05**	**6.542E+04**
2	1	0.134	0.539	2.013E+06	2.678E+04
	2	0.400	0.429	2.101E+06	8.027E+04
	3	0.400	0.429	2.117E+06	8.027E+04
	4	-	-	-	-
	5	-	-	-	-
	6	0.450	0.604	2.440E+06	9.068E+04
	7	0.450	0.604	2.213E+06	9.068E+04
	8	0.110	0.757	2.293E+06	2.235E+04
	Average	**0.324**	**0.560**	**2.196E+06**	**6.517E+04**
3	1	0.428	0.602	1.457E+06	8.728E+04
	2	0.256	0.409	9.064E+05	5.193E+04
	3	0.338	0.510	1.921E+06	6.859E+04
	4	0.338	0.510	2.054E+06	6.831E+04
	5	0.222	0.380	1.802E+06	4.437E+04
	6	0.204	-	-	4.094E+04
	7	-	-	-	-
	8	-	-	-	-
	9	0.204	-	-	4.094E+04
	Average	**0.284**	**0.482**	**1.628E+06**	**5.748E+04**

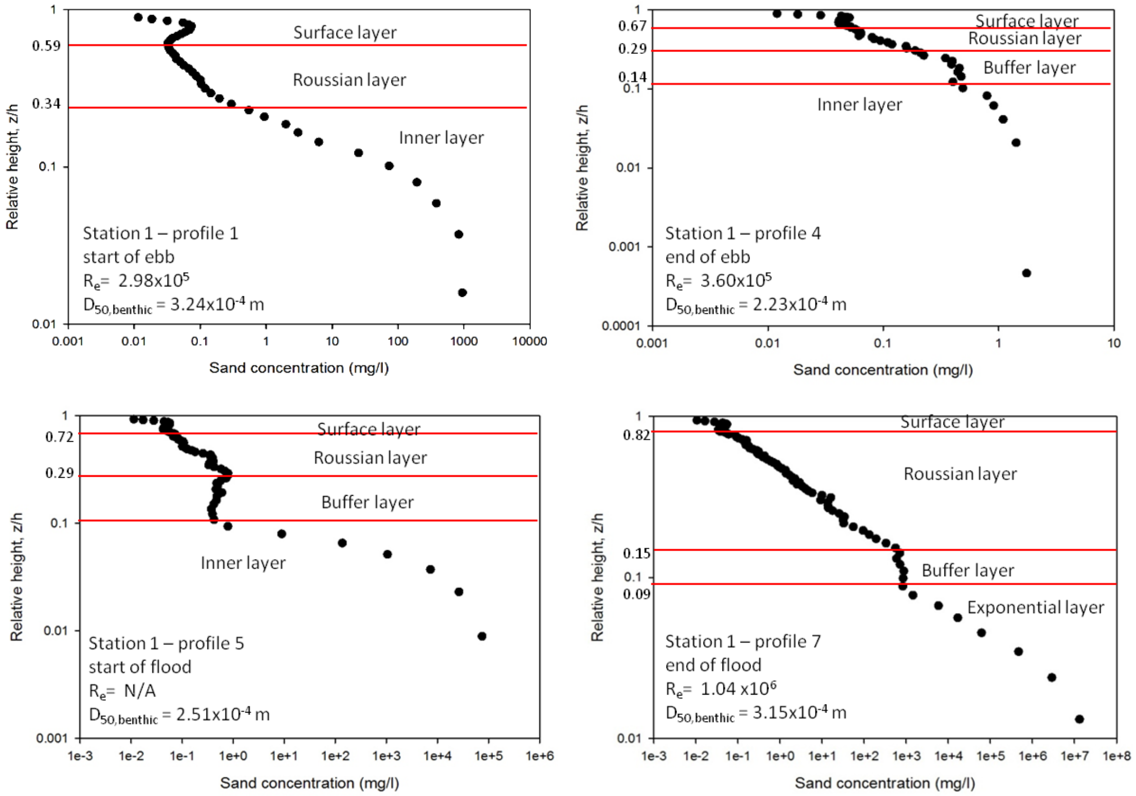

Figure 4.7: Sand concentration profiles 1, 4, 5, and 7 with relative height for Station 1 with the tidal stage, Reynolds number (R_e) of the Roussian layer, and the mean grain size (D_{50}) from the benthic trap sample collected at each interval.

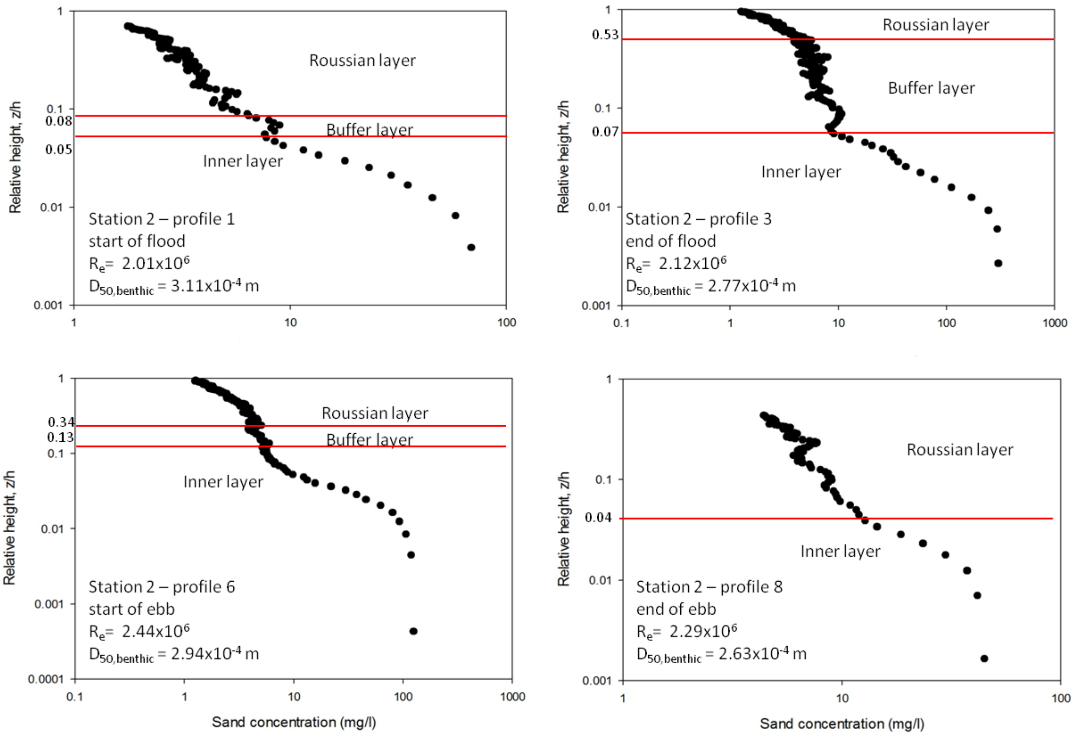

Figure 4.8: Sand concentration profiles 1, 3, 6, and 8 with relative height for Station 2 with the tidal stage, Reynolds number (R_e) of the Roussian layer, and the mean grain size (D_{50}) from the benthic trap sample collected at each interval.

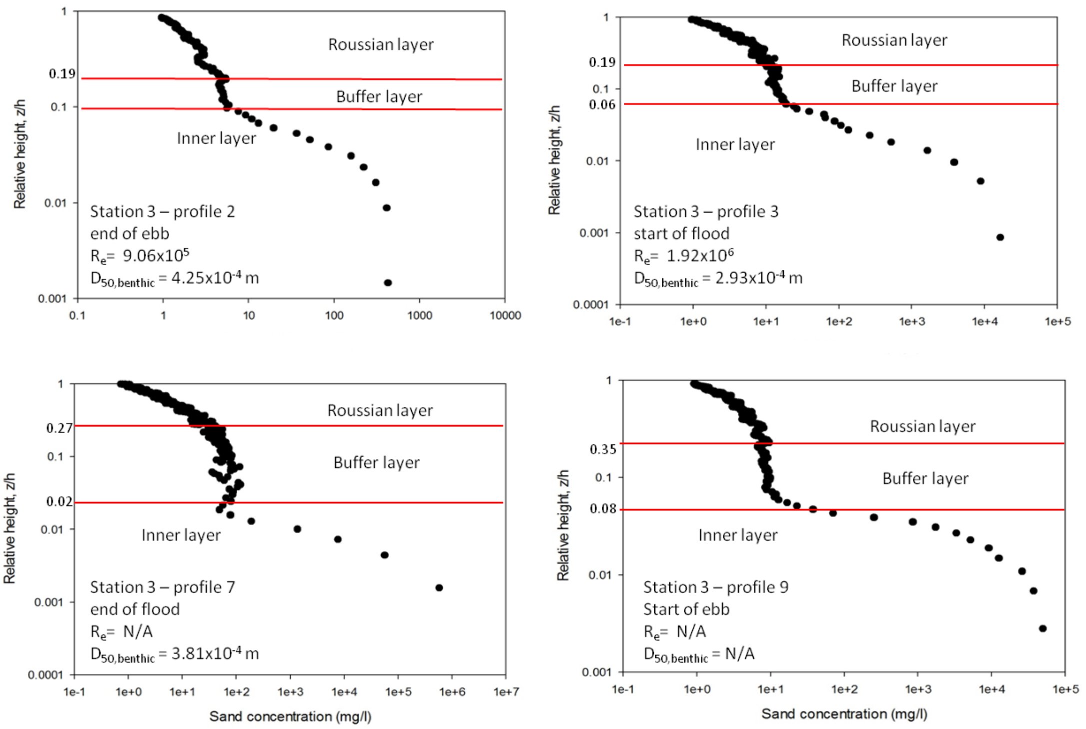

Figure 4.9: Sand concentration profiles 2, 3, 7, and 9 with relative height for Station 3 with the tidal stage, Reynolds number (Re) of the Roussian layer, and the mean grain size (D_{50}) from the benthic trap sample collected at each interval.

Sand concentrations were greatest during the flood tide at both Stations 1 and 3. Nevertheless, it can be seen that the concentration profiles did not vary much with the tidal stage (Figure 4.10). Sand in suspension was highest in the bottom 20% of the water column, which is part of the inner layer. This was also evident in the vertical distribution of sand concentration from the sand traps (Chapter 3, Figure 3.7). At Station 1, sand in suspension was at its maximum during the flood tide, while at Station 2, it was approximately the same throughout both ebb and flood. As for Station 3 suspended sand concentration maximized during the mid-flood tide and continued to be high throughout the ebb tide. This is due to tidal asymmetry of the estuary where the flood phase is shorter than the ebb. As the general trend of the vertical distribution of sand is the same for both the SIS and sand trap data, the variation with tidal stage is not similar. This difference between the two plots (Figure 4.10 and Figure 3.7) may be a result of different methods used when interpolating the data. The sand trap data is based on a maximum of six data points while the SIS has more data.

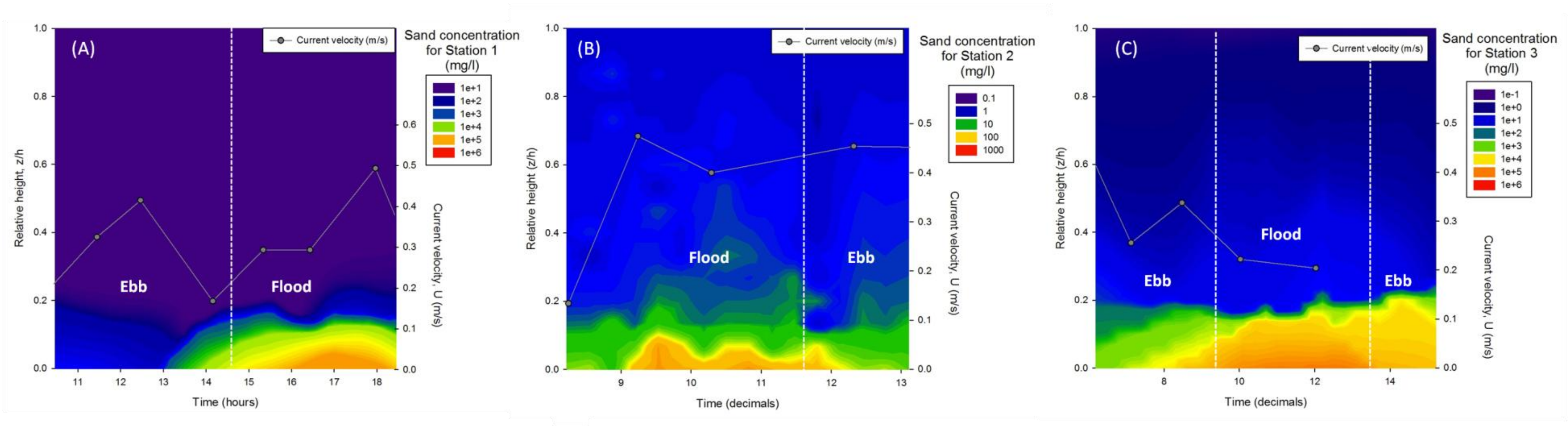

Figure 4.10: The distribution of sand concentration (mg/l) with relative height throughout a complete tidal cycle for Stations (A) 1, (B) 2, and (C) 3 and the corresponding current velocity (m/s). The ebb and flood stages are highlighted in a dotted white line.

4.5 Discussion

The benthic boundary layer in a steady uniform turbulent flow is mainly a function of bed friction, which causes a reduction in flow velocity close to the bed (Nielsen, 1992). The benthic boundary layer can be broken down into four layers: viscous sublayer, transition, turbulent logarithmic, and turbulent outer (Figure 4.11). The viscous sublayer is a thin layer close to the bed where turbulence is usually dissipated at a molecular level. The transition layer is a buffer layer where viscosity and turbulence are equally important. Viscous shear stresses are neglected in the turbulent logarithmic layer where the logarithmic velocity profile was derived. The layer closest to the surface is the turbulent outer layer where the velocities are almost constant. The sand concentration profiles measured in this chapter, illustrate the distribution of layers provisionally.

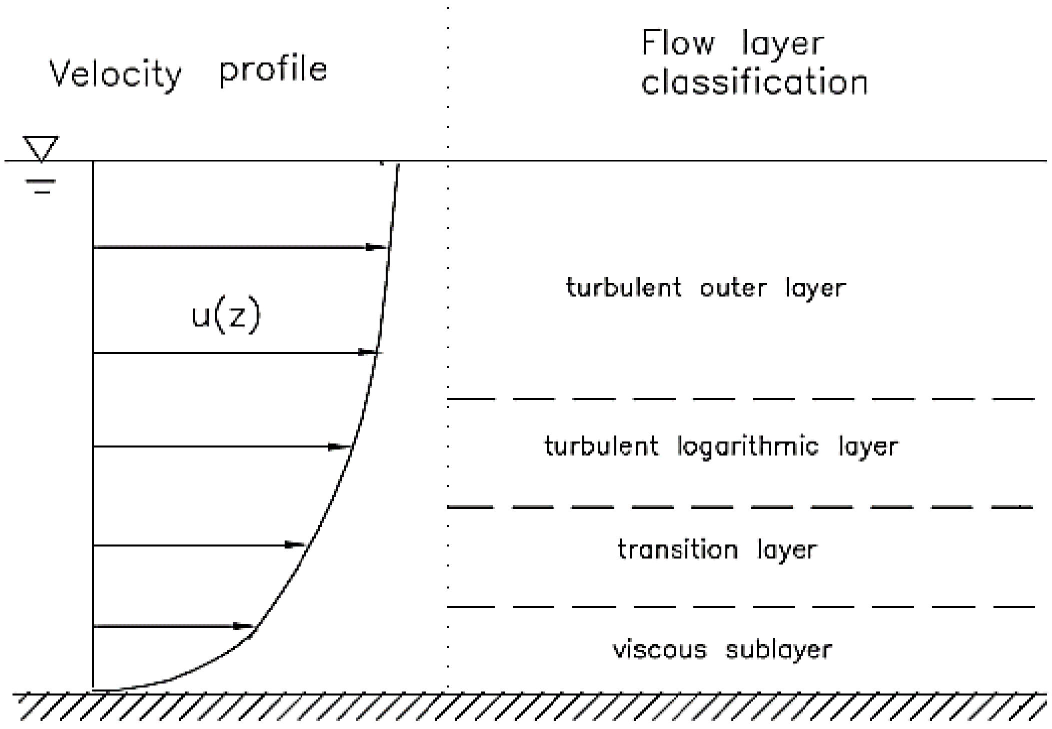

Figure 4.11: Flow velocity profile and the classification of flow layers (modified from Liu, 2001).

4.5.1 Sediment concentration profile layers

4.5.1.1 Roussian layer

The Roussian layer, which takes up most part of the water column, is where the sand concentration is shown as a straight line in a log-log plot (Figure 4.12). The best-fit line follows a power relationship. These results were similar to Bolaños (2012), where the best fit line was best represented by the power law at relative heights greater than 0.2. The Rouse parameter and the ratio w_s/u_* of this layer were calculated from the power function ($y = bx^m$) of the regression curves. The Rouse parameter, R = ($w_s/\beta k u_*$), where $\beta = 1$ and $k = 0.41$ was calculated as follows:

$$log_{10}\frac{z}{h} = m\, log_{10}\, C + b \tag{4.9}$$

then,

$$C = \left(\frac{z}{h}\right)^{\frac{1}{m}} 10^{-\frac{b}{m}} \tag{4.10}$$

where, C is the sand concentration and R = -1/*m* and w_s/u_* can then be calculated from the slope as follows:

$$\frac{1}{m} = \frac{w_s}{\beta k u_*} \tag{4.11}$$

Values for both the SIS and sand trap data from Chapter 3 are summarized in Table 4.4.

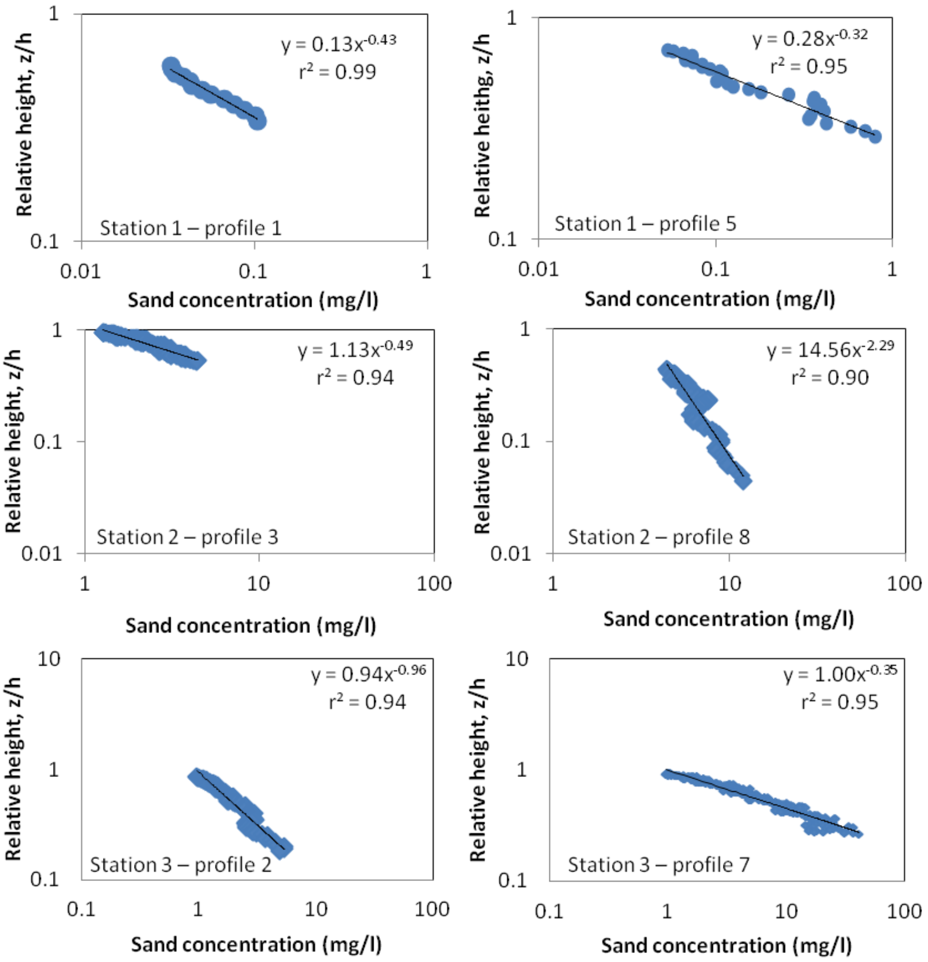

Figure 4.12: Sand concentration of the Roussian layer with relative height for profiles 1 and 5 at Station 1, profiles 3 and 8 of Station 2, and profiles 2 and 7 of Station 3. The best fit equation and correlation are shown in the upper right corner of each plot.

Table 4.4: The Rouse parameter, R, and the ratio w_s/u_* of each profile from the SIS with its corresponding profile from the sand trap for Stations 1, 2, and 3.

Sand trap data		**SIS data**	
Station 1			
$1/m = R$	w_s/u_*	$1/m = R$	w_s/u_*
0.53	0.22	0.43	0.18
0.44	0.18	0.45	0.18
0.45	0.18	0.30	0.12
0.48	0.20	0.52	0.21
0.26	0.11	0.32	0.13
0.33	0.14	0.43	0.18
0.46	0.19	0.20	0.08
0.51	0.21	0.27	0.11
Station 2			
0.66	0.27	1.74	0.71
0.69	0.28	1.96	0.80
0.69	0.28	0.49	0.20
1.18	0.48	0.84	0.34
1.18	0.48	1.05	0.43
0.54	0.22	2.29	0.94
Station 3			
0.47	0.19	0.47	0.19
0.38	0.16	0.96	0.39
0.47	0.19	0.57	0.23
0.47	0.19	1.14	0.47
0.53	0.22	1.16	0.48
0.25	0.10	0.35	0.14

Similar to the sand trap data, the Rouse parameter calculated from the SIS data is small for small w_s/u_* and vice versa. The average w_s/u_* values for stations 1, 2, and 3 are 0.15, 0.5, and 0.23 respectively. The average value of the Rouse parameter is 0.37 for Station 1, 1.24 for Station 2, and 0.7 for Station 3. The values from stations 2 and 3 are slightly higher than the sand trap Rouse values, but they all lie within the 95% confidence intervals of the SIS data (Figure 4.13). The same applies for the ratio w_s/u_* since it was derived from the Rouse parameter.

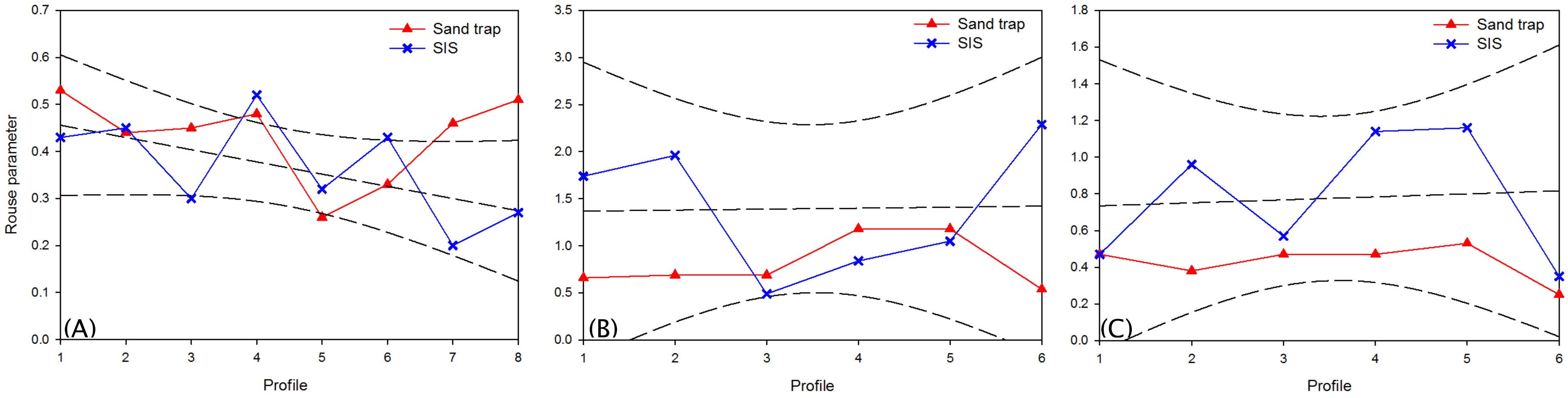

Figure 4.13: The Rouse parameter of the sand traps (red) and SIS (blue) with the best fit and 95% intervals of the SIS data in the dashed black lines for Station 1 (A), Station 2 (B), and Station (3).

4.5.1.2 Buffer layer

The buffer layer is a transitional layer where the sand concentration profile transforms from Roussian to inner (*i.e.* it neither conforms to the Rouse profile nor to an exponential fit). In some profiles, the sand concentration in the buffer layer is constant in the vertical (Figure 4.14). The thickness or indeed presence of the buffer layer is unpredictable as there is no apparent trend with tidal stage, water depth, Reynolds number, or grain size. The buffer layer could be associated with the turbulent buffer layer in a benthic boundary layer as it serves as a transition between the logarithmic layer and a near-bed (inner layer).

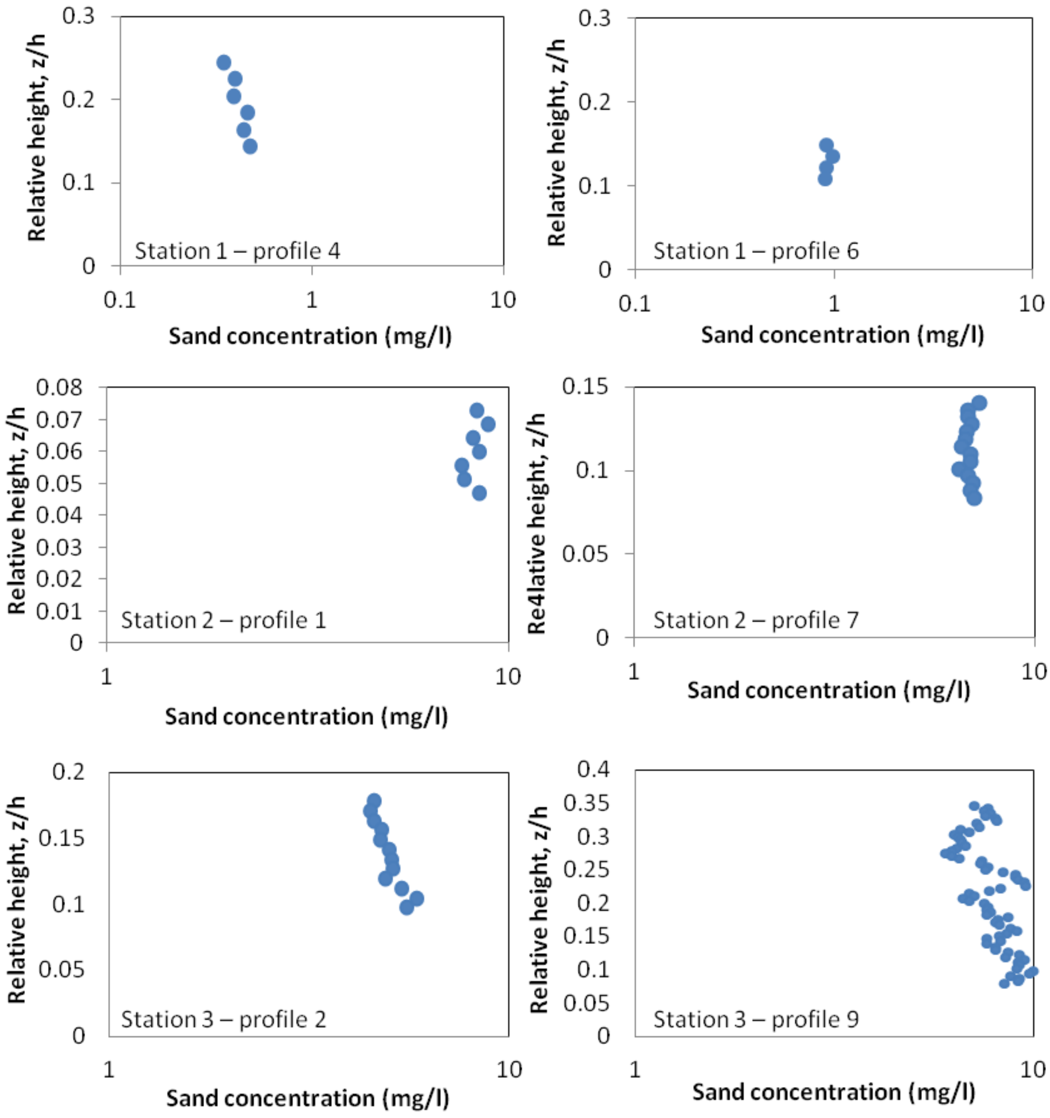

Figure 4.14: Sand concentration of the buffer layer with relative height for profiles 4 and 6 of Station 1, profiles 1 and 7 of Station 2, and profiles 2 and 9 of Station 3 showing the variability of the concentration with relative height.

4.5.1.3 Inner layer

The inner layer forms the lowest part of the water column where the sand concentration is at its highest. The best fit line of the concentration gradient (dc/dz) follows an exponential relationship (Figure 4.15). This was also evident in Bolaños et al., (2012) where the best fit was approximated by the exponential law in the bottom 0.2 of the water column.

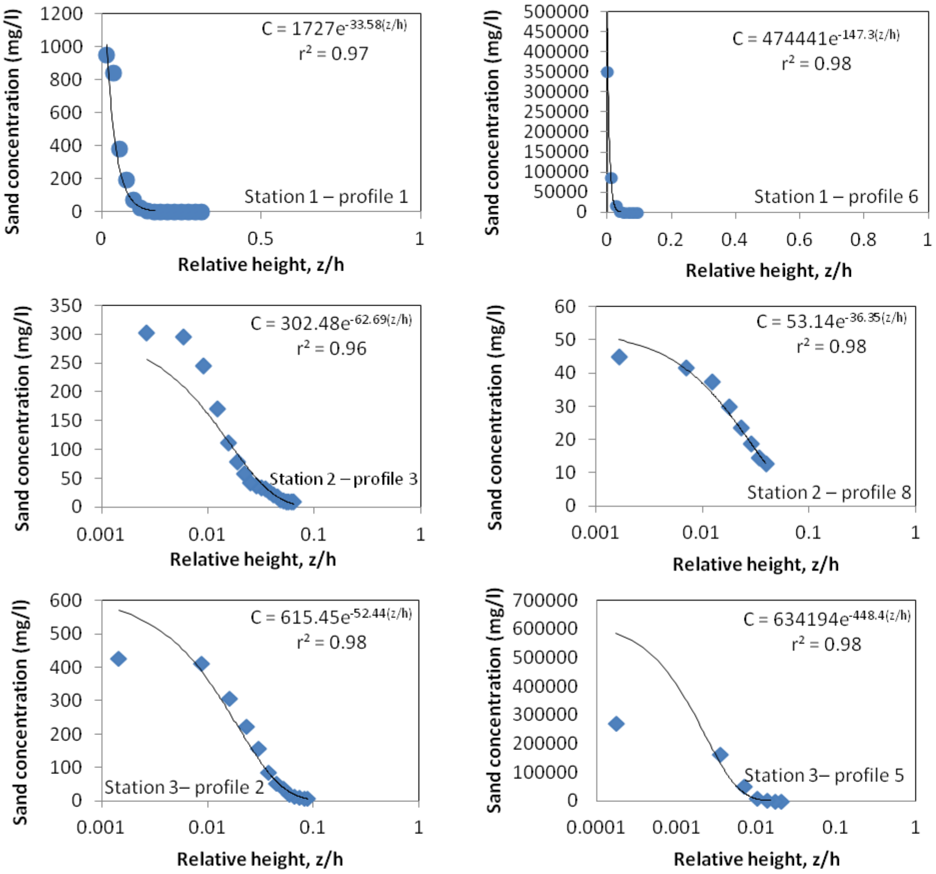

Figure 4.15: Sand concentration of the inner layer with relative height for profiles 1 and 6 of Station 1, profiles 3 and 8 of Station 2, and profiles 2 and 5 of Station 3. The best-fit equation and correlation are shown in the upper right corner of each plot.

Sand in suspension can cause density stratification in the water column resulting in changes in flow velocity profile from a logarithmic form (Soulsby et al., 1983). The density flux decreases with height, therefore part of a profile may be stably stratified while another may be near-neutral. In order to determine whether sand in suspension causes significant stratification in the water column, friction velocity, u_*, is plotted against median grain diameter, D_{50}, following Soulsby et al. (1983) (Figure 4.16). Most of the values fall under the curve where the entire profile is unstratified, which shows that density of sand in suspension does not influence the stratification of the profile. For the profiles where there is density stratification, it only affects the lower part of the profile, which is interpreted as part of the inner layer. The majority of data fall in the bedload transport region which suggests that the majority of sand transport is close to the bed.

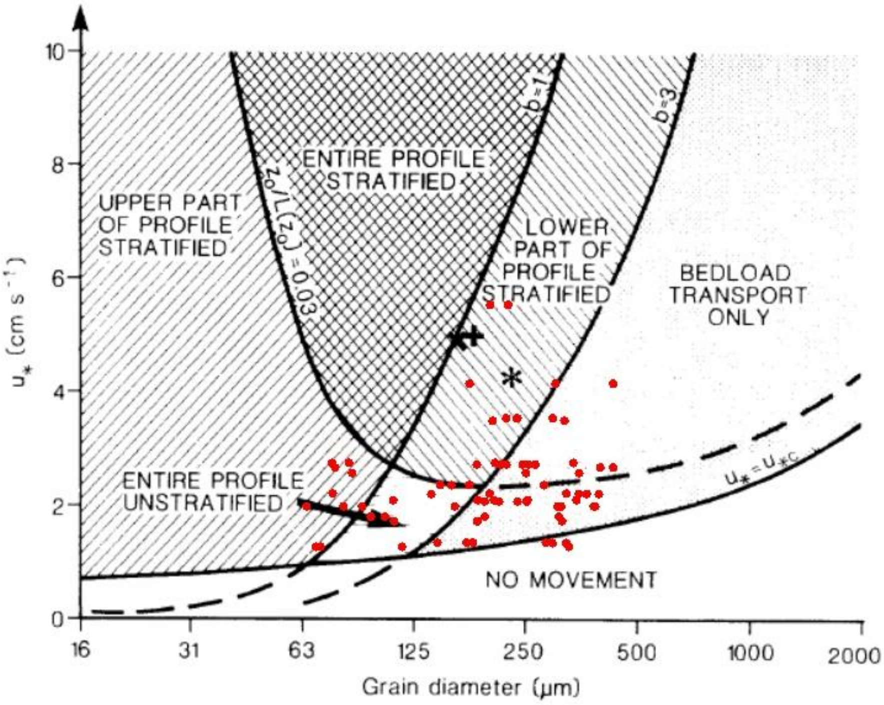

Figure 4.16: The gravitational stability of the water column when sand is in suspension as a function of friction velocity, u_*, and median grain diameter, D_{50} (from Soulsby et al., 1983)

4.5.2 Concentration layer thickness

The Roussian layer took up most of the water column, and for all of the profiles of all three Stations, it was the thickest layer, with average values of 0.5, 0.6, and 0.62 m for Stations 1, 2, and 3. The buffer layer thickness varied as the average was as low as 0.06 m for Station 1 and 0.15 and 0.14 m for Stations 2 and 3. From Figure 4.17, it can be seen that the buffer layer serves as a continuation for the Roussian layer. The inner layer is the thinnest layer with an average thickness of 0.15 m for Station 1, 0.07 m for Station 2, and 0.05 m for Station 3.

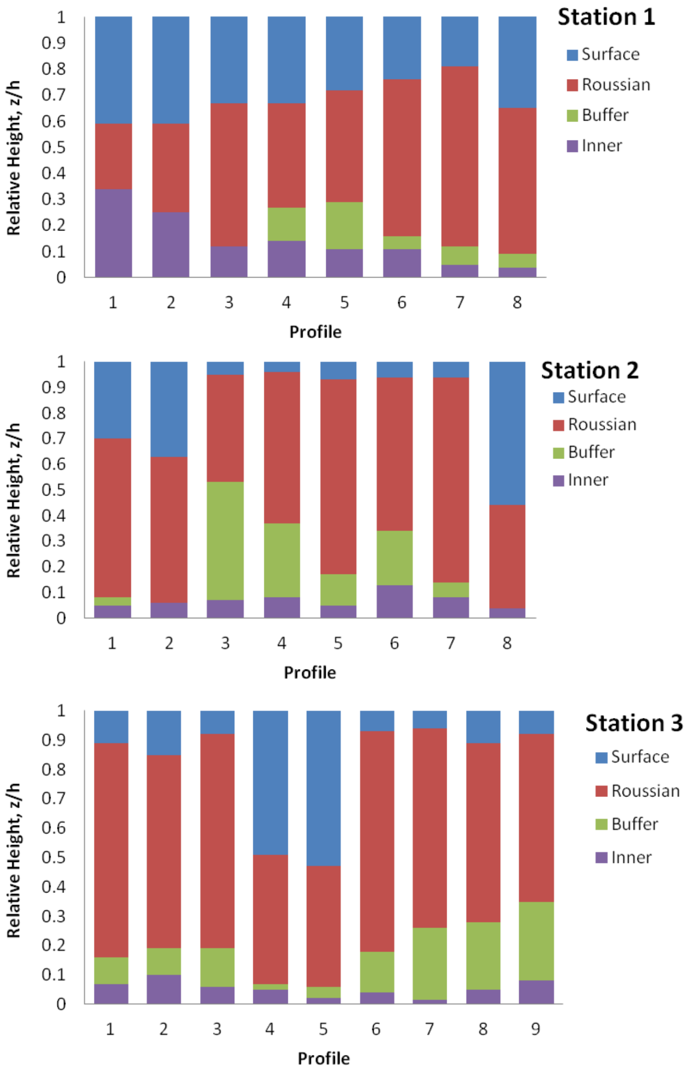

Figure 4.17: The thickness of the surface Roussian, buffer, and inner layers of each profile for Stations 1, 2, and 3.

While the surface and middle traps largely sample within the Roussian and buffer layers, the inner layer is sampled by both the epi-benthic and benthic traps. The thickness of each layer is governed by the distribution of grain size in the vertical as each layer is limited by a specific grain size. This means the coarser end decreases with height above the bed. This can be seen in the grain size sorting from the settling column of the sand samples from each trap (Figure 4.18). The grain size distributions in Figure

4.18 show a decrease from 0.256 mm (1.967 phi) at the bottom to 0.211 mm (2.245 phi) at the surface for profile 7 of Station 2. Thus, sand with a D_{50} of 0.256 mm can only reach the height of the benthic trap, similarly, sand with a D_{50} of 0.248 mm cannot go higher than the epi-benthic trap height. In total 4.5% of the coarse end is lost throughout the water column, from seabed to surface (Table 4.5).

The thickness of the layers was also correlated to sediment grain size in Long and Montreuil (2011), were density profiles with height were examined using a computed axial tomography (CT-scan). In their study, densimetric profiles (pertaining to sediment concentration) where computed over sand ripples as they migrated along a flume bed and showed a similar structure with 4 layers, with a relatively stable suspended transport thickness below which an upper bedload transport is present, in which shear stress decreases vertically in inverse proportion to the concentration. Two further thinner layers, namely the middle and lower bedload transport zones, are also present, where the fluid exerts weak influence due to viscous dissipation.

Table 4.5: The grain size distribution in the vertical of profile 7 of Station 2, showing the D50 in (φ) and (mm) and the percentage lost (%) at each layer.

Sample	**D_{50} (φ)**	**D_{50} (mm)**	**Incremental loss (%)**
Surface	2.245	0.211	1.4
Middle	2.15	0.225	2.3
Epi-benthic	2.014	0.248	0.8
Benthic	1.967	0.256	-

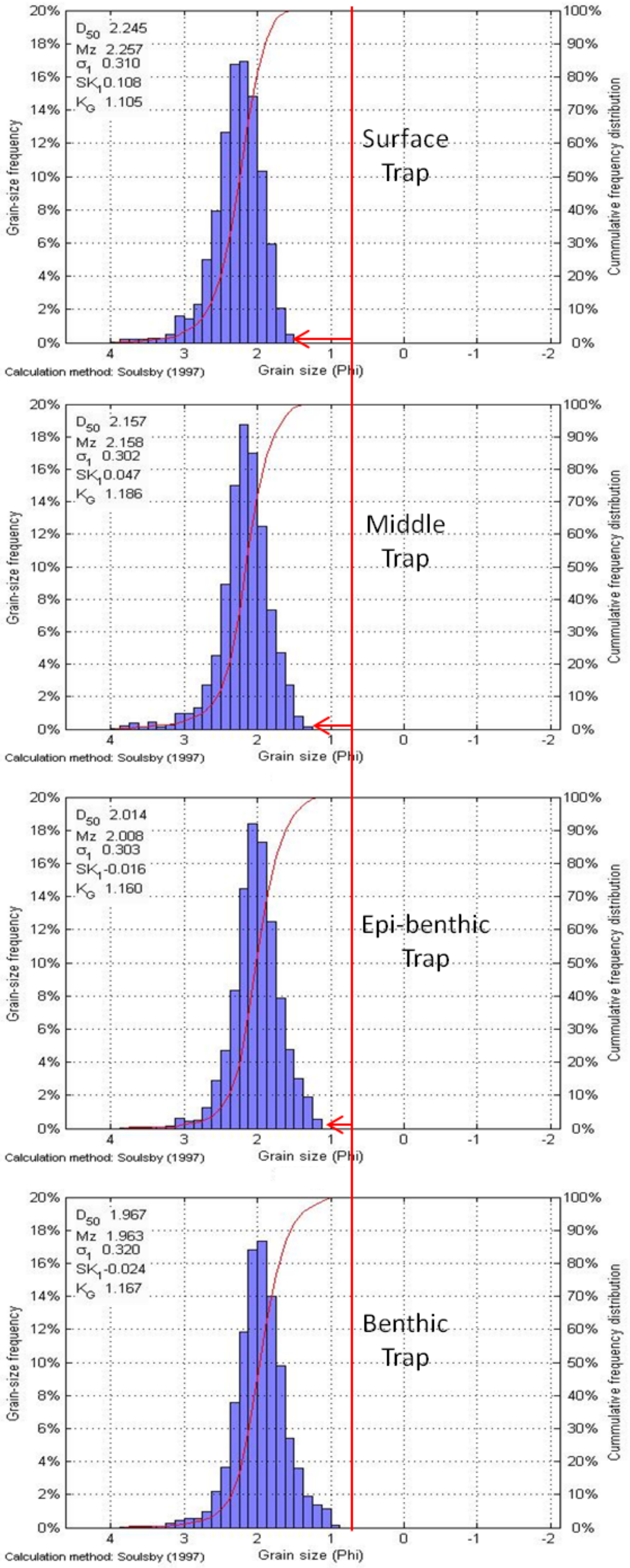

Figure 4.18: Grain size distribution of the surface, middle, epi-benthic, and benthic sand traps of profile 7 of Station 2. The red line indicates the maximum coarse end of the grain size from the benthic trap and the lengths of the red arrows show the incremental loss of the coarse end with height above the bed.

4.5.3 Sediment Flux

The suspended sediment flux, defined as the product of the time-averaged concentration profile and the corresponding mean current velocity for each layer has been calculated and plotted in Figure 4.19. Even though the inner layer was very thin compared to the Roussian layer, most of the sediment transport was taking place near the bed. As the fluid cannot lift the coarser near-bed material higher into the water column, changes at the bed dominate the dynamics of sediment transport, thus making the inner layer the most significant layer pertaining to the evolution of this estuary. An important factor here is the buoyancy force created by the density gradient, which makes it difficult to lift denser fluid and sediment upwards into a less dense fluid (Wright and Parker, 2004). The same applies to the downward flux of lighter fluid and sediment into denser fluid. For this reason, the majority of the sediment flux is observed within the inner layer.

The highest sediment flux occurs during the flood tide (Figure 4.20), where mean velocities exceed the threshold of motion as the tidal wave accelerates up the estuary and the lowest sand transport is observed around low velocities, which occur around peak ebb and peak flood. This was observed in Monge-Ganuzas et al., (2014) as the sand is transported to the ebb tidal delta and re-circulated through tidal currents inside the estuary.

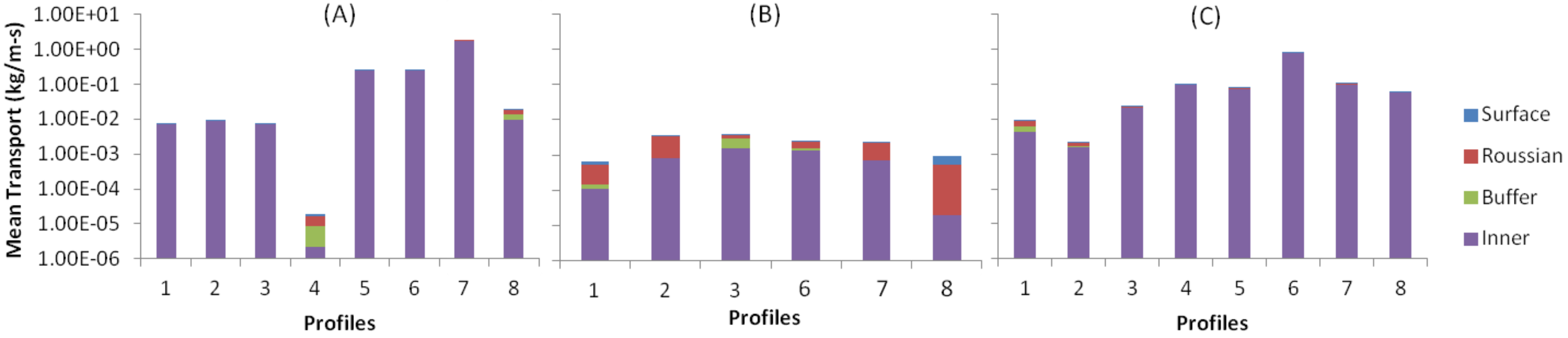

Figure 4.19: Sediment flux of the surface, Roussian, buffer, and inner layers of each profile for Station 1 (A) Station 2 (B) and Station 3 (C).

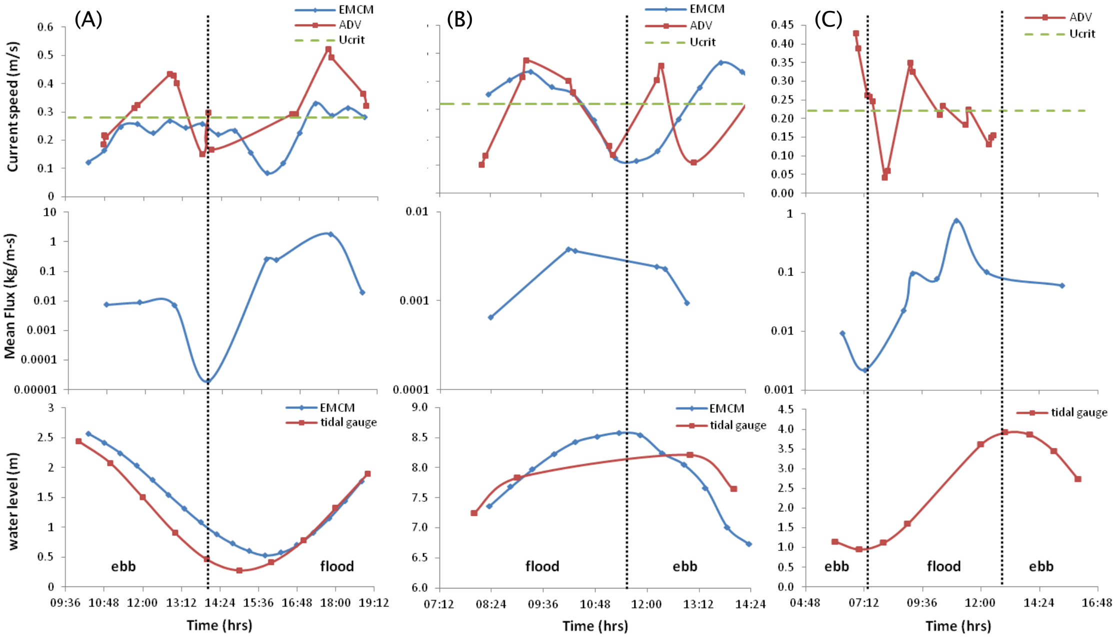

Figure 4.20: The current speed (measured from the EMCM (blue line) and the ADV (red line)), mean sediment flux, and water levels (measured from EMCM (blue line) and tidal gauge (red line)) with time for Station 1 (A), Station 2 (B), and Station 3 (C). The dotted black line indicates the change in tidal stage (ebb and flood). The green dashed line in the current speed figure indicates the critical velocity for initiation of motion.

4.5.4 Generation of a new formula: what is the best prediction of Cz?

The inner layer is the most important layer in the concentration profile, since the majority of sand transport takes place within it. The Rouse profile cannot be used in this layer, as the best fit relationship between sand concentration and relative height follows an exponential rather than power form. On this basis, a new empirical formula has been developed to predict sand concentration in the lower 0.1 m of the water column.

In order to rule out that the sand concentration in the inner layer is part of the bedload, the saltation height (H_s) has been calculated using Van Rijn’s (1993) equation:

$$H_s = 0.3 D_*^{0.7} T^{0.5} D_{50} \qquad (4.12)$$

where T is the transport stage and is calculated using Wiberg and Smith (1985) as follows:

$$T = \frac{\tau_b}{\tau_{cr}} \tag{4.13}$$

The average saltation height for Station 1 is 0.25 mm, 0.22 mm for Station 2, and 0.28 mm for Station 3, which is lower than the inner layer height by three orders of magnitude. The inner layer clearly contributes part of the suspended load. This also appears to conform to Engulend and Fredsϕe (1976) assumption that the bedload layer thickness (which encompasses rolling, sliding and saltation) approximates twice the median grain diameter.

The sediment concentration distribution with height above the bed in the inner layer is approximated by an exponential relationship as follows:

$$C_{(\frac{z}{h})} = ae^{-b(\frac{z}{h})} \tag{4.14}$$

where, $C_{(z/h)}$ is the concentration at a specific relative height *(z/h)*. The slope, *b*, of the best fit curve to the concentration profile in the inner layer is mainly dependent on the stage of the tide and the integral concentration of the inner layer (Figure 4.21). Insignificant correlations have shown it not to be related to the flow velocity, Reynolds number, or bed shear stress. As a consequence, no predictive formula was derived based on the hydrodynamic state. Therefore, at least one measure of concentration –which is grain-size-dependent– (preferably near the bed) is necessary to derive concentration profiles.

As the slope, *b*, becomes steeper, the concentration gradient increases. The slope, *b*, is related to sand concentration by $C = 0.0004b^{3.33}$ (this equation represents the dashed red line in Figure 4.21). A similar relationship is observed when the concentrations are inferred from sand trap measurements rather than SIS backscatter. The constant, *a*, in Equation 4.14 is the near-bed concentration, whose limit is (*z/h* = 0), which is the concentration from the benthic sand trap. Since the constant, *a*, the slope, *b*, and relative height, *z/h*, are known, the concentration at *z/h* can be calculated using Equation 4.14. The concentration at this upper limit of the inner layer (at *z/h* = 0.1), $C_{z/h=0.1}$, may then be used as the reference concentration, C_a, of the Rouse layer. Once this value is known, the concentration throughout the Roussian layer can be predicted using Equation 4.3.

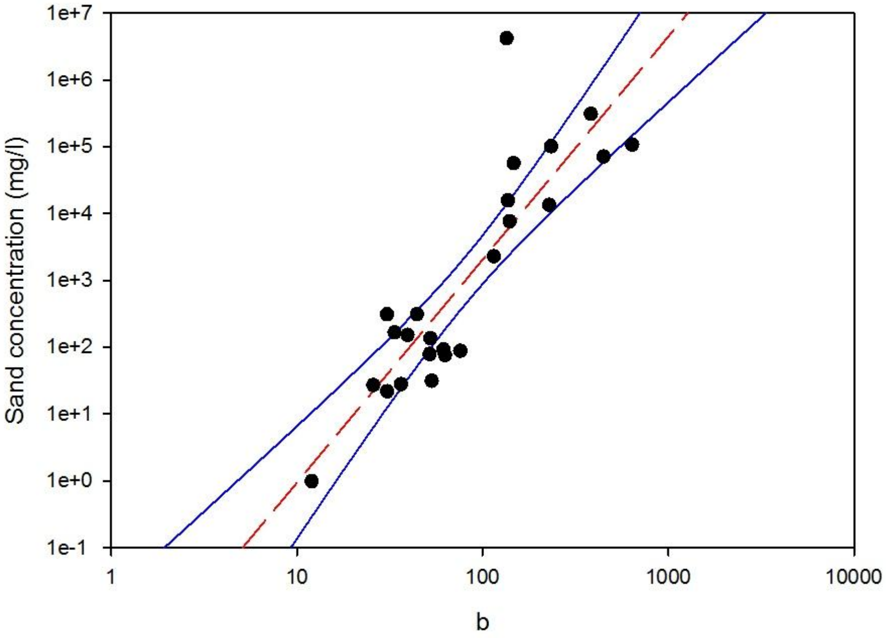

Figure 4.21: The slope (b) from the predicted exponential concentration (Equation 4.14) formula against sand concentration calculated from the SIS with the best fit line (n = 24, P = 0.02, r^2 = 0.76) and 95% confidence intervals.

In order to check the new equation (Equation 4.14), sand concentration at a relative height, z/h of 0.1 has been calculated for different profiles and compared to the concentration of the same height using the Rouse equation. Concentrations from the benthic traps were used to represent the near bed concentrations (Figure 4.22). Most of the concentrations calculated using the new Equation 4.14 are in the same range to those from the Rouse equation. Some concentrations from the Rouse equation are slightly higher than the new equation. This could be a result from the Rouse parameter as it is based on all four traps throughout the water column, while the new equation uses just the benthic trap.

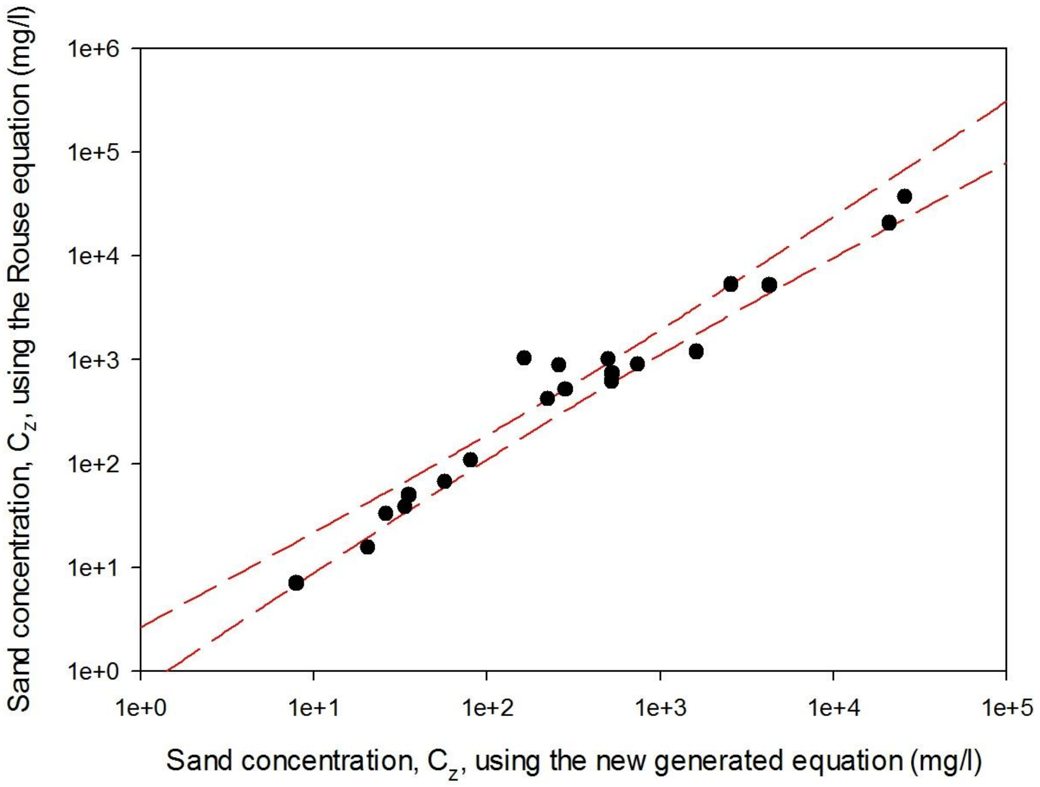

Figure 4.22: The sand concentration, C_z, calculated using the new generated Equation 4.14 versus sand concentration, C_z, calculated using the Rouse equation. The red dashed lines indicate the 95% confidence intervals.

4.6 Conclusions

There was considerable transport of sand both as bedload and in suspension at all stations mainly due to the strength of the tidal currents. Sand in suspension occupied almost the entire water column at peak flows (mid flood and mid ebb). The SIS data of concentration compares well to the sand trap data. Sand concentration was largely greater near the bed. One of the objectives of this chapter is to define the vertical distribution of sand in suspension. The concentration profile is more complex than simply Roussian as three layers have been recognized; a Roussian layer, a buffer layer, and an inner layer. The thickness of each layer is governed by the distribution of grain size in the vertical. The Rouse profile was present but was only applicable to the region that falls between the surface and the inner layers, and occupies most of the water column. A near-bed layer (inner) is characterized by an exponential increase in concentration to the bed and has a near constant relative thickness of 10% of the total water depth. One of the key findings is that the majority of the mass flux of sand at each station took place in the inner layer and was largely restricted to the lowest 10% of the water column, where the Rouse equation does not apply. Therefore, sand transport in the inner layer cannot be neglected, as it is where the majority of movement takes place. Neglecting the sand transport in this layer may lead to underestimating values. As well, using the Rouse equation to calculate the sediment transport in this case will result in discrepancies, which will have a negative effect on sediment transport prediction.

A new, simplified equation (Equation 4.14) to predict sand concentration in the inner layer is generated, which is appropriate to the data collected herein. The major input in this equation is the grain size. Another objective of this chapter is to use this new equation to predict sand concentration in the vertical, C_z. Unfortunately, Equation 4.14 can only be used to predict C_z in this case and cannot be used universally. On the basis of the available data, it has been found that the equation could not be related to the hydrodynamic state. Therefore, one grain size measurement from a benthic trap is required to predict sand concentration in the vertical.

Chapter 5: The distribution of friction velocity in the vertical

5.1 Introduction

Understanding the turbulent structure of the benthic boundary layer (the region adjacent to the seabed where the flow is affected by drag force at the bed), is fundamental to understand and predict the response of bed sediments to flow (Bowden, 1978; Heathershaw, 1979). The flow near a benthic boundary; the friction at this interface; the exchange of sediment between the water and seabed; and the turbulent response are all of great practical interest to understanding sediment transport in suspension. The flow characteristics of the boundary layer are well defined (Pope, 1991). As currents flow over the bed, the frictional drag is manifest by a reduction in momentum, causing the velocity to decrease. A velocity gradient is thus formed in the boundary layer to balance the drag force at the bed. There are different turbulent responses to the frictional drag influencing the velocity profile of the flow that may feed back into the stability of the bed (Bowden, 1978). Turbulent fluctuations cause a net transfer of momentum from the upper to lower fluid regions. This net flux of momentum is known as the stress. The bed shear stress under turbulent flows is a manifestation of the turbulent drag force (per unit area) and is defined, following the Reynolds decomposition, as:

$$\tau_b = -\rho\overline{u'w'} \tag{5.1}$$

where, ρ is the fluid density, u' and w' are the instantaneous velocity fluctuations in the horizontal and vertical directions. The bed shear stress is an important physical parameter in many geophysical and environmental engineering applications and its determination is one of the basic problems of boundary layer flow as the accuracy of sediment transport is strongly affected by its estimates (Bagherimiyab and Lemmin, 2013).

One of the most common boundary layer types is in neutral, non-rotating, steady flow (Bowden, 1978). In the simplest form, this boundary layer is created when a fluid of constant density flows over a flat surface. Over all, the shear stress is maximum at the bed and decreases in a linear fashion to zero at the top of the boundary layer (Figure 5.1). Viscous stresses dominate in the lowest part of the layer, where it represents a thin (quasi-) laminar flow layer where turbulence rarely exists. The layer above is a transition layer, where turbulence and viscosity are equally important. The turbulent logarithmic layer is where viscosity is neglected. The shear stress in this log layer is assumed to be nearly constant and equal to the bed shear stress. The logarithmic layer is a transitional layer between the inner layer (viscous sublayer and transitional (buffer) layer), which is dominated by viscous forces, and the outer layer, which is influenced by the total thickness of the boundary layer (Tennekes and Lumley, 1972). The final layer, outer layer, is where the velocities are almost constant and the shear stress decreases to zero.

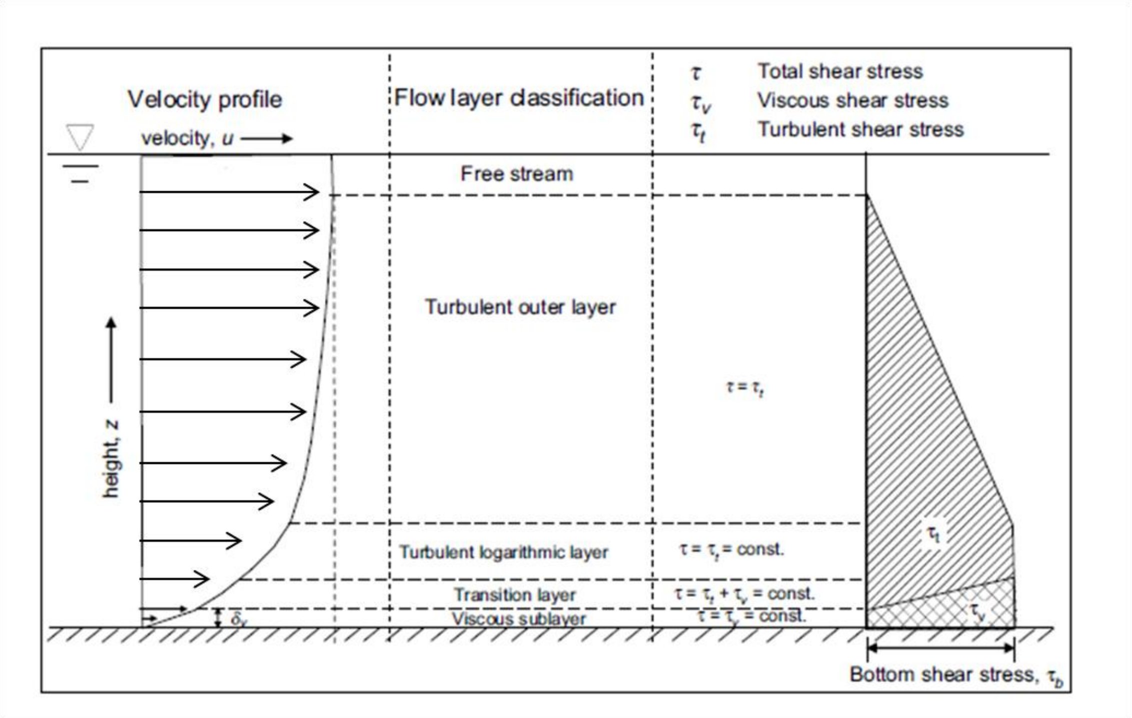

Figure 5.1: Velocity and shear stress distribution with height above the bed and the flow layer classification (modified from Ali and Lemchert, 2009).

In the constant stress region of a boundary layer advection and diffusion of turbulent energy are negligible and energy production and dissipation are equal (Heathershaw, 1979). This logarithmic layer occupies a portion of the boundary layer where the velocity increases as the logarithmic of the height above the seabed (Bowden, 1978; Soulsby, 1983). Identifying the existence of this layer is important as it is one way of estimating bed shear stress (Lueck and Lu, 1997).

The mean velocity distribution with height above the bed in the logarithmic layer is given by the von Karman-Prandtl equation, also known as the “Law of the Wall”.

$$u_z = \frac{u_*}{k} ln\left(\frac{z}{z_0}\right) \tag{5.2}$$

where, k is von Karman's constant and equals 0.41 and z_0 is the height above the bed where the velocity is zero (Dyer, 1970). The friction velocity, u_*, is related to bed shear stress, τ, and is defined by: $u_* = \sqrt{\frac{\tau_b}{\rho}}$ (Bagherimiyab and Lemmin, 2013). Since the bed shear stress decreases with height, the friction velocity is also assumed to decrease with height in the benthic boundary layer.

The friction velocity is a key parameter in the Rouse equation, as it is a function of the ratio of sediment fall velocity to bed friction velocity. The Rouse theory, which is usually used to describe the distribution of sand in suspension, assumes a constant friction velocity in the vertical. Previously in Chapter 3, the critical Shields parameter of suspension, derived from the field measurements, defines the suspension threshold better when the friction velocity is assumed constant. This could be a verification of the initial assumption. Therefore the distribution of u_* in the vertical is evaluated in this chapter in order to determine whether it is constant or variable with height above the bed.

In this study, friction velocity has been calculated using the inner log layer velocity profile data. The advantage of using the Karman-Prandtl equation is that it only requires the measurement of the mean velocity profile, which has been verified by many researchers who examined the current velocity profile within the bottom 1 to 2 m of the water column in areas of fully turbulent tidal flows. However, it does depend on accurate estimates of z_0 and on the flow being turbulent rough.

Bed shear stress is usually derived from velocity profile measurements as direct measurements of bed stress are rarely possible (Bowden, 1978). Nevertheless, there have been advances in oceanographic instrumentation which greatly expanded the ways bed shear stress can be estimated in an estuarine environment (Kraus et al., 1994). The instrumentation required must simultaneously measure the hydrodynamics and sediment concentration throughout the water column as well as bed morphology, using sufficient spatial and temporal resolution to direct turbulent scales (Bagherimiyab and Lemmin, 2013). Strong, reliable, and affordable acoustic and optical instruments are less intrusive and provide very high sampling frequencies and volumes. An acoustical approach is favoured over other techniques such as optical methods, due to its major advantage of detecting the bed and identifying the bed location (Bolaños et al., 2012). The Benthic Acoustic Stress Sensor (BASS), Acoustic Doppler Current Profiler (ADCP) and Acoustic Doppler Velocimeter (ADV) are some of the acoustic instruments that are currently being applied to estuarine bottom boundary layers. BASS was successfully used to measure currents, shear and Reynold stresses and its measuring system includes three axes velocity sensors, compass, tilt meters, and a data logger (Thwaites and Williams, 1996). An ADCP is capable of simultaneously measuring vertical profiles of current speed and acoustic backscatter of sound attenuation due to suspended particles in the water column (Defendi et al., 2010). The ADV provide measurements of 3D fluid velocity at a single point for both uniform and oscillatory water flow (Murray et al., 2012).

The aim of this chapter is to evaluate the magnitude of friction velocity, u_*, through a fully developed boundary layer under unidirectional flow. This will be achieved by undertaking a laboratory experiment, where u_* is measured at different heights for different bed roughnesses to determine whether it varies or remains constant in the vertical axis.

5.2 Methodology

5.2.1 Laboratory set up

The laboratory experiment was carried out at the National Oceanography Centre within the School of Ocean and Earth Science of the University of Southampton. The facility consists of a 7.5 m recirculating flume with a working length of 5 m, 0.3 m of width, and 0.45 m in depth, purchased from Armfield Ltd., UK (Lambkin, 2004).

The side walls of the open top flume are made of toughened glass while the base is painted metal. At each end (upstream and downstream) of the flume, moulded fibreglass riser tanks are used as stilling chambers for water pumped into or drained out of the flume (Figure 5.2). Freshwater is used in this flume and stored in separate reservoir tanks at room temperature. The discharge of water is controlled by opening a gate valve. In order to simulate unidirectional flow, which was used in this study, the flume is filled with water until a base-hinged weir at the downstream end was overtopped. The height of the weir defines the hydraulic head along the length of the flume. The water then circulates back to the reservoir tanks through a drain at the downstream riser tank. To accelerate the flow, the base-hinged weir is lowered, which also causes the water level to decrease. This may be compensated for by increasing the inflow. The flow reaches equilibrium when the rate of the overtopping is the same as the rate of the water input at the upstream end.

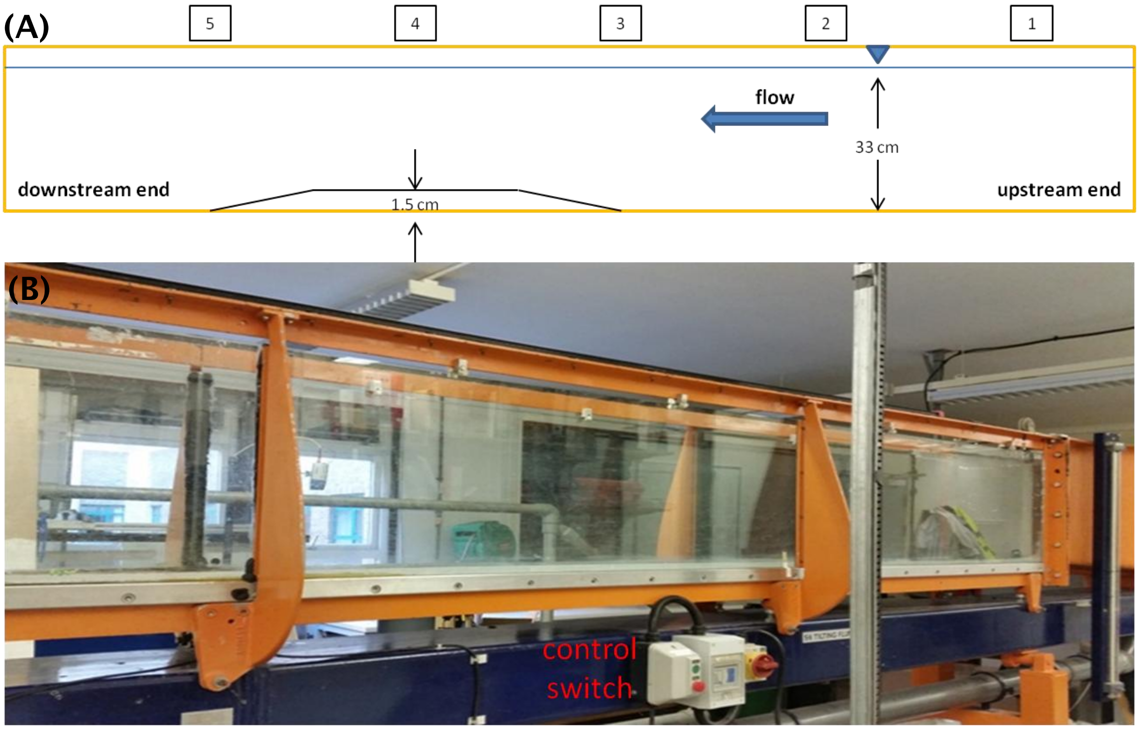

Figure 5.2: (A) A schematic diagram of the flume showing the upstream and downstream end, the direction of the flow, and the position of the Plexiglass base plate. The numbers on the top indicate the different positions of flow mapping (section 5.2.2), not to scale. (B) A picture of the 5 m long recirculating flume from the upstream end.

A steel ruled rod was attached perpendicular to a solid carriage mounted on linear bearings, where a Nortek ADV (measured flow at 25 Hz) was rigidly mounted, that moved along the top of the flume (Figure 5.3). The rod has an adjuster to lower and raise the ADV probe to a specific position above the bed.

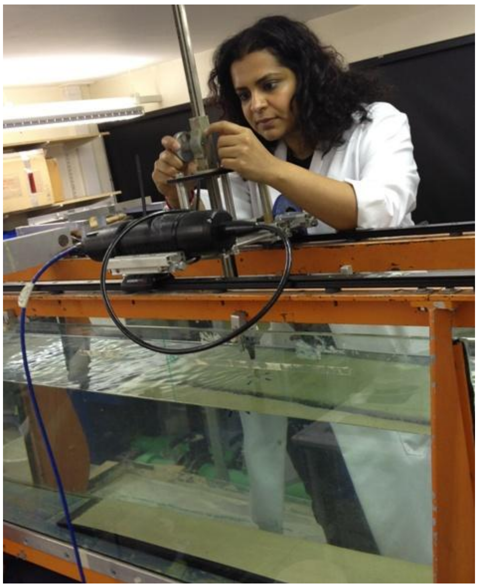

Figure 5.3: The ADV mounted on a linear carriage while its probe is attached to a perpendicular steel ruled rod, which was raised and lowered to the required height.

The flume was filled with water to the maximum possible depth of 0.33 m. The entrance and exit settings of the flume limited the working length of the flow (Lefebvre, 2009). A honeycomb structure was fitted at the entrance to ensure a fully rough flow developed. The first profile was taken at 0.75 m from the leading edge. To reduce the influence of a hydraulic jump at the exit, the last profile was taken 3.65 m from the leading edge. Since the volume of water pumped in the flume cannot be measured, the magnitude of the flow could not be guaranteed. Therefore to reduce any ambiguity, the water level was kept the same at 0.33 m for all runs, and the weir and the gate valve opening was adjusted accordingly.

5.2.2 Flow Mapping

In order to analyze the development of the benthic boundary layer under the unidirectional flow of the flume, first the flow was mapped at different positions (x) from the leading edge until a fully developed boundary layer was detected. Velocity measurements were taken at five different positions along the flume: x = 0.75, 1.50, 2.25, 3.00, and 3.65 m. The boundary layer thickness with distance x down flume was calculated from Liu (2001) as follows:

for turbulent smooth flow
$$\delta_l = 5\frac{U^{-0.5}x^{0.5}}{\upsilon^{-0.5}} \tag{5.3}$$

for turbulent rough flow
$$\delta_t = 0.4\frac{U^{-0.2}x^{0.8}}{\upsilon^{-0.2}} \tag{5.4}$$

where, U is the average flow (m/s) and v is kinematic viscosity (m^2/s).

A total of 3000 measurements were recorded at 25 Hz for each run at 15 different water depths of each profile. The lowest readings were in increments of 2 mm up to 20 mm above the bed, and in increments of 10-20 mm thereafter. The data was subjected to a quality control check, such that any data with a signal correlation lower than 70% were eliminated (Kassem, 2012). Data were then smoothed using a moving average algorithm and the axes were rotated to account for misalignment with the flow (see Appendix B), following the methodology of Thompson et al. (2013). An example plot of the pre-processed instantaneous velocity components U, V, and W (along-flume, across-flume, and in the vertical respectively) is shown in Figure 5.4.

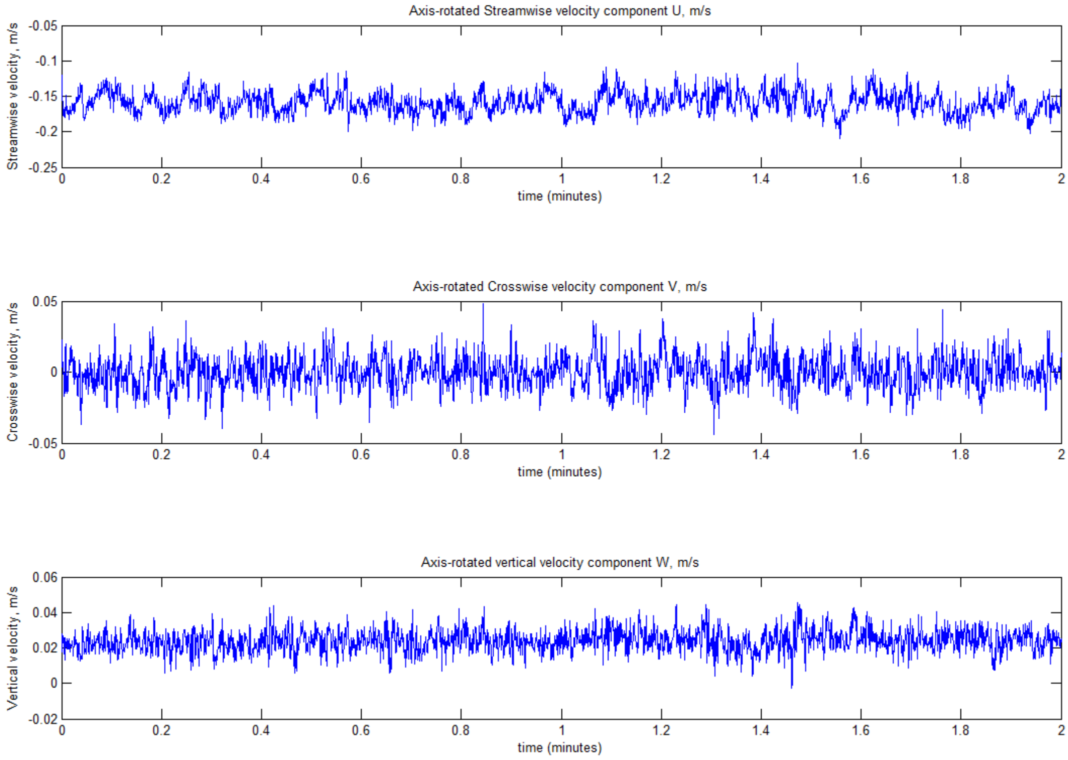

Figure 5.4: The pre-processed instantaneous velocities in the x, y, and z directions for map_4_5.8 run measured at z = 0.8 m and x = 3.0 m.

The magnitude of mean average velocity of the flow in a time series is calculated using:

$$\bar{U} = \sqrt{U^2 + V^2 + W^2} \tag{5.5}$$

The mean velocity for each time series is plotted against height above the bed, z, in Figure 5.5 for profiles 1 to 5. The velocity profile at x = 0.75 m does not follow a logarithmic distribution, as it was too close to the entrance for a boundary layer to develop. The logarithmic velocity distribution was apparent in profiles 2 to 4, but the maximum boundary layer thickness was present in Profile 4. The proximity of Profile 5 to the flow exit may cause disturbance and thus, deviation of the velocity distribution from Law of the Wall.

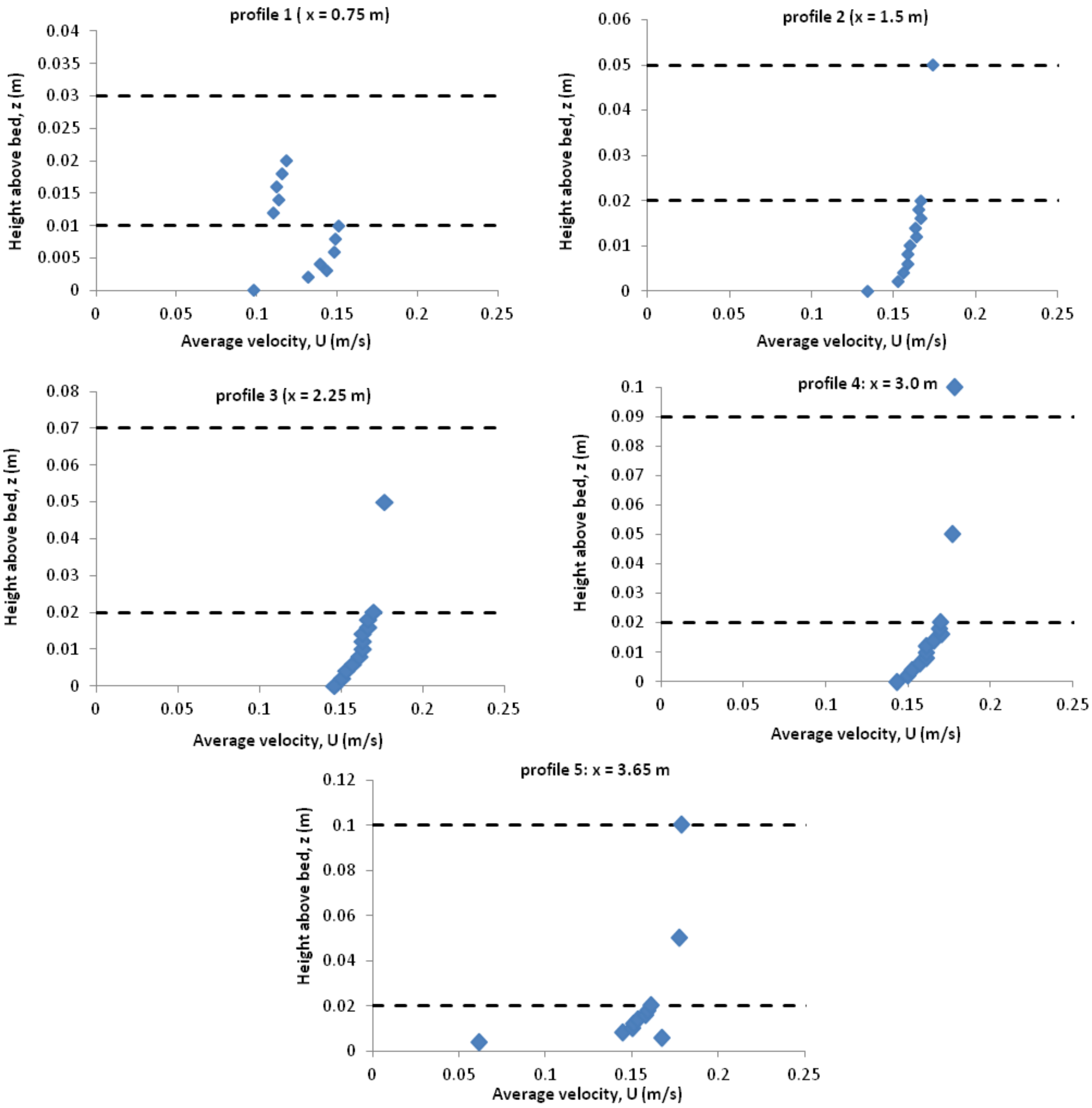

Figure 5.5: The mean velocity (m/s) with height above bed (m) for profiles 1 to 5. The dashed lines represent the estimated boundary layer thickness for both turbulent rough (top) and smooth flows (bottom).

These plots show that the best developed boundary layer, where the velocity profile approaches a parabolic distribution (logarithmic Law of the Wall), is observed in Profile 4, which takes place 3.0 m from the leading edge. Therefore, the ADV was positioned at that location, where the rest of the measurements were carried out.

5.2.3 Bed roughness

Five different bottom roughnesses were used in this experiment: smooth, fine sand, medium sand, coarse sand, and a rippled bed. For the smooth bed, a smooth 1 m long Plexiglass plate with a thickness of 15 mm was used (Figure 5.6A). For the sand samples, three different grain sizes (fine, medium, and coarse) were used. Well-sorted and evenly distributed sand was glued onto lining material and fixed onto the Plexiglass base on the flume floor. Sand with median grain size, D_{50} of 0.125 mm was used for fine sand (Figure 5.6B), D_{50} of 0.25 mm for medium sand (Figure 5.6C), and for coarse sand D_{50} of 0.5 mm (Figure 5.6D). The bottom was otherwise flat and so the roughness was due only to the skin friction related to the diameter of the sand grains. Strips of rippled plastic sheets were taped onto the Plexiglas plate onto the flume floor to create the rippled bed (Figure 5.6E). The ripple height was 0.01 m and the ripple wavelength length was 0.03 m. The 2D rippled sheets were otherwise smooth. The side view and top view of the apparatus using coarse sand as the bed before the flume was filled with water is shown in Figure 5.7.

Figure 5.6: (A) Plexiglas smooth 1 m base (B) fine sand (125 mm) (C) medium sand (0.25 mm) (D) coarse sand (0.5 mm) and (E) rippled plastic sheet.

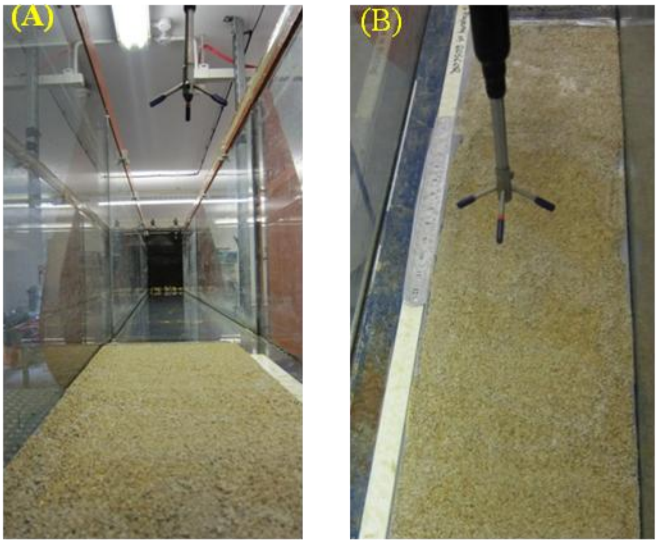

Figure 5.7: The side view (A) and top view (B) of the coarse sand adjusted on the flume bed before the flume is filled with water.

5.3 Results and discussion

The mean average velocity was calculated using Equation 5.2 and plotted against relative height. The average velocity shows a slight increase with height above the bed (Figure 5.8). For the bottom 10% of the water column, the average velocity appeared to be constant (Figure 5.9). This trend was observed for all bed types.

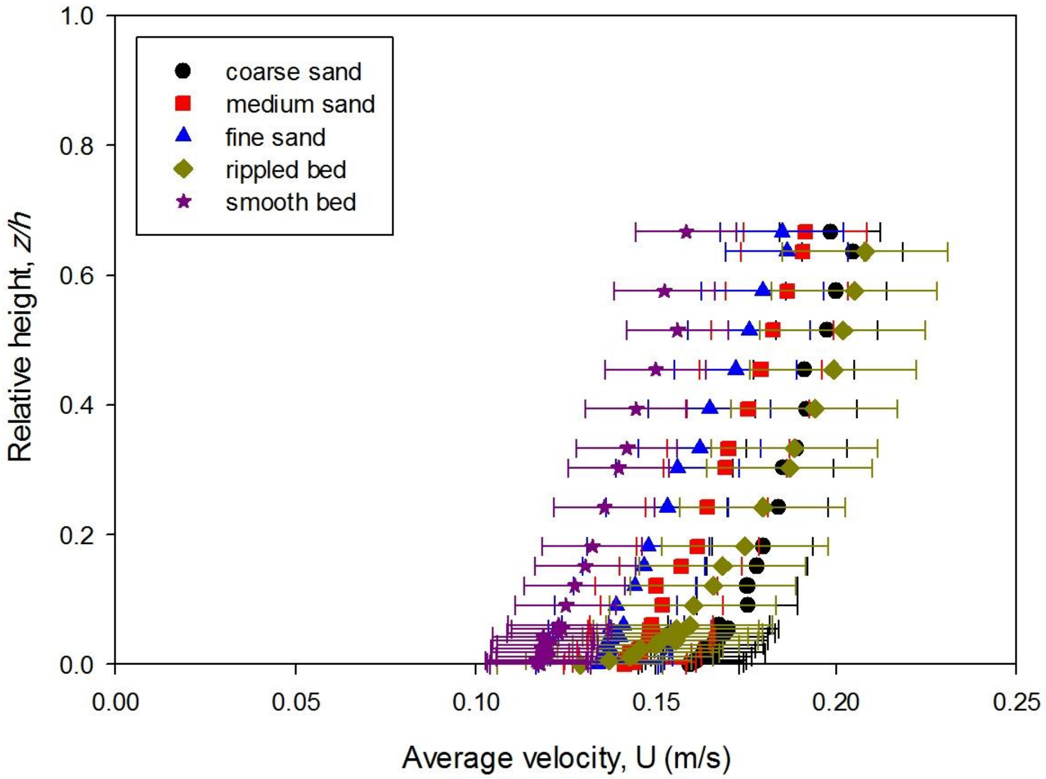

Figure 5.8: Average velocity with relative height (*z/h*) for coarse, medium, fine, rippled, and smooth beds.

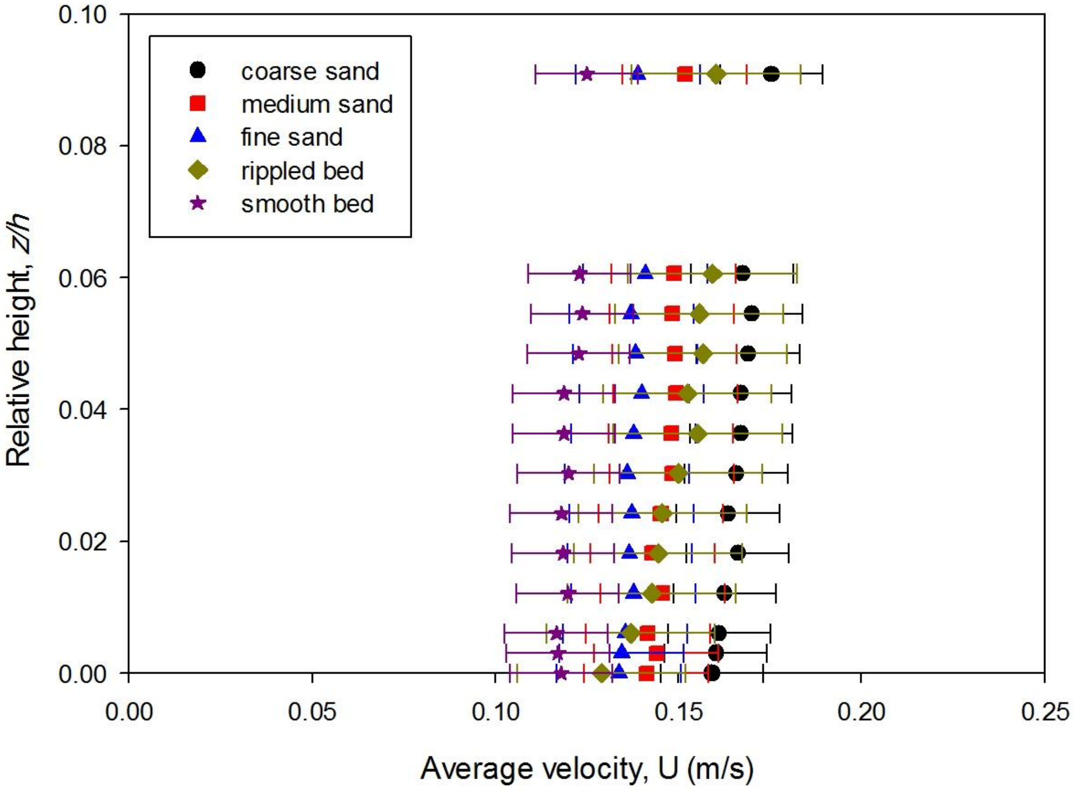

Figure 5.9: Average velocity with relative height (*z/h*) for coarse, medium, fine, rippled, and smooth beds in the lower 10% of the water column.

One of the common and most consistent approaches to estimate bed shear stress from velocity measurements is the Turbulent Kinetic Energy (TKE) method (Kim et al., 2000; Pope et al., 2006). TKE is a measure of the intensity of velocity fluctuations from the mean velocity and is defined as:

$$E = \frac{1}{2}\rho\left(\overline{u'^2} + \overline{v'^2} + \overline{w'^2}\right) \tag{5.6}$$

where, the fluctuations were calculated from the velocity time series. The bed shear stress can be calculated as:

$$\tau_b = 0.19E \tag{5.7}$$

where, the constant 0.19 is accepted for many bottom roughness (Thompson et al., 2003). Friction velocity, u_*, is calculated and plotted against relative height (Figure 5.10).

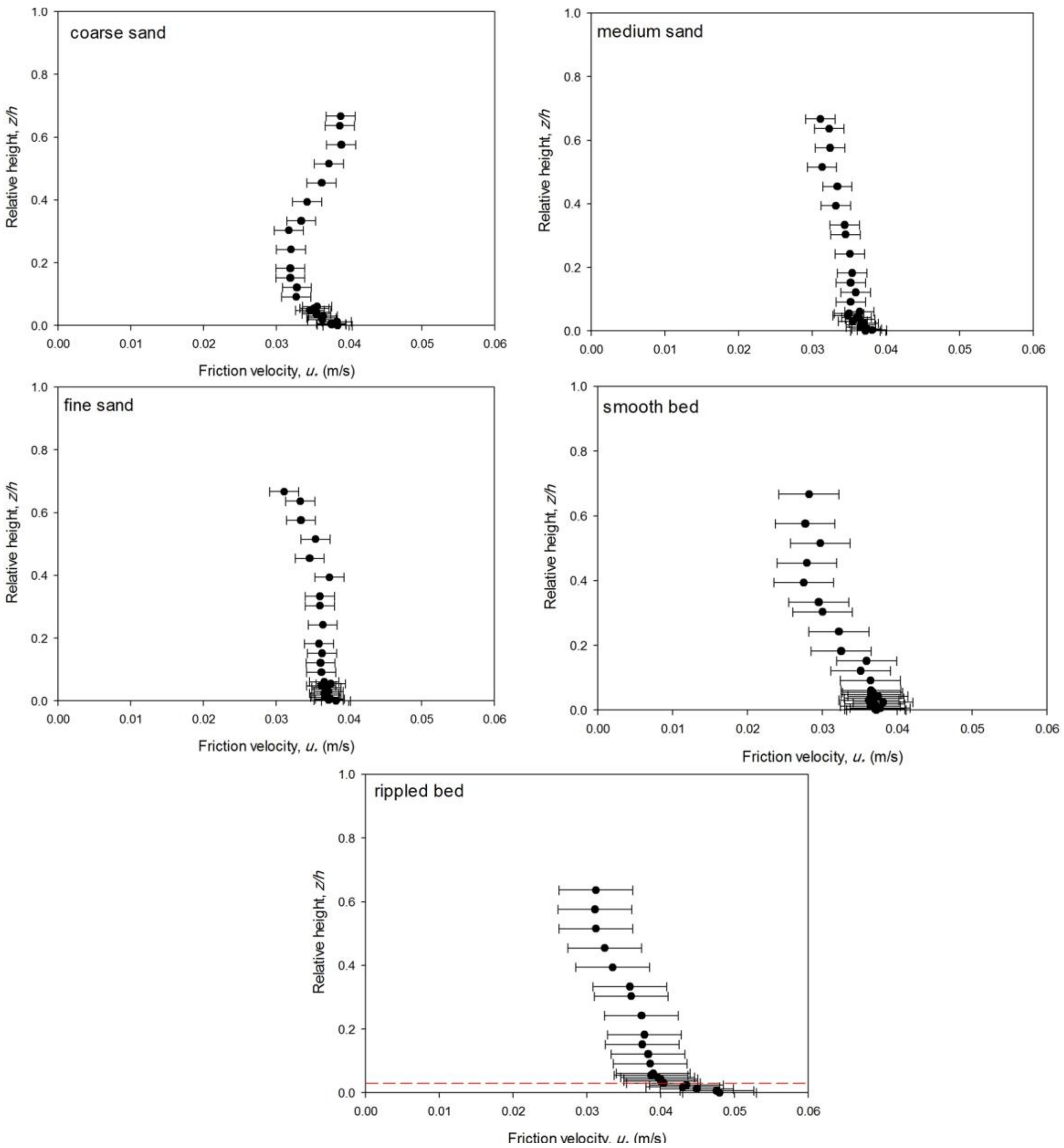

Figure 5.10: Friction velocity, u_*, with relative height (z/h) for coarse, medium, fine, smooth, and rippled beds (the dashed red line indicates the relative height of the ripple's crest).

Friction velocity for the smooth bed decreases slightly with relative height above the bed. The decrease with relative height is less obvious in the fine and medium sand friction velocity profiles. The friction velocity profile for the coarse bed decreased slightly with relative height and increased halfway through the water column. The only profile that showed a significant decrease with relative height above the bed was that of the rippled bed. Figure 5.11 shows the friction velocity profiles with relative height of the lower 10% of the water column.

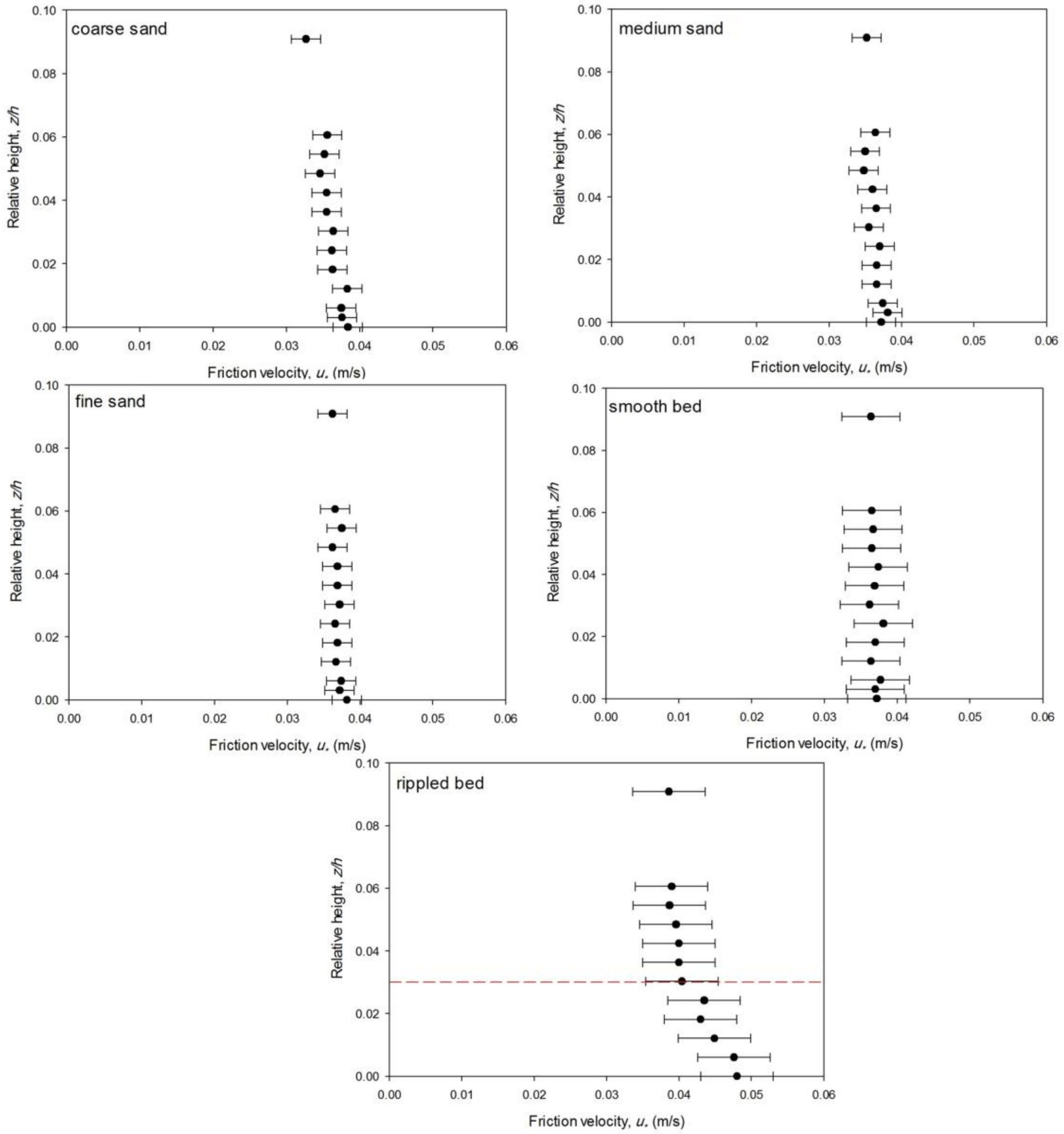

Figure 5.11: Friction velocity, u_*, with relative height (*z/h*) for coarse, medium, fine, smooth, and rippled beds in the lower 10% of the water column (the dashed red line indicates the relative height of the ripple's crest).

The friction velocity in the lower 10% of the water column for the smooth, fine, medium, and coarse profiles is constant. This means that the constant stress layer extends from the bottom up to a relative height of 0.1. The variations of the friction velocity above this level is relatively small ±0.002 m/s for the fine, medium, and coarse profiles and ±0.004 m/s for the smooth profile (Table 5.1). The friction velocity profile for the rippled bed is slightly different. The friction velocity is constant in the vertical above the ripple crest height. Below the crest the friction velocity increases as it reaches the bed. This could be due to the fact that the ADV was positioned at the trough of the ripples when taking the measurements. A similar trend was reported in Ali and

Lemckert (2009). The friction velocity magnitude was almost the same regardless of type of bed at an average value of 0.035 m/s.

Table 5.1: The summary of the average velocity, U (m/s) and friction velocity, u_* (m/s) averaged throughout the water column and the standard deviation for the smooth, fine, medium, coarse, and rippled bed.

Type of bed	Mean velocity		Friciton velocity	
	$\bar{U}$ (m/s)	Standard deviation	u_* (m/s)	Standard deviation
Smooth	0.130	0.014	0.034	0.004
Fine	0.150	0.017	0.036	0.002
Medium	0.159	0.017	0.035	0.002
Coarse	0.177	0.014	0.036	0.002
Rippled	0.168	0.023	0.039	0.005

Friction velocity is assumed to increase linearly with depth in the benthic boundary layer and as bottom shear stress is represented by the friction velocity, u_*, it follows the same trend (Liu, 2001). The Rouse (1937) formulation, on the other hand, takes u_* to be constant in the vertical. Bowden and Ferguson (1980) measured Reynolds stresses simultaneously at different heights above the bed of the Irish Sea and found no significant difference as the variances u^2, v^2 and w^2 were almost constant with height.

A series of eight different measurements from 0.15 to 2 m above the bed were conducted in Dyer (1971). The resulting velocity profiles fell into 4 classes one of which shows that the profile was logarithmic throughout the depth, which is similar to the results of this experiment. Usually, the height of the logarithmic layer is given as about 0.1 of the boundary layer thickness, δ (Soulsby, 1983). If the flow has no vertical density stratification, the logarithmic layer may extend well beyond the surface layer. On the other hand, when density stratification is present, only the lowest part of the surface layer will show a truly logarithmic velocity profile.

A near constant stress with height above the bed was also shown in Green (2012). High frequency three dimensional flow measurements using an ADCP were obtained from Southampton waters. These measurements were combined with those from a self-logging Valeport 802 electromagnetic current meter providing measurements 0.15 m above the bed to identify a complete velocity profile. Three different indirect methods (TKE, Reynolds Stresses, and Law of the Wall) of calculating shear stress in the benthic boundary layer were used. All three methods showed a similar trend, where a near-constant stress with height above the bed was observed. This suggests that the benthic boundary layer is contained within the turbulent logarithmic layer.

5.4 Conclusions

The essence of the majority of coastal management problems is the accurate prediction of the geographical distribution of bed level changes due to sedimentary processes (Soulsby et al., 1983). This can be addressed by sufficient knowledge of the local conditions of the area of interest such as grain size, water depth, current velocity or bed shear stress, and wave climate to be used as input parameters for sediment transport formulas. The most critical of these input parameters is the bed shear stress, therefore understanding its behaviour must be well established.

The TKE method was used to calculate the bed shear stress, as it considers the three components of velocity flow. In conclusion, constant stress is observed within the bottom 10% of the water column in all the velocity profiles. In the upper 90% of the water column stress is varied slightly with a maximum deviation of ±0.005 m/s. In this case, the assumption of a constant friction velocity is only valid in the bottom 10% of the water column. From Chapter 4, it was concluded that the majority of sediment transport takes place in the inner layer, which is also in the bottom 10% of the water column. Therefore, assuming a constant friction velocity is justified, since it is valid in the most important region.

In relation to the critical Shields parameter of suspension, where the suspension threshold is better defined when the friction velocity is assumed constant in the vertical, can be verified for the data points near the bed, from the epi-benthic and benthic traps. For the data points in the upper 90% of the water column (middle and surface traps), the variation in friction velocity values is small (maximum deviation of ±0.005 m/s) and may be neglected when plotted on the Shields diagram.

The friction velocity was measured in the laboratory under a controlled environment. In the lab, different types of bed roughnesses and velocity flows can be tested. This is not possible in the field, as you are limited to the conditions of the surveyed site. The results show that friction velocity increases towards the bed for a rippled bed. Therefore, in the presence of bed forms, the position of the ADV above the bedform height (whether it is positioned at the trough or crest) may have an influence on the results. Knowing the exact position of the ADV in relation to bedform height is difficult to determine in situ. During this experiment, the ADV used measures velocity at a single point. Hence, it was attached to a steel rod where the height can be adjusted (lowered or raised) accordingly. This cannot be easily done in the field. Therefore, the use of a profiling ADV in the field would be at an advantage, as it measures velocity at different heights. When a profiling ADV is used, direct measurements of velocity can be used which eliminates the need to make any further assumptions.

Chapter 6: Summary and Conclusions

The concern over pollutant transport, maintenance of harbours and channels and the prediction of sand transport is important for effective planning and management purposes (Kineke and Sternberg, 1989). This has highlighted the importance of soundly understanding the processes governing suspended sediment transport in coastal environments. Estuarine settings exhibit unique challenges for the use of analytical models for predicting sediment transport due to the complex interactions in such shallow water environments (Adams and Weatherly, 1981). To this date sand transport remains one of the most important limits to predicting estuarine morphodynamics. The accurate prediction of sand transport in suspension is particularly challenging. One of the most common applications used to define sand in suspension is the Rouse theory. This study is an attempt to examine the applicability of the Rouse theory to a tidal inlet in Spain.

The Rouse theory assumes the concentration of a suspension depends on the velocity gradient of the flow (Vanoni, 1984). The well known Rouse equation for the distribution of suspended sand in turbulent flow is based on a number of assumptions. These include:

1) a parabolic eddy viscosity, ε_v,
2) a constant settling rate, w_s,
3) a constant friction velocity, u_*, (hence constant stress layer),
4) the existence of a reference concentration, Ca, and a reference level, a, and
5) a single grain size (no account for particle size distribution in the vertical)

The sand concentration is calculated as:

$$\frac{C}{C_a} = \left(\frac{h-z}{z}\,\frac{a}{h-a}\right)^R$$

where, C is the sand concentration at height above bed z, h is the water depth, C_a is the reference concentration at reference height a, and R is the Rouse parameter ($w_s/\beta k u_*$), where w_s is the grain settling velocity, β is the ratio of eddy viscosity to particle eddy diffusivity, and u_* is the friction velocity. One of the Rouse's equation drawbacks is the requirement to have a value for C_a in order to calculate the concentration C. Various assumptions have been made in the literature when defining the reference concentration, C_a. Some of the empirical reference concentration formulas are related to excess bed shear stress through the Shields threshold parameter (Van Rijn 1984b). The most commonly known reference concentration formulas are from:

Smith and Mclean (1977): $$C_a = 0.004C_0\left(\frac{S}{1+0.004S}\right)$$

Van Rijn (1984b): $$C_a = 0.015\frac{D_{50}}{a}D_*^{-0.3}S^{1.5}$$

where, C_0 is the bed concentration (0.65) and $S = \left(\frac{\tau_0 - \tau_c}{\tau_c}\right)$. Smith and McLean (1977) may result in smaller concentrations because it is defined at a higher level then Van Rijn (1984b). Uncertainties in the assumptions listed above in application of the Rouse theory to sand transport lead to uncertainties in the validity of predicted concentration profiles. Nevertheless, it is still widely used.

This thesis aimed to evaluate the Rouse theory for the distribution of suspended sand throughout the turbulent benthic boundary layer in a tidal inlet to address some of these uncertainties. Tidal inlets are regions of active sand transport that are formed mainly in sandy settings, therefore, they serve as natural laboratories to study the factors governing sand in suspension. The Oka estuary, Spain, was chosen as the study area for its sandy environment, which is an essential characteristic, as well as the aspiration from the Basque community to do more research on the Oka estuary due to its natural Biosphere Reserve status. In the present study, the Rouse profile was evaluated by collecting field data using high resolution equipment as well as laboratory work carried out at the National Oceanography Centre, University of Southampton. The main factors influencing sand transport were used to define a relationship between sand in suspension and sand and flow properties. The perceived outcome is a better understanding of sand transport in tidal inlets and better model predictions.

6.1 The Rouse theory for sand suspension in the Oka estuary

Sand transport in the Oka estuary took place during the field campaign as both bedload and in suspension at all stations occupied. The values of the Rouse parameter confirmed that the sand transport in suspension was taking place throughout the benthic boundary layer. During periods of sand suspension, the grain size was considerably finer near the surface and coarser near the bed reflecting the fact that the settling velocity, w_s, was not constant in the vertical. This was evident at all stations. The analysis of the ratio of the settling velocity of sand in suspension to the bed friction velocity, w_s/u_*, which the Rouse theory assumes constant, is one of the objectives of this study.

The sand transport inside the estuary (Station 1) is dominated inwards. At the inlet (Station 2), the sand concentrations were ten times higher during the ebb tide suggesting seawards transport. The sand transport at the ebb delta (Station 3) as well, dominated towards the sea with even greater concentrations than Station 2. Ebb tidal deltas are strongly related to sediment transport processes in tidal inlets (Liria et al., 2009). Some of the factors that govern the volume of the ebb tidal delta include the tidal prism, offshore bathymetry, wave climate, sediment characteristics, littoral drift, and freshwater runoff. Due to the location of the Oka estuary's mouth (ebb tidal delta) facing north, the waves must be relatively high in order for the famous Mundaka wave to start breaking. This usually occurs in autumn – winter season. The field campaign was carried out during the summer where conditions were calm and no waves were experienced. Hence, seasonal changes must influence the sediment transport trends and different observations will be explored in an autumn or winter campaign.

Another matter that needs to be considered that would disturb the natural estuarine system is the dredging and dumping activities carried out by the shipyard company. These activities carried out between 1973 and 2003 have altered the natural channel distribution and sedimentary dynamics, which required regular dredging every 5 years to maintain the channel. Monge-Ganozas et al., (2013) established that the Oka estuary is unbalanced and is losing its capacity. This means that it may require further dredging in the near future (since the last dredging activity was more than 10 years ago). Therefore, results from this study along with additional field campaigns are good contributions to the future planning of the maintenance and preservation of the Oka estuary.

One issue that is not well-defined in sediment transport is the distinction of the transition zone in the vertical between bedload and suspended load. The level at which bedload is considered to be suspended load is called the reference level, a, which is one of the parameters in the Rouse equation. Due to the essential role in scaling of the concentration profiles, a reference concentration level and its magnitude must be clearly defined. A second major objective of this thesis was to evaluate the relevance (or existence) of the reference level, a, and reference concentration, C_a, of the Rouse equation. Results from the SIS show that the Rouse profile is not applicable throughout the whole water column as the concentration profile is more complex than simply Roussian. There was no apparent trend to the existence of a reference level and reference concentration, as they were not evident in many of the concentration profiles. Some of the concentration profiles showed no reference level.

Three layers have been recognized in the measured concentration profile of this study; a Roussian layer, a buffer layer, and an inner layer. The Rouse profile was found and even though it takes up a major part of the water column, it was only applicable in the central part as the near-bed layer is dominated by an exponential increase in concentration to bed with a constant inner layer thickness. The majority of the mass flux of sand at each station of the Oka estuary took place in the inner layer and was largely restricted to the lowest 10% of the water column. This phenomenon was also evident in Amos et al., (2010b) where transport of sand was greatest in the bottom 10% of the water column of two inlets of Venice lagoons. The inner layer follows an exponential relationship where the Rouse equation does not apply. This finding contradicts previous work that estimates mass transport solely from a Rouse profile therefore neglecting the sediment transport in the inner layer.

It has been established in this case the hydrodynamics have no influence on the inner layer but rather it may be influenced by the tidal stage. There are different possibilities to explain the behaviour of the inner layer and its relation to the stage of the tide. The relaxation time of a bed form, which is a function of ripple geometry, is a key factor in controlling near bed sediment transport (Allen and Friend, 1976; Austin, et al., 2007). As bed roughness varies in response to the tidal flows, bedforms may not have enough time to readjust. The time scale for ripple development ranges from tens of minutes to hours, which can be affected by relaxation time effects. The advection of sand may be greater than local suspension, *i.e*. sand suspended in the upstream can be measured downstream under different flow conditions. Another reason may be from the changes in the 3D flow components due to channel meandering.

As the Rouse profile was found to be only applicable in the central part of the water column, a general equation was generated to predict the mass transport of sand over a tidal cycle for the bottom 10% of the water column, or the inner layer. The inner layer was characterized by an exponential increase in concentration to the bed and has a near constant thickness of 0.1 m. The new, simplified equation generated to predict C_z requires the input of only the grain size of one sample of the sand in suspension from the benthic trap. This equation eliminates the uncertainty of the reference height and reference concentration that the original Rouse equation depends on. Since the hydrodynamics of the Oka estuary are not relative to the inner layer, the universality of the new generated equation is not possible and is only applicable in this case. Further work needs to be carried out to understand this behaviour and if there is a general equation that can be used to predict sediment transport near the bed for all types of tidal inlets.

One of the assumptions made in the Rouse formulation is that the friction velocity, u_*, is constant with height above the bed (a constant stress layer exists). Since shear stress, which is related to the friction velocity, decreases linearly with height in the benthic boundary layer, u_*, is also assumed to decrease with height. A Shields parameter derived from the field measurements defines the suspension thresholds better when friction velocity is assumed constant throughout the water column. This implies that the constant stress layer of the boundary layer is present to the surface, which addresses another objective of this study, the evaluation of the distribution of friction velocity, u_*, through the boundary layer. Laboratory results show that friction velocity is constant in the lower 10% of the water column for different bed roughnesses. This indicates that in the area of our concern, where the majority of the sand transport takes place, a constant friction velocity can be used.

One of the shortcomings in collecting data in the field is the limited access to certain equipment. Data is collected and analyzed according to the equipment that is available and affordable at the time of the field campaign. For example, only two valeports were available at the time of the Oka estuary field work, while three valeports were needed to be deployed (one at each station of the estuary). The third valeport provides extra hydrodynamic data at the estuary mouth so it can be correlated with the ADV and ADCP data. Another example is the use of a profiling ADV instead of a single point ADV, to provide direct velocity in the vertical rather than making assumptions. Using the right equipment in the field can have a positive influence on the quality of the data collected and used for analysis.

6.2 Conclusions

- Sand transport took place during the survey as both bedload and in suspension at three stations of the field campaign within the Oka Estuary, Spain, located within the inner estuary, at the tidal inlet, and within the ebb tidal delta. Suspension threshold of Bagnold (1966) was found to discriminate best between bedload and suspended load measured in this study.
- Sand in suspension occupied almost the entire water column at peak flows, which occurred during mid ebb and mid flood (standing tidal wave). This was evident though samples collected by modified Helley-Smith sand trap and the calibrated backscatter signals of a sediment imaging sonar (SIS). Both indicate maximum concentrations near the bed.
- The Rouse parameter confirmed that sand transport in suspension was taking place throughout the benthic boundary layer. The ratio w_s/u_* is dependent on the dimensionless grain diameter, D_* ($w_s/u_* = 0.25D_*$).
- The Shields parameters derived from the field measurements defines the suspension threshold better when friction velocity is assumed constant throughout the water column. This implies that the constant stress layer of the boundary layer is present to the surface, which has been verified in the laboratory results of Chapter 5.
- The concentration profile is more complex than simply Roussian as four consecutive layers have been recognized in the vertical. Form the surface downwards, these are: a surface layer (where concentration generally decreases to a minimum); a Roussian layer (which exhibits a power law form and

dominated most of the water column); a buffer layer (which serves as the transition between the inner and the Roussian layers); and an inner layer (roughly always 0.1 of the total depth, where most of the mass sediment flux takes place and which takes on an exponential form).

- A new, simplified equation to predict C_z in the inner layer is generated, where the reference concentration C_a can be derived and used in the Roussian layer, so that the concentration at a given relative height is given by:

$$C_{(\frac{z}{h})} = ae^{-b(\frac{z}{h})}$$

6.3 Recommendations for future work

This study highlights a multitude of opportunities for future work both to aid in a better understanding of the fundamental processes involved in moving sediment in suspension, and in defining sediment transport dynamics and hence morphological evolution of the Oka estuary.

- The field work was carried out in the summer where the conditions were calm and the wave influence was insignificant. During the winter season is when the waves are high and therefore has a major effect on the Oka estuary. Since waves break on the tidal ebb delta of the estuary mouth, how will it influence the direction and speed of sediment transport in and out of the inlet? What would be the seasonal changes?
- In general, most changes that occur to tidal inlets are a result of storms and parts of the Basque coast are exposed to large storms from the North West. Wave heights at the Oka estuary during extreme conditions are five times higher than those in winter. What kind of effect would it have on the distribution of sediment transport in the vertical? During normal conditions, the majority of sand transport took place in the bottom 10% of the water column. Would storms cause the resuspension of sediments higher in the water column?
- During the survey in addition to single point measurements, ADCP transects across the estuary were carried out every hour, throughout a complete tidal cycle, recording backscatter and flow. Analyzing this data would provide valuable information as it covers a larger area along the estuary. In what

direction is sand travelling and during what stage of the tide is it travelling most are questions that are likely to be answered here.

- A parabolic eddy viscosity was used in determining sand concentration. If a different eddy viscosity was used, what effect would it have on the shape and thickness of the profiles, in both the inner and Roussian layers?
- Why was there a strong difference in sand concentration between flood and ebb that is not reflected in the flow data? Could this be because of bed roughness, flow turbulence, or most importantly, the possible advection of sand into the monitoring site from elsewhere?
- It has been observed that the grain size distribution in the vertical has a major effect on the concentration profile. For each layer, one median grain size (from the settling column) is used for the calculations. It would be useful to look at the sorting of grain size in each layer in more detail to better understand the effects it has on the concentration profile.
- What is the role of bed forms on the distribution of shear stress in the vertical? Plots of the friction velocity in the vertical from Chapter 5 indicate that it is constant above the ripple’s height. A similar experiment with different types of bed forms (e.g. ripples and dunes) is recommended to understand the behaviour of friction velocity in the vertical for bed forms.

Appendices

Appendix A

Continental Shelf Research 78 (2014) 39–50

Contents lists available at ScienceDirect

Continental Shelf Research

journal homepage: www.elsevier.com/locate/csr

Research papers

An evaluation of the Rouse theory for sand transport in the Oka estuary, Spain

A. Al-Ragum[a,*], M. Monge-Ganuzas[b], C.L. Amos[a], A. Cearreta[c], I. Townend[d], E. Manca[e]

[a] School of Ocean and Earth Science and School of Civil and Environmental Engineering, University of Southampton, Southampton, UK
[b] Urdaibai Biosphere Reserve, Environment and Land Organization, Gernika-Lumo, Spain
[c] Departamento de Estratigrafia y Paleontologia, Universidad del Pais Vasco/UPV/EHU, Bilbao, Spain
[d] HR Wallingford Limited, Wallingford, UK
[e] Dipartimento di Scienze della Naturae del Territorio, Universita'di Sassari, Sassari, Italy

ARTICLE INFO

Article history:
Received 7 June 2013
Received in revised form
17 January 2014
Accepted 18 January 2014
Available online 13 February 2014

Keywords:
Rouse
Sand transport
Tidal inlet
Oka estuary
Urdaibai Biosphere Reserve

ABSTRACT

The Rouse profile has been traditionally used to represent the vertical distribution of suspended sand in a marine benthic boundary layer. Yet it is one of the biggest unknowns in estuarine morphodynamics, largely due to uncertainties of the ratio of the sediment fall velocity to bed friction on which the Rouse exponent ($R = w_s/\beta k u_*$) is based. A field campaign was carried out at three different locations in the Oka estuary, northern Spain, in order to examine these uncertainties. Each location differed in grain size and flow condition thus offering a wide range of settings. The first survey was inside the estuary (wave sheltered, flood tide dominated and relatively broad estuary section), the second was at the distal ebb delta (ebb tide dominated and narrow estuary section), and the third was over the wave exposed proximal ebb delta (wave/flood tidal current combined flows and open sea). The aim of this study is to evaluate the applicability of the Rouse (1937) theory for the distribution of sand in suspension throughout a turbulent benthic boundary layer. A modified version of a Helley–Smith sampler was used to trap sand and measure the vertical distribution of sand in the water column. As well, a 1200 ADCP was used to measure flow velocity and backscatter together with an ADV (turbulence). The sand traps were found to have a sampling efficiency of 44%. The grain size at all stations was finer near the surface and coarser near the bed. The sand transport inside the estuary (Station 1) is inwards dominant. By contrast, the sand concentration during the ebb tide was ten times higher than during the flood tide at Station 2 and even higher at Station 3, which suggests that the sand transport over the ebb delta is seawards. The average Rouse parameters for Stations 1, 2, and 3 are 0.48 ± 0.035, 0.78 ± 0.23, and 0.46 ± 0.06 respectively, which correspond to a coefficient of proportionality of the movability number, (χ) of 4 (Van Rijn, 1993). These differ from previous findings of Villatoro et al. (2010) and Amos et al. (2010b).

1. Introduction and background

Suspended sediment transport is amongst the most significant factors influencing estuarine morphodynamics, yet it is often one of the largest unknowns. Initiation of motion, suspension threshold, and the vertical distribution of sand concentration in the water column all need to be determined for an accurate estimate of sediment transport rate. Traditionally, sand in suspension has been defined by the Rouse (1937) theory. This proposes upward diffusion as the main mechanism controlling particle movement across a vertical concentration gradient, from areas of high concentration (near the bed) to areas of low concentration higher in a turbulent boundary layer (Atkins, 2005). The Rouse profile is often used to represent the vertical distribution of suspended sand in a turbulent benthic boundary layer; it is defined in part as a function of the ratio of the sediment fall velocity (w_s) to bed friction velocity (u_*). This ratio is the basis of the Rouse parameter (R) which is defined as $R = w_s/\beta k u_*$, where β is the ratio of eddy diffusivity to eddy viscosity and k is the Von Karman constant. However, there are several assumptions in the Rouse theory that do not necessarily apply in the present case. One of these is that the (inverse) movability number (the dimensionless ratio of the settling velocity of sand in suspension to the bed friction velocity, w_s/u_*) is a constant, whereas it is not (Van Rijn, 1993). Instead, there is growing evidence to suggest that this ratio is dependent on height above the bed, the Reynolds number, and the grain size. Accurate predictions of sand transport in suspension are not possible unless this ratio is accurately defined (Amos et al., 2010b; Villatoro et al., 2010), which makes sand trapping an attractive method of assessing this theory.

---

[*] Correspondence to: National Oceanography Centre, European Way, Southampton SO14 3ZH, UK.
E-mail address: anar1e10@soton.ac.uk (A. Al-Ragum).

http://dx.doi.org/10.1016/j.csr.2014.01.018

Nomenclature

a	reference concentration height (L)
β	ratio of eddy diffusivity to eddy viscosity
C_a	sand concentration at reference height a (ML^{-3})
C_D	drag coefficient
C_z	sand concentration at height z above bed (ML^{-3})
D_{50}	median grain diameter (L)
D_*	-dimensionless grain diameter
g	acceleration due to gravity (LT^{-2})
h	water depth (L)
k	Von Karman's constant
u_*	bed friction velocity (LT^{-1})
u_{*crit}	critical bed friction velocity (LT^{-1})
R	Rouse parameter
R_e	Reynolds number
ρ	seawater density (ML^{-3})
ρ_s	sediment density (ML^{-3})
s	specific gravity
θ	Shields parameter
θ_c	critical Shields parameter
τ	bed shear stress (MLT^{-2})
τ_c	critical bed shear stress (MLT^{-2})
υ	kinematic viscosity (L^2T^{-1})
w_s	still water grain settling velocity (LT^{-1})
w'_{up}	mean amplitude of upward-directed component of turbulent flow (LT^{-1})
w_{rms}	root mean square amplitude of vertical component of turbulent flow (LT^{-1})
χ	coefficient of proportionality of the movability number for $D_* < 10$
z	height above bed (L)

The aim of this study is to evaluate the validity of the Rouse theory in evaluating the distribution of sand in suspension throughout the turbulent benthic boundary layer of the Oka estuary, Spain (Fig. 1). This is achieved by the measurements of sand concentration with elevation above the bed, and through sampling the suspended material by trapping in order to determine the in situ grain size and settling rate of suspended material. The vertical distribution of sand in suspension was examined over a range of tidal conditions to provide a wide range of flow conditions and concentration profiles on which to undertake a robust assessment. The perceived outcome is more accurate sand transport evaluations and better model predictions. This study provides an opportunity to extend the Venetian work of Amos et al. (2010a) and Villatoro et al. (2010) over a wider range of sand sizes. The difference between the two sites is that in the Venice inlets the sediment in suspension was restricted to fine sand, whereas in the Oka estuary the sand is coarser and has a wider size range. As a result, field information on the suspension threshold will be obtained from situations where none exist at present.

1.1. Sand transport

Sediment fall velocity (w_s) is one of the key properties to assess in the study of sediment transport. Fall velocity is related to the balance between the immersed weight of the particle and the fluid drag on the particle induced by settling. It is determined by the sediment diameter and density, and at low grain Reynolds numbers, the viscosity of water (Soulsby, 1997). Using the balance of forces, w_s is evaluated as

$$w_s = \sqrt{\frac{4(s-1)gD_{50}}{3C_D}} \qquad (1)$$

where g is the gravitational acceleration, C_D is the drag coefficient of the settling particle, s is the specific gravity ($s = \rho_s/\rho = 2.65$ for

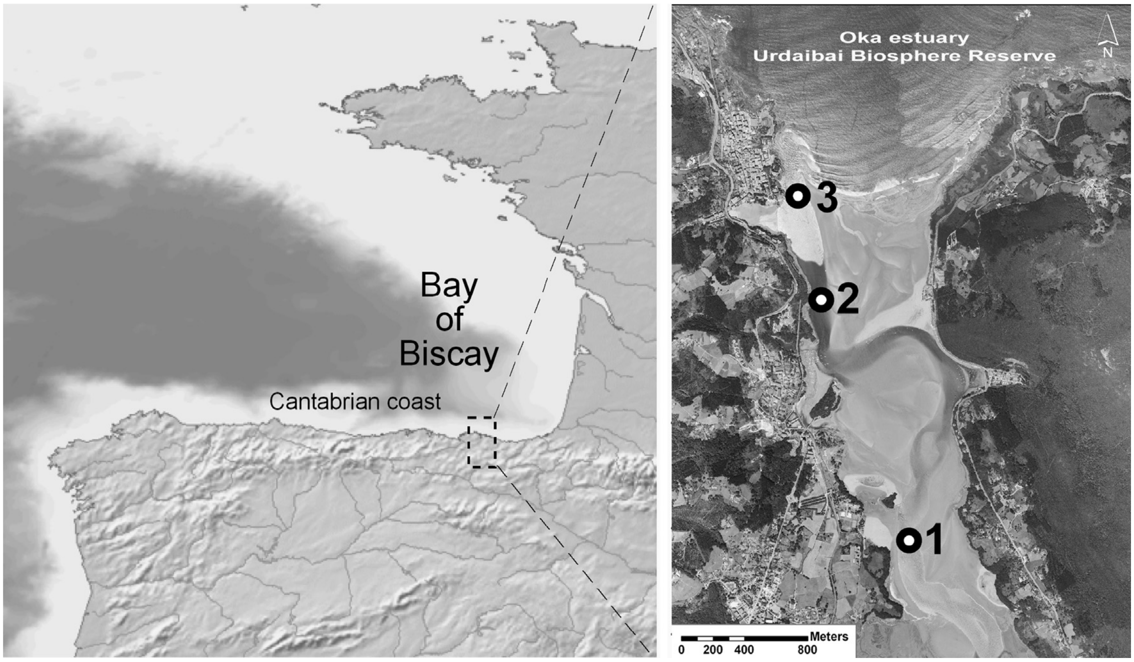

Fig. 1. The location of the Bay of Biscay and Oka estuary showing the location of the three stations.

sand, where ρ_s and ρ are sediment density and water density respectively), and D_{50} is the sand median diameter. Since the drag coefficient is dependent of Reynolds number ($R_e = w_s D_{50}/\upsilon$, where υ is the kinematic viscosity), two extreme conditions can be identified (Van Rijn, 2011). For low values of Reynolds number ($R_e < 1$) *i.e.* laminar flow around the settling particle, grains settle according to Stokes Law and the drag coefficient is defined as follows:

$$C_D = \frac{24}{R_e} \tag{2}$$

In this case, Eq. (1) can be rewritten as

$$w_s = \frac{(s-1)gD_{50}^2}{18\upsilon} \tag{3}$$

For high values of Reynolds number ($R_e > 1000$) grains follow a quadratic bluff body drag law, where the drag coefficient is assumed constant ($C_D \approx 0.4$) and the settling velocity is expressed as

$$w_s = \sqrt{3(s-1)gD_{50}} \tag{4}$$

Other formulae have been developed in the literature for calculating w_s based upon a specific range of the dimensionless particle diameter D_*, defined as,

$$D_* = \frac{(s-1)g^{1/3}}{\upsilon^2} D_{50} \tag{5}$$

However, Soulsby (1997) defined the fall velocity (w_s) based upon an empirical formula combining both the viscous and bluff body drag laws for all D_* and has the following universal form:

$$w_s = \frac{\upsilon}{D_{50}}\left(\sqrt{10.36^2 + 1.049D_*^3} - 10.36\right) \tag{6}$$

In all of the cases defined above, the particles are considered to be spherical, which is not true in reality. As a result, prediction of w_s from grain size may be inaccurate. Furthermore, assumptions on sediment density are made which may lead to further errors. Therefore, field trapping and direct measurements of sand settling velocity in a laboratory settling column is used in this study, thus avoiding several sources of errors including shape effects.

1.2. Initiation of motion

The forces that act on a sediment particle are mainly drag, lift, and pressure forces (Nielsen, 2009) and initiation of motion will occur when these forces are larger than the resisting forces relating to the particle submerged weight (Van Rijn, 1993). The Shields parameter is a measure of sediment movability that accounts for pressure gradients and drag. Shields, 1936 applied dimensional analysis to establish his well-known diagram of incipient motion for traction where he assumed that the drag force is equal to the gravitational force on an immersed particle at the onset of motion. The key parameters used in the Shields approach are the fluid-induced bed shear stress (τ), particle diameter, the fluid kinematic viscosity, and fluid drag acting on a particle at rest on the bed (Yang, 1996). The general equation of the entrainment function (θ_c) as defined by Shields is

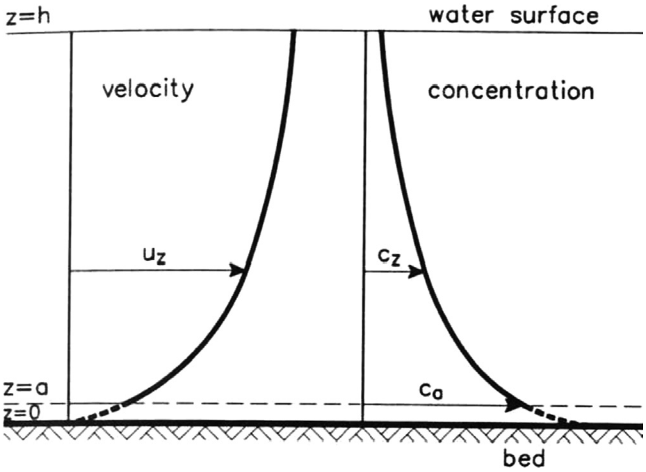

Fig. 2. The distribution of sand concentration, Ca, with height, z, above the bed (from Van Rijn, 1993).

$$\theta_c = \frac{\tau_c}{(\rho_s - \rho)gD_{50}} \tag{7}$$

where, τ_c is the critical bed shear stress and is equal to (ρu_{*crit}^2), where u_{*crit} is the critical bed friction velocity and the median particle diameter is used to represent the particle diameter in case of a non-uniform sediment material (Van Rijn, 1993). Bonneville (1963) and Yalin (1972) showed that the Shields curve can be expressed in terms of θ_c and dimensionless diameter (D_*). Suspension thresholds of Bagnold (1966), McCave (1984), Engelund (1965), and Van Rijn (1993) have been added to the classical Shields diagram. There is considerable variability in the suspension threshold as a function of D_*. It is generally considered that when $D_* < 3$, sand goes directly into suspension at the onset of motion (Amos et al., 2010b). For $D_* > 3$, traction (bedload) takes place initially, which may be followed by suspension at higher bed shear stresses. It is this upper threshold that dictates the onset of sand in suspension. Its accurate assessment is considered a necessary pre-cursor to the evaluation of Rouse theory and so is part of this study.

1.3. Rouse theory

The suspension of sand occurs when the critical Shields parameter for suspension is exceeded. The sand particles are lifted to a level until the upward turbulent drag on the sand is balanced by the submerged weight (Van Rijn, 1984). Several mechanisms have been proposed to account for the observed characteristics of suspension (Atkins, 2005). The behavior of the suspended sediment particles is described in terms of sediment concentration (Van Rijn, 1993). Observations show that suspended sediment concentration decreases hyperbolically with increasing height above the bed, (Fig. 2). The rate of the decrease depends on the ratio of fall velocity to bed frictional velocity as (w_s/u_*), also known as the movability number (Collins and Rigler, 1982). Implicit in this assumption is that u_* and thus w_s are constant in the vertical.

The Rouse profile is often used to represent the vertical distribution of suspended sediment, but the approximation of the Rouse profile is valid only when the sediment is transported in the part of the benthic boundary layer subject to constant stress (Amos et al., 2010a). The Rouse equation is expressed as

$$\frac{C_z}{C_a} = \left(\frac{h-z}{z}\frac{a}{h-a}\right)^R \tag{8}$$

where C_z is the sand concentration at height, z, above the bed, C_a is the reference concentration, h is the water depth, and a is the reference height. Various versions of Eq. (8) have been proposed by varying the expression of relative depth (z/h). These have been revised by Van Rijn (1993) who defined the types of distribution of suspended sand with height through the benthic boundary layer in terms of the exponent R. In this study, a simple form of relative depth was used. This overcomes the uncertainty in defining the reference concentration height (a).

2. Study region

This study was undertaken in the Oka estuary, Spain. The estuary is situated on the Basque coast in the south eastern of the Bay of Biscay (Fig. 1), which extends over 150 km and whose adjacent continental shelf is less than 20 km wide. Most of the coastline is erosional dominated by cliffs and a series of pocket beaches and small rias. The waters are generally clear of fine-grained sediment due to relatively limited fluvial supply. The estuaries are small having a maximum length of approximately 15 km and are less than 1 km wide. The dominant wave approach is from the northwest causing sand to accumulate in the eastern margins of the estuary mouths, where dunes and beaches are formed (Borja and Collins, 2004). Much of the sand is derived from the continental shelf and is transported across the breaker zone by waves. The tidal asymmetry enhances this landward transport creating sand-filled rias that are typical of the region. This material is constantly re-cycled through the inlet by tidal resuspension and wave overwashing.

The effect of river flow (mean value of 0.59 m^3/s) during the survey period was insignificant compared with the mean tidal prism of 5×10^6 m^3 (Liria et al., 2009). As well, the weather conditions were calm as was the sea state. The tidal wave in the Bay of Biscay is semi-diurnal and standing (i.e. peak flows at mid tide). The mean tidal range during neap tides is 1.5 m (low meso-tidal). During spring tides, the tidal range is 4 m (high meso-tidal). During spring tides, the flood phase is shorter than the ebb phase, which produces stronger currents on the flood and longer periods of slack water during low tide (Monge-Ganuzas et al., 2012). In general, a headward residual sediment transport in suspension takes place as a result of the tidal asymmetry observed in the estuary (Monge-Ganuzas et al., 2008).

By the second half of the 19th century, human activity had transformed 60% of the original Oka estuary. In 1984, the Oka estuary was granted a UNESCO Biosphere Reserve status and it is considered as the best preserved estuary of the Basque coast. The main physical impact on the estuary has resulted from dredging of the sand which infills the estuary (Cearreta et al., 2004). The last dredging activity (287,000 m^3) was carried out in 2003, however the natural infilling with sand continues to the present day (Monge-Ganuzas et al., 2008).

3. Methodology and data collection

An indirect method was used to measure sediment transport in suspension in the Oka estuary, which is based on simultaneous measurements on independent time-averaged velocity and sediment concentrations. A modified version of the Helley–Smith sampler (Helley and Smith, 1971) was used to measure the vertical distribution of sand in the water column. This sampler has been successfully used in previous similar field studies in two tidal inlets of Venice lagoon (Amos et al., 2010a; Villatoro et al., 2010) In addition to being easy to handle, the Helley–Smith samplers can collect sufficient sand for analysis (>100 g). The sand traps consist of a nozzle, a sample bag, and a frame (Fig. 3). The sample bag is made of 60-μm mesh polyester, commonly used for plankton nets. Four sand traps were used in this study. Two sand traps had a square entrance nozzle of 120×120 mm^2 and two sand traps had a smaller square entrance nozzle of 60×60 mm^2. The smaller traps were used in the water column, whereas the larger (more stable) traps were used in the benthic and epi-benthic modes as defined by Villatoro et al. (2010). The sand traps were deployed hourly from an anchored boat for a duration of 10–15 min (in order to collect vertical profiles) throughout a complete tidal cycle. As the traps were lowered in the water, they aligned with the flow. The benthic and epi-benthic traps were lowered to the seabed once aligned. The epi-benthic trap was attached to a base that lifted the sample mouth 0.12 m above the seabed. The middle sand trap was lowered to about mid-depth. When the water depth was $h < 2$ m, the middle sand trap was omitted. The surface trap was lowered into the water until the nozzle was completely submerged. The mean time delay between sampling of the lower two and upper two traps was 10 min, but for present purposes was considered to be synchronous based on arguments presented by Soulsby (1980). The sand samples obtained were used to determine the sand concentration as a function of elevation in the benthic boundary layer. A pump sampler was used to collect approximately 400 L of seawater which was then passed through a 63-μm sieve. This was used to derive a calibrated concentration from the dry mass of sand retained on the sieve. The surface sand concentration was determined as the mass (M) trapped by the sieve divided by the pumped volume of water (V). Simultaneously, a surface trap was deployed and the material collected and analyzed for sand concentration. Calibration of a 60-μm mesh size yielded a sampling efficiency of between 4% and 7% (Amos et al., 2010a) in the plankton rich waters of Venice lagoon. Sand traps generally are less than 100% efficient due to the influence of the trap on the flow, (bio) fouling, blockage and drag caused by the fine mesh of the trap nets. The trap efficiency was evaluated at the surface and it was assumed to be constant throughout the water column. Our initial assumption is that all four sand traps (including the benthic trap) can be used to define the suspended profile.

Optical and acoustic sensors were also used in order to supplement the sand concentrations collected from the traps. An RDI Workhorse Acoustic Doppler Current Profiler (ADCP) was used to record hourly measurements of acoustic backscatter, flow direction and velocity throughout the water column. The ADCP was mounted downward from a stationary boat (Fig. 3) and measured at a frequency of 1200 kHz with a 0.5 m vertical cell size. The bottom and surface 0.3 m of the water column were not recorded by this instrument and were extrapolated for velocity assuming *law of the wall* as described by Helsby (2008). The ADCP recorded data for the period the middle and surface sand traps were deployed in the water so the values of mean flow from the ADCP can be used for sand concentration collected from the sand traps.

Two self-recording Valeport® 802 current meters were fixed on a triangular frame (Fig. 3) and deployed at two locations in the estuary to measure turbidity, suspended particle matter, and mean flow for a duration of 6 days. The Valeports consist of an electromagnetic current meter situated at $z=0.18$ m, an optical backscatter sensor (OBS) at $z=0.35$ m, and a pressure sensor at $z=0.4$ m. The Valeports recorded continuously at 4 Hz for 6 min every 30 min.

A Nortek® Acoustic Doppler Velocimeter (ADV) was used to provide burst sample three-dimensional flow, which was used to derive the friction velocity using the turbulent kinetic energy (TKE) method (Thompson et al., 2003). This method is independent of estimates of bed friction. The ADV measured the flow at 25 Hz at $z=0.22$ m. The *law of the wall* was then used to calculate the water flow at the sampling height of the lower traps. The ADV was fixed on a triangular frame (Fig. 3) and deployed from a stationary boat hourly for a duration of about 5 min yielding appriximately 7000 data points per burst. The “Vectrino plus” firmware used to measure, record, and convert data was supplied by Nortek AS. The output files from the ADV includes the velocity in three orthogonal directions. The latter data were extracted for comparison with the concentration data derived from the epi-benthic trap, which sampled at the same height and at the same time period.

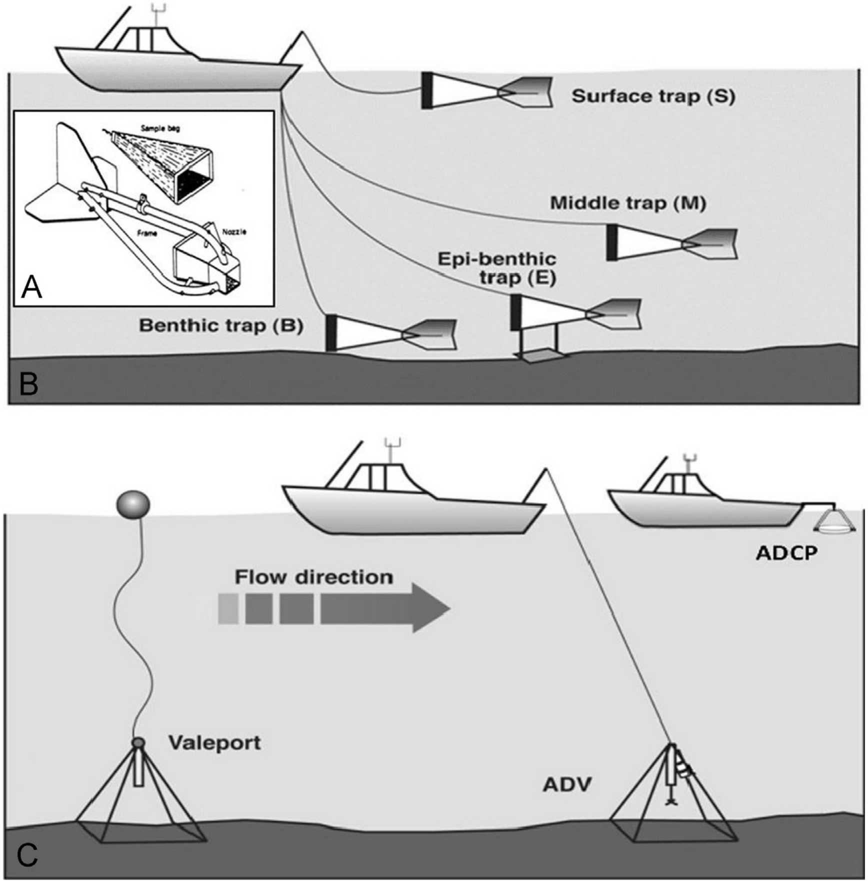

Fig. 3. (A) A sketch of the Helley–Smith sand sampler showing the nozzle and sample bag (from Helley and Smith, 1971), (B) a diagram showing the general sand trap deployment, and (C) the deployments of the Valeport, ADV, and ADCP (modified from Villatoro et al., 2010).

Finally, water samples were collected hourly using a one litre Niskin bottle to measure the content of fines ($D_{50} < 63$ μm) in the water column, at three different levels (bottom, middle, and surface). Water samples were filtered through 47 mm glass microfibre filters (GF/F) to yield mass concentration of fines, after first passing through a 63-μm sieve to remove the sand. In all cases, the organic material in the sediment was removed by ashing in a muffle furnace at 450 °C for 5 h. The organic content was evaluated by the loss on ignition (LOI) method.

The data were collected in the Oka estuary in June, 2010 at three different locations in the vicinity of the main tidal inlet shown in Fig. 1. The first survey location, Station 1, was inside the estuary where it is sheltered from waves and flood-tide dominated, Station 2 was in the inlet mouth which is ebb-tide dominated, and Station 3 was on the ebb tide delta. The field survey was based on a two boat operation. An anchored boat (Starfisher) was used to deploy the sand traps and the ADV. The ADCP measurements and Niskin water samples were collected from a small 4 m zodiac.

4. Results and discussion

4.1. Hydrodynamics

The Oka estuary is well-mixed (Monge-Ganuzas, 2008) with an average temperature of 18.3 °C and kinematic viscosity, ν, of 1.08×10^{-6} m^2/s. The Reynolds numbers for all three stations show that the flow is rough turbulent ($R_e > 5 \times 10^5$). That is, the drag coefficient used in the derivation of bed stress may be considered as constant. Hydrodynamic data of the three stations are summarized in Table 1. Estimates of u_* are based on the assumption that the ADV was in the constant stress layer. In order to validate this assumption, the boundary layer thickness, δ, has been calculated using two methods. The first method is using Ekman's theory which is based on the Earth's rotation (Bowden, 1978). Ekman's depth is given by

$$L_E = 0.4u_*f \tag{9}$$

where f is the angular velocity of rotation ($f = 2w \sin\phi$, w is the rate of angular rotation of Earth, 6.94×10^{-4}, and ϕ is the latitude of Oka estuary, 43°). In the lower part of this layer, $0.1L_E$, stress is generally assumed constant. In the second method (using Liu, 2001), for turbulent flow, the boundary layer thickness is expressed as

$$\delta = 0.4x\left(\frac{Ux}{\nu}\right)^{-0.2} \tag{10}$$

where x is the horizontal distance over which the boundary layer has developed which has been scaled from Google Earth. The estimates of boundary layer thickness using Eqs. (9) and (10) are given in Table 1. The Ekman boundary layer occupies the entire water column in most cases, and the constant stress layer is never less than 0.5 m, therefore, the ADV ($z = 0.22$ m) is within this constant stress layer.

4.2. Sand trap efficiency

Fig. 4 shows the regression line from which the efficiency was determined using the surface measurements from all three stations. The observed concentration varied over a range of 0.06 mg/l to 8 mg/l. The linear best fit regression yielded SC = 0.44CC mg/l

Table 1
Hydrodynamics data of Stations 1, 2, and 3 including tide stage, average velocities (U) at $z=0.22$ m and at the surface, friction velocity u_*, water depth (D), kinematic viscosity (ν), Reynolds number Re, and boundary layer thickness (δ) calculated using: (a) Ekman's theory (Bowden, 1978) and (b) Liu (2001).

Station	Profile	Stage of tide	Average velocity at $z=0.22$ m, $\bar{U}$ (m/s)	Average velocity at surface, $\bar{U}$ (m/s)	Friction velocity, u_* (m/s)	z_0 (m)	Water depth (m)	Water temp. (°C)	Kinematic viscosity (m^2/s)	Reynolds number, Re	Ekman boundary layer thickness (m)	Boundary layer thickness for turbulent flow (m)
1	1	Ebb	0.205	0.397	0.0123	0.0003	3.18	18.27	1.092E-06	1.156E+06	5.20	4.46
	2	Ebb	0.325	0.548	0.0176	0.0001	2.74	18.78	1.079E-06	1.392E+06	7.44	4.17
	3	Ebb	0.415	0.500	0.0271	0.0005	2.22	19.30	1.065E-06	1.042E+06	11.45	4.24
	4	Ebb	0.168	0.441	0.0550	0.0543	1.75	19.81	1.053E-06	7.332E+05	23.24	4.33
	5	Flood	0.293	–	0.0205	0.0005	1.31	19.64	1.057E-06	–	8.66	–
	6	Flood	0.293	–	0.0205	0.0005	1.26	19.64	1.057E-06	–	8.66	–
	7	Flood	0.493	0.660	0.0345	0.0005	1.96	19.81	1.053E-06	1.229E+06	14.58	4.00
	8	Flood	0.344	0.469	0.0217	0.0003	2.61	18.61	1.083E-06	1.130E+06	9.17	4.30
2	1	Flood	0.134	0.539	0.0168	0.0071	4.10	17.93	1.101E-06	2.008E+06	7.10	2.02
	2	Flood	0.475	0.432	0.0130	5.77E-08	5.61	17.76	1.105E-06	2.193E+06	5.49	2.11
	3	Flood	0.400	0.429	0.0232	0.0002	5.49	18.10	1.096E-06	2.148E+06	9.80	2.11
	5	Ebb	0.450	0.604	0.0203	0.0002	3.66	18.27	1.092E-06	2.025E+06	8.58	1.97
	6	Ebb	0.110	0.757	0.0350	0.0524	3.18	18.61	1.083E-06	2.223E+06	14.79	1.88
	7	Ebb	0.450	0.737	0.0268	0.0003	3.11	19.81	1.053E-06	2.178E+06	11.32	1.88
	8	Ebb	0.450	–	0.0268	0.0003	2.00	19.81	1.053E-06	–	11.32	–
3	1	Ebb	0.428	0.602	0.0411	0.0027	2.46	18.78	1.079E-06	1.373E+06	17.37	5.36
	2	Ebb	0.256	0.409	0.0263	0.0042	2.50	18.61	1.083E-06	9.442E+05	11.11	5.79
	3	Ebb	0.051	–	0.0129	0.0451	2.53	18.61	1.083E-06	–	5.45	–
	4	Flood	0.338	0.510	0.0253	0.0009	5.07	18.44	1.087E-06	2.378E+06	10.69	5.54
	5	Flood	0.222	0.380	0.0216	0.0037	5.46	17.93	1.101E-06	1.885E+06	9.13	5.90
	6	Ebb	0.204	–	0.0194	0.0036	7.00	18.10	1.096E-06	–	8.20	–
	8	Ebb	0.204	–	0.0194	0.0036	5.00	18.10	1.096E-06	–	8.20	–

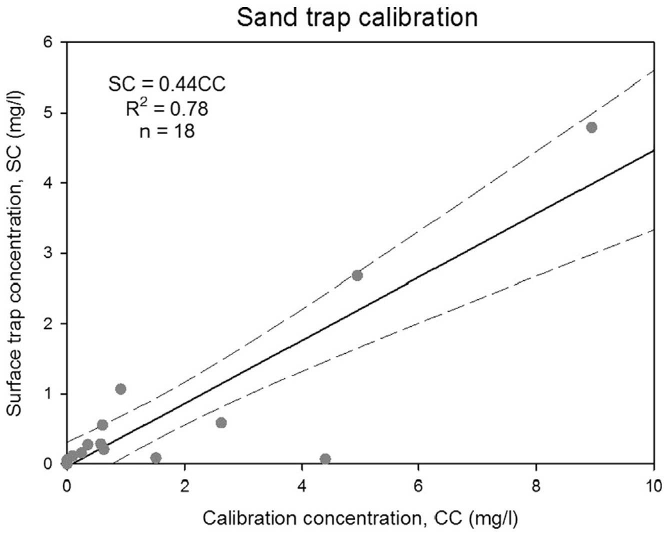

Fig. 4. The sand trap calibration showing the regression between the surface trap concentration and the calibration concentration (with 95% confidence intervals).

($n=18$), where SC is the surface trap concentration and CC is the calibration concentration. The relationship is significant (the p-value, $p=0.01$). The trap efficiency for the Oka estuary was 44%. This value was used to adjust the sand concentration calculated for all sand trap deployments. The constant trap efficiency in the vertical is justified in that the water column is well mixed (the benthic boundary layer extends to the surface) during periods of sand in suspension and low in phytoplankton (which affects bio-fouling of the nets).

4.3. Grain size and sand concentration

A total of eight profiles were collected with the sand traps at each station. The material collected was used to determine the sand particle size, the settling velocity, and the vertical sand concentration (Table 2).

4.3.1. Station 1

The organic content of sand decreased from 17% to 2% during ebb-tide and from 10% to 1% during flood-tide towards the bed at this station, while the sand concentration increased from 0.09 mg/l to 15.70 mg/l during the ebb and from 0.25 mg/l to 65.43 mg/l during the flood. The grain size also increased towards the bed, reflecting greater settling rates. Medium sand ($0.20\text{ mm} < D_{50} < 0.30\text{ mm}$) was found in the benthic and epi-benthic traps while only very fine sand ($0.08\text{ mm} < D_{50} < 0.11\text{ mm}$) was found in the upper levels of the water column. Fig. 5a shows the best fit lines of sand concentration through the water column for eight profiles over a tidal cycle for Station 1. The concentration of sand appears higher on the flood-tide than the ebb-tide suggesting a net landward movement over the survey period. This result was also evident in the ADCP data previously collected by Monge-Ganuzas (2008) and analyzed for sand transport by Vianna (2012). The sand concentration fits a power law in all profiles and slopes of the profiles are similar in value (Table 3).

4.3.2. Station 2

Fig. 5b shows the sand concentration through the water column over a tidal cycle for Station 2. The organic content (maximum value up to 17%) was higher during flood tide but shows no trends with depth. The material is classified as fine-medium sand (0.24 mm) in the lower water column and fine sand (0.18 mm) in the upper. The sand concentration increased towards the bed and was sensitive to the change of tide. As well, the sand concentration during the ebb-tide was 10 times higher than during the flood-tide. This suggests that the sand transport on the distal ebb delta is, as expected, dominantly seawards.

4.3.3. Station 3

The results of the sand trap sampling at Station 3 are shown in Fig. 5c. The organic content decreased towards the bed (from 12%

Table 2
Average values of sand concentration (SC) and organic content, grain diameter (D_{50}), and settling velocity (w_s) for the surface, middle, benthic and epi-benthic samples, at all stations.

Station	Sample	Ebb tide					Flood tide				
		Organic %	D_{50} (mm)	D_*	w_s (m/s)	SC (mg/l)	Organic %	D_{50} (mm)	D_*	w_s (m/s)	SC (mg/l)
1	Surface	17.08	0.11	2.602	0.010	0.089	9.71	0.09	2.158	0.006	0.253
	Middle	27.56	0.08	1.935	0.005	0.070	–	–	–	–	–
	Epi-benthic	11.03	0.18	4.283	0.021	5.008	2.78	0.20	4.592	0.023	3.544
	Benthic	1.80	0.30	6.885	0.041	15.705	1.10	0.31	7.116	0.042	65.431
2	Surface	2.17	0.21	4.805	0.025	16.369	16.65	0.13	3.109	0.012	0.637
	Middle	1.43	0.23	5.369	0.029	25.063	9.70	0.16	3.834	0.017	1.756
	Epi-benthic	2.12	0.22	5.138	0.027	440.603	15.57	0.18	4.177	0.020	5.256
	Benthic	1.13	0.26	6.150	0.035	2981.468	1.60	0.29	6.732	0.040	135.750
3	Surface	11.97	0.11	2.460	0.009	1.875	16.07	0.10	2.365	0.007	0.631
	Middle	6.59	0.16	3.731	0.016	–	2.74	0.35	8.041	0.049	2.150
	Epi-benthic	2.33	0.33	7.667	0.046	127.411	7.10	0.23	5.297	0.029	0.901
	Benthic	1.37	0.38	8.854	0.054	3693.444	1.18	0.37	8.513	0.052	214.247

to 1% during ebb and from 16% to 1% during flood) and was greatest at the surface at the proximal ebb delta (Table 2). The grain size increased with depth; in the lower parts of the water column it was three times that of the surface. The sand in the upper water column was very fine (0.10 mm); in the middle part was medium sand (0.30 mm), and near the bed was medium to coarse sand (0.23–0.38 mm). There was a large difference in sand concentration throughout the water column as well as throughout the tidal cycle. The sand concentration during the ebb-tide was greater than during the flood-tide by an order of magnitude. The sand concentration increased significantly in the lower part of the water column. As in Station 2, the sand transport in the proximal ebb delta (Station 3) was seawards and also presents higher sand concentrations than Station 2.

Due to tidal asymmetry in the estuary, where the ebb phase is longer than the flood phase, sand transport was dominantly seawards at Stations 2 and 3, even when there was a net inflow of water (as occurs on a neap to spring phase of the tide).

4.4. Rouse parameter and movability number

In order to calculate the Rouse parameter, the sand concentrations were plotted against the relative height to obtain a best fit line. Each profile had a maximum of four data points. To increase the number of data points for each profile, backscatter measurements from the ADCP were converted to concentration units (mg/l) and added to the sand trap concentrations. Since the ADCP backscatter is sensitive to the type of suspended particulate matter, it was calibrated in situ. Fig. 6 shows the calibration of the ADCP backscatter from all surface and middle samples for the three stations; backscatter (db) is plotted against sand concentration.

The slope, intercept, and correlation coefficient of each profile is shown in Table 3. The movability number (w_s/u_*) was calculated from the Rouse parameter, $R=(w_s/\beta k u_*)$, where $\beta=1$ and $k=0.41$. From the power function ($y=bx^m$) of the regression lines (Fig. 7), for each profile we calculated the Rouse parameter as follows:

$$\log_{10}\frac{z}{h}=m\log_{10}C+b \tag{11}$$

then,

$$C=\left(\frac{z}{h}\right)^{(1/m)}10^{-(b/m)} \tag{12}$$

where C is the sand concentration and $R=-1/m$. The average Rouse parameter for Station 1 was 0.48 ± 0.035 (profiles with two data points were omitted). The average movability number (w_s/u_*) was 0.20 ± 0.015. This value will be compared to other movability numbers derived using different methods, as defined by Amos et al. (2010b). The same analysis was repeated for Stations 2 and 3. The average Rouse parameter for Station 2 was 0.78 ± 0.23. The Rouse parameter varied slightly with the tide, and the values were higher on the flood-tide than on the ebb-tide. The average movability number, w_s/u_*, was 0.32 ± 0.095. The Rouse parameter did not vary during the tidal cycle at Station 3. The average Rouse parameter for this station was 0.46 ± 0.06. The average movability number for the survey was 0.19 ± 0.025.

The Rouse parameter at all three stations was less than unity demonstrating full suspension uniformly distributed throughout the boundary layer (Van Rijn, 1993). Unlike that described by Villatoro et al. (2010), there was no apparent trend with stage of the tide (flood versus ebb) as mean velocities were similar. The sensitivity of the Rouse parameter to grain size is ambiguous: coarser sand was found at Station 3, whereas the highest values of the Rouse parameter were found at Station 2. Given the vertical variation in grain size of suspended material evident in Table 2, it appears that the Rouse profile is as strongly influenced by sediment sorting (sediment availability to feed the vertical variation) as by the median grain size. That is, the Rouse profile cannot develop if the appropriate sediment sizes are not available at the bed to feed it.

The ratio w_s/u_* is considered fundamental in determining the distribution of sand in suspension as well as estimating the critical Shields parameter for suspension. Different methods have been used to test the accuracy of the estimations of this ratio as follows:

- The first method is based on measured profiles of sand concentration. The movability ratio is calculated by associating the inverse slope to the Rouse parameter ($1/m=w_s/\beta k u_*$), and assuming the ratio of eddy diffusivity to eddy viscosity, $\beta=1$ and Von Karman's constant, $k=0.41$.
- The second method uses the National Oceanography Centre settling column to obtain direct measurements of the settling velocity (w_s). Friction velocity (u_*) is derived from independent ADV measurements and using the TKE method (Thompson et al., 2003).
- The third method is based on Bagnold's (1966) sand transport theory where the motion of suspended particles are governed by the following assumptions: (1) suspension of a grain occurs when its settling velocity (w_s) is equal to, or greater than, the upward instantaneous velocity of the turbulent flow in the water column (w'_{up}), (2) the upward velocity in the water

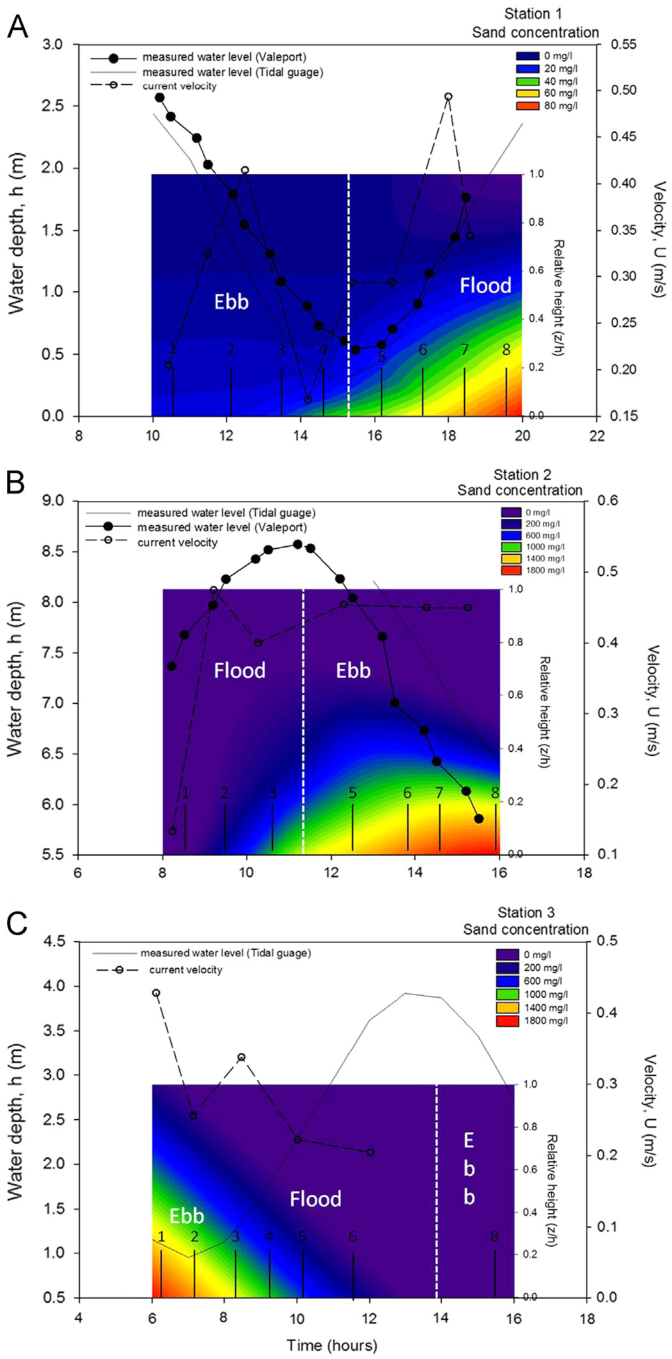

Fig. 5. Vertical profiles of sand concentration at Station 1 (A), Station 2 (B), and Station 3 (C) throughout the tidal cycle and the corresponding water level measurements. Flood and ebb are defined based on the observed flow direction and therefore do not always correspond to the tidal elevation.

Table 3
Number of samples (n), inverse slope ($1/m$), intercept (b), correlation coefficient (r^2), movability number (w_s/u_*), and tide stage for the profiles of all stations.

Station	Profile	n	$1/m = -R$	b	r^2	w_s/u_*	Tide
1	1	6	−0.53	0.09	0.55	0.22	Ebb
	2	6	−0.44	0.17	0.38	0.18	Ebb
	3	6	−0.45	0.18	0.58	0.18	Ebb
	4	4	−0.48	0.26	0.69	0.20	Ebb
	5	2	−0.26	0.08	1.00	0.11	Flood
	6	2	−0.33	0.07	1.00	0.14	Flood
	7	4	−0.46	0.35	1.00	0.19	Flood
	8	4	−0.51	0.14	0.57	0.20	Flood
2	1	4	−0.66	0.25	0.73	0.27	Flood
	2	6	−0.92	0.60	0.85	0.38	Flood
	3	6	−0.69	0.42	0.79	0.28	Flood
	5	6	−1.18	3.1	0.77	0.48	Ebb
	6	6	−0.54	2.95	0.95	0.22	Ebb
	7	6	−0.70	3.79	0.93	0.29	Ebb
	8	2	−0.65	0.68	1.00	0.27	Ebb
3	1	4	−0.47	0.78	0.99	0.19	Ebb
	2	4	−0.38	0.70	1.00	0.16	Ebb
	3	2	−0.25	0.12	1.00	0.10	Ebb
	4	4	−0.47	0.23	0.43	0.19	Flood
	5	6	−0.53	2.39	0.57	0.22	Flood
	7	2	−0.25	0.03	1.00	0.10	Flood

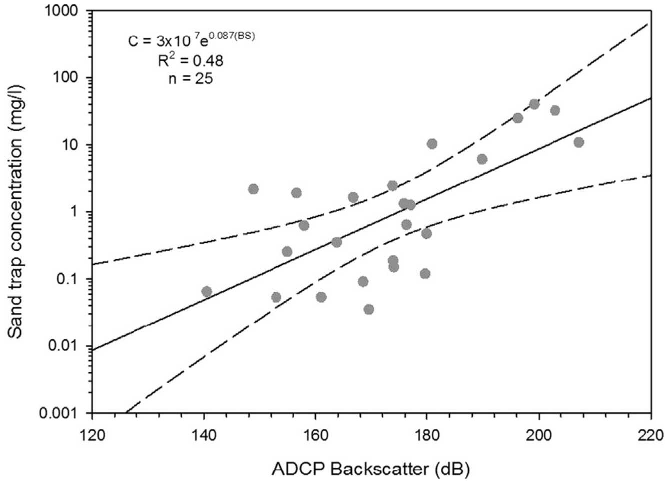

Fig. 6. The ADCP backscatter calibration showing the equation of the best fit line between the sand trap concentration (C) and ADCP backscatter (BS) with 95% confidence intervals.

column (w'_{up}) is equal to 1.56 times the root-mean-square vertical turbulent fluctuations (w'_{rms}), and (3) the root-mean-square vertical turbulent fluctuations (w'_{rms}) is 0.8 times the friction velocity, u_*. These assumptions result in a value of $w_s/u_* = 1.25$. Values of w'_{up} were extracted from the ADV and plotted against friction velocity in Fig. 8. The results from Stations 1 and 2 gave values higher than those of Bagnold (1966), as w_s/u_* is 1.41 and 1.36 respectively; those of Station 3, on the other hand, were lower with a value close to unity.

- The fourth method is based on the relationship between the movability number and the dimensionless grain diameter. According to Van Rijn (1993), the movability number, $w_s/u_* = D_*/\chi$ for $D_* < 10$ and it is constant when $D_* > 10$. The value of χ is defined as 4 by Van Rijn (1993). The movability number is plotted against the dimensionless grain diameter showing a positive correlation in Fig. 9. The values of χ for Stations 1, 2, and 3 are 4, 4.2, and 3.7 respectively. These values are similar to Van Rijn (1993) which supports the conclusion that the ratio varies in the vertical in proportion to the varying value of D_*. An average value of D_* was calculated for each station and divided by its corresponding χ in order to calculate w_s/u_* (Table 4).

The results varied between all the four methods. Methods 2 and 4 yielded similar values for Station 1; methods 2, 3, and 4 gave similar results for Station 2; and for Station 3, methods 2 and 4 yielded similar values. Method 1 yielded the lowest values of less than unity for all stations. Methods 2 and 4 yielded the movability number in the vertical. Note that benthic and epi-

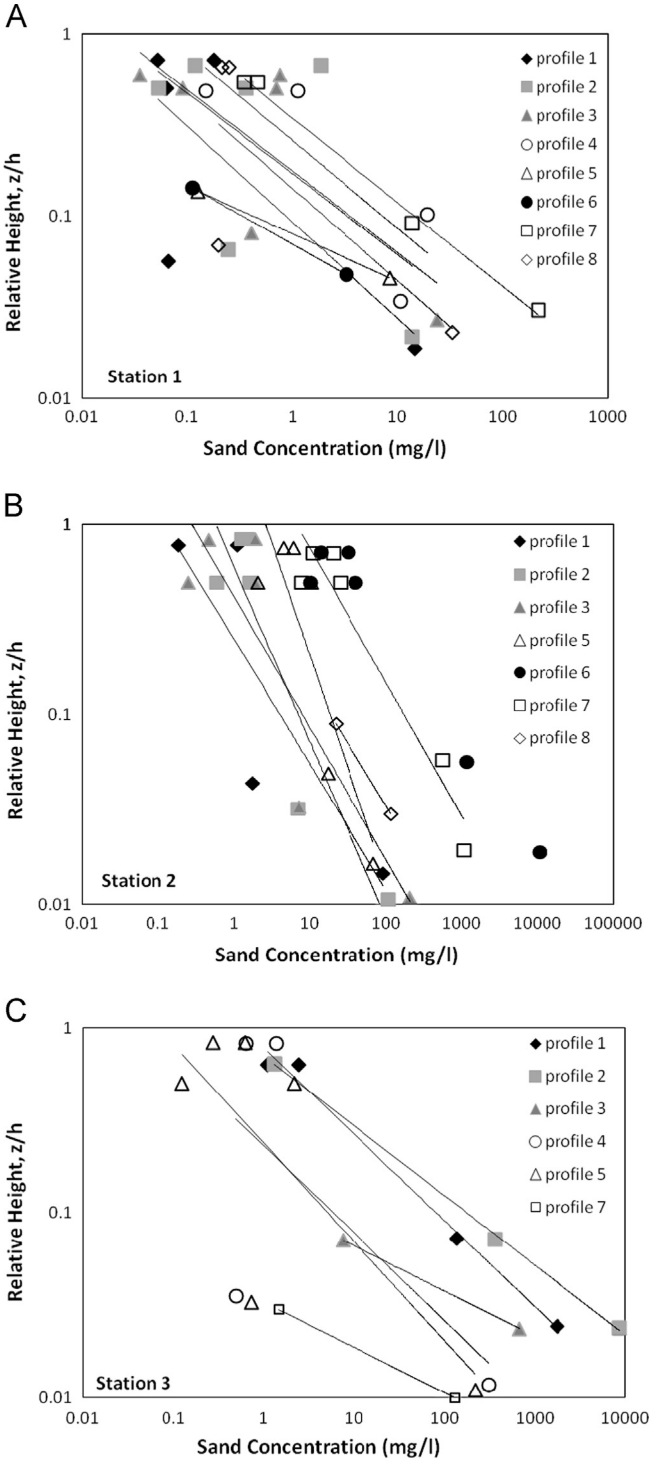

Fig. 7. Sand concentration profiles of (A) Station 1, (B) Station 2, and (C) Station 3 with relative height (z/h).

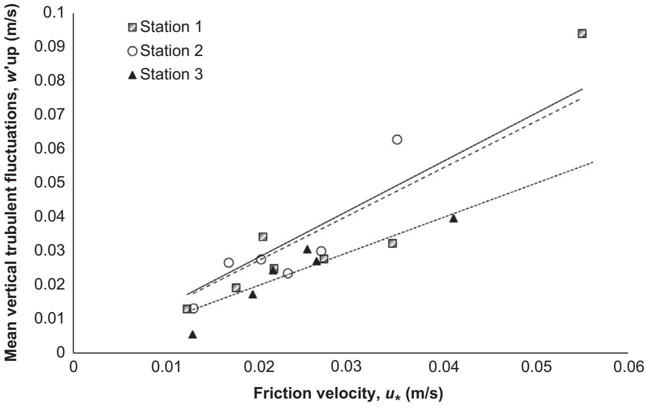

Fig. 8. The upward vertical turbulent eddies (w'_{up}) plotted against equivalent friction velocity (u_*) for all stations. Best fit line for Station 1 with equation $w'_{\mathrm{up}}/u_*=1.41$ ($r^2=0.82$) is shown as a solid line, for Station 2 ($w'_{\mathrm{up}}/u_*=1.36$; $r^2=0.71$) is shown as a dashed line and for Station 3 ($w'_{\mathrm{up}}/u_*=1.00$; $r^2=0.86$) is shown as a dotted line.

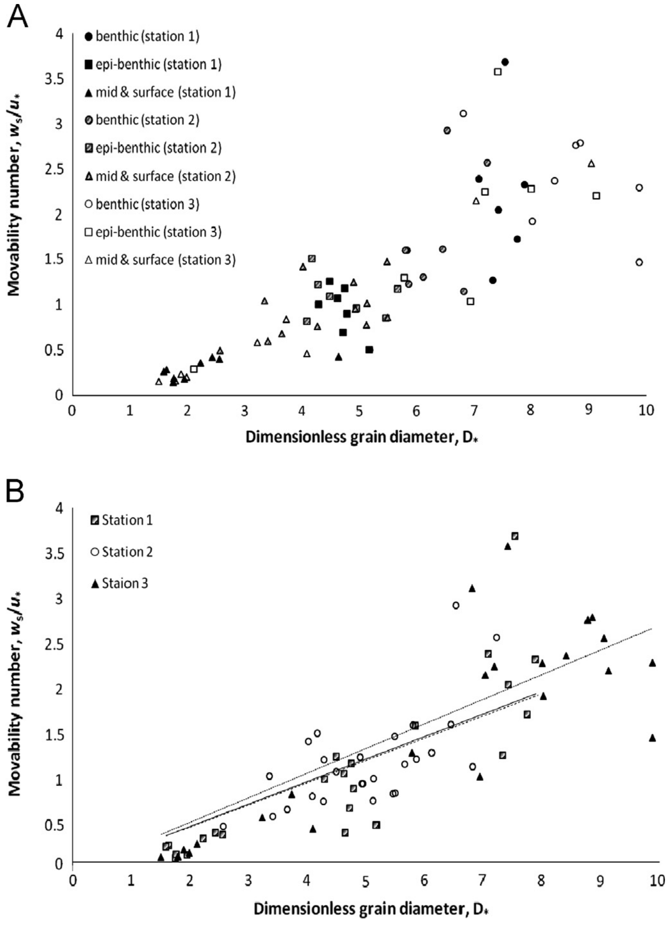

Fig. 9. The movability number (w_s/u_*) plotted against the dimensionless grain diameter (D_*) for all stations. (A) Benthic, epi-benthic, middle, and surface samples plotted individually to show the increase of the movability number with height above the bed and increasing grain size. (B) Best fit line of samples of all heights combined for Station 1 with equation $w_s/u_*=0.25D_*$ ($r^2=0.63$) is shown as a solid line, for Station 2 ($w_s/u_*=0.24D_*$; $r^2=0.40$) is shown as a dashed line and for Station 3 ($w_s/u_*=0.27D_*$; $r^2=0.69$) is shown as a dotted line.

benthic traps are within the estimated constant stress layer, where a constant u_* value is justified in the derivation. The middle and surface traps however, show reductions in this number perhaps reflecting that the bed u_* is higher than expected for the measured settling rate of suspended sand or that w_s/u_* is decreasing in the vertical as a function of decreasing dimensionless grain size (D_*) as described by Van Rijn (1993). In general, method 2 is preferred to calculate the movability number as it was based on direct measurements with fewer assumptions whilst providing information on vertical changes in this ratio. A further study is planned to examine the variation in u_* with height throughout a rough turbulent benthic boundary layer.

Table 4
Comparison of the movability number (w_s/u_*) obtained using four different methods: (1) based on measured profiles of sand concentration, (2) the laboratory direct measurements of the settling velocity (w_s) and friction velocity (u_*), (3) Bagnold's (1966) sand transport theory, and (4) the relationship between the movability number (w_s/u_*) and the dimensionless grain diameter D_*.

Method	**w_s/u_***					
	Station 1		**Station 2**		**Station 3**	
1	0.20 ± 0.02		0.32 ± 0.10		0.19 ± 0.03	
2	Surface	0.31	Surface	0.84	Surface	0.30
	Middle	0.27	Middle	1.09	Middle	1.86
	Epi-benthic	0.92	Epi-benthic	1.09	Epi-benthic	1.85
	Benthic	1.95	Benthic	1.78	Benthic	2.39
	Average	0.86 ± 0.78	Average	1.20 ± 0.40	Average	1.60 ± 0.90
3	1.41		1.36		1.00	
4	Surface	0.61	Surface	0.98	Surface	0.65
	Middle	0.48	Middle	1. 14	Middle	1.78
	Epi-benthic	1.17	Epi-benthic	1.13	Epi-benthic	1.80
	Benthic	1.75	Benthic	1.54	Benthic	2.34
	Average	1.00 ± 0.58	Average	1.20 ± 0.24	Average	1.64 ± 0.71

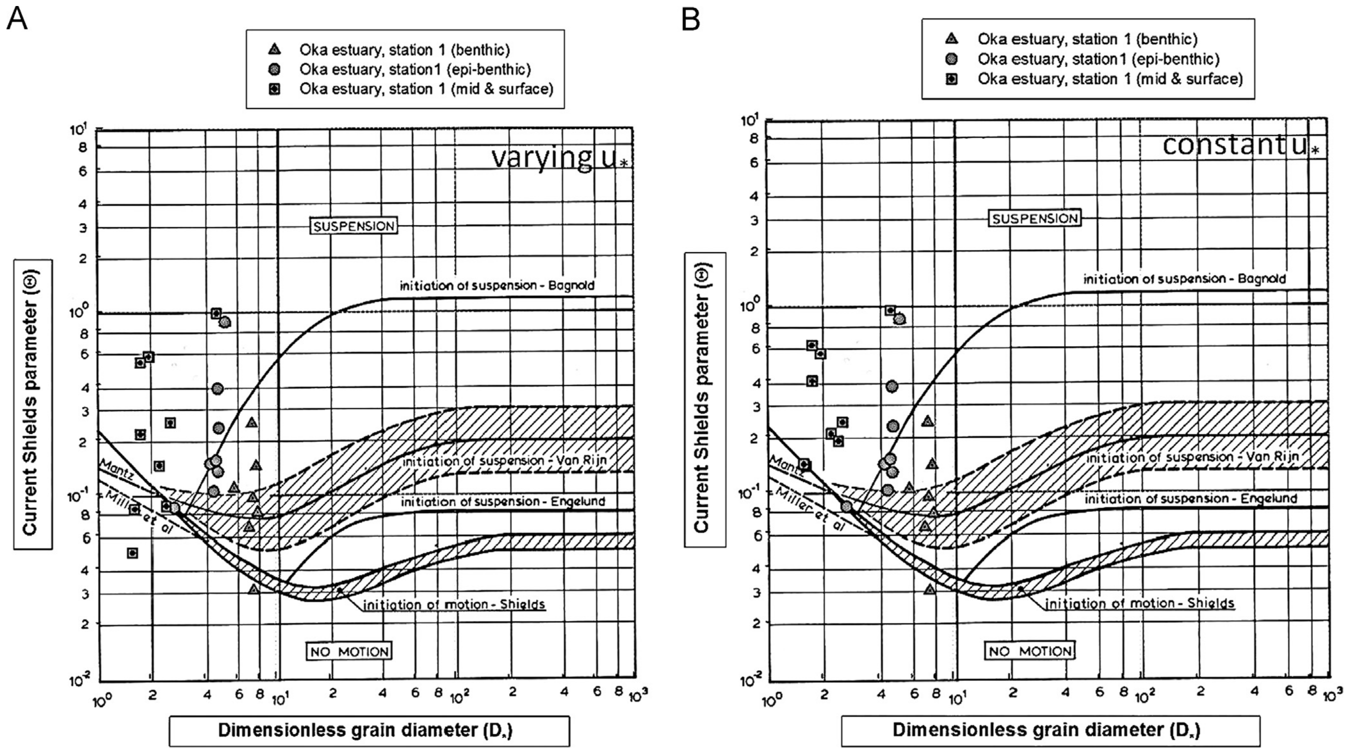

Fig. 10. The Shields parameter plotted against dimensionless grain diameter with varying (A) and constant (B) friction velocity for Station 1(modified from Van Rijn, 1993).

4.5. Shields parameter for suspension

The Shields parameter of each sample was plotted against its dimensionless grain diameter, D_*, on the Shield's diagram (after Van Rijn, 1993) in order to evaluate the published thresholds evident in Figs. 10–12. Two approaches were used to solve for the Shields parameter. The first is based on the assumption of a constant friction velocity in the vertical (u_*), taken from the level of the ADV measurements at $z=0.22$ m and the second assumed a varying friction velocity in the vertical (u_{*z}) following a linear decrease in shear stress with height above the bed:

$$u_{*z}^2 = \text{constant}; \quad z < 0.1\delta \tag{13a}$$

$$u_{*z}^2 = u_*^2\left(1 - \frac{z}{h - 0.1\delta}\right); \quad z > 0.1\delta \tag{13b}$$

Eq. (13b) is considered appropriate for *a* benthic boundary layer in a channel modified from Liu (2001). The resulting Shields parameters for each station were plotted on Figs. 10–12. All the benthic and epi-benthic data fall in the $4 < D_* < 10$ region, while most of the surface and middle data fall in the $2 < D_* < 4$. The suspension threshold of Bagnold (1966) appears to separate well bed load and suspended load in this study. For all stations, the Shields parameters derived from surface and mid-water traps fall above this threshold when a constant u_* is assumed but this is not the case when a depth varying u_* (using Eqs. (13a) and (13b)) is used. This could be a result of either underestimating the values of u_* in the vertical or is a verification of our initial assumption that u_* is in fact constant in the vertical. The values of the epi-benthic Shields parameters for Stations 1 and 2 straddle the suspension threshold of Bagnold (1966) suggesting a mixed population of bed load and suspended load (possibly saltation or intermittent suspension).

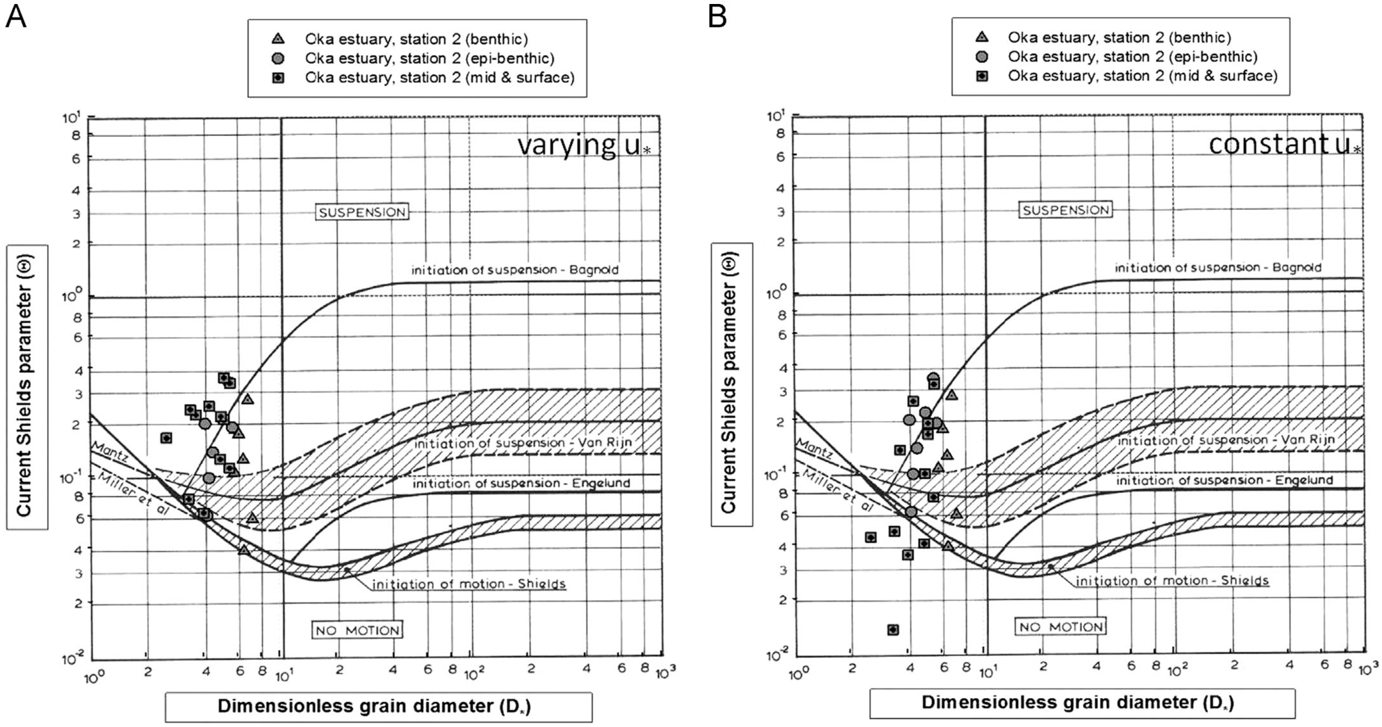

Fig. 11. The Shields parameter plotted against dimensionless grain diameter with varying (A) and constant (B) friction velocity for Station 2 (modified from Van Rijn, 1993).

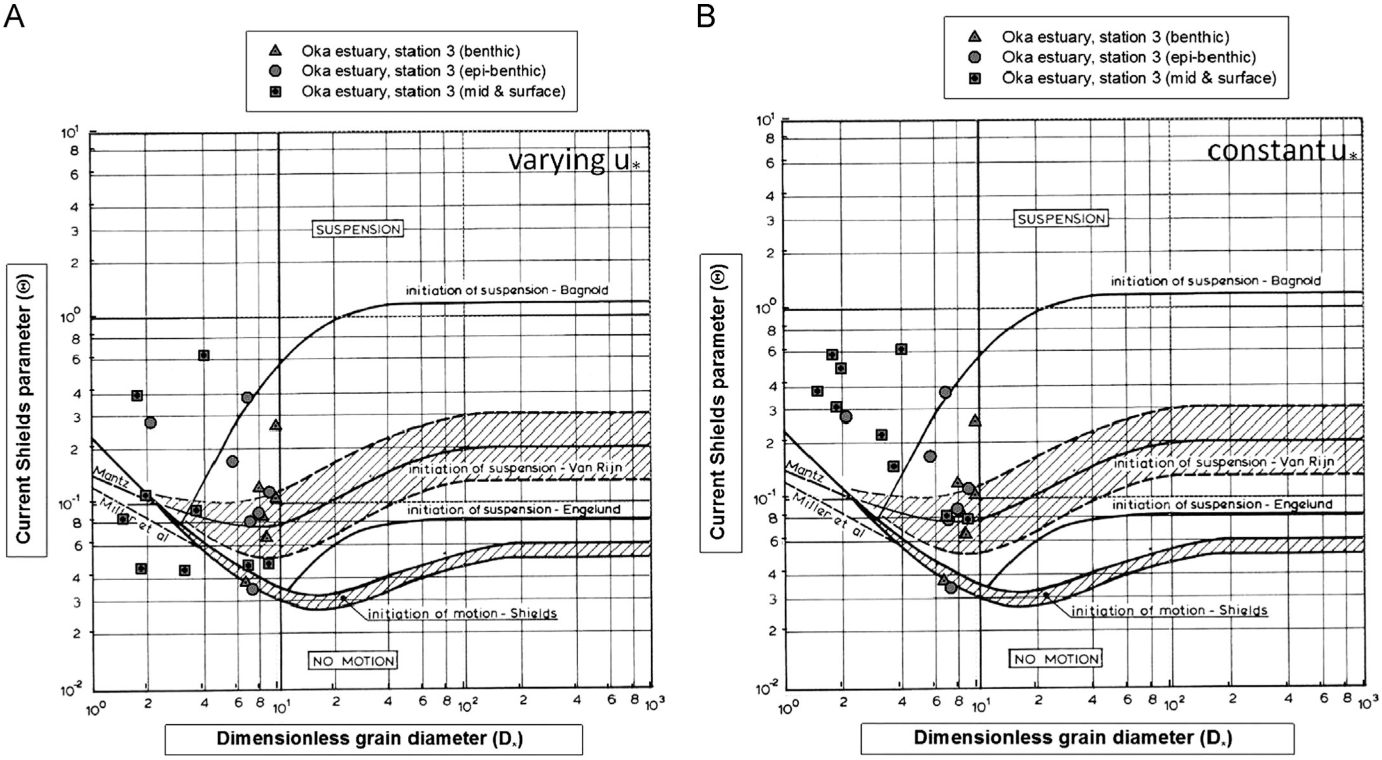

Fig. 12. The Shields parameter plotted against dimensionless grain diameter with varying (A) and constant (B) friction velocity for Station 3 (modified from Van Rijn, 1993).

The results from Station 3 appear to show that the epi-benthic load was below the suspension threshold and hence dominated by bed load (saltation). This is probably due to the coarse nature of the sand in transport (Table 2). The benthic Shields parameters fall between the thresholds for traction and suspension suggesting that the sediment transport at the height of this trap is dominated by bedload.

5. Conclusions

This paper reports on a field campaign to measure sand transport in a sandy tidal ria in northern Spain. It expands on previous work undertaken in Venice lagoon (on fine and very fine sand) by extending the range of grain sizes monitored for the suspension threshold and the applicability of the Rouse theory to coarse sand. The following are the major points of conclusion of this study.

Sand transport took place during the survey as both bedload and in suspension at all stations. Sand was mixed to the surface of the water column during peak flows. During periods of sand suspension, the grain size was considerably finer near the surface and coarser near the bed reflecting the fact that the settling velocity (w_s) was not constant in the vertical. This was evident at all stations and shows that predictions of a full concentration profile needs to consider a range of grain sizes, not just from the mean.

The values of the Rouse parameter confirmed that the sand transport in suspension was taking place throughout the benthic boundary layer. The D_* values for sand in suspension for the three stations were less than 10. This suggests that w_s/u_* is dependent on D_* and hence variable in time. This dependency had a value of $D_*/4$ which is close to the value suggested by Van Rijn (1993).

The Shields parameters derived from the field measurements defines the suspension thresholds better when friction velocity is assumed constant throughout the water column. This implies that the constant stress layer of the boundary layer is present to the surface.

Finally, the suspension threshold of Bagnold (1966) was found to discriminate best between bed load and suspended load measured in this study.

Acknowledgments

This project was completed by collaboration between the University of Southampton, The University of Basque Country UPV/EHU, and HR Wallingford. We wish to record our thanks to the great effort and team work of the people involved who were key parts of the study. Additional thanks goes to the extra helping hands in the field: Armando Guillarte (our boat skipper), Iván Absalón, and Iñigo Martínez de Alegría. Financial support for the field campaign was provided by the projects K-Egokitzen II (Basque Government, Etortek 2010) and Harea-Coastal Geology Group (Basque Government, 80IT365-10).

References

Amos, C.L., Umgiesser, G., Tosi, L., Townend, I.H., 2010a. The coastal morphodynamics of Venice lagoon, Italy: an introduction. Cont. Shelf Res. 30, 837–846.
Amos, C., Villatoro, M., Helsby, R., Thompson, C., Zaggia, L., Umgiesser, G., 2010b. The measurement of sand tranport in two inlets of Venice lagoon, Italy. Estuar., Coast. Shelf Sci. 87, 225–236.
Atkins, R., 2005. Sediment suspended by waves. Encycl. Coast. Sci., 850–853.
Bagnold, R.A., 1966. An approach to the sediment transport problem from general physics. U.S Geological Survey Professional Paper, 422-I. 37p.
Bonneville, R., 1963. Essais de synthese des lois debut d'entrainment des sediment sous l'action d'un courant en regime uniform, vol. 5. Bulletin Du CREC, Chatou.
Borja, Á., Collins, M., 2004. Preface. Elsevier Oceanogr. Ser. 70, v–viii.
Bowden, K.F., 1978. Physical problems of the benthic boundary layer. Geophys. Surv. 3, 255–296.
Cearreta, A., Irabien, M.J., Pascual, A., 2004. Human activities along the Basque coast during the last two centuries: geological perspective of recent anthropogenic impact on the coast and its environmental consequences. Elsevier Oceanogr. Ser. 70, 27–50.
Collins, M.B., Rigler, J.K., 1982. The use of settling velocity in defining the initiation of motion of heavy mineral grains, under unidirectional flow. Sedimentology 29, 419–426.
Engelund, F., 1965. A criterion for the occurrence of suspended load. La Houille Blanche 8, 7.
Helley, E.J., Smith, W., 1971. Development and calibration of a pressure difference-bedload sampler. USGS Water Resources Division Open File Report.
Helsby, R., 2008. Sand Transport in Northern Venice Lagoon Through the Tidal Inlet of Lido (Ph.D. Thesis). University of Southampton, Southampton, UK 260p.
Liria, P., Garel, E., Uriarte, A., 2009. The effects of dredging operations on the hydrodynamics of an ebb tidal delta: Oka Estuary, northern Spain. Cont. Shelf Res. 29, 1983–1994.
Liu, Z., 2001. Sediment Transport. Aalborg University, Aalborg, Denmark.
McCave, I.N., 1984. Size spectra and aggregation of suspended particles in the deep ocean. Deep Sea Res. Part A. Oceanogr. Res. Pap. 31, 329–352.
Monge-Ganuzas, M., 2008. Evolución Temporal de la Dinámica Sedimentaria en el estuario inferior del Oka (Reserva de la Biosfera de Urdaibai): Una Herramienta Geológica para la Gestión Integrada de Zonas Costeras (Ph.D. thesis). Universidad del Pais Vasco/UPV/EHU, Bilbao, Spain, 560 pp.
Monge-Ganuzas, M., Cearreta, A., Iriarte, E., 2008. Consequences of estuarine sand dredging and dumping on the Urdaibai Reserve of the Biosphere (Bay of Biscay): the case of the "Mundaka left wave". J. Iber. Geol. 34, 215–234.
Monge-Ganuzas, M., Cearreta, A., Evans, G., 2012. Morphodynamic consequences of dredging and dumping activities along the lower Oka estuary (Urdaibai Biosphere Reserve, south eastern Bay of Biscay, Spain). Ocean Coast. Mang. 77, 40–49.
Nielsen, P., 2009. Coastal and estuarine processes. Advanced Series on Ocean-Engineering, 29. World Scientific Publishing, Singapore 360p.
Rouse, H., 1937. Modern conceptions of the mechanics of turbulence. Trans. Am. Soc. Civil Eng. 102, 436–505.
Shields, A., 1936. Application of similarity principles and turbulence research to bed-load movement. Report 167, 26 pp.
Soulsby, R.L., 1980. Selecting record length and digitization rate for near-bed turbulence measurements. J. Phys. Oceanogr. 10, 208–219.
Soulsby, R.L., 1997. Dynamics of Marine Sands: A Manual for Practical Applications. Thomas Telford Publications, London 249p.
Thompson, C., Amos, C., Jones, T., Chaplin, J., 2003. The manifestation of fluid-transmitted bed shear stress in a smooth annular flume: a comparison of methods. J. Coast. Res. 19, 1094–1103.
Van Rijn, L., 1984. Sediment transport, Part I: bed-load transport. J. Hydraul. Eng. 110 (10), 1431–1456.
Van Rijn, L., 1993. Principles of Sediment Transport in Rivers, Estuaries, and Coastal Seas. Aqua Publications, The Netherlands 715p.
Van Rijn, L., 2011. Principles of Fluid Flow and Surface Waves in Rivers, Estuaries, and Coastal Seas. Aqua Publications, The Netherlands 900p.
Vianna, C., 2012. An Analysis of the use of ADCP in Estimating Sand Transport in a Tidal Inlet, Mundaka, Northern Spain (M.Sc. Dissertation). University of Southampton, UK, Inedit 80p.
Villatoro, M., Amos, C., Umgiesser, G., Ferrarin, C., Zaggia, L., Thompson, C., 2010. Sand transport measurements in Chioggia inlet, Venice lagoon: theory versus observations. Cont. Shelf Res. 30, 1000–1018.
Yalin, M.S., 1972. Mechanics of Sediment Transport. Pergamon Press, Oxford, New York 290p.
Yang, C.T., 1996. Sediment Transport, Theory and Practice. McGraw–Hill, New York 396p.

Appendix B

```
% Simplified code for smoothing the data using (smooth_average) function.

function [Y,Nsum,IND] = smooth_maverage(X,Fr,Fc,IND);
%SMOOTH_MAVERAGE   Smooths elements by moving average, ignoring NaN's.
%
%  Syntax:
%    [Y,Nsum,IND] = smooth_maverage(X,Fr,Fc,IND);
%
%  Input:
%    X   - Matrix with finite elements with/without Nan's.
%    Fr  - Window semi-length in the rows. A positive scalar (default 0).
%    Fc  - Window semi-length in the columns. A positive scalar (default
%          0).
%    IND - Indicates de linear index of the elements to be smoothed.
%          By default it smooths the NaN's elements.
%
%  Output:
%    Y    - X with the IND elements smoothed.
%    Nsum - Number of not NaN's elements that fixed on the moving window.
%           Provided to get a sum instead of a mean: Y(IND).*Nsum. Is a
%           vector of length equal as IND.
%    IND - Indicates de linear index of the elements that were smoothed.
%
%  Description:
%     This program interpolates the elements defined by IND or the NaN's
%     ones, by averaging it along with the surrounding elements that fit
%     on the little matrix of size (2Fr+1)x(2Fc+1) centered on it and
%     ignoring NaN's. It smooths also in the edges. If Fc is 0 or empty,
%     the smoothing will be done columnwise; rowwise with Fr is 0 or
%     empty. If Fc is not specified and X is a row vector, it will be
%     smoothed by Fr.
%
%  Example:
%     x = round(rand(5)*10)
```

```
%     IND = [1 13 23 24];
%     x([1 13 17 23]) = NaN
%     smooth_maverage(x,1)
%     smooth_maverage(x,1,0,IND)
%     smooth_maverage(x,2,2,IND)
%     smooth_maverage(x,1,1)
%     smooth_maverage(x,[],1)
%
%   See also NANMEAN on the Statistical Toolbox and NANMOVING_AVERAGE,
%   NANMOVING_AVERAGE2 by Carlos Vargas.

% Copyright 2008  Carlos Vargas, nubeobscura@hotmail.com
%     $Revision: 1.0 $  $Date: 2008/03/04 11:00:00 $
%   Written by
%   M. in S. Carlos Adrian Vargas Aguilera
%   Physical Oceanography PhD candidate
%   CICESE
%   Mexico,  march 2008
%   nubeobscura@hotmail.com
%   Download from:
%
http://www.mathworks.com/matlabcentral/fileexchange/loadAuthor.do?objec
tType=author&objectId=1093874

%% Errors checking
if ~nargin
 error('Interp2nanmovingaverage:Inputs','There are not inputs.')
end
if ndims(X)~=2
 error('Interp2nanmoving_average:Inputs','Entry must be a matrix.')
end
[M,N] = size(X);
if nargin<2 || isempty(Fr)
 Fr = 0;
end
```

```
if nargin<3 || isempty(Fc)
 Fc = 0;
 if M==1  % row vector?
  Fc = Fr;
  Fr = 0;
 end
end
if nargin<4 || isempty(IND)
 IND = 1:M*N; IND(~isnan(X(:))) = [];
 if isempty(IND)
  Y = X;
  return
 end
end

%% MAIN
Y = X;
Nind = length(IND);
ynans = repmat(NaN,2*Fr+1,2*Fc+1);
Ny = (2*Fr+1)*(2*Fc+1);
Nsum = repmat(NaN,Nind,1);
for k = 1:Nind
 [i,j] = ind2sub([M N],IND(k));
 rows = i-Fr:i+Fr; rowsi = ((rows>0)+(rows<M+1))>1;
 cols = j-Fc:j+Fc; colsi = ((cols>0)+(cols<N+1))>1;
 y = ynans;
 y(rowsi,colsi) = X(rows(rowsi),cols(colsi));
 nnan = ~isnan(y(:));
 Nsum(k)   = sum(  nnan);
 Y(IND(k)) = sum(y(nnan))/Nsum(k);
end
% Resize in order to get the sum by Y(IND).*Nsum:
Nsum = reshape(Nsum,size(Y(IND)));

% Carlos Adrian Vargas Aguilera. nubeobscura@hotmail.com
```

Appendix B

```
%%
% Simplified Matlab Code for the analysis of a single run from ADV
% Created by: Hachem Kassem, 01/12/2014
%           Ocean and Earth Science, University of Southampton,
%           National Oceanography Centre, Southampton
% ******************************************************************
% *****     ANALYSIS OF THE HYDRODYNAMICS                    *****
% ******************************************************************
%% General Information

clear all
close all
clc
%%

%setting default fonts so it looks Bang tidy!
set(0,'DefaultFigureWindowStyle','docked');
set(0,'defaulttextinterpreter','tex')
set(0,'DefaultTextFontname', 'Cambria','DefaultAxesFontName', 'Cambria')
set(0,'defaultaxesfontsize',12,'defaulttextfontsize',12);
set(0,'defaulttextfontweight','Demi');
set(0,'DefaultFigureColor', [1 1 1]);

%%
cd ('C:\Users\anar1e10\Desktop\Matlab Analysis File2\station1')  % change to
the right folder ALANOUD !! ;)
addpath('C:\Users\anar1e10\Desktop\Matlab Analysis File2\Functions');%
CHANGE TO THE
FOLDER WITH THE FUNCTIONS

%%
prompt={'Run Number'};

%name of the dialog box
name='Enter Run Number';
```

```
%number of lines visible for your input
numlines=1;

%the default answers
defaultanswer={ '1'};
options.Resize='on';
options.WindowStyle='modal';
options.Interpreter='tex';

%creates the dialog box. the user input is stored into a cell array
answer=inputdlg(prompt,name,numlines,defaultanswer,options);
Run.nb = str2num(answer{1});
%% Importing important parameters from header file:
clear answer prompt numlines name options defaultanswer
%%
headerdata_ADV1 = importfile_headerdata(uigetfile('multiselect', 'off', '*.hdr')) ;
%%
ADV1_headerdata.date = cell2mat(headerdata_ADV1(2,5));
ADV1_headerdata.StartTime_ADV1 = cell2mat(headerdata_ADV1(2,6));
ADV1_headerdata.EndTime_ADV1 = cell2mat(headerdata_ADV1(3,6));
ADV1_headerdata.Nbmeas_ADV1 = cell2mat(headerdata_ADV1(1,4));
ADV1_headerdata.Temp_ADV1= cell2mat(headerdata_ADV1(7, 2));
ADV1_headerdata.ADVsampling_rate =  cell2mat(headerdata_ADV1(4, 3));
ADV1_headerdata.Z_ADV1= cell2mat(headerdata_ADV1(6, 2));

save ADV1_headerdata.mat ADV1_headerdata
clear headerdata_ADV1

% text = sprintf('ADV data from Torcello Triple Junction' ADV1_headerdata.date
ADV1_headerdata.StartTime_ADV1 'to' ADV1_headerdata.EndTime_ADV1);
clc
%%
% String1 = string({'ADV data from Torcello Triple Junction, Venice Lagoon'
ADV1_headerdata.date 'Run' Run.nb ADV1_headerdata.StartTime_ADV1 'to'
ADV1_headerdata.EndTime_ADV1});
```

```
prompt={'Header for Images'};

%name of the dialog box
name='Enter general Header for Images';
%number of lines visible for your input
numlines=1;

%the default answers
defaultanswer={ 'ADV data from Torcello Triple Junction, Venice Lagoon'};

options.Resize='on';
options.WindowStyle='modal';
options.Interpreter='tex';

%creates the dialog box. the user input is stored into a cell array
answer=inputdlg(prompt,name,numlines,defaultanswer,options);
substring1 = (answer{1});

String1 = sprintf('%s; %s Run %d - %s to %s', ...
        substring1, ADV1_headerdata.date, Run.nb,
ADV1_headerdata.StartTime_ADV1, ADV1_headerdata.EndTime_ADV1);
delete answer prompt numlines name options

%% Getting ambient water parameters from header file _ADV1

openvar ('ADV1_headerdata');
%winopen('density&viscosity_calculator.xls')

%%
%GUI to prompt for important inputs
prompt={'Water Density \rho (kg/m^3)', 'Kinematic Viscosity \nu (m^2/s)'};

% to Calculate Density and viscosity use:
% EXCEL spreedsheet, available at: www.ifh.uni-
karlsruhe.de/science/.../density&viscosity_calculator.xls?
```

```
% by Karlsruhe, using equation of El-Dessouky, Ettouny (2002): Fundamentals
of Sea Water Desalination (Appendix A: Themodynamic Properties)

%name of the dialog box
name='Get user Input for ADV1 from Header File data';
%number of lines visible for your input
numlines=1;

%the default answers
defaultanswer={ '1014.6', '0.963E-6'};

options.Resize='on';
options.WindowStyle='modal';
options.Interpreter='tex';

%creates the dialog box. the user input is stored into a cell array
answer=inputdlg(prompt,name,numlines,defaultanswer,options);

Rho_ADV1 = str2num(answer{1}); % (kg/m^3); density of seawater at the given
temperature and salinity
kin_viscosity_ADV1 = str2num(answer{2});% kinematic viscosity of  water

kappa = 0.41;    % von Karmans constant

clear answer defaultanswer options prompt numlines name

Rho = Rho_ADV1;
rho = Rho;
%% -------------------------------------------------------
% **************************************
% START HERE
% **************************************
%%--------------------------------------------------------
%% Import data
% QUICK CHECK OF Compatibility of the trimmed records:
```

Appendix B

```
data_ADV1 = load(uigetfile('multiselect', 'on', '*.dat')) ;
dt = length(data_ADV1(1:end, 1))-1;
dt_min = dt./(25*60)
%%

t0 = 1; % start from first measurement, can change into 25*60 to ignore the
first minute!

% Getting velocity field for Master ADV - Higher     8 min is : 18975:30975
Xvel_adv1 = data_ADV1(t0:1+dt,3);          % cross-shore velocity
Yvel_adv1 = data_ADV1(t0:1+dt,4);          % long-shore velocity
Zvel_adv1 = data_ADV1(t0:1+dt,5);          % Z1 vertical velocity
Z2_adv1   = data_ADV1(t0:1+dt,6);          % Z2 vertical velocity; Not used in
analyses
corr_X_adv1  = data_ADV1(t0:1+dt,15);      % correlation on X
corr_Y_adv1  = data_ADV1(t0:1+dt,16);      % correlation on Y
corr_Z_adv1  = data_ADV1(t0:1+dt,17);      % correlation on Z1
corr_Z2_adv1 = data_ADV1(t0:1+dt,18);      % correlation on Z2

%%
ADVsampling_rate = 25;
% The threshold for correlation according to Elgar et al., 2005:
Corr_thresh = 0.3 + 0.4*sqrt(ADVsampling_rate./25)- 0.1;
%%
tic
% Get rid of bad velocity data for Master (ADV1)
index_1= corr_X_adv1(:,1)<(Corr_thresh*100); Xvel_adv1=Xvel_adv1(:,1);
Xvel_adv1(index_1)=NaN;  % 85% should normally be set as threshold for good
correlation
index_1= corr_Y_adv1(:,1)<(Corr_thresh*100); Yvel_adv1=Yvel_adv1(:,1);
Yvel_adv1(index_1)=NaN;
index_1= corr_Z_adv1(:,1)<(Corr_thresh*100); Zvel_adv1=Zvel_adv1(:,1);
Zvel_adv1(index_1)=NaN;
```

```
Ux_adv1 = Xvel_adv1; LengthUx_adv1 = length(Ux_adv1);      % raw streamwise velocity component, u along x-axis (along flume)
Vy_adv1 = Yvel_adv1; LengthVy_adv1 = length(Vy_adv1);      % raw crosswise velocity component, v along y-axis  (across/transverse flume)
Wz_adv1 = Zvel_adv1; LengthWz_adv1 = length(Wz_adv1);      % raw vertical velocity component, w along z-axis (vertical)

% percentage of removed values due to low correlations for Master (ADV1)
NaNArrayUx_adv1 = isnan(Ux_adv1);                          % check percentage of data removed by quality control
how_many_NaNsUx_adv1 = sum(sum(NaNArrayUx_adv1));
percentageNaNsUx_adv1 = 100*(how_many_NaNsUx_adv1)/LengthUx_adv1;

NaNArrayVy_adv1 = isnan(Vy_adv1);
how_many_NaNsVy_adv1 = sum(sum(NaNArrayVy_adv1));
percentageNaNsVy_adv1 = 100*(how_many_NaNsVy_adv1)/LengthVy_adv1;

NaNArrayWz_adv1 = isnan(Wz_adv1);
how_many_NaNsWz_adv1 = sum(sum(NaNArrayWz_adv1));
percentageNaNsWz_adv1 = 100*(how_many_NaNsWz_adv1)/LengthWz_adv1;

clc
[{'Correlation Threshold'} Corr_thresh*100]
[{'% BAD DATA'} {'X'} {'Y'} {'Z'}]
[percentageNaNsUx_adv1 percentageNaNsVy_adv1 percentageNaNsWz_adv1]

meanU_ADV1 = nanmean(sqrt((Ux_adv1.^2)+(Vy_adv1.^2)+(Wz_adv1.^2)));
[{'Ubar_ADV1_raw'} {'='} meanU_ADV1  {'m/s'}]

% this gives Ubar ~= 0.3737 m/s Run3

% at corr = 70%;
% '% BAD DATA'  'X'  'Y'  'Z' = %
clear ans
```

```
% at corr = 70%;
% '% BAD DATA'  'X'  'Y'  'Z' =  0.3975    0.3312    7.6184

%% Smoothing the data!
clc
% you need to have the function smooth_maverage in the same directory
% Download from:
%
http://www.mathworks.com/matlabcentral/fileexchange/loadAuthor.do?objec
%   tType=author&objectId=1093874

% Filling in the NaNs for Master ADV1
[Ux_smooth_ADV1] = smooth_maverage(Ux_adv1,5) ;  % no NANs left after
this!! this is like 1 Seconds
[Vy_smooth_ADV1] = smooth_maverage(Vy_adv1,7) ;  % filtered over 1 sec
[Wz_smooth_ADV1] = smooth_maverage(Wz_adv1,5) ;  % filtered over 1 sec

NaNArrayUx_smooth_ADV1 = isnan(Ux_smooth_ADV1);
how_many_NaNsUx_smooth_ADV1 = sum(sum(NaNArrayUx_smooth_ADV1));
percentageNaNsUx_smooth_ADV1 =
100*(how_many_NaNsUx_smooth_ADV1)/length(Ux_adv1);

NaNArrayVy_smooth_ADV1 = isnan(Vy_smooth_ADV1);
how_many_NaNsVy_smooth_ADV1 = sum(sum(NaNArrayVy_smooth_ADV1));
percentageNaNsVy_smooth_ADV1 =
100*(how_many_NaNsVy_smooth_ADV1)/length(Vy_adv1);

NaNArrayWz_smooth_ADV1 = isnan(Wz_smooth_ADV1);
how_many_NaNsWz_smooth_ADV1 = sum(sum(NaNArrayWz_smooth_ADV1));
percentageNaNsWz_smooth_ADV1 =
100*(how_many_NaNsWz_smooth_ADV1)/length(Wz_adv1);

[{'Correlation Threshold'} Corr_thresh*100]
[{'% BAD DATA'} {'X'} {'Y'} {'Z'}]
```

```
[percentageNaNsUx_smooth_ADV1 percentageNaNsVy_smooth_ADV1
percentageNaNsWz_smooth_ADV1 ]

%% axes rotations
[U_ADV1,V_ADV1,W_ADV1] =
axis_rotate(Ux_smooth_ADV1,Vy_smooth_ADV1,Wz_smooth_ADV1);
meanU_ADV1_rotated = mean(sqrt((U_ADV1.^2)+(V_ADV1.^2)+(W_ADV1.^2)));

Vel.ADV1.meanU_ADV1 = meanU_ADV1;
Vel.ADV1.meanU_ADV1_rotated = meanU_ADV1_rotated;
Vel.ADV1.U_ADV1 = U_ADV1;
Vel.ADV1.V_ADV1 = V_ADV1;
Vel.ADV1.W_ADV1 = W_ADV1;

save Vel.mat Vel

%% MEAN Vel

[{'Ubar_ADV1_raw'} {'='} meanU_ADV1  {'m/s'}]
[{'Ubar_ADV1_smooth/rot'} {'='} meanU_ADV1_rotated {'m/s'}]
std_Ubarraw = nanstd((sqrt((Ux_adv1.^2)+(Vy_adv1.^2)+(Wz_adv1.^2))))
std_Ubarsmooth =  std((sqrt((U_ADV1.^2)+(V_ADV1.^2)+(W_ADV1.^2))))

% Ubar_ADV1_raw = 0.0331 m/s Run8

% smoothing after filtering at 60% then rotate axis gives: mean U = 0.0323
% m/s Run4

%% Two Initial Plots:

dt_trimmed = length(Xvel_adv1(1:end, 1))-1;

t = 1:1:dt_trimmed +1;
t = t./(60.*ADVsampling_rate);              % 60 x 25 Hz = 1500
t = t';
```

Appendix B

```
% Figure 1 - To show the 'bad data' that was smoothed

figure(1), clf
set(gcf,'Color',[1,1,1]);

subplot(311),
plot(t, Ux_smooth_ADV1 , '-', 'Color', rgb('tomato'), 'LineWidth', 1.5); hold on
plot(t, Ux_adv1, '-', 'Color', rgb('dodgerblue')), hold off
ylabel('Streamwise velocity, U_x (m/s)','FontWeight','demi','FontSize',11); grid on
xlabel('Time (minutes)','FontWeight','demi','FontSize',11);
title('Streamwise velocity component U,
(m/s)','FontWeight','demi','FontSize',12);
axis([0 max(t) -0.2 0.2])
legend ('smoothed', 'raw')

subplot(312), plot(t, Vy_smooth_ADV1,'-', 'Color', rgb('tomato')); hold on
plot(t,Vy_adv1, '-', 'Color',rgb('lightseagreen')), hold off
ylabel('Crosswise velocity, V_y (m/s)','FontWeight','demi','FontSize',11); grid on
xlabel('Time (minutes)','FontWeight','demi','FontSize',11);
title('Crosswise velocity component V, (m/s)','FontWeight','demi','FontSize',12);
axis([0 max(t) -0.5 0.2])

subplot(313), plot(t, Wz_smooth_ADV1,'-', 'Color', rgb('tomato')); hold on
plot(t,Wz_adv1, '-', 'Color', rgb('darkslateblue')); hold off
ylabel('Vertical velocity, W_z (m/s)','FontWeight','demi','FontSize',11); grid on
xlabel('Time (minutes)','FontWeight','demi','FontSize',11);
title('vertical velocity component W, (m/s)','FontWeight','demi','FontSize',12);
axis([0 max(t) -0.2 0.2])

annotation(figure(1),'textbox',[0.1303 0.955 0.65 0.04],...
   'String',{String1},'FitBoxToText','off');

%%
```

```
% Figure 2 - To show smoothed and axis rotated data
figure(2), clf
set(gcf,'Color',[1,1,1]);

axes1 = axes('Parent', figure(2), 'Position',[0.13 0.708 0.57 0.216]); box(axes1,
'on'),
plot(t, U_ADV1, '-', 'Color', rgb('Blue'));axis([0 max(t) -0.2 0.2])
ylabel(' U_x (m/s)','FontWeight','demi','FontSize',11); grid on, hold on
% xlabel('Time (minutes)','FontWeight','demi','FontSize',11);
y1 = (ones(1, length(t))*std(U_ADV1))+abs(mean(U_ADV1));
plot (t, y1, 'LineWidth', 1 ,'Color', rgb('orangered'),'LineStyle','--'); hold on
plot (t, -y1, 'LineWidth', 1, 'Color', rgb('orangered'),'LineStyle','--'); hold off
title('Smoothed and axis-rotated velocity component
(m/s)','FontWeight','demi','FontSize',12);

axes2 = axes('Parent',figure(2),'YTickLabel','','Position',[0.72 0.708 0.2
0.216],...
   'CLim',[1 2]);
hist(U_ADV1,20,-1:1), title('Histogram','FontWeight','demi','FontSize',12);
set(gca,'YTickLabel',[]); xlim([-0.2 0.2]);
h = findobj(gca,'Type','patch'); set(h,'FaceColor',rgb('Blue'),'EdgeColor','w');
box on,

%
axes3 = axes('Parent', figure(2), 'Position',[0.13 0.434 0.57 0.216]); box(axes3,
'on'),
plot(t, V_ADV1,'-', 'Color', rgb('green')); hold on
ylabel(' V_y (m/s)','FontWeight','demi','FontSize',11); grid on
axis([0 max(t) -0.2 0.2])
y2 = ones(1, length(t))*std(V_ADV1)+abs(mean(V_ADV1));
plot (t, y2, 'LineWidth', 1 ,'Color', rgb('orangered'),'LineStyle','--'); hold on
plot (t, -y2, 'LineWidth', 1, 'Color', rgb('orangered'),'LineStyle','--'); hold off

axes4 = axes('Parent',figure(2),'YTickLabel','','Position',[0.72 0.434 0.2
0.216],...
```

```
    'CLim',[1 2]);
hist(V_ADV1,20,-1:1),
set(gca,'YTickLabel',[]); xlim([-0.2 0.2]);
h = findobj(gca,'Type','patch'); set(h,'FaceColor',rgb('green'),'EdgeColor','w');
box on,
%
axes5 = axes('Parent', figure(2), 'Position',[0.13 0.16 0.57 0.216]); box(axes5,
'on'),
plot(t, W_ADV1,'-', 'Color', rgb('black')); hold on
ylabel(' W_z (m/s)','FontWeight','demi','FontSize',11); grid on
xlabel('Time (minutes)','FontWeight','demi','FontSize',11);
axis([0 max(t) -0.2 0.2])
y3 = ones(1, length(t))*std(W_ADV1)+abs(mean(W_ADV1));;
plot (t, y3, 'LineWidth', 1 ,'Color', rgb('orangered'),'LineStyle','--'); hold on
plot (t, -y3, 'LineWidth', 1, 'Color', rgb('orangered'),'LineStyle','--'); hold off

axes6 = axes('Parent',figure(2),'YTickLabel','','Position',[0.72 0.16 0.2 0.216],...
    'CLim',[1 2]);
hist(W_ADV1,20,-1:1),
set(gca,'YTickLabel',[]); xlim([-.2 .2]);
h = findobj(gca,'Type','patch'); set(h,'FaceColor',rgb('black'),'EdgeColor','w');
box on,
xlabel('Velocity (m/s)','FontWeight','demi','FontSize',11);

%
annotation(figure(2),'textbox',[0.13 0.96 0.65 0.04],...
  'String',{String1},'FitBoxToText','off');

%%
statU.mean_U_ADV1 = mean(U_ADV1), statU.Stdev_U_ADV1= std(U_ADV1),
statU.Skew_U_ADV1= skewness(U_ADV1), statU.Kurt_U_ADV1=
kurtosis(U_ADV1);
statV.mean_V_ADV1 = mean(V_ADV1), statV.Stdev_V_ADV1= std(V_ADV1),
statV.Skew_V_ADV1 = skewness(V_ADV1), statV.Kurt_V_ADV1=
kurtosis(V_ADV1);
```

```
statW.mean_W_ADV1 = mean(W_ADV1), statW.Stdev_W_ADV1= std(W_ADV1),
statW.Skew_W_ADV1 = skewness(W_ADV1), statW.Kurt_W_ADV1=
kurtosis(W_ADV1);

%%

String_statU = sprintf('%s %2.2f %c %2.2f m/s \n Skew = %2.2f \n kurt = %2.2f',
'Mean=', statU.mean_U_ADV1, char(177), statU.Stdev_U_ADV1,
statU.Skew_U_ADV1, statU.Kurt_U_ADV1);
String_statV = sprintf('%s %2.2f %c %2.2f m/s \n Skew = %2.2f \n kurt = %2.2f',
'Mean=', statV.mean_V_ADV1, char(177), statV.Stdev_V_ADV1,
statV.Skew_V_ADV1, statV.Kurt_V_ADV1);
String_statW = sprintf('%s %2.2f %c %2.2f m/s \n Skew = %2.2f \n kurt = %2.2f',
'Mean=', statW.mean_W_ADV1, char(177), statW.Stdev_W_ADV1,
statW.Skew_W_ADV1, statW.Kurt_W_ADV1);

%%
annotation(figure(2),'textbox',[0.717 0.837 0.35 0.09],'String',{String_statU},...
   'FontWeight','light','FitBoxToText','off','LineStyle','none', 'FontSize', 10);

annotation(figure(2),'textbox', [0.717 0.563 0.35 0.09],'String',{String_statV},...
   'FontWeight','light','FitBoxToText','off','LineStyle','none', 'FontSize', 10);

annotation(figure(2),'textbox',[0.717 0.289 0.35 0.09],'String',{String_statW},...
   'FontWeight','light','FitBoxToText','off','LineStyle','none', 'FontSize', 10);

%% Detrending Reynold's Decomposition

% Calculate the zero-mean flow component time-series (waves + turbulence)
% This is in essense a Reynolds decomposition.
U_M_ADV1 = U_ADV1 - mean(U_ADV1);
V_M_ADV1 = V_ADV1 - mean(V_ADV1);
W_M_ADV1 = W_ADV1 - mean(W_ADV1);

% Now de-trend, linearly, the u, v, w time-series (waves + turbulence)
```

```
u_M_ADV1 = detrend(U_M_ADV1,'linear');    % streamwise velocity fluctuation,
i.e. streamwise turbulence component
v_M_ADV1 = detrend(V_M_ADV1,'linear');    % crosswise velocity fluctuation, i.e.
crosswise turbulence component
w_M_ADV1 = detrend(W_M_ADV1,'linear');    % vertical velocity fluctuation, i.e.
vertical turbulence component

% Apply moving average as low pass filter, then remove the moving
% average from the original wave form to obtain high-frequency turbulence
% This is a zero-phase, forward and reverse digital filter which ensures
% zero-distortion.

  a=1; b=(ones(1,5))/5;   % a=1; % b=(ones(1,9))/9;
  u_wave_M_ADV1 = filtfilt(b,a,u_M_ADV1);
  u_turb_M_ADV1 = u_M_ADV1 - u_wave_M_ADV1;

  v_wave_M_ADV1 = filtfilt(b,a,v_M_ADV1);
  v_turb_M_ADV1 = v_M_ADV1 - v_wave_M_ADV1;

  w_wave_M_ADV1 = filtfilt(b,a,w_M_ADV1);
  w_turb_M_ADV1 = w_M_ADV1 - w_wave_M_ADV1;

%% Exclude outliers using Nobuhito Mori's code
tic
% Despiking the wave signal

[Uwave_ADV1,Vwave_ADV1,Wwave_ADV1,ipwave_ADV1]=func_despike_phases
pace3d_3var(u_wave_M_ADV1, v_wave_M_ADV1, w_wave_M_ADV1, 2);
[U2_ADV1,V2_ADV1,W2_ADV1,ip]=func_despike_phasespace3d_3var(u_turb_M_
ADV1, v_turb_M_ADV1, w_turb_M_ADV1, 2);

u_prime_ADV1 = U2_ADV1; v_prime_ADV1 = V2_ADV1; w_prime_ADV1 =
W2_ADV1;

fluctuations_ADV1.u_prime_ADV1 = u_prime_ADV1(1:end, :);
```

```
fluctuations_ADV1.v_prime_ADV1 = v_prime_ADV1(1:end, :);
fluctuations_ADV1.w_prime_ADV1 = w_prime_ADV1(1:end, :);

toc
save fluctuations_ADV1.mat fluctuations_ADV1;

%%
% Figure 3 - After De-spiking
figure(3), clf
set(gcf,'Color',[1,1,1]);

axes1 = axes('Parent', figure(3), 'Position',[0.13 0.708 0.57 0.216]); box(axes1,
'on'),
plot(t, u_prime_ADV1, '-', 'Color', rgb('Blue'));axis([0 max(t) -0.05 0.05])
ylabel(' u'' (m/s)','FontWeight','demi','FontSize',11); grid on, hold on
% xlabel('Time (minutes)','FontWeight','demi','FontSize',11);
y1 = ones(1, length(t))*std(u_prime_ADV1)+abs(mean(u_prime_ADV1));
plot (t, y1, 'LineWidth', 1 ,'Color', rgb('orangered'),'LineStyle','--'); hold on
plot (t, -y1, 'LineWidth', 1, 'Color', rgb('orangered'),'LineStyle','--'); hold off
title('Fluctuating Turbulence component
(m/s)','FontWeight','demi','FontSize',12);

legend('u''', '\pm 1.0 \sigma_d_e_v');

axes2 = axes('Parent',figure(3),'YTickLabel','','Position',[0.72 0.708 0.2
0.216],...
   'CLim',[1 2]);
hist(U_ADV1,20,-1:1), title('Histogram','FontWeight','demi','FontSize',12);
set(gca,'YTickLabel',[]); xlim([-0.1 0.1]);
h = findobj(gca,'Type','patch'); set(h,'FaceColor',rgb('Blue'),'EdgeColor','w');
box on,
%
axes3 = axes('Parent', figure(3), 'Position',[0.13 0.434 0.57 0.216]); box(axes3,
'on'),
plot(t, v_prime_ADV1,'-', 'Color', rgb('green')); hold on
```

```
ylabel(' v'' (m/s)','FontWeight','demi','FontSize',11); grid on
% xlabel('Time (minutes)','FontWeight','demi','FontSize',11);
axis([0 max(t) -0.05 0.05])
y2 = ones(1, length(t))*std(v_prime_ADV1)+abs(mean(v_prime_ADV1));
plot (t, y2, 'LineWidth', 1 ,'Color', rgb('orangered'),'LineStyle','--'); hold on
plot (t, -y2, 'LineWidth', 1, 'Color', rgb('orangered'),'LineStyle','--'); hold off
legend('v'''),
axes4 = axes('Parent',figure(3),'YTickLabel','','Position',[0.72 0.434 0.2
0.216],...
    'CLim',[1 2]);
hist(v_prime_ADV1,20,-1:1),
set(gca,'YTickLabel',[]); xlim([-0.05 0.05]);
h = findobj(gca,'Type','patch'); set(h,'FaceColor',rgb('green'),'EdgeColor','w');
box on,

%
axes5 = axes('Parent', figure(3), 'Position',[0.13 0.16 0.57 0.216]); box(axes5,
'on'),
plot(t, w_prime_ADV1,'-', 'Color', rgb('black')); hold on
ylabel(' w'' (m/s)','FontWeight','demi','FontSize',11); grid on
xlabel('Time (minutes)','FontWeight','demi','FontSize',11);
axis([0 max(t) -0.05 0.05])
y3 = ones(1, length(t))*std(w_prime_ADV1)+abs(mean(w_prime_ADV1));
plot (t, y3, 'LineWidth', 1 ,'Color', rgb('orangered'),'LineStyle','--'); hold on
plot (t, -y3, 'LineWidth', 1, 'Color', rgb('orangered'),'LineStyle','--'); hold off
legend('w'''),

axes6 = axes('Parent',figure(3),'YTickLabel','','Position',[0.72 0.16 0.2 0.216],...
    'CLim',[1 2]);
hist(w_prime_ADV1,20,-1:1),
set(gca,'YTickLabel',[]); xlim([-.05 .05]);
h = findobj(gca,'Type','patch'); set(h,'FaceColor',rgb('black'),'EdgeColor','w');
box on,
xlabel('Velocity (m/s)','FontWeight','demi','FontSize',11);
```

```
annotation(figure(3),'textbox',[0.13 0.96 0.65 0.04],...
    'String',{String1}, 'FitBoxToText','off');

%%
clc; statu.mean_u_prime_ADV1 = mean(u_prime_ADV1),
statu.Stdev_u_prime_ADV1= std(u_prime_ADV1),statu.Skew_u_prime_ADV1 =
skewness(u_prime_ADV1), statu.Kurt_u_prime_ADV1= kurtosis(u_prime_ADV1),
clc; statv.mean_v_prime_ADV1 = mean(v_prime_ADV1),
statv.Stdev_v_prime_ADV1= std(v_prime_ADV1),statv.Skew_v_prime_ADV1 =
skewness(v_prime_ADV1), statv.Kurt_v_prime_ADV1= kurtosis(v_prime_ADV1),
clc; statw.mean_w_prime_ADV1 = mean(w_prime_ADV1),
statw.Stdev_w_prime_ADV1= std(w_prime_ADV1),statw.Skew_w_prime_ADV1 =
skewness(w_prime_ADV1), statw.Kurt_w_prime_ADV1=
kurtosis(w_prime_ADV1),
%%
String_statu = sprintf('%s %2.2f %c %2.2f m/s \n Skew = %2.2f \n kurt = %2.2f',
'Mean=', statu.mean_u_prime_ADV1, char(177), statu.Stdev_u_prime_ADV1,
statu.Skew_u_prime_ADV1, statu.Kurt_u_prime_ADV1);
String_statv = sprintf('%s %2.2f %c %2.2f m/s \n Skew = %2.2f \n kurt = %2.2f',
'Mean=', statv.mean_v_prime_ADV1, char(177), statv.Stdev_v_prime_ADV1,
statv.Skew_v_prime_ADV1, statv.Kurt_v_prime_ADV1);
String_statw = sprintf('%s %2.2f %c %2.2f m/s \n Skew = %2.2f \n kurt = %2.2f',
'Mean=', statw.mean_w_prime_ADV1, char(177), statw.Stdev_w_prime_ADV1,
statw.Skew_w_prime_ADV1, statw.Kurt_w_prime_ADV1);

%%
annotation(figure(3),'textbox',[0.717 0.837 0.35 0.09],'String',{String_statu},...
   'FontWeight','light','FitBoxToText','off','LineStyle','none', 'FontSize', 10);

annotation(figure(3),'textbox', [0.717 0.563 0.35 0.09],'String',{String_statv},...
   'FontWeight','light','FitBoxToText','off','LineStyle','none', 'FontSize', 10);

annotation(figure(3),'textbox',[0.717 0.289 0.35 0.09],'String',{String_statw},...
   'FontWeight','light','FitBoxToText','off','LineStyle','none', 'FontSize', 10);
```

Appendix B

```
%% Figure 4_ Instantaneous Stuff:

TKE_ADV1 =
0.5*1000*(sqrt((u_prime_ADV1.^2)+(v_prime_ADV1.^2)+(w_prime_ADV1.^2)));
mean_TKE_ADV1 = mean(TKE_ADV1)
std_TKE_ADV1 = std(TKE_ADV1)
Taw_bedtke_ADV1 = 0.19*mean(TKE_ADV1)
u_star_ADV1 = sqrt(Taw_bedtke_ADV1./1000)

figure(4); clf
subplot(3,1,1); plot(t, u_prime_ADV1, 'Color', rgb('blue'), 'LineWidth', 1); hold
on,
plot(t, v_prime_ADV1, 'Color', rgb('green')); hold on
plot(t, w_prime_ADV1, 'Color', rgb('black')); hold off
ylabel('u^,_i (m/s)', 'FontWeight', 'Demi'); xlim([0, max(t)]); ylim([-0.05 0.05]);
legend ('u''', 'v''', 'w''');
a=axes; set(a,'xticklabel',[]);
hold off
subplot(3,1,2); plot(t, TKE_ADV1, 'Color', rgb('blue'), 'LineWidth', 1); xlim([0,
max(t)]); hold on,
ylabel('TKE, \it{k} \rm \bf{(m^2/s^2)}', 'FontWeight', 'Demi')
subplot(3,1,3); plot(t, -u_prime_ADV1.*w_prime_ADV1, 'Color', rgb('black'),
'LineWidth', 1);  xlim([0, max(t)]); ylim([-5E-4 5E-4]);
ylabel('-u^,_Mw^,_M', 'FontWeight', 'Demi')
xlabel ('Time (min)','FontWeight', 'Demi');
annotation(figure(4),'textbox',[0.13 0.93 0.65 0.04],...
    'String',{String1},'FitBoxToText','off');
%%
String_Stress = sprintf('mean(TKE)= %2.2f %c %2.2f m^2/s^2 \n \\tau _0,_T_K_E
= %2.2f Pa \n u^* = %2.2f m/s', mean_TKE_ADV1, char(177), std_TKE_ADV1,
Taw_bedtke_ADV1, u_star_ADV1);

annotation(figure(4),'textbox',...
   [0.705 0.55 0.2 0.067],'String',{String_Stress},'HorizontalAlignment','right',...
   'FontWeight','demi','FontSize',11, 'FitBoxToText','off','LineStyle','none');
```

List of References

Absi, R. 2010. Concentration profiles for fine and coarse sediments suspended by waves over ripples: An analytical study with the 1-DV gradient diffusion model. Advances in Water Resources, 33: 411-418.

Adams, C.E. and Weatherly, G.L. 1981. Suspended-sediment transport and benthic boundary layer dynamics. Marine Geology, 42: 1-18.

Agrawal, Y. and Traykovski, P. 2001. Particles in the bottom bounday layer: concentration and size dynamics. Journal of Geophysical Research, 106: 9533-9542.

Ali, A. and Lemckert, C. 2009. A traversing system to measure bottom boundary layer hydraulic properties. Estuarince, Coastal and Shelf Science, 83: 425-433.

Allen, J.R. and Friend, P. 1976. Relaxation time of dunes in decelerating aqueous flows. Journal of Geological Society, 132: 17-26.

Al-Ragum, A., Monge-Ganuzas, M., Amos, A., Cearretta, A., Townend, I., and Manca, E. 2014. An evaluation of teh Rouse theory for sand transport in the Oka estuary, Spain. Continental Shelf Research, 78: 39-50.

Amos, C.L., Li, M.Z., and Sutherland, T.F. 1998. The contribution of ballistic momentum flux to the erosion of cohesive beds by flowing water. Journal of Coastal Research, 14(2): 564-569.

Amos, C. L., Umgiesser, G., Tosi, L., and Townend, I.H. 2010a. The coastal morphodynamics of Venice lagoon, Italy: An introduction. Continental Shelf Research, 30: 837-846.

Amos, C., Villatoro, M., Helsby, R., Thompson, C., Zaggia, L., and Umgiesser, G. 2010b. The measurement of sand tranport in two inlets of Venice lagoon, Italy. Estuarine, Coastal and Shelf Science, 87: 225 – 236.

Atkins, R. 2005. Sediment suspended by waves. Encyclopedia of Coastal Science: 850-853.

Bibliography

Austin, M.J., Masselink, G., O'Hare, T.J., and Russell, P.E. 2007. Relaxation time effects of wave ripples on tidal beaches. Geophysical Research Letters, 32: L16606

Bagherimiyab, F. and Lemmin, U. 2013. Shear velocity estimates in rough-bed open-channel flow. Earth Surface Processes and Landforms, 11 pp.

Bagnold, R.A. 1956. The flow of cohesionless grains in fluids. Philosophical Transactions of the Royal Society of London 249: 235-297.

Bagnold, R.A., 1966. An approach to the sediment transport problem from general physics. U.S Geological Survey Professional Paper, 422-I. 37 pp.

Bailey, S.C.C., Valikivi, M., Hultmark, M., and Smits, A.J., 2014. Estimating the value of von Karman's constant in turbulent pipe flow. Journal of Fluid Mechanics, 749:79 – 98.

Bolaños, R., Thorne, P. D. & Wolf, J. 2012. Comparison of measurements and models of bed stress, bedforms and suspended sediments under combined currents and waves. Coastal Engineering, 62, 19-30.

Bonnefille, R. 1963. Essais de synthese des lois debut d'entrainment des sediment sous l'action d'un courant en regime uniform. Chatou: Bulletin Du CREC, No. 5.

Borja, Á. and Collins, M. 2004. Preface. Elsevier Oceanography Series. Elsevier. 70: v-viii.

Bowden, K. F. 1978. Physical problems of the benthic boundary layer. Geophysical Surveys, 3: 255 – 296.

Bowden, K.F. and Ferguson, S.R. 1980. Variations with height of the turbulence in a tidally-induced bottom boundary layer. Marine Turbulence, Proceedings of the 11th International Liége Colloquium on Ocean Hydrodynamics, 259-286.

Brunn, P., 1978. Stability of Tidal Inlets. Theory and Engineering. Elsevier Scientific Publishing, Amsterdam, The Netherlands, 509 pp.

Bruun, P. and F. Gerritsen. 1959. Natural by-passing of sand at coastal inlets. Journal of the Waterways and Harbors Division 85: 75 - 107.

Cearreta, A., Irabien, M.J. and Pascual, A. 2004. Human activities along the Basque coast during the last two centuries: geological perspective of recent anthropogenic impact on the coast and its environmental consequences. Elsevier Oceanography Series, 70: 27-50.

Cheng, C., Song, Z., Wang, Y., and Zhang, J. 2013. Parametrized expresssions for an improved Rouse equation. International Journal of Sediment Research, 28: 523-534.

Chadwick, A., Morfett, J., and Borthwick, M. 2004. Hydraulics in civil and environmental engineering. CRC Press. 4th Edition. 680 pp.

Chow, V.T. 2009. Open channel hydraulics. Blackburn Press, 680 pp.

Collins, M.B. and Rigler, J.K. 1982. The use of settling velocity in defining the initiation of motion of heavy mineral grains, under unidirectional flow. Sedimentology, 29: 419 – 426.

Conley DC, Falchetti S, Lohmann IP, Brocchini M. 2008. The effects of flow stratification by non-cohesive sediment on transport in high-energy wave driven flows. Journal of Fluid Mechanics, 610:43–67.

Cowell, P. J., Thom, B. G., Jones, R. A., Everts, C. H. and Simanovic, D. 2006. Management of Uncertainty in Predicting Climate-Change Impacts on Beaches. Journal of Coastal Research, 232-245.

Dalrymple, R.W., Zaitlin, B.A., and Boyd, R. 1992. Estuarine facies model: conceptual basis and stratigraphic implications. Journal of Sedimentary Petrology, 62: 1130-1146.

Davies, J. L. 1964. A morphogenic approach to world shorelines. Zeitschrift für. Geomorphologie, 8: 27 - 42.

Davis, Jr. R. and Zarillo, G. 2003. Human-induced changes in back-barrier environments as factors in tidal inlet instability with emphasis on Florida. Coastal and Hydraulic Engineering Technical Note. US Army Corps of Engineers. IV-57. 18pp.

Dean, R. and Dalrymple, R. 2004. Coastal processes with engineering applications. Cambridge, Cambridge University Press, 210 - 266.

Defendi, V., Kovačević, V., Arena, F., and Zaggia, L. 2010. Estimating sediment transport from acoustic measurements in the Venice lagoon inlets. Continental Shelf Research, 30: 883-893.

Delft Hydraulics, 1982. Initiation of motion and suspension, Development of concentration profiles in a steady uniform flow without initial sediment load. Report M1531 – III, Delft The Netherlands.

Dyer, K.R. 1970. Current velocity profiles in a tidal channel. Journal of Geophysics, 22: 153-161.

Dyer, K.R. 1971. The distribution and movement of sediment in the Solent, southern England. Marine Geology, 11: 175-187.

Dyer, K, R., 1980. Velocity profiles over a rippled bed and the threshold of movement of sand. Estuarine and Coastal Marine Science, 10: 184 – 199.

Dyer K. R. 1986. Coastal and Estuarine Sediment dynamics. John Wiley & Sons. Chichester. 342 pp.

Dyer, K.R. and Soulsby, R.L. 1988. Sand transport on the continental shelf. Annual Review Fluid Mechanics, 20: 295-324.

Einstein, H.A. 1950. The bed-load function for sediment transport in open channel flow.Technical Bulletin No. 1026, USDA, Washington, D.C.

Engelund, F., 1965. A criterion for the occurrence of suspended load. La Houille Blanche, 8: 7.

Engelund, F. and Fredsϕe, J. 1976. A sediment transport model for straight alluvial channels. Nordic Hydrology, 7: 293-306.

Escoffier, F. 1977. Hydraulics and stability of tidal inlets. GITI Report 13, U.S. Army Engineer Waterways Experiment Station, Vicksburg, MS. 75 pp.

Evans, G. and Prego, R. 2003. Rías, estuaries and incised valleys: is a ría an estuary? Marine Geology, 196: 171-175.

FitzGerald, D.M. 1982. Sediment bypassing at mixed energy tidal inlets. Proceedings of the Eighteenth Coastal Engineering Conference, 1094–1118.

FitzGerald, D. 2005. Tidal inlets. Encyclopedia of Coastal Science. Dordrecht, Springer: 958 - 964.

Folk, R.L. and Ward, W.C., 1957. Brazos River bar: A study in the significance of grain size parameters. Journal of Sedimentary Petrology, 27(1): 3-26.

Fredsϕe, J. and Deigaard, R., 1992. Mechanics of Coastal sediment transport. Advanced Series on Ocean Engineering, 3. World Scientific Publishing Co. Pte. Ltd.

Fredsϕe J. 1993. Modelling of non-cohesive sediment transport processes in the marine environment. Coastal Engineering, 1993, 21:71–103.

Glenn, S. and Grant, W. 1987. A suspended sediment stratification correction for combined wave and current flows. Journal of Geophysical Research, 92: 8244-8264.

González, M., Uriarte, A., Fontán, A., Mader, J., and Gyssels, P. 2004. Marine dynamics. Elsevier Oceanography Series, 70: 133-157.

Goodwin, P. 1996. Predicting the stability of tidal inlet for wetland and estuary management. Journal of Coastal Research (SI 23): 93 - 102.

Green, M. and Black, K. 1999. Suspended-sediment reference concentration under waves: field observations and critical analysis of two predictive models. Coastal Engineering, 38: 115-141.

Ha, H.K., Maa, J.P.-Y., Park, K., and Kim, Y.H. 2011. Estimation of high-resolution sediment concentration profiles in bottom boundary layer using pulse-coherent acoustic Doppler current profilers. Marine Geology, 279: 199-209.

Hayes, M.O., 1975. Morphology of sand accumulation in estuarie: An introduction to the symposium. Gelogy and Engineering, Academic Press, 3 – 22.

Hayes, M.O. 1980. General morphology and sediment patterns in tidal inlets. Sedimentary Geology, 26: 139-156.

Heathershaw, A.D. 1979. The turbulent structure of the bottom boundary layer in a tidal inlet. Journal of Geophysical Research, 58: 395-430.

Heathershaw, A. D. 1981. Comparisons of measured and predicted sediment transport rates in tidal currents. Developments in Sedimentology. Elsevier, 32: 75-104.

Helley, E.J. and Smith, W. 1971. Development and calibration of a pressure differencebedload sampler, USGS Water Resources Division Open File Report.

Helsby, R. 2008. Sand transport in northern Venice lagoon through the tidal inlet of Lido, PhD Thesis, University of Southampton, Southampton, UK, 260 pp.

Hill, P.S., Nowell, A.R.M., and Jumars, P.A., 1988. Flume evaluation of the relationship between suspended sediment concentration and excess boundary shear stress. Journal of Geophysical Research, 93: 12499 – 12500.

Hume, T. and Herdendorf, C. 1988. Furkert-Heath' relationship for tidal inlet stability reviewed. New Zealand Journal of Marine and Freshwater Research 22(1): 129 - 134.

Jarrett, J.T. 1976. Tidal prism - inlet area relationships. GITI Report No. 3, U.S. Army Engineer Waterways Experiment Station, Vicksburg, MS. 60 pp.

Kassem, H. 2012. Intermittent turbulent bursting and sediment resuspension in the nearshore: analysis of data from BARDEX II. MSc Thesis, University of Southampton, Southampton, UK, 109 pp.

Khorram, S. and Ergil, M. 2010. Most influential parameters for the bed-load sediment flux equations used in alluvial rivers. Journal of American Water Resources Association

Kim, S.-C., Friedrichs, C.T., Maa, J.P.-Y., and Wright, L.D. 2000. Estimating bottom stress in tidal boundary layer from acoustic Doppler Velocimeter data. Journal of Hydraulic Engineering, 126: 399-406.

Kineke, G.C. and Sternberg, R.W. 1989. The effect of particle settling velocity on computed suspended sediment concentration profiles. Marine Geology, 90: 159-174.

Komar, P.D., 1996. Tidal-inlet processes and morphology related to the transport of sediments. Journal of Coastal Research, 23 -45.

Komar, P.D. and Clemens, K.E., 1985. The relationship between a grain's settling velocity and threshold of motion under unidirectional currents. Journal of Sedimentary Petrology, 56: 258-266.

Komar, P.D. and Miller, M.C., 1973. The threshold of sediment movement under oscillatory water waves. Journal of Sediment Petrology, 43: 1101-1110.

Kraus, N. 2009. Engineering of tidal inlets and morphologic consequences. Handbook of Coastal and Ocean Engineering. Y. C. Kim. Singapore, World Scientific: 867 - 901.

Kraus, N., Lohrmann, A., and Cabrera, R. 1994. New acoustic meter for measuring £D laboratory flows. Journal of Hydraulic Engineering, 120: 406-412.

Lambkin, D. 2004. The effects of variation in wave period and flow asymmetry in sediment dynamics. PhD Thesis, University of Southampton, Southampton, UK, 256 pp.

Lane, E.W. and Kalinske, A.A., 1941. Engineering calculations of suspended sediments.Transactions of the American Geophysical Union, 22: 603-607.

Lee, G., Dade, W.B, Friedrichs, C.T., and Vincent, C.E., 2004. Examination of reference concentration under waves and currents on the inner shelf. Journal of Geophysical Research, 109: 1 - 10.

Lees, B.J., 1981. Sediment transport measurements in the Sizewell-Dunwich Banks area, East Anglia, UK. In: Holocene Marine Sedimentation in the North Sea Basin, Special Publication no.5 of the International Association of Sedimentologists, Blackwell, Oxford, 269 – 281.

Leeder, M. R. 1982. Sedimentology: process and product. London, Chapman & Hall.

Lefebvre, A. 2009. Bed roughness over vegetated beds: sonar imaging techniques and effect on unidirectional currents, PhD Thesis, University of Southampton, UK, 212 pp.

Liu, Z., 2001. Sediment transport. Aalborg University, Aalborg, Denmark.

Liria, P., Garel, E. & Uriarte, A. 2009. The effects of dredging operations on the hydrodynamics of an ebb tidal delta: Oka Estuary, northern Spain. Continental Shelf Research, 29: 1983-1994.

Long, B. and Montreuil, S. 2011. Evolution of ripple field architecture during sediment transport, as measured by CT scanning. InTech, 237-260.

Lorenzo, F., Alonso, A., and Pagés, J.L. 2003. Evolución y erosion comparada de tres sistemas playa/flecha en las rías de Ortigueira, O Barqueiro y Viveiro (Galicia, España). Cuaternario y Geomorfología, 17: 75-89.

Lueck, R., and Victoria, B., 2009. Turbulenc in the benthic boundary layer, Elements of Physcial Oceanography: A derivative of the *Encyclopedia of Ocean Sciences*, 311.

Lueck, R. and Lu, Y. 1997. The logarithmic layer in a tidal channel. Continental Shelf Research, 17(14): 1785-1801.

Mehta, A.J. and Joshl, P.B. 1988. Tidal inlet hydraulics. Journal of Hydraulic Engineering, ASCE, 114: 1321-1338.

McCave, I. N. 1971. Sand waves in the North Sea off the coast of Holland. Marine Geology, 10: 199-225.

McCave, I.N. 1984. Size spectra and aggregation of suspended particles in the deep ocean. Deep Sea Research Part A. Oceanographic Research Papers, 31: 329-352.

Monge Ganuzas, M. 2008. Evolucion temporal de la dinimica sedimentaria en el esturio inferior del Oka (Reserva de la Biosfera de Urdaibai): una herramienta geologica para la Gestion Integrada de Zonas Costeras. PhD Thesis, UPV/EHU, Spain, 576 pp.

Monge-Ganuzas, M., Cearreta, A. and Iriarte, E. 2008. Consequences of estuarine sand dredging and dumping on the Urdaibai Reserve of the Biosphere (Bay of Biscay): the case of the “Mundaka left wave”. Journal of Iberian Geology, 34: 215-234.

Monge-Ganuzas, M., Cearreta, A. and Evans, G. 2013. Morphodynamic consequences of dredging and dumping activities along the lower Oka estuary (Urdaibai Biosphere Reserve, south eastern Bay of Biscay, Spain). Ocean & Coastal Mangement,77: 40-49.

Monge-Ganuzas, M., Evans, G. and Cearreta, A. 2014. Sand-spit accumulations at the mouths of the eastern Cantabrian estuaries: The example of the Oka estuary (Urdaibai Biosphere Reserve). Quaternary International. In press.

Moore, S.A., Coz, J. Le., Hurther, D., and Paquier, A. 2012. On the application of horizontal ADCPs to suspended sediment transport surveys in rivers. Continental Shelf Research, 46: 50-63.

Morang, A. and Parson, L. 2002. Coastal Morphodynamics. Coastal Engineering Manual, Part IV, Engineering Manual 1110-2-1100. U.S. Army Corps of Engineers. Washington D.C, 86 pp.

Murray, R.B., Hodgson, D., Thorne, P. 2012. Wave groups and sediment resuspension process over evolving sandy bedforms. Continental Shelf Research 46: 16-30.

Nielsen, P. 1984. Field measurements of time-averaged suspended sediment concentrations under waves. Coastal Engineering, 8: 51-72.

Nielsen, P. 1986. Suspended sediment concentrations under waves. Coastal Engineering, 10: 23-31.

Nielsen, P. 1992. Coastal bottom boundary layers and sediment transport. Advanced Series on Ocean-Engineering, 4. World Scientific Publishing, Singapore, 340 pp.

Nielsen, P. 2009. Coastal and estuarine processes. Advanced Series on Ocean-Engineering, 29. World Scientific Publishing, Singapore, 360 pp.

Niño, Y., Lopez, F. and Garcia, M., 2003. Threshold for particle entrainment into suspension. Sedimentology, 50(2): 247-263.

O’Brien, M.P. 1931. Estuary tidal prism related to entrance areas. Civil Engineering, 1(8): 738-739.

Paphitis, D. 2001. Sediment movement under unidirectional flow: an assessment of empirical threshold curves. Coastal Engineering, 43(3-4): 227 - 245.

Pascual, A., Cearreta, A., Rodriguez-Lazaro, J. & Uriarte, A. 2004. Geology and Palaeoceanography. Elsevier Oceanography Series. Elsevier, 70: 53-73.

Pope, S.B. 1991. Application of the velocity-dissipation probabulity density function model in homogenous turbulent flows. Phys. Fluids A, 3(8): 1947-1957.

Pope, N.D., Widdows, J., and Brinsley, M.D. 2006. Estimation of bed shear stress using the turbulent kinetic energy approach – a comparison of annular flume and field data. Continental Shelf Research, 26: 959-970.

Prandtl, L. 1925. Bericht uber untersuchungen zur ausgebildeten turubulenz. Zs. Angew. Math. Mech., 5:136-139.

Rallo, A. and Borja, A. 2004. Marine research in the Basque Country: an historical perspective. Elsevier Oceanography Series, 70: 3-25.

Reynolds, O. 1883. An experimental investigation of the circumstances which determine whether the motion of water shall be direct or sinuous, and of the law of resistance in parallel channels. Philosophical Transactions of the Royal Society of London, 174: 935-982.

Rose, C. and Thorne, P. 2001. Measurements of suspended sediment transport parameters in a tidal estuary. Continental Shelf Research, 1551 - 1575.

Rouse, H. 1937. "Modern conceptions of the mechanics of turbulence." Transactions of the American Society of Civil Engineers 102: 436 - 505.

Samaga, B.R., Ranga-Raju, K.G. and Garde, R.J., 1986. Suspended load transport of sediment mixtures. Journal of Hydraulic Engineering, 11: 1019-1034.

Shields, A., Ott, W.P., and van Uchelen, J.C. 1936. Application of similarity principles and turbulence research to bed-load movement. Technical Report. California Institute of Technology, Pasadena, CA., 47 pp.

Smith, P. E., Counts, R. C. & Clutter, R. I. 1968. Changes in Filtering Efficiency of Plankton Nets Due to Clogging Under Tow. Journal du Conseil, 32, 232-248.

Smith, R. L. and S. R. McLean 1977. Spatially averaged flow over a wavy surface. Journal of Geophysical Research, 1735 - 1746.

Soulsby, R.L. 1980. Selecting record length and digitization rate for near-bed turbulence measurements. Journal of Physical Oceanography, 10: 208–219.

Soulsby, R.L. 1983. The bottom boundary layer of shelf seas, in *Physical Oceanography of Coastal and Shelf Seas*, Elsevier Sci., New York, 189-266.

Soulsby, R.L. 1997. Dynamics of Marine Sands: A Manual for Practical Applications. Thomas Telford Publications, London, 249 pp.

Soulsby, R.L., Davies, A.G., and Wilkinson, R.H. 1983. The detailed processes of sediment transport by tidal currents and by surface waves. Institute of Oceanographic Sciences. Report No. 152, 80 pp.

Tennekes, H., Lumley, J.L. 1972. A first course in turbulence, The Massachusetts Institute of Technology Press, Cambridge-Massachusetts, 300 pp.

Thompson, C., Amos, C., Jones, T., and Chaplin, J. 2003. The manifestation of fluid-transmitted bed shear stress in a smooth annular flume: a comparison of methods. Journal of Coastal Research, 19: 1094 – 1103.

Thorn, M.F.C., 1975. Deep tidal flow over a fine sand bed. Proceedings of XVIth Congress IAHR, Sao Paolo, 217 – 223.

Thwaites, F.T. and Williams III, A.J. 1996. Develoment of modular acoustic velocity sensor. OCEANS'96. MTS/IEEE. Prospects for the 21st Century Conference Proceeding, 2: 607-612.

Uriarte, A., Collins, M., Cearreta, A., Bald, J., and Evans, G. 2004. Sediment supply, transport and deposition: contemporary and Late Quaternary eveolution. Elsevier Oceanography Series, 70: 97-131.

Usabiaga, J.I., Aguirre, J.S., Valencia, V., and Borja, A. 2004. Climate and Meteorology: variability and its influence on the Ocean. Elsevier Oceanography Series, 70: 75-95.

Van Rijn, L. 1984a. Sediment transport, Part I: bed-load transport. Journal of Hydraulic Engineering, 110: 1431-1456..

Van Rijn, L. 1984b. Sediment transport, Part II: Suspended load transport. Journal of Hydraulic Engineering, 110: 1613-1641.

Van Rijn, L. 1993. Principles of sediment transport in rivers, estuaries, and coastal seas. The Netherlands, Aqua Publications, 715 pp.

Van Rijn, L. C. 1998. Principles of coastal morphology. Amsterdam, The Netherlands, Aqua Publications, 730 pp.

Van Rijn, L.C., 2007. Manual sediment transport measurements in rivers, estuaries and coastal seas. Aqua publications.

Van Rijn, L. 2011. Principles of fluid flow and surface waves in rivers, estuaries, and seas and oceans. Vol 11. Amsterdam, The Netherlands: Aqua Publications.

Vanoni, V.A., 1975. Sedimentation engineering, Hydraulics Division, ASCE, Reston, Va. 424 pp.

Vanoni, V.A. 1984. Fifty years of sedimentation. Journal of Hydraulic Engineering, 110: 1021-1057.

Vianna, C. 2012. An analysis of the use of ADCP in estimating sand transport in a tidal inlet, Mundaka, Northern Spain, Msc Dissertation, University of Southampton, UK, Inedit, 80 pp.

Villatoro, M., Amos, C., Umgiesser, G., Ferrarin, C., Zaggia, L., and Thompson, C. 2010. Sand transport measurements in Chioggia inlet, Venice lagoon: Theory versus observations. Continental Shelf Research, 30: 1000 – 1018.

Wiberg, P. and Smith, J. 1985. A theoretical model for saltating grains in water. Journal of Geophysical Research, 90: 7341-7354.

Wright, S. and Parker, G. 2004. Density stratification effects in sand-bed rivers. Journal of Hydraulic Engineering, 130: 783-795.

Yalin, M. S. 1972. Mechanics of sediment transport, Pergamon Press, Oxford, New York, 290 pp.

Yang, C. T. 1996. Sediment transport, theory and practice, McGraw–Hill, New York, 396 pp.